Design and Synthesis of Porous Materials for Visible Light-Driven Carbon Dioxide Reduction: A Pathway to Sustainable Energy Solutions

A Thesis Submitted for the Degree of

Doctor of Philosophy

in the Faculty of Science

by

Anupam Jana

Department of Chemistry

JADAVPUR UNIVERSITY, KOLKATA - 700 032

INDIA

June, 2025

Dr. Asamanjoy Bhunia, Ph. D.
Assistant Professor
Department of Chemistry
Inorganic Chemistry Section

JADAVPUR UNIVERSITY
Kolkata – 700 032, India
Telephone:
abhunia.chemistry@jadavpuruniversity.in

CERTIFICATE FROM THE SUPERVISOR

This is to certify that the thesis entitled “**Design and Synthesis of Porous Materials for Visible-Light-Driven Carbon Dioxide Reduction: A Pathway to Sustainable Energy Solutions**” submitted by Mr. Anupam Jana, who registered for the Ph. D. (Science) degree at Jadavpur University on 25th november 2020, is an original piece of research carried out under the supervision of Dr. Asamanjoy Bhunia.

I further certify that this thesis is entirely based on the candidate's independent research work and has not been submitted, in whole or in part, for any other degree, diploma, or academic award at any institution prior to this submission.

Asamanjoy Bhunia
17.06.2025

……………………………………………………………..

June, 2025 (Dr. Asamanjoy Bhunia)

Jadavpur Signature of the supervisor date with official seal

Dedicated to
Baba and Maa
whose blessings, endless love and inspiration
empower me to move forward

Acknowledgement

It has been an incredibly amazing and rewarding adventure to pursue and get my Ph.D. in Chemistry. It has seemed like the fulfilment of a lifelong ambition. From enrolling as a research scholar to finally submitting my thesis, the entire experience has been both intellectually enriching and personally transformative. This journey would not have been possible without the unwavering support, guidance, encouragement, and love of many individuals who have been with me every step of the way. Now I want to acknowledge those persons who played a role directly or indirectly for the successful completion of my thesis.

First and foremost, I would like to express my deepest gratitude to my supervisor, Dr. Asamanjoy Bhunia, Department of Chemistry, Jadavpur University, Kolkata – 700032. His constant encouragement, insightful guidance, and the freedom he gave me to explore my ideas have been instrumental in shaping my research. I am especially thankful for his meticulous feedback and patience while reviewing my thesis, which played a crucial role in bringing this work to completion.

I would also like to extend my sincere thanks to the members of my Research Advisory Committee (RAC): Prof. Hari Pada Nayek (Subject Expert, Department of Applied Chemistry, IIT (ISM), Dhanbad), Prof. Kajal Krishna Rajak (Head, Department of Chemistry, JU), and Dr. Asamanjoy Bhunia (Supervisor). Their valuable suggestions and consistent support during the RAC meetings greatly helped refine my work. I am also thankful to Prof. Swapan Kumar Bhattacharya (Former Head, Department of Chemistry) and all other faculty members of the department for fostering a collaborative and research-friendly environment, and for always being approachable and supportive.

My heartfelt thanks to my wonderful lab-mates — Aruntima Das, Arijit Maity, Osman Ali, and Sinthia Saha. Their shared knowledge, and emotional support kept me motivated through challenging phases, and I am truly grateful to have been part of such a warm and encouraging group.

I am also thankful to all my collaborators, especially Dr. Bibhutibhushan Show (Department of Chemistry, Kolkata) and Dr. Preeti A. Bhobe (Department of Physics, IIT Indore) for their valuable contributions and genuine enthusiasm in our collaborative efforts.

My sincere appreciation goes to all the faculty members and non-teaching staff of the department, whose helpful attitude made day-to-day life in the lab easier. I also thank the authorities of Jadavpur University for providing the infrastructure and support necessary for my research. I am grateful to the Council of Scientific & Industrial Research (File No. 09/028(1008)/2017-EMR-I) for awarding me the fellowship that sustained me throughout this journey.

I also wish to thank Dr. Sandeep Dey for his support, especially with the X-ray Photoelectron Spectroscopy (XPS) measurements.

I'm also thankful to Uday Shee, Taposi Trishna Neog, Ritika Samanta, Debasish Jana, Jayanta Mondal, Prasenjit Giri, Dibendu Dey, Mainak Bose, and several other friends and well-wishers who stood by me throughout this journey with their constant encouragement.

Finally, and most importantly, I owe everything to my parents, Sri Ajit Kumar Jana and Smt. Alpana Jana. Words can never truly express my gratitude for them. Their love, sacrifices, and unwavering belief in me have been the bedrock of my life. If I have come this far, it is because of them. I know I can never repay their love, but I will forever strive to reflect their strength and selflessness in all that I do

Anupam Jana
18|06|2025

Anupam Jana
Department of Chemistry
Jadavpur University

ABSTRACT

Carbon dioxide (CO_2) reduction has emerged as a vital approach to address two pressing global challenges: climate change and sustainable resource management. As a major greenhouse gas, CO_2 has significantly contributed to global warming, primarily due to rapid industrialization and urban expansion over the past century. To mitigate its environmental impact, CO_2 can be treated not as waste but as a valuable raw material. Among the emerging technologies, photocatalytic CO_2 reduction stands out for its ability to convert CO_2 into valuable products such as fuels and chemicals by harnessing renewable, abundant, and inexpensive solar energy. This strategy not only helps reduce greenhouse gas emissions but also supports the development of a circular carbon economy, while simultaneously addressing the global energy crisis by enabling the production of value-added fuels and chemicals from CO_2. This scientific approach embraces the concept of transforming waste into valuable resources, paving the way toward a cleaner and more sustainable future.

To address these challenges, in this thesis, we focus on the design and development of a series of porous polymers including covalent triazine-based frameworks (CTFs), metal-organic frameworks (MOFs), and conjugated microporous polymers (CMPs) with diverse backbone architectures. These porous materials have been further employed as solid supports for the incorporation of redox-active metal centres and metal coordination complexes through various post-synthetic modification strategies. This approach aims to develop robust and efficient photocatalysts for sustainable CO_2 reduction into value-added chemicals under visible light irradiation. The core findings and detailed discussions are presented across four main chapters, namely **Chapters** 2, 3, 4, and 5.

In **Chapter 2**, we report the development of a series of Co^{2+}-loaded covalent triazine-based framework (CTF) photocatalysts, prepared via a simple deposition method. The incorporation of isolated Co^{2+} sites significantly enhanced the photocatalytic reduction of CO_2 to CO, achieving 1515 μmol/gm of CO, approximately 37 times higher than the pristine CTF-TPE (40 μmol/gm) over 2 hours. EXAFS and XPS analyses confirmed the presence of single-site Co^{2+} centers and their crucial role in catalytic efficiency.

In **chapter 3**, we report the solvothermal synthesis of Zn (II)- and Co (II)-based imidazolate framework photocatalysts, including IFP-1(Zn), and IFP-5(Co), for CO_2 reduction. Furthermore, we have also prepared a metal exchanged IFP-1(Zn/Co) through partial substitution of Zn (II) with redox-active Co (II) in IFP-1(Zn). with a marked enhancement in

CO evolution (637 µmol g^{-1}) compared to IFP-1(Zn) (29 µmol g^{-1}). Among these, IFP-5(Co) exhibited the highest activity (1174 µmol g^{-1}), attributed to the presence of catalytically active cobalt centers.

In **Chapter 4**, we report the first successful incorporation of a Ru (II) bis-terpyridine complex, $[Ru(cptpy)_2]$, into a Zr-based MOF featuring a naphthalene diimide (NDI) linker via solvent-assisted ligand exchange (SALE). The resulting hybrid, Zr-NDI@Ru-tpy, exhibited excellent photocatalytic CO_2 reduction under visible light, achieving a CO production rate of 2449 µmol g^{-1} h^{-1} with 97% selectivity and a turnover number (TON) of 123 over 6 hours. Mechanistic insights were supported by photophysical, electrochemical, and in situ DRIFT spectroscopic analyses.

In **chapter 5,** we report the design and synthesis of two metal–salen-based conjugated microporous polymers, salen-CMP@Co and salen-CMP@Zn, as photocatalysts for visible-light-driven CO_2 reduction. Both materials efficiently generated syngas (CO + H_2), with salen-CMP@Co showing superior activity, achieving CO and H_2 evolution rates of 3041 and 20,212 µmol g^{-1}, respectively. Importantly, the syngas composition could be precisely tuned by adjusting the acetonitrile-to-water ratio in the reaction medium.

Asamanjoy Bhunia
17.06.2025

CONTENTS

Page Number

CHAPTER 1

CHAPTER 2

List of Figures

Figures caption	**Page No**

Figures caption **Page No**

List of Tables

Chapter 1

Introduction and literature survey

1. Introduction and literature survey:

1.1 Excessive use of non-renewable fossil fuels and its effects on society, economy, and the environment

The continuous growth of the global economy, rapid population expansion, and advancements in technology have collectively led a significant surge in the worldwide primary energy consumption.[1] In 2012, the global energy consumption rate was recorded at 16.3 TW, and it is projected to rise substantially, reaching approximately 40 TW by 2050 and nearly 60 TW by 2100.[2] To meet this escalating energy demand, fossil fuels such as oil, coal and natural gas still serve as the primary energy sources, supplying around 80% of the global demand for energy. Fossil fuels are expected to continue being the leading primary source of energy until 2050 (Figure 1.1).[3] These energy sources, formed from the photosynthetic activity of ancient organisms over millions of years, continue to supply the majority of the energy required for modern technologies, residential heating, and the production of various chemicals and materials essential for daily life. This continuous rise in fossil fuel consumption, particularly in densely populated regions of the world, has significant social, economic, and environmental implications, both positive and negative. On the positive side, they contribute the highest

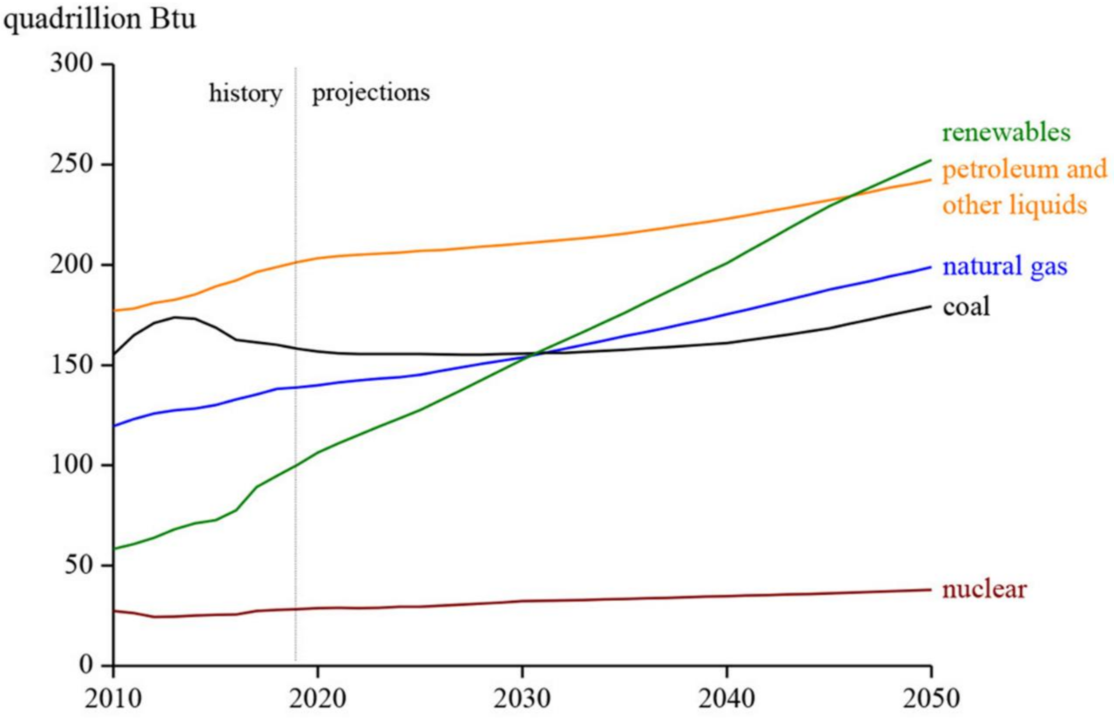

Figure 1.1: Global primary energy consumption by different energy sources. Copyright 2019 U.S. Energy Information Administration (EIA).[4]

number of employment opportunities and generate substantial tax revenues. However, they also present the greatest risks to public health and social well-being, posing significant challenges for communities and societies. The growing demand for energy can lead to higher energy unit prices, which contributes to energy-driven inflation and potentially hinders economic growth. However, the availability of these reserves is finite, and their depletion is inevitable. Even before reaching a state of scarcity, the continuous and growing reliance on fossil fuels (gas, oil, and coal) is expected to have detrimental effects on the ecosystems.

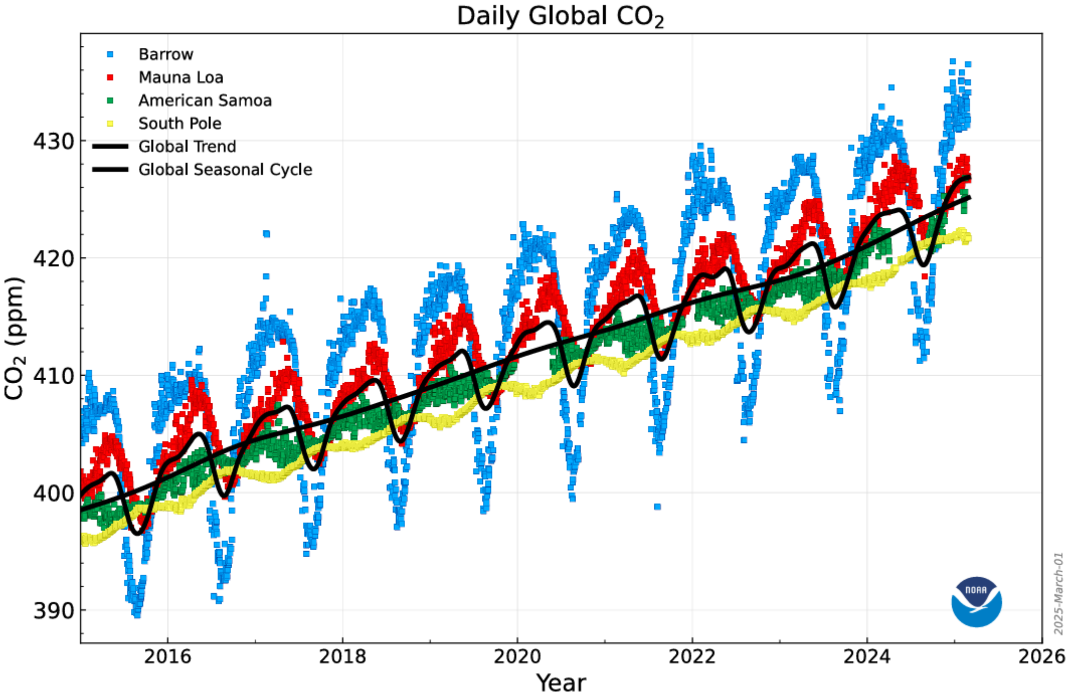

Figure 1.2: The daily averaged CO_2 concentrations are recorded from four Global Monitoring Laboratory baseline observatories. This data is taken from the National Oceanic and Atmospheric Administration (NOAA).[5]

The combustion of fossil fuels to fulfil the global energy needs results in the release of significant greenhouse gases with carbon dioxide (CO_2) being a primary by-product. Analysis of daily observations collected by the Global Monitoring Laboratory across four international observatories (Figure 1.2) demonstrates a substantial upward trend in global CO_2 concentrations. The Intergovernmental Panel on Climate Change (IPCC) projects that CO_2 concentration may reach as high as 590 ppm by 2100, potentially leading to a global temperature increase of approximately 1.9 °C.[6] This increasing level of atmospheric carbon dioxide leads to the severe environmental consequences, contributing to global warming, ocean acidification, and extreme weather patterns which threaten ecosystems and human settlements. Changes in climate patterns also intensify droughts, storms, and wildfires, disrupting agriculture, water resources, and biodiversity. In addition to their harmful environmental effects, fossil fuels are finite resources, and their prices fluctuate significantly. These price variations affect industries that produce and consume oil, disrupting revenues and reducing consumers' ability to afford goods and services.[7] Hence, energy shortages, along with rising prices and limited supply, can lead to social instability and increased energy poverty. Therefore, it is imperative to develop strategies for alternative fuels and the reduction of anthropogenic CO_2 emissions to maintain a balanced atmospheric CO_2 level, thereby promoting sustainable energy solutions and combating climate change.

1.2 Mitigating the increasing level of CO_2

Reducing emissions and mitigating atmospheric CO_2 concentrations are pressing global challenges that require urgent development of the sustainable and carbon-neutral energy technologies. Given that Fossil fuels will likely to be remain a leading source of energy for the near future, one of the most effective approaches to lowering anthropogenic CO_2 emissions is capturing CO_2 directly from origins like as flue gases emitted by power plants that rely on fossil fuels. This can be achieved through carbon capture and storage (CCS) technologies. However, the widespread implementation of CCS faces several challenges, primarily due to the high energy demands associated with CO_2 separation, purification, compression, transportation, and storage.[8] In industrial applications, the most commonly used method for CO_2 capture is the direct chemisorption of CO_2 using alcohol-amine solutions. While this approach offers high capture efficiency, it presents significant challenges for large-scale implementation due to its high regeneration energy requirements and its corrosive effects on equipment.[9] Additionally, CCS technology faces economic and technical challenges, including high capture costs and concerns regarding the long-term safety of CO_2 sequestration, posing significant obstacles to the advancement of CCS technologies.[9]

Given these limitations, an emerging approach involves not only capturing CO_2 but also catalytically transforming it into valuable chemicals including CO, CH_4, CH_3OH, C_2H_5OH, etc. This strategy builds upon CCS by transforming sequestered CO_2 into useful products, offering a more sustainable and economically viable alternative which addresses contemporary environmental concerns and the energy crisis. By transforming CO_2 into useful products, this strategy provides a dual benefit: reducing greenhouse gas emissions while simultaneously generating valuable resources, making it an exciting area for future research and development in carbon management. In context to conversion of CO_2 to value added chemicals, different state-of-art catalytic strategies have been developed such as thermo-catalytic,[10] electrocatalytic[11] and enzymatic approaches.[12] However, these technologies face challenges such as high operational costs, secondary dependence on fossil fuels, and the need for complex reaction conditions, limiting their feasibility in meeting the demands of the modern, competitive world.

On the contrary, visible-light-induced photocatalytic reduction of CO_2 is becoming recognized as a promising approach over the past few years due to the abundance of solar energy on the planet which is pollution-free, inexhaustible and cost-free. Solar energy is generated by continuous nuclear fusion reactions within the sun, and only a fraction of this energy reaches the Earth's atmosphere. Although only a tiny fraction of the sun's total radiant energy, approximately 1 in 2.2 billion reaches Earth's atmosphere,[13] it remains an immense energy source capable of supporting industrial production and daily human activities. It is worth mentioning that, the solar energy that reaches the Earth's surface, estimated at around 1.3×10^5 terawatts, is nearly 10,000 times greater than the world’s current energy demand, highlighting its immense and untapped potential as a sustainable power source.[14] Consequently, transforming this plentiful solar radiation into chemical forms of energy through photocatalytic CO_2 reduction into fuels (H_2, CO, HCOOH, HCHO, CH_3OH, CH_4) has gained widespread recognition from the global scientific community, promoting the advancement of artificial photocatalytic systems that mimic natural photosynthesis. One of the key benefits of photocatalysis is its ability to harness solar energy, providing a renewable and abundant energy source for CO_2 conversion without the need for external energy inputs, unlike thermo-catalysis, which relies on high temperatures. Additionally, photocatalysis operates under mild environments, typically at room temperature and normal pressure, making it more energy-efficient and cost-effective compared to thermo-catalytic and electrocatalytic methods that require elevated temperatures or electricity from potentially non-renewable sources.

1.3 Basics of photocatalytic CO_2 reduction

Over the course of billions of years, plants along with other photosynthetic organisms have sustained aerobic life on Earth by producing oxygen and organic compounds through photosynthesis. This process converts carbon dioxide (CO_2) and water (H_2O) into oxygen (O_2)

and carbohydrates, such as glucose ($C_6H_{12}O_6$), using energy from sunlight.[15] Essentially, sunlight is converted into chemical energy and stored in these organic molecules.

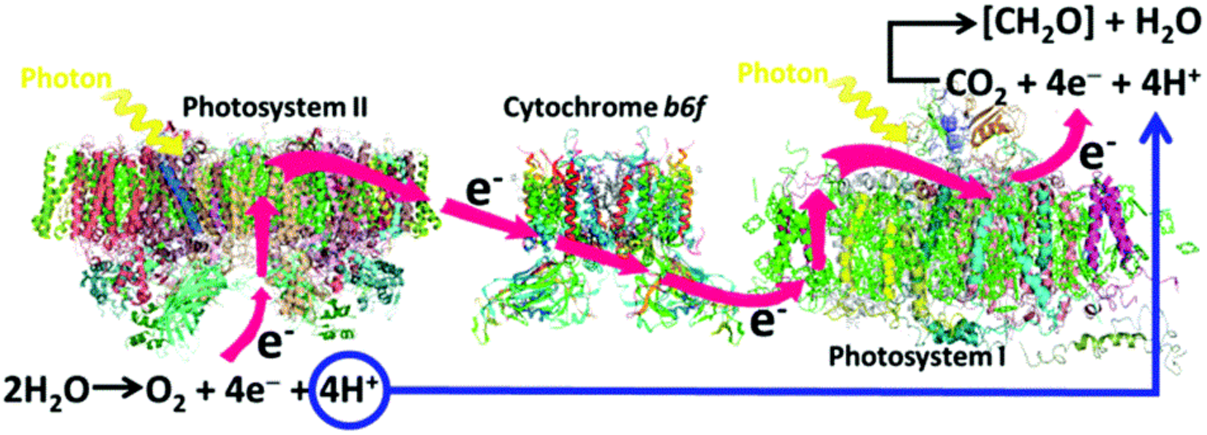

Figure 1.3: Diagrammatic illustration of the natural photosynthetic pathway within the photosystems. The diagram was adapted with permission from reference 16.

Photosynthesis relies on the coordinated functions of photosystem II (PS II) and photosystem I (PS I).[17,18] In PS II, water molecules are split under the influence of sunlight, generating oxygen, along with four protons and an equal number of electrons. These protons and electrons are subsequently transported by cytochrome *b6f* to PS I, where they participate in the reduction of CO_2, ultimately leading to carbohydrate production (Figure 1.3).

The overall process of photosynthesis is highly complex, making it impossible to precisely replicate their structures and compositions. Although, their fundamental functions and associated chemical reactions can be mimicked to achieve artificial photosynthesis (AP). This approach efficiently harnesses solar energy, converting it into chemical energy that can be stored in the form of synthetic fuels for long-term use (Figure 1.3). Consequently, there is significant scientific interest in developing efficient artificial photocatalytic systems that can capture solar energy and convert CO_2 into valuable chemical fuels through photoreduction processes.

It is known that CO_2 is a chemically stable molecule with a linear and symmetrical structure featuring carbon atoms in its high oxidation state. The average bond dissociation energy of the C=O double bond is approximately 804.4 kJ mol^{-1} at 298 K, reflecting its thermodynamic stability. This inherent stability makes CO_2 reduction thermodynamically challenging and requires significant energy input to drive the reaction.[19,20] Moreover, the use of catalysts is essential due to the inherent inertness. Usually, semiconductors are employed as photocatalysts for the reduction of CO_2 under visible light irradiation, serves as an effective approach to transform solar energy into chemical fuels and address environmental issues. For instance, in 1978, Halmann[21] initially discovered that CO_2 could undergo photoelectrochemical reduction to methanol (CH_3OH) using a gallium phosphide (GaP) electrode exhibiting p-type semiconducting behaviour. The year after, Inoue *et al.*[22] demonstrated that methanol, formic acid, and formaldehyde can be generated via the photocatalytic reduction of CO_2 in water-based suspensions containing semiconductor materials such as ZnO, TiO_2, GaP, CdS, and SiC.

It is widely acknowledged that photocatalytic performance of these semiconductors primarily arise from the creation of charge carriers (electrons and holes) when photons possessing energy equal to or exceeding the band gap (E_g) are absorbed.[23] Upon excitation, photogenerated holes (h^+) in the valence band (VB) migrate to the surface of the semiconductor, where they react with H_2O to generate H^+ and HO^-.[24] In photocatalytic CO_2 reduction (PCR), water (H_2O) plays a crucial role as a proton (H^+) donor. Although, because of the significant oxidation potential of the O_2/H_2O pair (+0.81 V vs. normal hydrogen electrode (NHE)), the valence band (VB) energy level of an effective photocatalyst should be positioned at more positive potential than +0.82 V vs. NHE to facilitate proton generation. These protons subsequently migrate to activated CO_2 molecules, enabling the production of value-added products. Enhancing the water oxidation reaction is beneficial, as it helps consume photogenerated holes, increases the availability of electrons for CO_2 reduction, and ultimately improves PCR performance.

However, the hydrogen evolution reaction (HER) presents a challenge due to its reduction potential (-0.41 V vs. NHE), which is similar to that of CO_2 reduction and thus H_2 generation become difficult to supress. As a result, the selectivity of PCR is often limited by HER competition. To achieve efficient CO_2 photoreduction, the conduction band (CB) should lie at a potential more negative than that required for CO_2 reduction, whereas the valence band (VB) must be positioned at a more positive potential than the oxidation threshold for converting H_2O to O_2. Furthermore, higher CO_2 reduction efficiency is observed when the CB potential positioned at more negative relative to the redox potential of a given CO_2 reduction process.

A direct transfer of a single electron to CO_2, forming a $CO_2^{\cdot -}$ radical, is generally unfeasible due to its elevated reduction potential (-1.9 V vs. NHE), which exceeds the conduction band energy of most semiconductor materials. In contrast, the reduction potentials for producing CO (-0.53 V), HCOOH (-0.66 V), HCHO (-0.48 V), CH_3OH (-0.39 V), and CH_4

(-0.246 V) are relatively lower and more positive than the CB edges of several semiconductors, making their formation more favourable. Instead of single-electron transfer, the process primarily follows a proton-coupled electron transfer (PCET) process, where transfer of electron to CO_2 is accompanied by proton transfer, enhancing reaction feasibility. A summary of the formal reduction potentials for key CO_2 and H_2O photoreduction reactions at pH 7 is provided in equation 1-9. [24,25,26]

$$CO_2 + 2e^- + 2H^+ \rightarrow CO + H_2O \qquad -0.53\ \text{V (vs NHE)} \tag{1}$$

$$CO_2 + 2e^- + 2H^+ \rightarrow HCOOH \qquad -0.61\ \text{V (vs NHE)} \tag{2}$$

$$CO_2 + 4e^- + 4H^+ \rightarrow HCHO + H_2O \qquad -0.48\ \text{V (vs NHE)} \tag{3}$$

$$CO_2 + 6e^- + 6H^+ \rightarrow CH_3OH + H_2O \qquad -0.38\ \text{V (vs NHE)} \tag{4}$$

$$CO_2 + 8e^- + 8H^+ \rightarrow CH_4 + 2H_2O \qquad -0.24\ \text{V (vs NHE)} \tag{5}$$

$$2CO_2 + 12e^- + 12H^+ \rightarrow C_2H_4 + 4H_2O \qquad -0.34\ \text{V (vs NHE)} \tag{6}$$

$$2CO_2 + 14e^- + 14H^+ \rightarrow C_2H_6 + 4H_2O \qquad -0.27\ \text{V (vs NHE)} \tag{7}$$

$$2H^+ + 2e^- \rightarrow H_2 \qquad -0.41\ \text{V (vs NHE)} \tag{8}$$

$$2H_2O + 4h^+ \rightarrow 4H^+ + O_2 \qquad +0.81\ \text{V (vs NHE)} \tag{9}$$

(Water oxidation reaction)

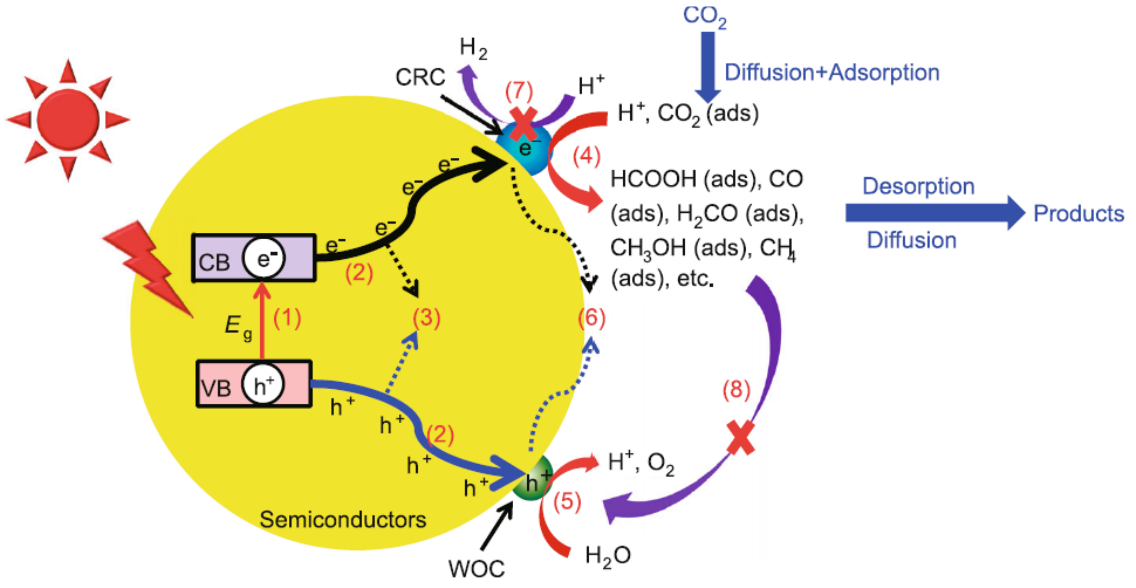

Figure 1.4: Schematic diagram illustrating the mechanism for CO_2 conversion, images adapted with permission from Reference 27.

In addition to suitable band gap (E_g) and band potential the performance of photocatalytic CO_2 conversion is influenced by multiple factors, including the underlying photocatalytic reactions and the dynamics of CO_2 reduction. This process involves several key steps, namely excitation, charge transport, charge separation, oxidation and reduction. As illustrated in Figure 1.4, photocatalytic CO_2 reduction on a semiconductor surface can be divided into eight distinct stages: (1) Generation of electron–hole pairs upon light absorption, (2) Separation and transport of photogenerated charge carriers, (3) bulk charge recombination, (4) CO_2 reduction facilitated by a co-catalyst, (5) water oxidation with a co-catalyst or oxidation of sacrificial electron donors, (6) Recombination of charge carriers at the material's surface, (7) hydrogen (H_2) evolution as a competing reaction, and (8) oxidation of CO_2 reduction products.

The process begins with photon absorption, which promotes electrons from the valence band (VB) to the conduction band (CB), creating an equivalent number of holes in the VB. This charge excitation (Step 1) is crucial for initiating the photocatalytic reaction. In the next step (Step 2), these photogenerated charge carriers move towards the surface, where they take part in oxidation-reduction processes. However, an undesirable process, bulk charge recombination (Step 3), can occur, where electrons and holes recombine within the material, leading to energy loss and reduced efficiency.

For effective CO_2 reduction, the conduction band potential should lie at a more negative value than the CO_2 reduction potential, whereas the valence band must be positioned more positively than the potential for the water oxidation (0.817 V vs. SHE at pH 7). Additionally, an adequate overpotential ($E_{overpot}$) is essential for facilitating the reaction efficiently. A reduced band gap width ($E_g < 3.0$ eV or $\lambda > 415$ nm) is preferable, as a larger band gap would limit solar energy absorption. Once the photoexcited electrons and holes reach the surface of the material, they take part in separate half-reactions: electrons facilitate CO_2 reduction at CO_2 reduction active sites or co-catalysts, producing C1 or C2 fuels like as CO, HCOOH, CH_4, CH_3OH, or C_2H_5OH (Step 4), while holes participate in water oxidation at water oxidation co-catalysts (WOC), generating molecular O_2 (Step 5).

However, In the absence of adequate active sites or co-catalysts, electrons and holes may undergo surface charge recombination (Step 6), mirroring the bulk recombination process in Step 3. Additionally, unwanted reactions such as hydrogen evolution (Step 7) and the oxidation of CO_2 reduction products (Step 8) can occur, competing with the desired CO_2 reduction pathway. These unfavourable processes, steps 3, 6, 7, and 8 should be minimized to maximize the efficiency of photocatalytic CO_2 reduction by ensuring effective charge separation, surface reaction kinetics, and selective catalysis.

1.4 Various types of photocatalysts for CO_2 reduction reaction

The photocatalytic transformation of CO_2 into value-added compounds can be accomplished using both homogeneous and heterogeneous photocatalysts. Homogeneous photocatalysts primarily consist of molecular metal complexes, which offer well-defined active sites and tunable electronic properties, enabling efficient light absorption and charge transfer. In contrast, heterogeneous photocatalysts are typically solid semiconductor materials that provide structural stability and facilitate long-term photocatalytic activity. Both approaches have been extensively explored to enhance CO_2 reduction efficiency.

1.4.1 Homogeneous photocatalyst

Homogeneous photocatalysts serve as a key factor in driving efficient CO_2 photoreduction by facilitating efficient charge transfer, light absorption, and catalytic activity in a uniform reaction medium. These catalysts, typically composed of molecular complexes, offer well-defined active sites, tunable electronic properties, and high selectivity for CO_2 conversion. In homogenous photocatalytic CO_2 reduction, molecular complexes containing second- and third-row transition metals, such as rhenium (Re), and ruthenium (Ru) are regarded as benchmark catalysts due to their superior performance. These metal complexes demonstrate excellent photocatalytic activity, efficient charge transfer, and high selectivity for CO_2 reduction.[28] The properties of these catalysts, such as stability, redox behaviour, inductive effects, and steric factors, can be finely controlled by modifying their ligands, allowing precise control over their reactivity. This tunability is particularly significant, as selectivity remains a key challenge in CO_2 reduction because many of the possible products share comparable reduction potentials. Tuning of the catalysts is key to boosting overall system performance. These molecular catalysts also offer the benefit of having well-defined structural features, which facilitates detailed mechanistic studies. Understanding the relationship between molecular structure and catalytic efficiency provides valuable insights that can guide the development of highly efficient and selective photocatalytic materials for the CO_2 conversion. Despite their advantages, molecular photocatalysts also have certain limitations. The strong absorption of light increases their vulnerability to photo-induced dissociation or photo-isomerization, reducing their stability and robustness. Additionally, as homogeneous catalysts, their recyclability is challenging, which limits their long-term applicability. Another major drawback is their reliance on noble and rare metals, making them costly and less environmentally sustainable. This issue is further compounded by the frequent need for additional components, such as noble metal-based photosensitizers and sacrificial electron donors, to enhance their photocatalytic efficiency. These factors collectively hinder the large-scale implementation of homogeneous photocatalysts for CO_2 reduction, necessitating further research to develop more stable, cost-effective, and sustainable alternatives.

1.4.2 Heterogeneous photocatalysts

1.4.2.1 Inorganic semiconductors as catalyst for CO_2 reduction

Fujishima, Honda, and their colleagues conducted ground-breaking research on the photocatalytic reduction of CO_2 in water using heterogeneous semiconductor powders suspended in an aqueous medium.[29] Since their pioneering work, a large number of semiconductors, including TiO_2, $BaLa_4Ti_4O_{15}$, $SrTiO_3$, WO_3 nanosheets, $NaNbO_4$, $KNbO_4$, $Sr_2Nb_2O_7$, Zn_2GeO_4, Zn_2GaO_4, Zn_2SnO_4, and various metal sulfides, have been identified as efficient photocatalysts for CO_2 conversion with H_2O. This research domain has seen significant progress in recent times, leading to rapid advancements in photocatalytic CO_2 conversion.[30]

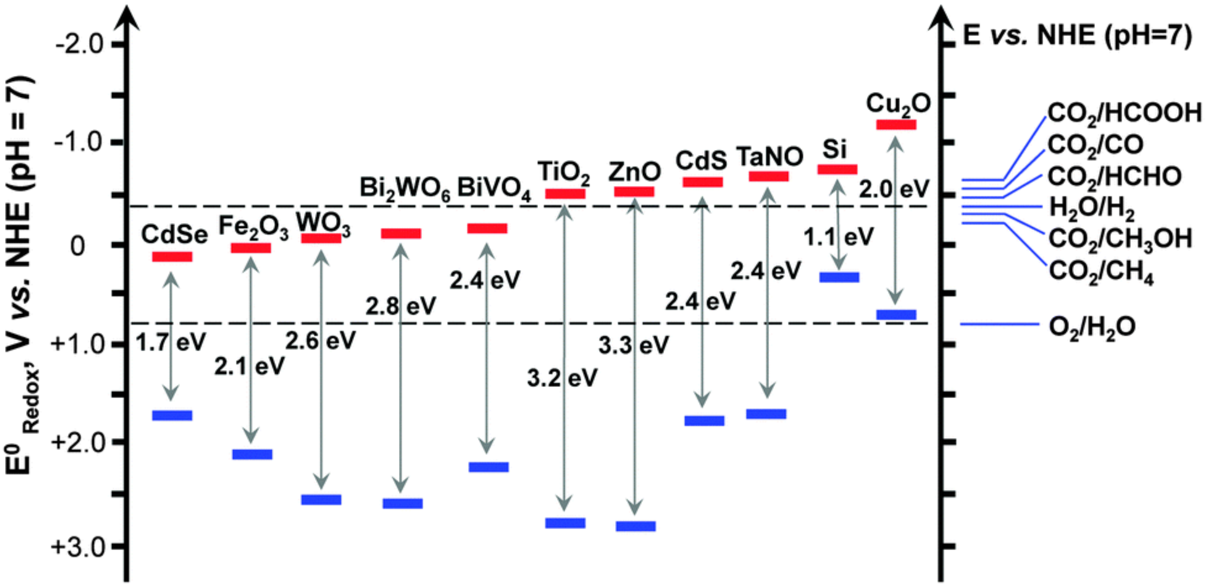

Figure 1.5: The alignment of energy band edges in different semiconductor photocatalysts with respect to the redox potentials of the species involved in CO_2 reduction. Image used with permission from the reference 31.

TiO_2 is among the most extensively studied inorganic semiconductors due to its excellent photocatalytic activity, affordability, and low toxicity.[32] However, Due to its 3.2 eV band gap (Fig. 1.5), TiO_2 is limited to absorbing ultraviolet (UV) light with wavelengths below 400 nm, which constitutes less than 5% of sunlight. To enhance its photocatalytic efficiency, several modification strategies have been explored, including impurity doping,[33] metal deposition,[34] alkali treatment,[35] heterojunction formation,[36] and the incorporation of carbon-based materials.[37] For example, in 2014, Garcia and colleagues enhanced the performance of commercial TiO_2 (P25) through incorporating nanoparticles of Au-Cu alloy as a cocatalyst.[38] This modification resulted in a production rate of CH_4 exceeding 2000 μmol g^{-1} h^{-1}, primarily due to the surface plasmon resonance of Au. Nonethless, the enhanced photocatalytic efficiency was sustained only under simulated sunlight.

However, a wide range of inorganic photocatalysts face limitations due to either unfavourable conduction and valence band alignment or comparatively wide band gaps (Figure 1.5), which restrict their ability to absorb visible light. The durability over extended periods remains a challenge for the majority of inorganic photocatalysts. Furthermore, the efficiency of inorganic semiconductors remains inadequate for industrial applications due to several limitations, including poor CO_2 adsorption capacity, low specific surface area, wide band gaps, rapid electron-hole recombination in nonporous structures,[39] and low selectivity for photocatalytic CO_2 reduction into high-value fuels. Another important aspect of heterogeneous inorganic catalysts is the challenge of achieving precise molecular-level control over their structure. Additionally, the most efficient catalytic systems often depend on the use of precious metals, which can limit their practicality and sustainability.

Therefore, the advancement of photocatalysts that exhibit both high activity and selectivity toward CO_2 reduction is key research prior. Such systems should possess broad visible-light absorption, long-term stability, effective separation of photo-induced charge carriers, strong CO_2 adsorption capacity, and abundant catalytic sites available for CO_2 reduction. Achieving these attributes will significantly enhance the overall performance and practicality of photocatalytic CO_2 conversion for sustainable energy applications.

1.4.2.2 Porous materials as heterogenous catalyst for CO_2 reduction

Porous materials have gained considerable interest within the domain of photocatalytic CO_2 reduction Because of their unique features. Polymeric porous photocatalysts offer the advantages of both homogeneous and heterogeneous photocatalysis, making them a promising class of materials with a highly tuneable molecular structure. They are primarily composed of earth-abundant and lightweight elements, making them more cost-effective and less toxic than inorganic semiconductors. Despite their molecular backbone, these photocatalysts exhibit excellent stability, durability, scalability, and can easily recovered. These chemically and thermally stable porous materials can act as solid supports to heterogenized the molecular complex. Porous photocatalysts generally exhibit superior performance compared to their non-porous counterparts in both environmental and energy-related photocatalytic applications. This enhanced efficiency can be attributed to four key factors: (1) effective capture and diffusion of reactants, such as CO_2, moisture, and organic molecules, because of their highly porous structure and considerable surface area, which facilitates subsequent photocatalytic reactions;[40,41] (2) improved light absorption resulting from reflection and scattering within the porous structure; (3) a higher density of active catalytic sites, leading to greater photocatalytic activity; and (4) shorter distances for charge carrier movement to the surface, reducing recombination losses and enhancing charge separation efficiency. The combined effect of adsorption and photocatalysis in porous materials makes them highly attractive for developing multifunctional photocatalytic systems. Furthermore, the ability of porous materials to capture CO_2 enhances their effectiveness in photocatalytic CO_2 reduction by increasing the concentration of CO_2 molecules at active sites, thereby facilitating its conversion into value-added fuels.[42] Owing to these advantages, numerous types of porous catalysts have been extensively developed and synthesized for solar-driven CO_2 conversion into value-added chemicals. These include covalent organic frameworks (COFs),[43] metal-organic frameworks (MOFs),[44] porous organic polymers (POPs),[45] covalent triazine-based frameworks (CTFs),[46] conjugated microporous polymers (CMPs),[47]and other carbon-based photocatalytic systems.[48]

1.5 Classifications of porous materials

According to the International Union of Pure and Applied Chemistry (IUPAC), porous materials are categorized into three types based on their pore diameter. Materials possessing pores with diameters smaller than 2 nm are referred as microporous, while those with pore diameters ranging between 2 to 50 nm are referred to as mesoporous. If the pore size exceeds 50 nm, the material is categorized as macroporous.[49,50,51,52] Beyond pore size, porous materials may also be categorized according to the nature of their structural building units or framework components, as depicted in Figure 1.6. The functionality of porous materials is largely influenced by key factors such as pore shape, distribution, and density. These materials exist in various physical forms, including particles, fibers, wires, membranes, and foams. The selection of a specific form is determined by the intended application, ensuring optimal performance in diverse fields.

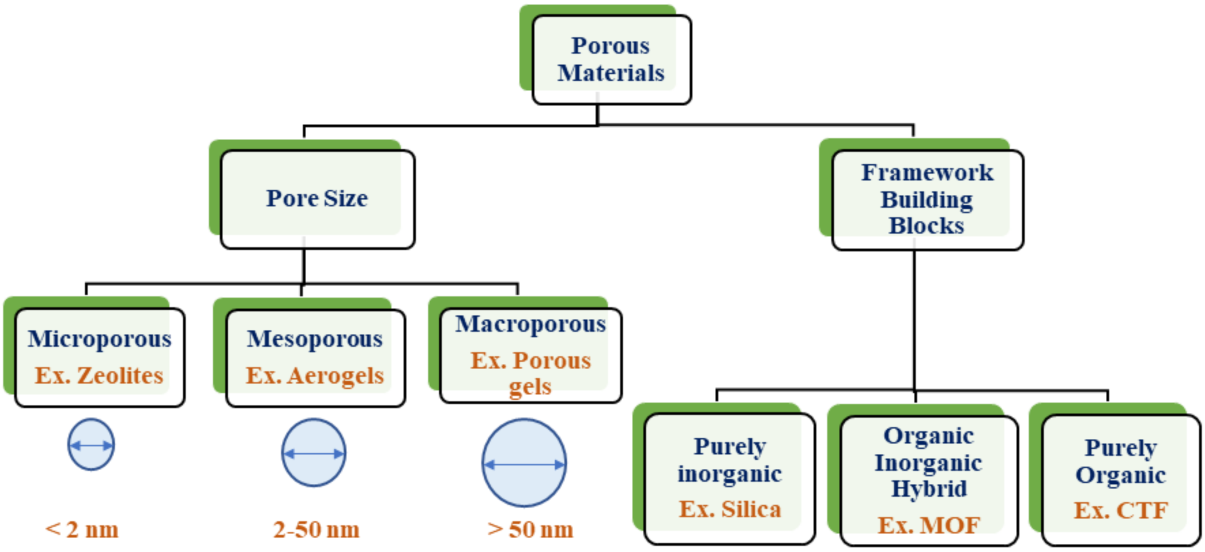

Figure 1.6: Different types of porous materials.

One of the widely used methods to evaluate the permanent porosity of various porous materials is the isothermal sorption of gases. Gas adsorption onto a surface occurs through two main mechanisms: physisorption and chemisorption. In chemisorption, a chemical bond forms between the adsorbate (gas molecule) and the adsorbent (solid surface).[53] Conversely, in physisorption, the adsorbate is held on the surface by weak physical forces, primarily van der Waals interactions.[54] For gas adsorption in porous materials, physisorption is particularly significant because the gas can be removed from the surface without undergoing any chemical change. Adsorption isotherms describe the relationship between the porous structure and the sorption behavior of gases. There are six primary types of adsorption isotherms, as depicted in Figure 1.7.[55] These isotherms are characteristic of different types of adsorbents: Type I is associated with microporous materials, Types II, III, and VI are typical of nonporous and macroporous materials, and Types IV and V are characteristic of mesoporous materials. Types IV and V share similarities with Types II and III, respectively, but specifically correspond to porous adsorbents. When gas-solid interactions are stronger than gas-gas interactions, the adsorption isotherm follows Types II and IV. Conversely, when gas-gas interactions dominate, the adsorption isotherm corresponds to Types III and V. Type VI isotherms are observed for macroporous or nonporous solids with uniform surfaces, where adsorption takes place in distinct multilayer steps. These adsorption isotherms are crucial in determining specific material characteristics including surface area, mean pore size, particle size distribution, and the average size of deposited particles.

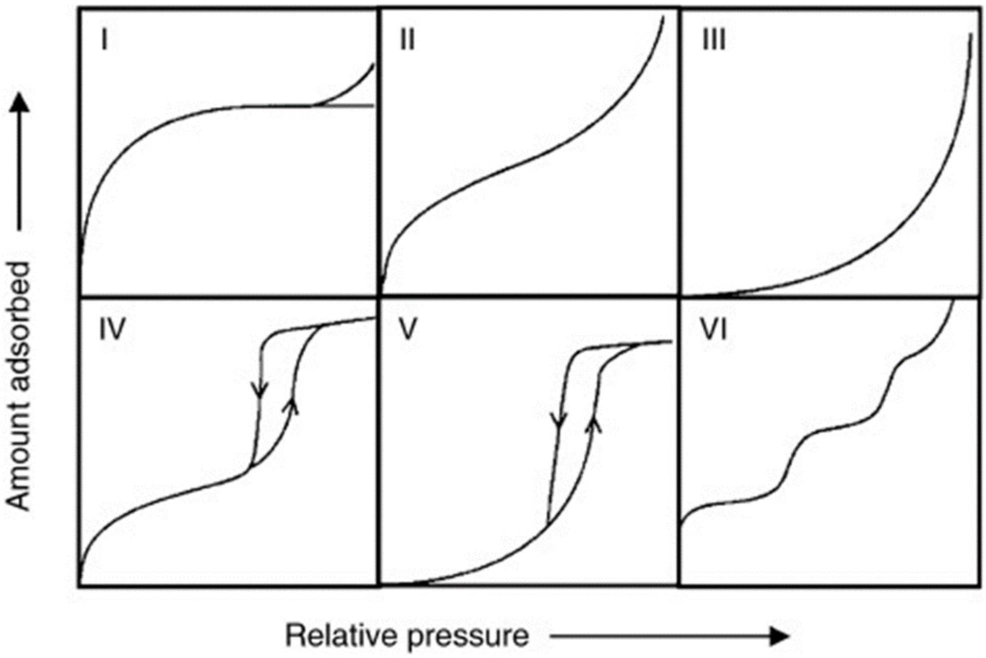

Figure 1.7: Different types of adsorption isotherm based on *IUPAC.* Image used with permission from the reference 55.

Over the years, extensive research has resulted in the discovery of hundreds of porous materials, offering diverse applications. Recently, a notable increase has been observed in research interest in MOFs, CTFs, and CMPs due to their exceptional functional properties and versatile applications. These materials exhibit remarkable characteristics, including high porosity, tuneable chemical properties, and accessible coordination sites, making them highly versatile.

In this section, we focus on CTFs, MOFs and CMPs. Specifically, we explore their role as solid supports for immobilizing molecular catalysts and their potential in catalytic applications, particularly for photocatalytic CO_2 reduction to carbon monoxide (CO).

1.5.1 Covalent triazine-based frameworks (CTFs)

CTFs are the novel subclass of porous organic polymer (POP), characterized by the presence of aromatic 1,3,5-triazine units and extended planar π-conjugation.[56,57] The interaction between the aromatic units and triazine rings enhances π-conjugation across the framework, resulting in a reduction of the system's overall electronic energy, thereby enhancing its chemical stability.[58,59] Among, the various classes of porous organic polymer (POPs), the triazine-based POP family stands out due to its exceptionally high nitrogen content within the framework possessing semiconductive properties. It exhibits outstanding physical characteristics, remarkable chemical robustness, and high thermal stability, primarily attributed to the strong planar π-conjugation present within its aromatic ring structure. Additionally, these materials exhibit a well-developed porous structure, consisting of both micropores and mesopores. Their synthesis is not only cost-effective but also utilizes readily available chemical precursors. [60,61] These materials exhibit exceptional structural precision, allowing for meticulous control over their pore architecture, surface area, semiconducting behaviour and chemical functionality. This tunability makes them highly versatile and enabling their use in various fields, including gas adsorption and separation, energy storage as well as in heterogenous photocatalytic applications.

With continued progress in materials research, CTFs have emerged as promising materials particularly in the field of photocatalysis. Several factors contribute to their growing popularity: (1) Unlike inorganic materials, CTFs are organic porous frameworks with highly tunable and designable structures, offering significant versatility for photocatalytic applications;[62,63] (2) Their ordered π-conjugated networks impart exceptional chemical and thermal stability, as well as ease of recyclability, making them highly suitable for photocatalytic reactions; (3) Their high specific surface area and well-developed porous morphology enhance the exposure of catalytic active sites, thereby improving overall reaction efficiency; (4) The triazine units within the framework can coordinate effectively with transition metal atoms. Additionally, the introduction of heteroatoms allows for the anchoring of metal complexes via nitrogen-containing functional groups (triazine ring) helping to prevent metal agglomeration. The structural diversity of CTFs also enables the formation of high-affinity binding sites for various guest species, expanding their potential across a broad spectrum of catalytic applications.[64,65] Since the first CTF introduced by Thomas and his team in 2008 via ionothermal method,[66] numerous triazine based materials have been developed through different synthestic process. Covalent triazine framework (CTFs) can be strategically designed to meet specific application requirements by utilizing a diverse range of commercially available monomers and versatile synthetic approaches. Various ditopic, tritopic and tetratopic nitrile containing monomers used for triazine ring are summarized in figure 1.8.

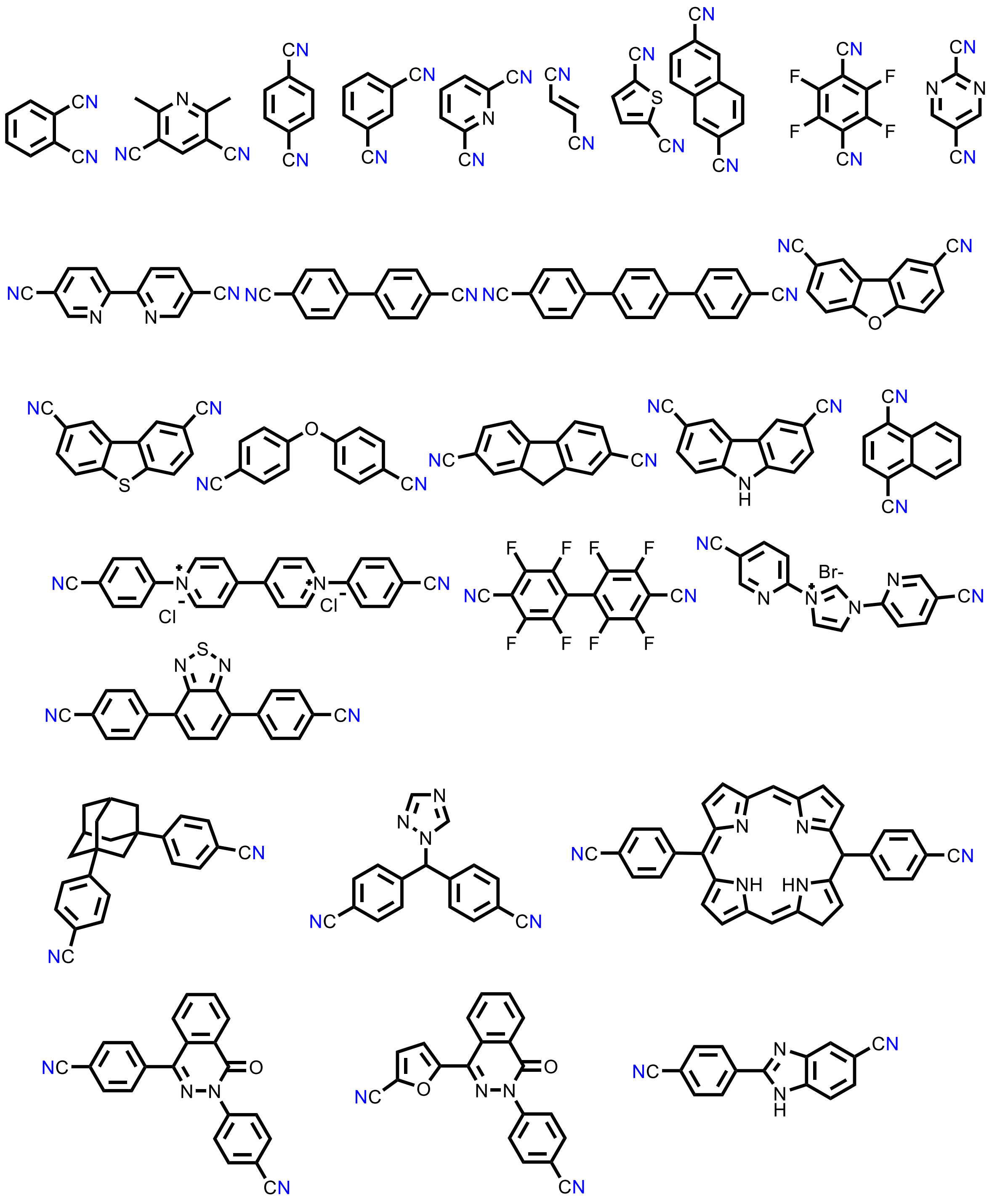

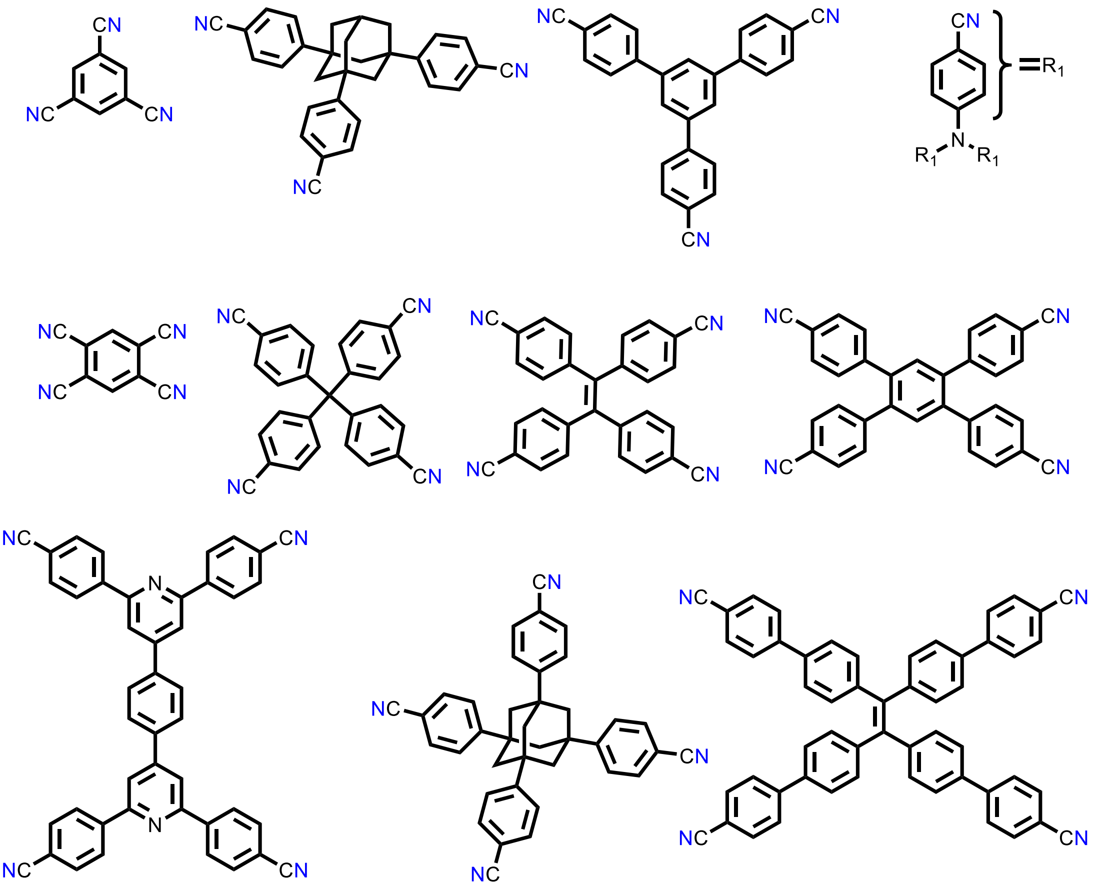

Figure 1.8: Structures of different monomers for the synthesis of CTFs.

The structural and functional properties of covalent triazine frameworks (CTFs), including their crystallinity, specific surface area, porosity, optical absorption, and chemical robustness, are largely determined by the structural features of the monomeric units and the type of covalent linkages formed between them. For instance, CTFs formed through exceptionally strong covalent bonds tend to exhibit amorphous or semicrystalline structures. This is because, during the highly dynamic polymerization process, stronger covalent bonding makes it increasingly challenging to achieve an ordered framework.[67] So, by carefully selecting and combining different building units, the band gaps of CTFs can also be precisely tuned, allowing for the optimization of their electronic properties for various applications. The integration of monomers containing heteroatoms, enables the introduction of various coordination within their porous polymeric framework of CTFs. Consequently, CTFs have been extensively explored as heteroatom-enriched porous carbon frameworks for applications in heterogeneous catalytic processes and electrocatalysis.[68,69,70,71] Additionally, their well-defined porosity and chemical stability make them excellent supports for immobilizing metal catalysts, further enhancing their potential as metal-loaded heterogeneous catalysts.[72,73,74]

1.5.1.1 Synthesis of CTFs

The synthesis of triazine-based materials generally follows two main approaches. The first involves forming the triazine unit during the synthesis process, while the second incorporates preformed triazine-containing monomers directly. Covalent triazine frameworks (CTFs) were first synthesized by Kuhn, Antonietti, and Thomas *et al*. via the ionothermal trimerization of aromatic nitriles,[66] inspiring further research into alternative synthetic strategies. The construction-based approach includes ionothermal synthesis using $ZnCl_2$ and superacid-catalyzed methods. Meanwhile, direct monomer incorporation techniques involve Friedel-Crafts coupling, P_2O_5-catalyzed synthesis, and amidine-based polycondensation. A schematic overview of these synthesis pathways is illustrated in Fig. 1.9.

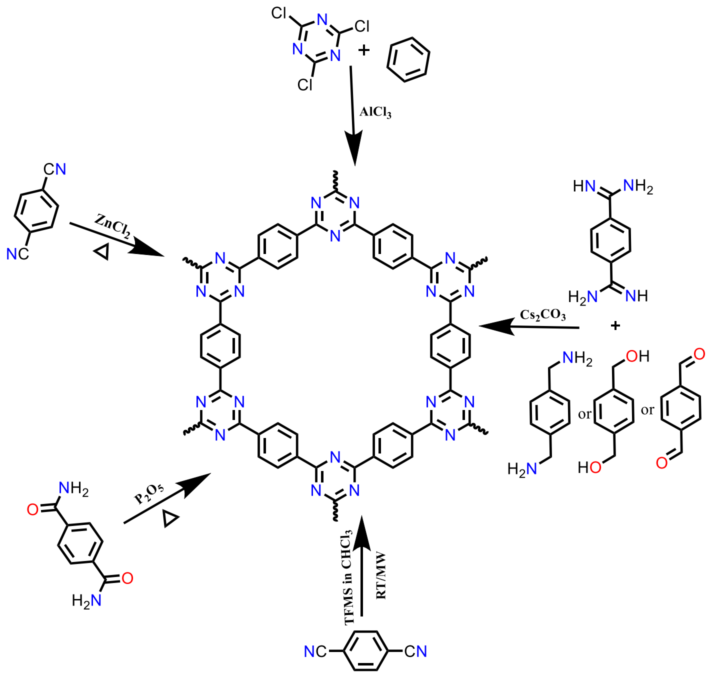

Figure 1.9: Different pathways for synthesizing CTFs.

(a) $ZnCl_2$-catalyzed ionothermal method

In early studies, most covalent triazine frameworks (CTFs) were synthesized using the ionothermal method, where cyano-functionalized monomers underwent trimerization in molten zinc chloride at temperatures exceeding 400 °C (Figure 1.10a).[66,75,76] Zinc chloride acted as both a catalyst and a solvent, ensuring compatibility with the monomers and forming a uniform liquid phase at the appropriate temperature. Thomas and co-workers pioneered the synthesis of CTF-1 through ionothermal polymerization of p-benzenedicarbonitrile (pDCB) at 400 °C, utilizing molten $ZnCl_2$ as both the reaction medium and the catalysts (Figure 1.10b).

Higher reaction temperatures facilitated reversible trimerization, which was essential for achieving crystalline structures. However, reducing the reaction temperature or time often resulted in incomplete polymerization, leading to the formation of oligomers.[77]

Only a limited number crystal CTFs have been successfully produced,[66,75,78] as achieving crystallinity requires monomers with a planar structure, while distorted monomers tend to form semicrystalline or amorphous frameworks. Although these CTFs exhibit high porosity and structural order, their dark coloration and unstable band structure make them less suitable for photocatalytic applications.[79] Additionally, the harsh reaction conditions and extended synthesis times pose challenges for large-scale production. The presence of residual metal within the polymer structure further adds uncertainty to their photocatalytic performance, limiting their practical applicability.[76]

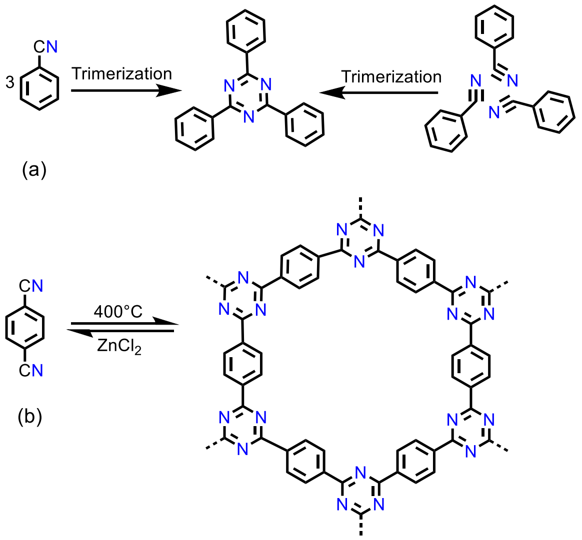

Figure 1.10: (a) Schematic illustration of the cyclotrimerization of nitrile groups leading to the formation of a triazine ring. (b) Molten $ZnCl_2$ mediates the trimerization of pDCB, leading to the construction of the triazine-based framework CTF-1. Adapted with permission from reference 66.

(b) Phosphorus pentoxide-catalyzed method

In 2018, Baek *et al.* developed an alternative approach for synthesizing CTFs to eliminate the use of $ZnCl_2$, a catalyst that is challenging to remove completely. Instead, they employed phosphorus pentoxide (P_2O_5) as both reaction medium and a catalyst to facilitate cyclotrimerization of nitrile-functionalized aromatic amides (Fig. 1.11).[80] In this process, the amide functionality (C(=O)-NH_2) of terephthalamide undergoes a dehydration reaction, converting into a nitrile group (C≡N), which then undergoes condensation to form s-triazine rings under the catalytic influence of P_2O_5. The resulting material, pCTF-1, exhibited remarkable properties, including a large specific surface area of 2034.1 m^2 g^{-1}, high crystallinity and outstanding stability. In contrast to ionothermal or superacid polymerization, this approach offers greater flexibility in monomer selection while preventing $ZnCl_2$ contamination associated with ionothermal synthesis. However, despite these advantages, carbonization of the framework remains unavoidable due to harsh reaction condition.

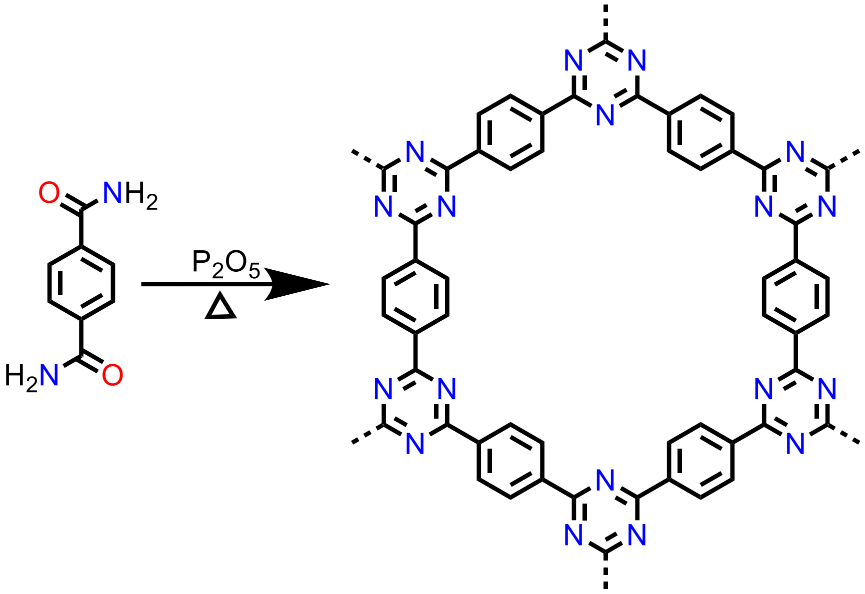

Figure 1.11: Schematic representation of pCTF-1 synthesis through aromatic amide condensation. Reproduced with authorization from reference 80.

(c) Superacid-catalyzed method

The photocatalytic applications of dark-colored and carbonized CTF synthesis at high temperature, were hindered by their mismatched band structures, necessitating the development of milder synthesis methods. In 2012, Cooper and co-workers demonstrated that CTFs can be synthesized from aromatic nitriles using strong Brønsted acids, such as CF_3SO_3H.[81] This coloured CTFs maintain their semiconductive properties, optical properties by preventing carbonization which is crucial for photocatalysis. The study emphasized that TfOH played a crucial role in the process due to its strong acidity, which results from electron-withdrawing nature of fluorine atoms. CTFs synthesized using this approach were later demonstrated to be effective in photocatalytic water splitting.[82] In addition, CTFs have also been constructed using terephthalonitrile as the monomer, with trifluoromethanes serving as the catalyst, and either trichloromethane or dichloromethane employed as solvents. Figure 1.12 provides an overview of representative monomers utilized in superacid-catalyzed polymerization processes.

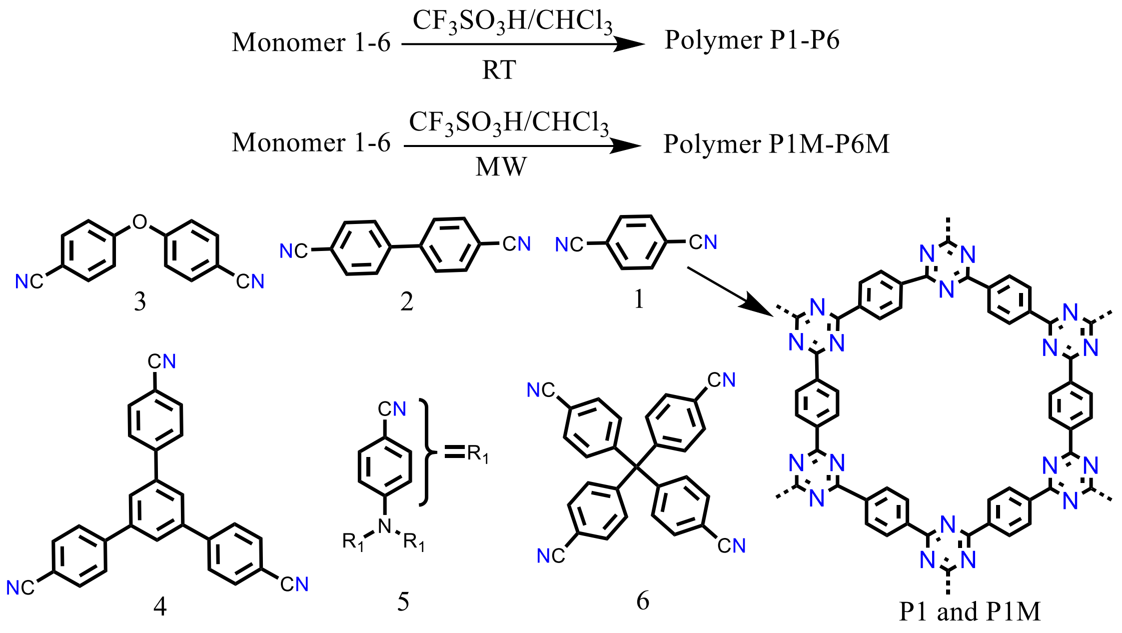

Figure 1.12: Representative monomers used in superacid-catalyzed polymerization. Reproduced with permission from reference 81.

(d) Amidine−aldehyde condensation method

In 2017, Tan *et al.* introduced a scalable and efficient approach for synthesizing CTFs while circumventing the need for elevated thermal conditions or highly corrosive acidic media commonly employed in traditional methods. Their strategy involved a single-step polycondensation reaction between amidines and aldehydes, carried out under mild conditions (Fig. 1.13).[83] This synthesis proceeded through a two-step mechanism: first, a Schiff base reaction between amidine dihydrochloride and aldehyde, followed by a Michael addition, leading to the formation of the desired CTFs. Dimethyl sulfoxide (DMSO) serves as the solvent because of its low oxidizing potential and high boiling point, while Cs_2CO_3 is selected as the base because of its optimal basicity. With a relatively low synthesis temperature of 120 °C and a straightforward open-system approach, the one-pot amidine-aldehyde condensation method offers a more efficient and sustainable strategy for large-scale CTF production.

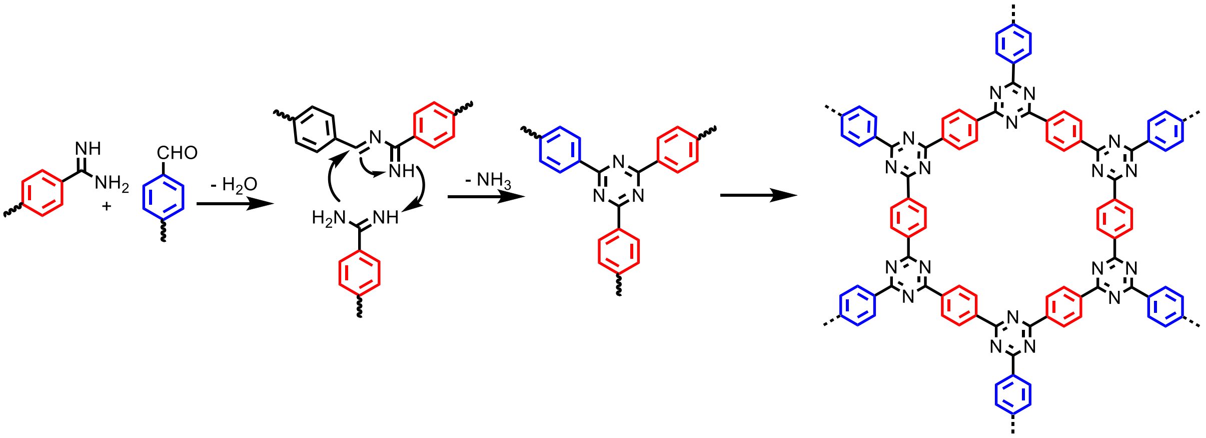

Figure 1.13: Formation of CTFs via the condensation reaction between aldehydes and amidines. Reproduced with authorization from reference 83.

(e) Friedel−Crafts method

The Friedel-Crafts reaction between cyanuric chloride and aromatic precursors provides an alternative approach for synthesizing triazine-based porous materials.[84,85,86,60] In this process, cyanuric chloride, in the presence of $AlCl_3$, undergoes conversion into a cyanuric carbocation, which subsequently reacts with three benzene molecules through a nucleophilic reaction to form the desired triazine-based structures. Methane sulfonic acid and anhydrous aluminium chloride, both strong protonic acids, were chosen as catalysts which play a pivotal function in driving the polymerization process.[87,88] CTFs produced through the Friedel Crafts method are typically amorphous and illustrated in Figure 1.14. This method stands out for being more cost-effective, rapid, and safer compared to other techniques, as it operates under milder conditions and lower reaction temperatures. The effective application of this approach expanded the selection of available monomers, as aromatic compounds proved to be more practical than nitrile monomers.[84] Additionally, the use of heteroatom-containing aromatics enabled the seamless incorporation of heteroatoms into the backbone of CTFs, further enhancing their structural versatility.[85,86] Furthermore, the resulting materials exhibit a high surface area and possess diverse properties, including an amorphous structure, making this synthesis route highly versatile and efficient.

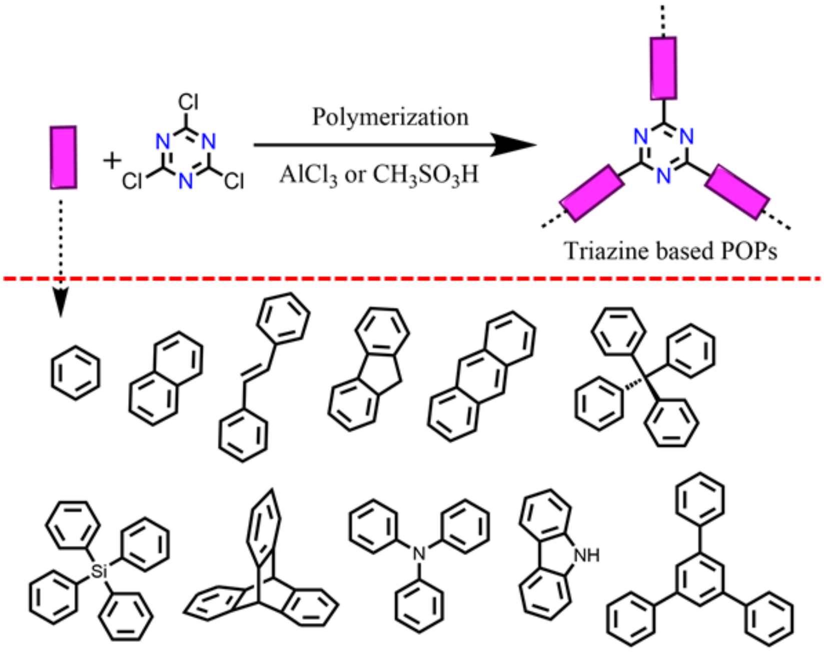

Figure 1.14: Triazine-based porous materials were synthesized via Friedel–Crafts reaction method through reaction of different aromatic monomer with cyanuric chloride.

(f) Coupling reaction

Beyond cyclization approaches, CTFs can be synthesized by directly linking triazine units with other monomers. As an alternative synthetic strategy, coupling reactions have also been employed for the construction of CTFs. This method avoids harsh conditions and offers modularity, enabling systematic evaluation of composition effects on photocatalytic performance. For example, Copper and coworkers have reported three CTFs through Suzuki-Miyaura type condensation reaction in N, N-dimethylformamide (DMF) solvent at 150°C, using aqueous K_2CO_3 as a base (Figure 1.15).[89] UV–vis analysis reveals that increasing the length of the 1,4-phenylene linker between triazine units reduces the band gap of CTFs. Notably, CTF-2 and CTF-3 Suzuki polymers exhibit photocatalytic activity for hydrogen evolution under visible light (>420 nm).

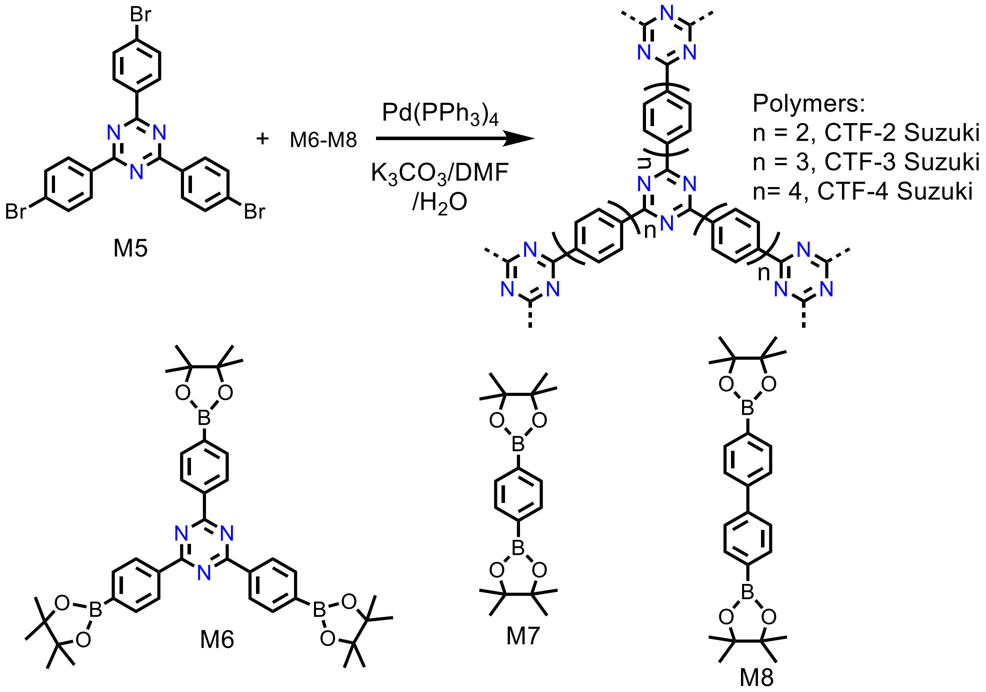

Figure 1.15: Schematic illustration of the synthesis of CTFs via the Suzuki coupling reaction. Reproduced with permission from reference 89.

1.5.1.2 CTF for photocatalytic CO_2 reduction

CTFs hold significant promise as photocatalysts for CO_2 reduction, owing to their large specific surface area and well-developed porosity, which enable efficient diffusion and transport of reactant molecules during catalysis. Their exceptional thermal and chemical stability, even under extreme conditions, ensures long-term cycle performance. Additionally, the nitrogen-rich framework of CTFs plays a crucial role in anchoring single metal atoms through nitrogen atom of the triazine ring to make robust single atom photocatalyst.[90] Furthermore, the strong affinity between the nitrogen atoms in the triazine cores and the polarized, distorted geometry of CO_2 molecules makes the CTFs highly effective photocatalysts for CO_2 reduction.[91] These interactions, including dipole or quadrupole forces, significantly lower the energy barrier associated with the CO_2 reduction by promoting electron transfer, thereby boosting the overall efficiency of the photoreduction process.[92] All these distinctive features have inspired the development of various CTF-based photocatalysts that are highly effective for sustainable photocatalytic CO_2 reduction.

Cao *et al.* were the first to report photochemical CO_2 reduction using metal-incorporated CTFs as catalysts in a solid–gas system.[93] They have synthesized a pyridine-based

CTF (CTF-py) derived from 2,6-dicyanopyridine which was used as a porous platform to anchor the Re carbonyl complex (Re-CTF-py) (Figure 1.16), achieving efficient photocatalytic CO_2 reduction to CO. It exhibited a turnover number (TON) of 4.8 and a CO evolution rate of 353.05 μmol g^{-1} h^{-1} under full light irradiation for 10 hours in a solid–gas system. The single-site Re-CTF-py catalyst also prevented Re species dimerization and leaching, demonstrating the potential of CTFs as stable platforms for heterogeneous catalysis.

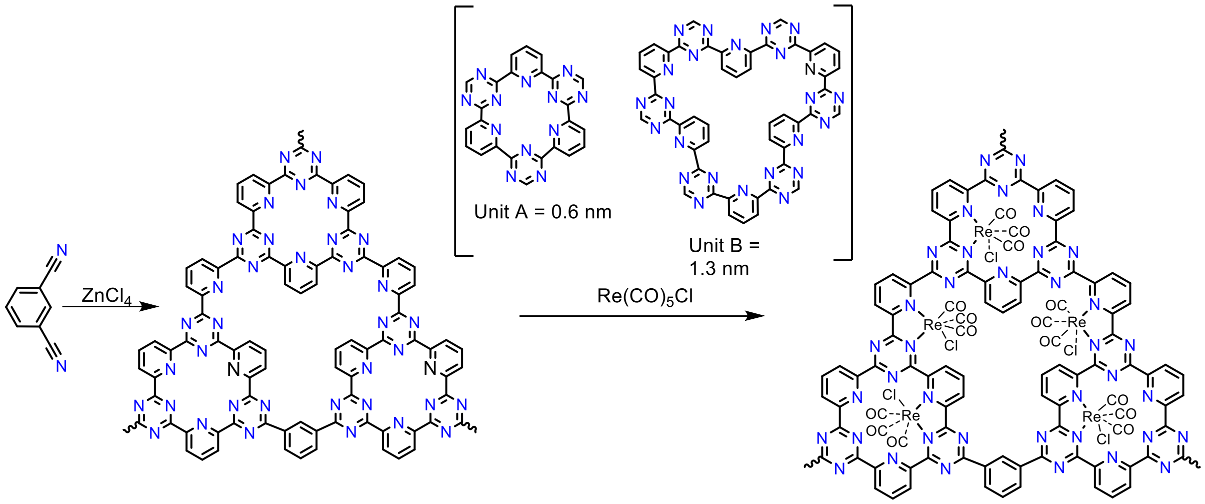

Figure 1.16: Schematic illustration for the preparation of CTF-py and Re-incorporated CTF-py materials. Adapted with permission from reference 93.

CTFs can incorporate various transition metals (Re, Co, Fe, Ru) which can acts as active catalytic sites.[94] For instance, Ran and co-workers reported the development of a series of triazine-based covalent organic frameworks (SAS/Tr-COFs), designed to act as versatile supports for anchoring a range of single-atom metal sites, including Co, Fe, Ni, Cu, Zn, Mn, and Ru, for enhanced photocatalytic CO_2 reduction (Figure 1.17a).[94d] Among them, Fe SAS/Tr-COF achieved a high CO generation rate of 980.3 μmol g^{-1} h^{-1} with 96.4% selectivity. The incorporation of Fe lowered the *COOH formation energy barrier, enhancing charge migration and CO_2 reduction efficiency. Among these, the Fe-functionalized SAS/Tr-COF demonstrated outstanding photocatalytic activity, achieving a CO production rate of 980.3 μmol g^{-1} h^{-1} with a high selectivity of 96.4%. Notably, the energy barrier for *COOH intermediate formation on Fe SAS/Tr-COF was calculated to be 0.34 eV, significantly lower than that of the metal-free Tr-COF (0.41 eV). This reduction in activation energy indicates that the incorporation of atomically dispersed Fe centers promotes more efficient charge transfer between the COF matrix and the active metal sites. Consequently, the electron-rich Fe centers effectively stabilize the *COOH intermediate, thereby enhancing the overall efficiency of the CO_2

photoreduction reaction (Figure 1.17b). Based on these findings, a plausible reaction mechanism was also proposed (Figure 1.17c).

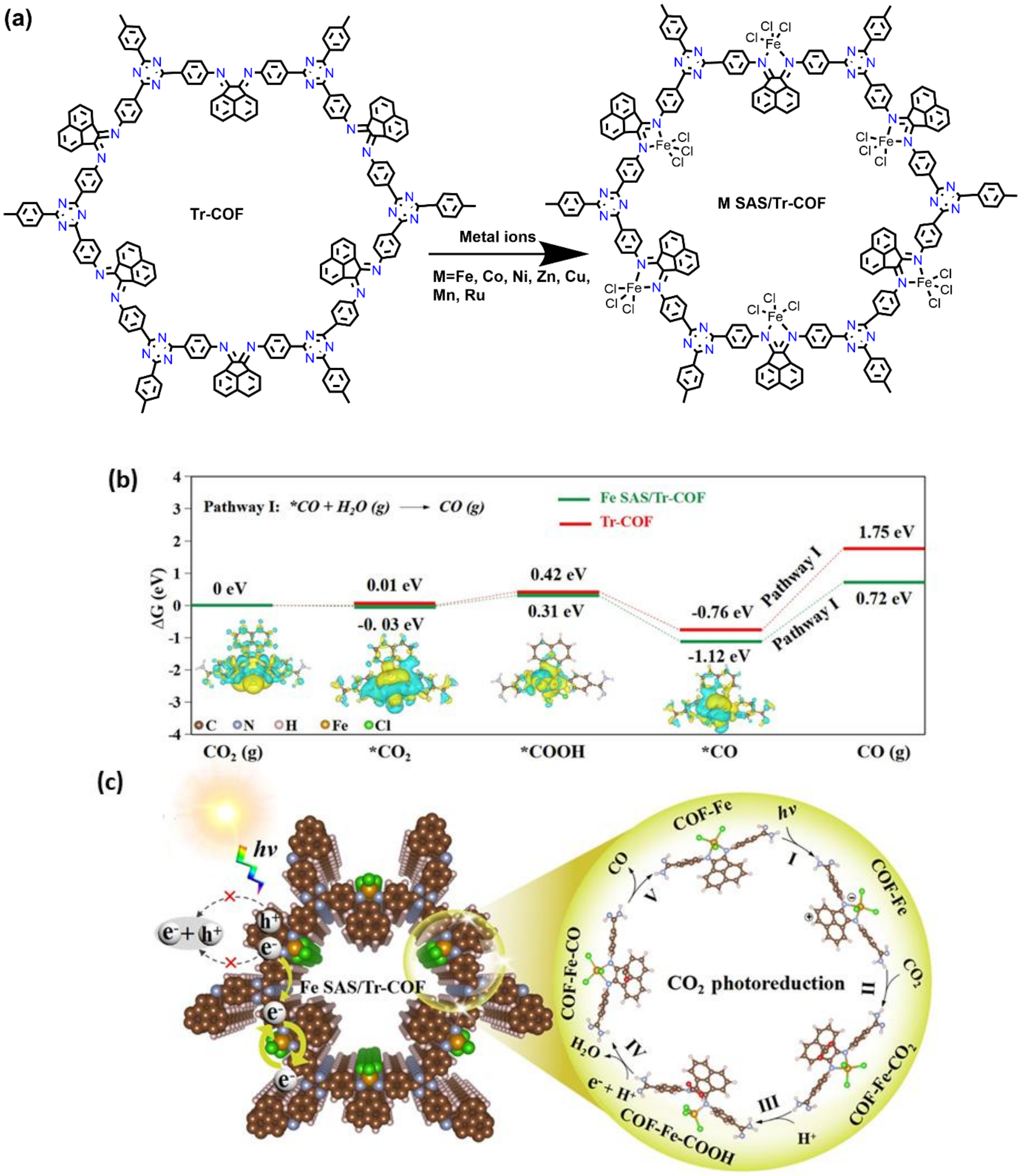

Figure 1.17: (a) Schematic illustration of the synthesis process for Fe SAS/Tr-COFs. (b) DFT-derived Gibbs free energy profiles and charge density maps for CO_2 reduction on Fe SAS/Tr-COFs and Tr-COFs. Sky blue and yellow indicate electron accumulation and depletion, respectively **(c)** Proposed reaction mechanism for CO generation via photocatalytic CO_2 reduction over Fe SAS/Tr-COFs. Reproduced with permission from reference 94d.

Another effective strategy for enhancing the photocatalytic performance of CTFs is the formation of metallized CTF composites by incorporating metal-based materials such as nanoparticles, oxides, or hydroxides. These composites combine the high surface area and tunable structure of CTFs with the catalytic activity of metal sites, resulting in synergistic improvements. For instance, Tian *et al.* developed a Ni-CTAB-CTF composite using Ni nanoparticles and CTAB with CTF-1 via simple impregnation.[95] The optimized catalyst achieved a CO selectivity of 98.9% and exhibited superior charge separation and electron transfer. However, excessive metal loading can block pores and hinder light absorption, highlighting the need for balanced composition.

Photocatalytic efficiency can be enhanced through the incorporation of photosensitizers. Upon light excitation, these photosensitizers generate excited states capable of initiating electron transfer. The transferred electrons are then accepted by the CTFs, promoting the activation of the CO_2 reduction reaction.[96] As a representative example, Tan *et al.* [97] developed a bipyridine-functionalized covalent triazine framework (CTF-Bpy), which served as a scaffold for anchoring isolated cobalt sites to construct an efficient photocatalyst for CO_2-to-CO conversion. The photocatalytic performance of the resulting CTF-Bpy-Co material was evaluated under visible light using $[Ru(Bpy)_3]Cl_2$ as a photosensitizer and triethanolamine (TEOA) as the electron donor. Under 10 hours of irradiation, the system generated 120 μmol of CO with a selectivity of 83.8%. This study underscores the potential of integrating atomically dispersed metal centers within CTF matrices to achieve high selectivity and efficiency in CO_2 photoreduction. In a similar approach, Wu and co-workers[98] synthesized covalent triazine-based frameworks (CTFs) embedded with atomically dispersed cobalt sites (Co-SA/CTF) to serve as efficient photocatalysts for CO_2 reduction and hydrogen evolution. The photocatalytic system utilized $[Ru(Bpy)_3]Cl_2$ as a visible-light photosensitizer and triethanolamine (TEOA) as the electron donor. Under these conditions, the Co-SA/CTF catalysts exhibited outstanding performance, achieving CO and H_2 production rates of 1665.74 $\mu mol\ g^{-1}\ h^{-1}$ and 1293.18 $\mu mol\ g^{-1}\ h^{-1}$, respectively.

Despite their potential, CTFs have been explored to a limited extent in photocatalytic CO_2 reduction. Enhancing their crystallinity and structural design could further improve their efficiency, facilitating better CO_2 capture, activation, and charge transfer for advanced photocatalytic performance.

1.5.2 Metal-organic framework (MOFs)

MOFs, also referred as porous coordination polymers (PCPs), represent a prominent category of crystalline porous materials, garnering widespread attention in recent decades. These materials are composed of metal ions or clusters connected to organic ligands, resulting in one-, two-, or three-dimensional network structures (Figure 1.18).[99] Their exceptional structural features such as high surface area, porosity, controllable morphology, tunable pore dimensions, high stability, and multifunctionality, distinguishing them from other traditional porous materials like zeolites and activated carbons.[100,101,102]

The development of MOFs began in the early 1990s, when scientists first focused on exploring their synthesis methods and structural architectures. The pioneering work of Omar M. Yaghi and his team in the mid-to-late 1990s is often credited with the discovery of MOFs. In 1995 and later in 1998, researchers successfully synthesized one of the earliest and most well-known MOFs, designated as MOF-5, with the chemical formula $Zn_4O(BDC)_3\cdot(DMF)_8(C_6H_5Cl)$. This framework is composed of tetrahedral $[Zn_4O]^{6+}$ secondary building units connected by 1,4-benzenedicarboxylate (BDC) linkers, forming a three-dimensional cubic network. MOF-5 exhibited remarkable properties, including high porosity, a surface area of approximately 6,500 $m^2\ g^{-1}$, well-defined single-crystal X-ray structure, and gas sorption capabilities.[103,104]

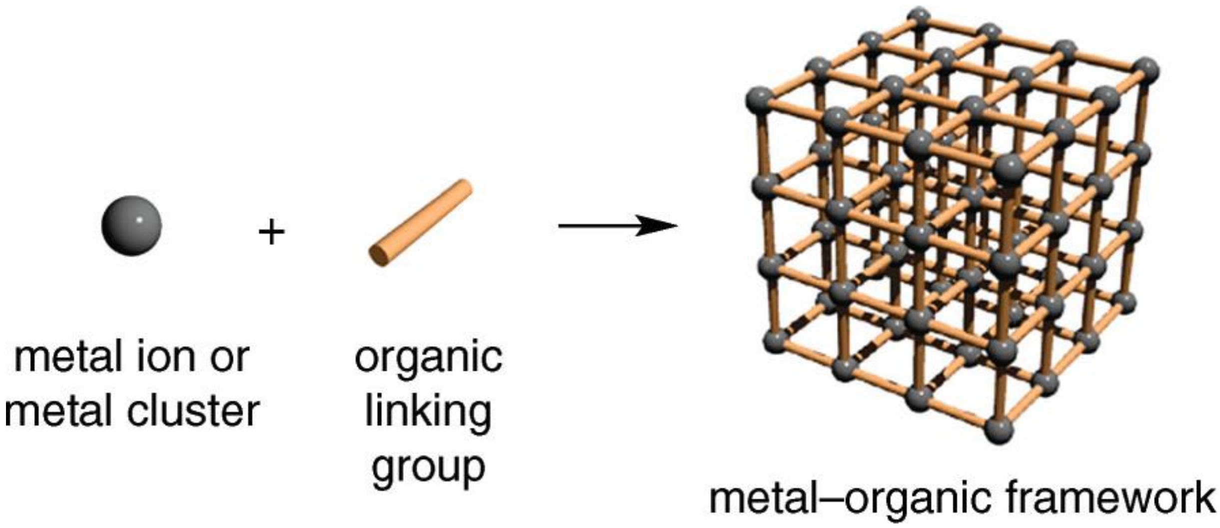

Figure 1.18: Schematic representation of crystalline and porous metal−organic framework (MOF). Reproduced with the permission from reference 99.

The success of MOF-5 served as a foundation for further progress in the field, ultimately resulting in the emergence of isoreticular metal-organic frameworks (IRMOFs), including IRMOF-1 to IRMOF-16, which maintained the fundamental topology of MOF-5.[105] This breakthrough initiated an era of rapid growth in MOF research, focusing on the fine-tuning of their properties including pore size, particle dimensions, and surface area through careful selection of linkers and metal precursors. This structural tunability of MOFs has established them as multifunctional materials suitable for diverse applications, including gas storage and separation, catalysis, drug delivery, sensing, and energy storage. Additionally, their catalytic activity can be tailored by incorporating functional groups or active sites within the framework, making them promising candidates for heterogeneous catalysis.

With their exceptional structural diversity and functional adaptability, MOFs continue to be at the forefront of research in porous materials, offering innovative solutions for a wide range of scientific and industrial applications.

1.5.2.1 Post synthetic modification of MOF

Post-synthetic modification (PSM) has become an effective approach for introducing new functionalities into pre-synthesized MOF materials,[106] particularly when direct synthetic routes are challenging or when functional groups are incompatible with MOF synthesis conditions. PSM can be performed via coordination or covalent interactions on the metal centers or organic linkers, enabling the incorporation of photoactive species without altering the framework structure. Various PSM strategies, such as coordination at unsaturated metal centers, ligand substitution or functionalization, metalation of accessible coordination sites, and metal ion exchange, can be applied independently or in combination to improve the photocatalytic properties of MOFs

(a) Metal exchange

Metal exchange is a significant post-synthetic modification (PSM) strategy in metal-organic frameworks (MOFs), enabling the replacement of existing metal ions with alternative ones without altering its overall structure (Figure 1.19). This approach is particularly advantageous for tuning the electronic, catalytic, and optical properties of MOFs by introducing metals with desired functionalities. This strategy has been widely utilized to enhance the photocatalytic efficiency of MOFs by incorporating metal centres that facilitate charge separation, improve light absorption, or act as active catalytic sites. The ability to selectively exchange metals post-synthetically expands the versatility of MOFs, making them highly adaptable for various applications, including photocatalysis, gas storage, and sensing. For example, Langner *et al.* successfully modified nano-ZIF-8 (Zn) and nano-ZIF-67 (Co) by replacing Zn and Co with Fe^{2+} through a metal exchange process.[107] This substitution occurred without disrupting the structural framework of the MOF, leading to the formation of bimetallic frameworks. Such modifications enhance the catalytic and electronic properties of the MOFs, demonstrating the effectiveness of metal exchange as a post-synthetic modification strategy for tailoring MOF functionality. Transmetalation also serves as an effective strategy for incorporating catalytically active metal centers into MOF linkers, significantly enhancing their functional properties. This approach has been particularly beneficial in the synthesis of catalytic MOFs containing salen- or porphyrin-based linkers. For instance, Shultz *et al.* demonstrated the versatility of metal ion exchange by systematically replacing Mn^{3+} in the salen linker of a pillared-paddlewheel MOF [Zn_2(tcpb)(salen)] with various metal ions, including Co^{2+}, Zn^{2+}, Cr^{2+}, Cu^{2+}, Ni^{2+}, and Mn^{2+}.[108] This stepwise metal substitution resulted in a series of structurally stable MOFs with tailored catalytic properties, showcasing the potential of metal exchange for tuning the reactivity and functionality of MOFs.

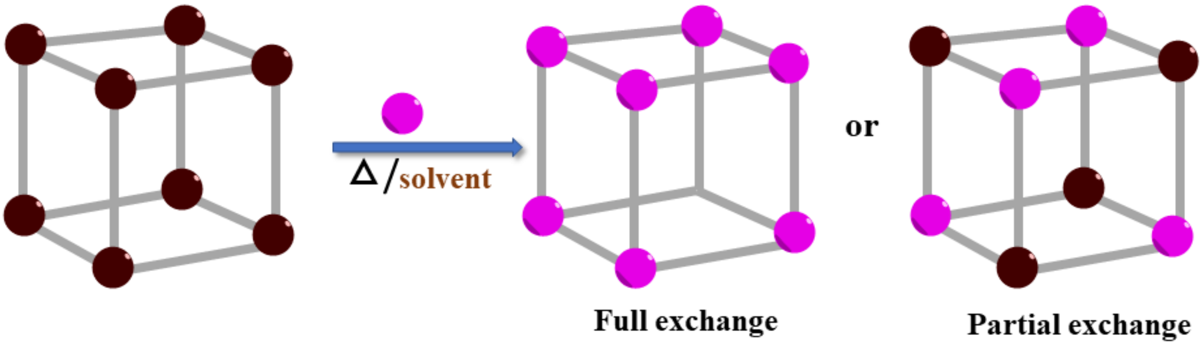

Figure 1.19: Diagram showing metal ion exchange through post-synthetic modification.

(b) Solvent-assisted linker exchange

Solvent-assisted ligand exchange (SALE) is a well-established and widely recognized strategy for designing robust and versatile functional metal-organic frameworks (MOFs). This method enables the exchange of ligands in pre-synthesized MOFs with alternative functionalized ligands, while retaining the crystallinity and architectural stability of the framework (Figure 1.20). Successful ligand exchange generally requires that the incoming ligands possess similar size and bearing identical binding groups to those of the existing linkers in the MOF. Compared to direct synthesis, post-synthetic ligand exchange offers advantages such as mild reaction conditions and reduced interference from functional groups during MOF formation. Typically, this process is followed in Zr-based MOFs. In 2013, Cohen, Ott and coworkers have successfully incorporated the molecular complex [FeFe]-(dcbdt)$(CO)_6$ (1, dcbdt = 1,4-dicarboxylbenzene-2,3-dithiolate) into a structurally stable zirconium(IV)-based metal–organic framework (MOF) using a solvent-assisted ligand exchange (SALE) approach. This was achieved by substituting the 1,4-benzenedicarboxylate (BDC) ligands in the parent framework thereby introducing functionalized ligands without compromising the structural integrity of the MOF.[109] Fontecave *et al.* reported the synthesis of a mixed-ligand Cp*Rh@UiO-67 through post-synthetic ligand exchange. This process involved the exchange of ligands biphenyl-4,4'-dicarboxylate (bpdc) in UiO-67(Zr) with Cp*Rh(bpydc)Cl_2 (Cp* = pentamethylcyclopentadiene), resulting in the incorporation of the rhodium complex into the framework.[110] Compared to direct synthesis, post-synthetic ligand exchange offers advantages such as mild reaction conditions and reduced interference from functional groups during MOF formation.

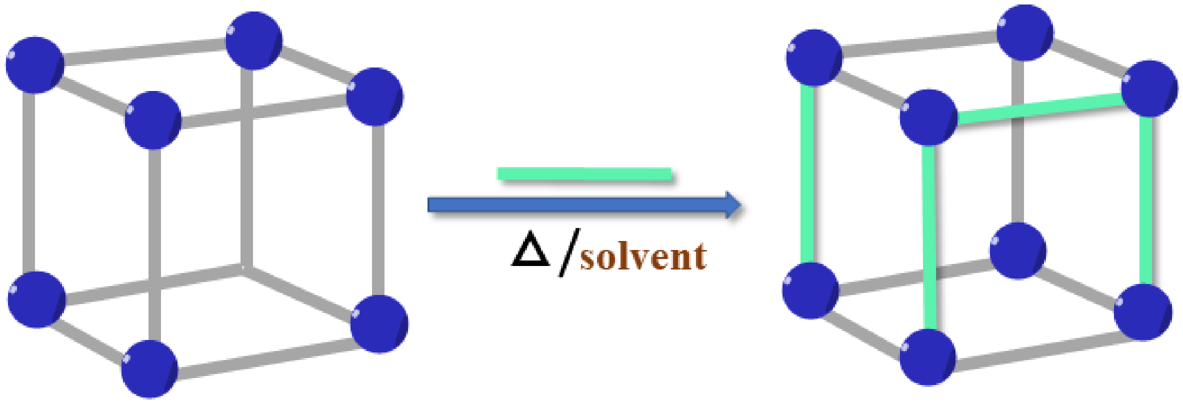

Figure 1.20: Illustration of ligand exchange through post-synthetic modification in coordination polymers (CPs) or MOFs.

1.5.2.2 Synthesis of MOFs

In the previous two decades, various synthetic strategies have been employed to develop MOFs featuring diverse crystal structures, large specific surface areas, controlled particle sizes, tailored pore size distributions, and distinct morphologies. These synthetic approaches provide researchers with a versatile platform to fine-tune the structural and functional properties of MOFs, enabling their optimization for specific applications. Some of the well-known methods are described below:

(a) Solvothermal synthesis

Solvothermal synthesis is the most widely used method for MOF fabrication, involving reactions conducted in sealed vessels under elevated temperature and pressure. In this process, reaction mixtures are heated beyond the boiling point of the solvent, typically using organic solvents with high boiling points, including dimethylformamide (DMF), dimethyl sulfoxide (DMSO). When water is used as the reaction medium instead of organic solvents, the process is specifically referred to as hydrothermal synthesis.

(b) Slow evaporation method

The slow evaporation method is a commonly used technique for synthesizing MOFs that does not require an external energy source. A key advantage of this approach is that it operates under ambient conditions, typically at room temperature (25–30°C). However, its primary limitation is the extended time required for crystal formation compared to other conventional synthesis methods. In this process, a solution containing the precursor materials undergoes gradual solvent evaporation at a controlled temperature, leading to the slow and steady crystallization of the MOF structure.

(c) Electrochemical synthesis

The electrochemical synthesis method offers a unique approach to MOF fabrication without the need for metal salts. Instead, metal ions are introduced into the reaction mixture, which contains organic linkers and electrolytes through anodic dissolution. This technique presents several advantages, including significantly reduced synthesis time, precise control over film thickness and morphology by adjusting the applied current or voltage, and the ability to operate under mild reaction conditions.

(d) Microwave-assisted synthesis

Microwave-assisted synthesis is an efficient and rapid approach for MOF fabrication, significantly reducing reaction times. This method involves exposing a reaction mixture to microwave irradiation, typically for about an hour, to facilitate the formation of nanosized crystals. The use of microwave heating enhances reaction kinetics, accelerates crystal nucleation and growth, and results in high product yields. Additionally, this technique minimizes the formation of secondary products, allowing for the efficient isolation of the desired MOF structures.

(e) Mechanochemical synthesis

Mechanochemical synthesis is a solvent-free approach for MOF fabrication that offers both economic and environmental advantages. This method typically involves liquid-assisted grinding (LAG), where a minimal amount of solvent is introduced into a solid-state reaction mixture to facilitate the process. Grinding is commonly performed using ball mills, mortar and pestle, or similar mechanical techniques. While this method is cost-effective and sustainable, its primary drawback is the potential formation of undesired or structurally amorphous byproducts, which can affect the purity and crystallinity of the final MOF material.

(f) Sonochemical synthesis

In this technique, MOFs are synthesized through chemical transformations induced by high-intensity ultrasonic radiation, typically in the frequency range of 20 kHz to 10 MHz. The process is driven by acoustic cavitation, wherein bubbles form, expand, and rapidly collapse within the liquid medium. This phenomenon generates localized hotspots with transiently high temperatures and pressures, facilitating the formation of MOF structures through enhanced reaction kinetics and improved precursor interactions.

1.5.2.3 MOF for photocatalytic CO_2 reduction

MOFs, a distinctive category of porous materials formed through the coordination of metal ion clusters and organic linkers, have been widely investigated as photocatalysts for CO_2 reduction. Their large surface area, tuneable pore structures for efficient reactant diffusion, high CO_2 adsorption capacity, abundant catalytically active sites, and adaptable functional groups make them highly promising for CO_2 photoreduction applications. MOFs serve as excellent hosts or supports for homogeneous metal complexes. Unlike conventional solid supports with randomly dispersed active sites, MOFs offer well-defined and spatially isolated anchoring sites for catalytic species. This unique feature makes them highly attractive for designing supported single-site catalysts with enhanced precision and efficiency.[111] Incorporating photoactive organo- or metal-organo complexes as linkers in MOF construction enables the development of photo catalytically active MOFs with well-isolated catalytic sites. These structures not only retain or even enhance the performance of their homogeneous counterparts but also offer the added benefit of a heterogeneous catalytic system, allowing for easy recovery and reuse. A diverse range of MOFs has been explored for photocatalytic CO_2 reduction, showcasing their versatility and potential in sustainable energy applications.

Lin and co-workers were among the first to develop a catalytic system utilizing a MOF scaffold by embedding molecular complexes into the UiO-67(Zr) framework for applications in both water oxidation and visible-light-driven photocatalytic CO_2 reduction. They constructed a MOF by integrating [$Re^{I}(CO)_3$(dcbpy)Cl] (where dcbpy stands for 2,2'-bipyridine-5,5'-dicarboxylic acid) into the UiO-67 structure. This MOF catalyst demonstrated remarkable efficiency in the photocatalytic reduction of CO_2 to CO, reaching a turnover number (TON) of 10.9, which was approximately threefold greater than that observed for the homogeneous [$Re^{I}(CO)_3$ (dcbpy)Cl] complex.[112,113] While the homogeneous Re complex is capable of reducing CO_2 to CO with a moderate turnover number (TON), its catalytic performance declines rapidly, as the system becomes nearly inactive after the second photocatalytic cycle. This observation highlights the stabilizing effect of the MOF framework on the homogeneous Re complex. The improved stability of the Re-incorporated MOF is credited to the inhibition of a bimolecular pathway, where a CO_2-bridged Re dimer formation typically leads to the deactivation of the Re complex. When the Re complex is integrated into the MOF framework, this pathway is suppressed, resulting in improved catalytic performance and longevity.

Fu *et al.* reported an amine-functionalized titanium-based metal-organic framework (MOF), NH_2-MIL-125(Ti), capable of reducing CO_2 under visible light (Figure 1.21).[114] This MOF, having formula $Ti_8O_8(OH)_4(bdc\text{-}NH_2)_6$ (where bdc = benzene-1,4-dicarboxylate), features free-standing NH_2 groups that remain uncoordinated. Adsorption isotherms reveal that amine functionalization enhances CO_2 uptake compared to its parent MOF. When exposed to visible light (420–800 nm) in acetonitrile with triethanolamine (TEOA) as a sacrificial electron donor, NH_2-MIL-125(Ti) facilitates CO_2 photoreduction, yielding formate— a product not observed with the parent MOF under similar conditions. Under UV irradiation (365 nm), both the functionalized and original MOFs transform CO_2 to formate, though the amine-functionalized variant exhibits slightly higher catalytic activity.

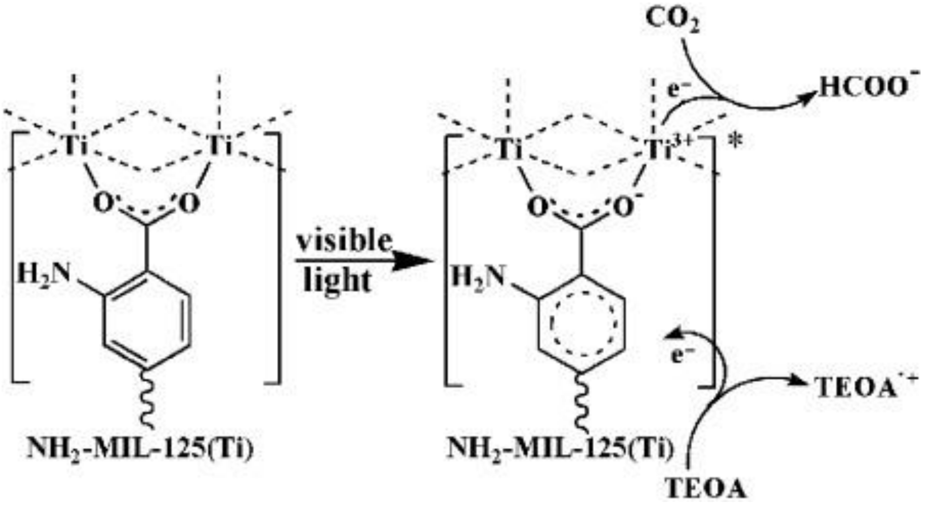

Figure 1.21: Photocatalytic CO_2 reduction mechanism on NH_2-MIL-125(Ti) under visible light illumination. Adapted with permission from reference 114.

Wang *et al*. explored the performance of photocatalytic reduction of CO_2 over three Fe-based MOFs (MIL-101(Fe), MIL-53(Fe), MIL-88B(Fe), along with their amine-functionalized counterparts.[115] Among them, MIL-101(Fe) exhibited the most effective catalytic performance for formate production. This superior catalytic activity was due to the presence of coordinatively unsaturated iron sites, which facilitate CO_2 activation. Moreover, amine functionalization further boosted catalytic efficiency across all three MOFs, highlighting the role of surface modifications in enhancing CO_2 reduction. The presence of dual excitation pathways in these amino-functionalized Fe-based MOFs (Figure 1.22), combined with their improved CO_2 adsorption capacity, significantly contributes to their superior photocatalytic efficiency in CO_2 reduction.

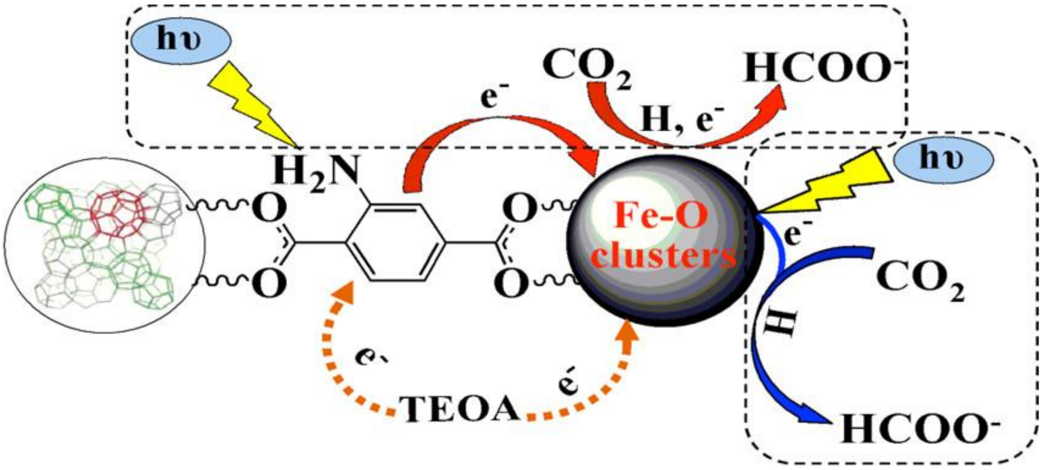

Figure 1.22: Dual excitation Mechanisms in Amino-Functionalized Fe-Based MOFs. Adapted with permission from reference 115.

Partially replacing metal ions in MOFs has proven to be an effective strategy for constructing oxygen-bridged bimetallic structures, significantly enhancing their photocatalytic properties. The incorporation of metals such as Ti or Zr into MOF frameworks lowers photon absorption energy and broadens light absorption, as supported by theoretical calculations.[116] This improvement is primarily due to enhanced ligand-to-metal charge transfer, which boosts overall photocatalytic efficiency. In addition to improving light absorption, the doped metal ions also serve as electron mediators, facilitating charge transfer and promoting better charge separation and migration. For instance, Ti-substituted NH_2-UiO-66(Zr), synthesized via a cation exchange approach, demonstrate superior photocatalytic CO_2 reduction activity in comparison to the unmodified parent MOF.[117] This enhancement was ascribed to the incorporation of Ti ions in the framework, which played a crucial role in accelerating charge transfer.These findings highlight metal doping is an effective approach for tuning the electronic structure of MOFs, thereby optimizing their photocatalytic efficiency for CO_2 reduction.

The exceptional CO_2 adsorption capability of MOF-based photocatalysts results in elevated local concentrations of CO_2 near the catalytic sites, thus improving the overall performance of photocatalytic processes. This effect is further supported by their excellent CO_2 conversion performance, even under conditions of low CO_2 concentration. For instance, Kitagawa and colleagues developed a Ru-based metal-organic framework (MOF), Zr-bpdc/RuCO, through a ligand exchange strategy utilizing H_2RuCO (Ru^{II}(H_2bpydc)(terpy)$(CO)_2$, where bpydc = 2,2′-bipyridine-5,5′-dicarboxylate and terpy = 2,2′:6′,2″-terpyridine) as the substitutive ligand (Figure 1.23a).[118] This MOF exhibited superior CO_2 adsorption compared to pristine Zr-bpdc, resulting in enhanced catalytic activity and selectivity, particularly under low CO_2 concentrations. The incorporation of the photoactive Ru^{II}-CO complex, Ru^{II}(5,5'-dcbpy)(tpy)$(CO)_2$, into the UiO-67 framework (denoted as UiO-67/RuCO) results in greater CO_2 uptake compared to the unmodified UiO-67 (Figure 1.23b). This enhancement is attributed to reduced pore size and the introduction of additional adsorption sites.[118] Notably, while the photocatalytic activity of the homogeneous Ru^{II}-CO catalyst significantly declines under reduced CO_2 partial pressure, the UiO-67/RuCO composite maintains stable performance even at low CO_2 concentrations (5%), as illustrated in Figure 1.23c. This behavior indicates the MOF’s ability to effectively concentrate CO_2 molecules near the active sites, thereby sustaining efficient catalysis.

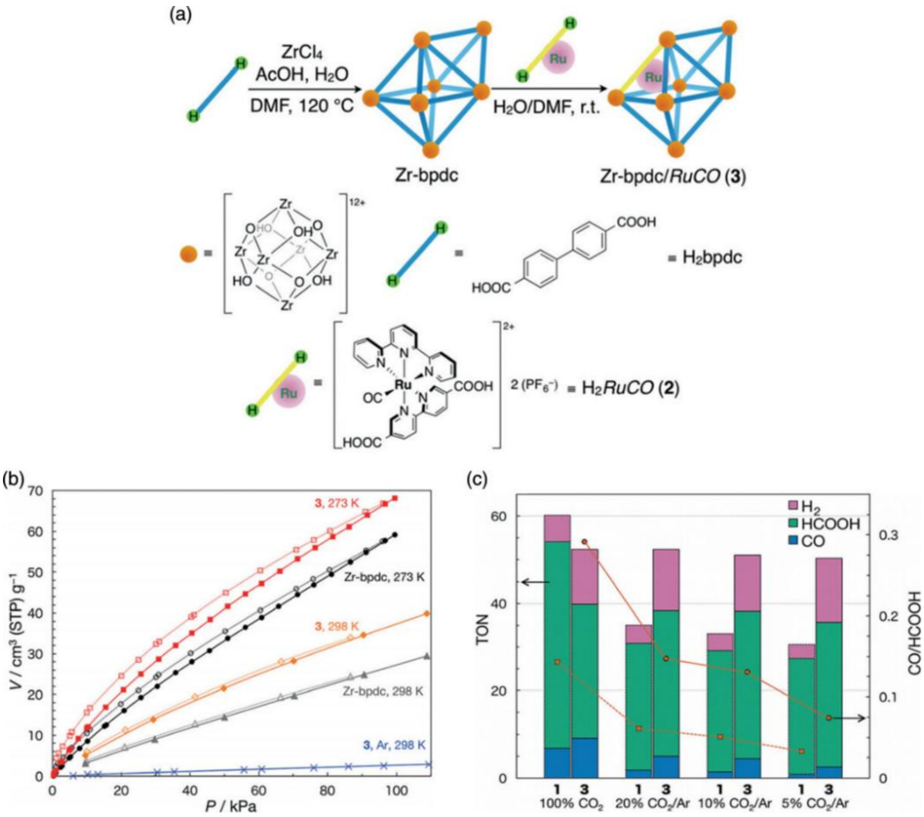

Figure 1.23: (a) Schematic illustration of ligand exchange strategy on Zr-bpdc MOF. (b) CO_2 adsorption isotherms for Zr-bpdc (black and gray) and compound 3 (red and orange) measured at 273 K and 298 K, along with Ar adsorption isotherms for compound 3 (blue) at 298 K. Filled symbols indicate adsorption, while open symbols indicate desorption. (c) Photocatalytic CO_2 reduction using Ru^{II}-CO (1) and UiO-67/RuCO (3): catalytic activity is presented on the left y-axis (bar chart), while product selectivity is shown on the right y-axis (line plot). Adapted from Reference 118 with permission.

The unique microenvironment of MOFs plays a critical role in stabilizing metal complexes, preventing their degradation in the reaction medium, and facilitating efficient charge transport. This structural advantage significantly enhances the performance of MOFs in photocatalytic CO_2 reduction. For example, Zr-MBA-Ru/Re-MOF was prepared by incorporating a Ru-based photosensitizing unit and a Re catalytic complex into the MOF-808 framework.[119] This hybrid MOF exhibited remarkable photocatalytic activity, attaining a maximum CO_2-to-CO conversion rate of 440 μmol g^{-1} h^{-1} with a selectivity exceeding 99%, even without the use of a sacrificial electron donor. The confinement effect provided by the MOF framework extended the lifetime of photoexcited electrons produced by the embedded photosensitizer and simultaneously reduced the charge carrier transport distance between the light-harvesting units and catalytic sites. These synergistic effects contributed to the significant improvements in both the efficiency and selectivity of the CO_2 reduction process.

Lin *et al.* has reported a series of zirconium polyphenolate-decorated-(metallo) porphyrin metal–organic frameworks (MOFs), ZrPP-n.[120] Among them, ZrPP-1-Co stands out due to the with Co metalation within the electron-rich conjugated porphyrin linker, exhibited exceptional CO_2 adsorption capacity (90 $cm^3\ g^{-1}$ at 1 atm, 273 K), one of the highest among Zr-based MOFs. This MOF also demonstrated high photocatalytic activity for CO_2 conversion to CO, achieving a rate of 14 mmol $g^{-1}\ h^{-1}$ under visible-light irradiation without the need for a cocatalyst (Figure 1.24). Electron spin resonance (ESR) analysis and theoretical calculations provided insights into the electron trapping mechanisms and reaction kinetics, revealing that the eclipsed metalloporphyrin array in ZrPP-1-Co plays a crucial role in CO_2-specific capture and CO_2-adduct stabilization. This study presents a stable framework for light-driven CO_2-to-CO creduction by effectively isolating active sites within the MOF structure, thereby enhancing photocatalytic efficiency.

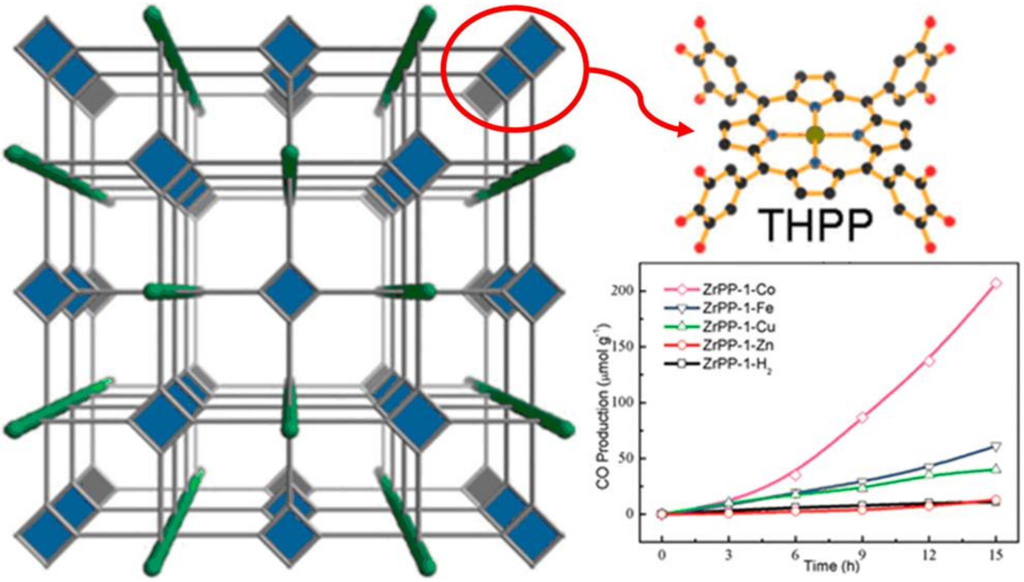

Figure 1.24: structure of ZrPP-1-Co and time-dependent CO evolution profiles from CO_2 photoreduction using ZrPP-1-M catalysts under visible light irradiation. Reproduced from Reference 120 with permission.

In conclusion, MOFs have gained significant attention as highly effective photocatalysts for CO_2 reduction due to their tunable structures, high surface areas, and ability to stabilize active sites. The incorporation of various photosensitizers, transition metal complexes, and electron-rich linkers within MOF architectures has demonstrated significant improvements in CO_2 adsorption, charge separation, and catalytic efficiency. Furthermore, the ability to rationally design MOFs by incorporating functional ligands and metal centers enables precise control over their catalytic performance. Despite these advancements, challenges such as optimizing long-term stability, improving catalytic efficiency under ambient conditions, and developing scalable synthesis methods remain. Future research should focus on further enhancing MOF-based photocatalysts through advanced structural modifications, synergistic co-catalyst integration, and mechanistic studies to unlock their full potential for sustainable CO_2 conversion and utilization.

1.5.3 Conjugated microporous polymers (CMPs)

CMPs represent a unique class of advanced organic materials, characterized by an extended π-conjugated network formed through the alternating arrangement of electron-rich and electron-deficient building blocks. This π-conjugation enables efficient charge carrier delocalization, significantly enhancing the electronic and optical properties of these materials. Additionally, the intrinsic microporosity of CMPs arises from their well-defined nanostructured pores, which contribute to their high surface area and adsorption capabilities.[121] Due to their exceptional combination of electronic conductivity, light-harvesting ability, and tunable porosity, CMPs have garnered considerable interest in various fields, including optoelectronics, chemical sensing, energy storage, and heterogeneous photocatalysis.

Since the pioneering work of Cooper in developing the first CMP,[122] the field has witnessed remarkable growth, attracting significant interest from chemists and materials scientists. The continuous expansion of the CMP family has been driven by the exploration of diverse building blocks, ranging from simple phenyl units to extended arenes, heterocyclic aromatics, and large macrocyclic structures. With minimal restrictions on size, geometry, and functional groups, CMPs exhibit exceptional structural versatility. This inherent flexibility allows for precise tuning of their π-conjugated porous architecture, enabling the optimization of both the polymer backbone and its functional properties. In particular, by carefully selecting different electron donor–acceptor combinations, CMPs can be designed with tailored band gaps and band positions, making them highly suitable as photoactive materials for specific applications.[123] The ability to engineer their electronic properties, combined with their tunable porosity and high stability, positions CMPs as strong contenders for next-generation technologies in optoelectronics, photocatalysis, energy storage, and environmental remediation.

1.5.3.1 Synthesis of CMPs

CMPs involve the formation of a conjugated skeleton by covalently linking building blocks through π-conjugated bonds, thereby creating a three-dimensional polymer network. The conductivity and electrochemical properties of CMPs are highly dependent on several factors, including the mode of conjugation, effective conjugation length, stereo- and regio-regularity, and the nature of the substituents present in the polymer structure.

The first-ever CMP was synthesized by Jiang and colleagues using the Sonogashira–Hagihara cross-coupling reaction.[124] This reaction typically involves the coupling of aryl halides with alkynyl monomers under alkaline conditions, facilitated by a metal catalyst. However, it requires strict anaerobic and anhydrous conditions, which can present challenges for large-scale synthesis. Another widely used method is the Suzuki–Miyaura cross-coupling reaction, which enables the efficient formation of aryl–aryl linkages under relatively mild conditions.[125] This reaction demonstrates compatibility with a broad range of functional groups, making it a versatile choice for CMP synthesis. However, it may produce byproducts that need to be carefully managed. The Yamamoto coupling reaction is another valuable strategy, requiring only halogenated monomers for successful polymerization. While effective, this method is highly sensitive to moisture, which limits its practicality for industrial applications. Additionally, the Heck reaction (also known as the Mizoroki–Heck reaction) allows for the coupling of unsaturated halides with alkene hydrocarbons under anaerobic and alkaline conditions.[126] This method provides another route to synthesize conjugated CMPs.

The choice of synthetic strategy depends on the desired polymer properties and the structural diversity of the building blocks, which can vary in terms of geometry, reactive groups, and π-conjugation systems. This diversity enhances the flexibility in designing both the polymer skeleton and the pore architecture of CMPs. Figure 1.25 illustrates various other reactions used in CMP synthesis.[125b]

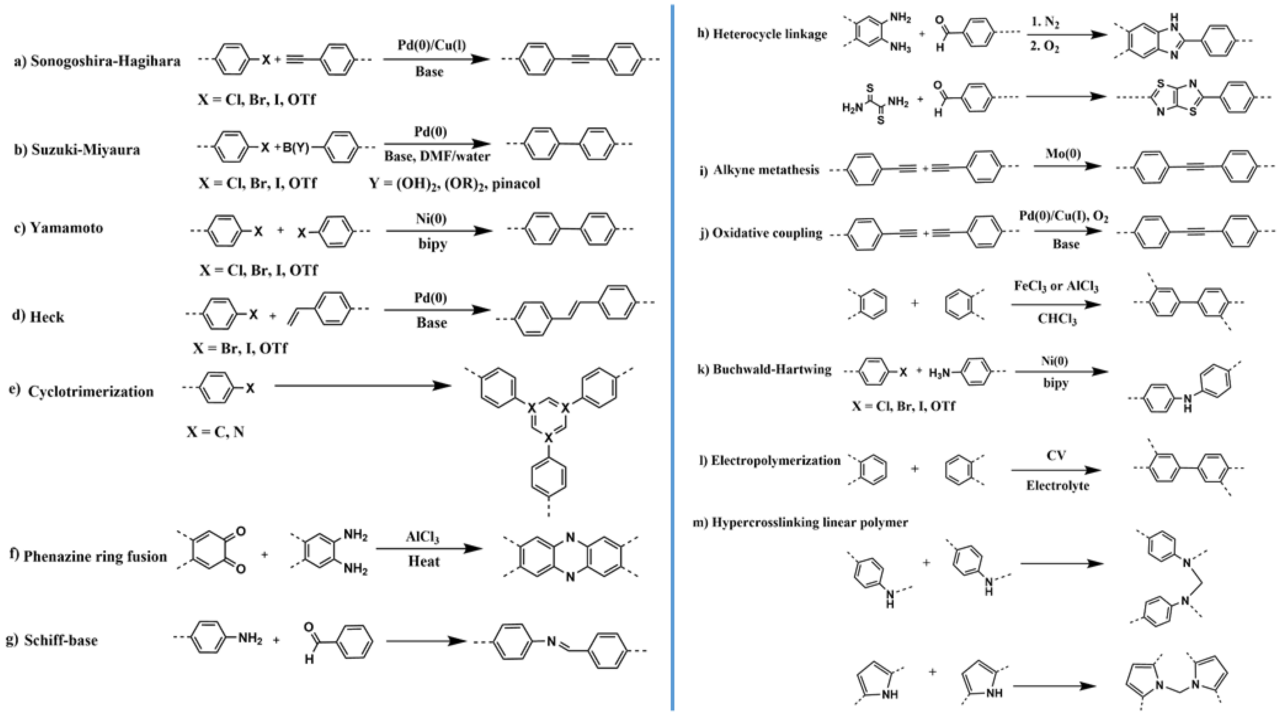

Figure 1.25: Reaction schemes for the synthesis of CMPs.[125b]

1.5.3.2 CMP For photocatalytic CO_2 reduction

In recent years, there has been a growing interest in CMPs due to their unique structural and electronic properties. These materials exhibit highly tunable architectures along with extended π-conjugation, making them particularly attractive for photocatalytic applications, including CO_2 reduction. Their porous nature, combined with the ability to modify electronic structures through molecular design, enables efficient light absorption and charge separation, essential for enhancing photocatalytic performance.

The success of CMP-based photocatalysts in hydrogen production has driven their exploration for CO_2 reduction. A key approach to enhancing performance involves integrating extended planarized units into the polymer backbone. In 2017, Chen *et al.* synthesized pyrene-based conjugated polymers with carbazole, dibenzo[b,d]furan, and dibenzo[b,d]thiophene units, achieving band gaps of 2.17–2.86 eV. Using an ionic liquid for CO_2 and H_2O capture, CP5 (containing dibenzo[b,d]thiophene) converted CO_2 to CO under visible light at 47.37 μmol g^{-1} with 98.3% selectivity.[127] Despite this promising outcome, the efficiency was lower than that of inorganic photocatalysts and g-C_3N_4. Factors such as CP5's limited surface area, residual nickel, and the ionic liquid's restricted CO_2 adsorption hindered performance, highlighting the need for further material optimization.

The incorporation of abundant heteroatoms into the structure of CMPs plays a crucial role in enhancing their photocatalytic efficiency by improving physical adsorption properties. Maji *et al.* designed a CMP, TPA-PQ, by integrating tris(4-ethynylphenyl) amine (TPA) as an electron donor and phenanthrenequinone (PQ) as an electron acceptor.[128] The superior photocatalytic performance of TPA-PQ arises from precisely controlled donor-acceptor interactions and improved physisorption due to the presence of numerous heteroatoms. This material exhibited remarkable efficiency in the photocatalytic conversion of CO_2 to CH_4, achieving a yield of 32.2 mmol g^{-1} with an impressive rate of 2.15 mmol h^{-1} g^{-1} and exceptional selectivity exceeding 97%.

A key challenge in photocatalytic CO_2 reduction lies in achieving selective product formation while maintaining high conversion efficiency. In this regard, Mjahi *et al.* reported the development of a conjugated microporous polymer (CMP), TEB-BPY, synthesized through C–C coupling between 1,3,5-triethynylbenzene and 5,5′-dibromo-2,2′-bipyridine (Figure 1.26a).[129] To enhance its catalytic properties, the polymer was covalently functionalized with $[Re(CO)_5Cl]$, forming the metalated Re@TEB-BPY catalyst. This hybrid photocatalyst demonstrated significant efficiency in the visible-light-driven reduction of CO_2. When triethylamine (TEA) was used as the sole sacrificial electron donor, Re@TEB-BPY facilitated the conversion of CO_2 to CO, achieving a production of 1.1 mmol g^{-1} in 12 h (Figure 1.26b). Interestingly, the reaction pathway shifted when 1-benzyl-1,4-dihydronicotinamide (BNAH) was introduced as a sacrificial electron donor alongside TEA as a base, favoring the production of CH_4 instead of CO. Under these conditions, Re@TEB-BPY catalyzed CH_4 formation at a remarkable rate of 24.6 mmol g^{-1} in 12 h (Figure 1.26c), exhibiting a high selectivity of nearly 96% and an apparent quantum efficiency of 0.22%. These findings highlight the versatility of CMP-based catalysts in tuning the selectivity of CO_2 reduction, offering promising avenues for the development of efficient and targeted photocatalytic systems.

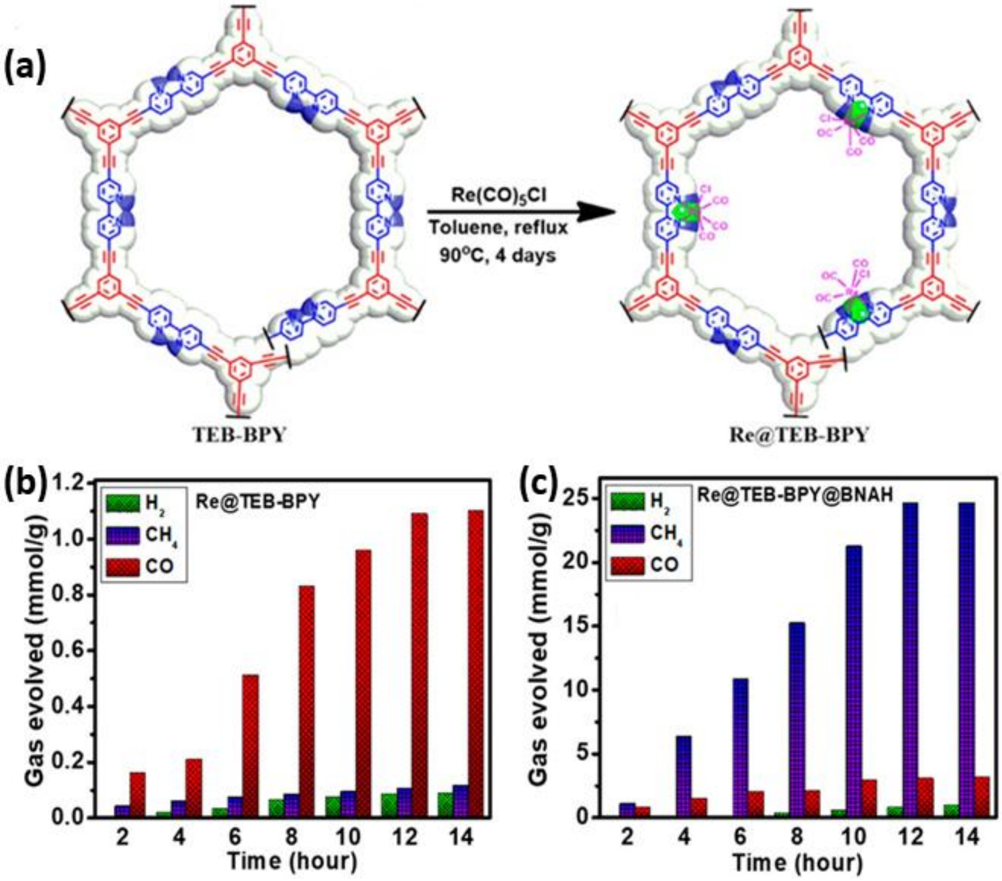

Figure 1.26: (a) Schematic diagram for synthesis of Re@TEB-BPY. (b) Photocatalytic performance of Re@TEB-BPY without the addition of BNAH (c) Photocatalytic performance in presence of BNAH. Images Adapted with permission from reference 129.

The impact of monomer structural flexibility on polymer backbone properties has been largely overlooked in research. However, a recent study by Yang *et al.* demonstrated that incorporating flexible monomers can significantly enhance the specific surface area of polymers. This increase in surface area facilitates greater CO_2 adsorption, leading to a higher concentration of CO_2 around the catalytic sites and ultimately boosting the efficiency of the photocatalytic reaction.[130]

Metal–salen complexes, widely recognized for their catalytic versatility, have been successfully integrated into CMPs to enhance photocatalytic performance. Dai *et al.* synthesized a series of CMPs incorporating N, N′-bis(salicylidene)ethylenediamine (salen) units via a 3+2 Sonogashira–Hagihara coupling reaction (Figure 1.27).[131] These polymers exhibited a high BET surface area of up to 981 $m^2\ g^{-1}$ and excellent CO_2/N_2 selectivity (82 at 273K). Notably, Zn-coordinated CMPs outperformed their Ni-based counterparts by improving CO_2 capture and charge transport efficiency under light irradiation. Under simulated solar conditions, TEPT-Zn achieved a CO production rate of 304.96 μmol h^{-1} g^{-1} in the air without any cocatalyst. Furthermore, under ambient sunlight, a CO yield of 152.52 μmol g^{-1} was obtained within 3 hours, highlighting the potential of CMP-based catalysts for sustainable CO_2 reduction.

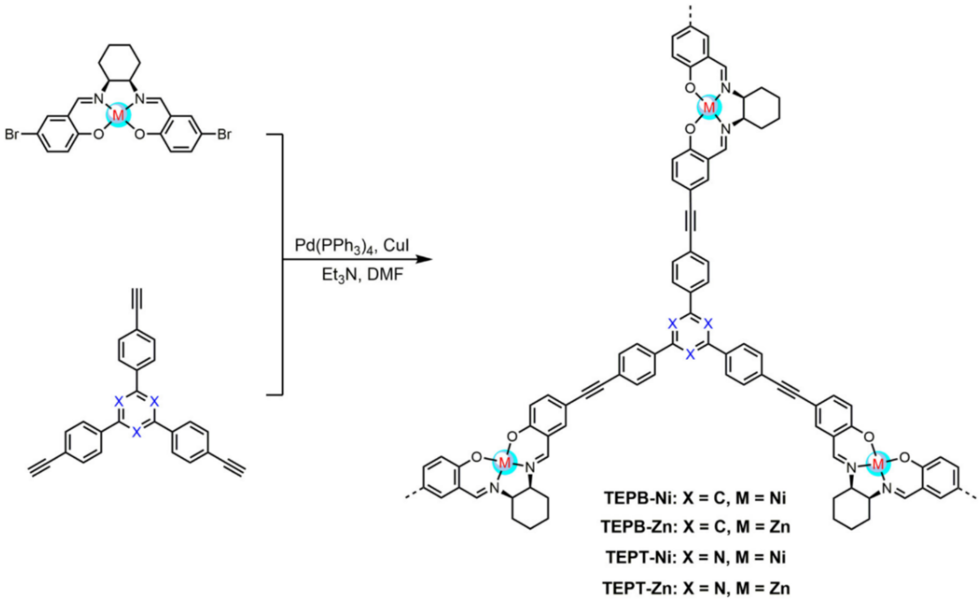

Figure 1.27: Synthetic pathway of metal salen-incorporated conjugated microporous polymers. Images Adapted with permission from reference 131.

In summary, recent advancements in the photocatalytic reduction of CO_2 using porous organic polymers have primarily centered on improving the intrinsic optoelectronic properties of catalysts. However, there has been relatively little emphasis on strategies to enhance CO_2 concentration near active sites or facilitate the conversion of low-concentration CO_2. To tackle this challenge, chemical adsorption emerges as a promising strategy and is expected to drive future advancements by providing an effective pathway for enhancing CO_2 capture and conversion.

1.6 References

1. D. Gielen, F. Boshell, D. Saygin, M. D. Bazilian, N. Wagner, and R. Gorini, *Energy Strategy Rev.*, 2019, **24**, 38-50.

2. J. Barber, and P. D. Tran, *J. R. Soc. Interface*, 2013, **10**, 20120984.

3. P. E. Brockway, P. E. Owen, A. Owen, L. I. Brand-Correa, and L. Hardt, *Nat. Energy*, 2019, **4**, 612– 621.

4. P. J. Megía, A. J. Vizcaíno, J. A. Calles and A. Carrero, *Energy Fuels*, 2021, **35**, 16403-16415.

5. AOAN, Global Monitoring Laboratory - Carbon Cycle Greenhouse Gases, https://www.esrl.noaa.gov/gmd/ccgg/trends/, (accessed 2 march 2025).

6. K. Li, B. Peng, and T. Peng, *ACS Catal.*, 2016, **6**, 7485−7527.

7. W. Thorbecke, *Energy Policy*, 2019, **128**, 628-638.

8. D. M. D'Alessandro, B. Smit and J. R. Long, *Angew. Chem., Int. Ed.*, 2010, **49**, 6058–6082.

9. Z. Zhong, X. Wang and B. Tan, *Chem. Eur. J.*, 2025, e202404089

10. A. Cherevotan, J. Raj, L. Dheer, S. Roy, S. Sarkar, R. Das, C. P. Vinod, S. Xu, P. Wells, U. V. Waghmare and S. C. Peter, *ACS Energy Lett.*, 2021, **6**, 509-516.

11. C. Yang, Y. Wang, L. Qian, A. M. Al-Enizi, L. Zhang and G. Zheng, *ACS Appl. Energy Mater.*, 2021, **4**, 1034-1044.

12. S. Bierbaumer, M. Nattermann, L. Schulz, R. Zschoche, T. J. Erb, C. K. Winkler, M. Tinzl and S. M. Glueck, *Chem. Rev.*, 2023, **123**, 5702-5754.

13. The Sun Facts Information, History, Size, Formation & Definition, https://nineplanets.org/the-sun/, (accessed 2 May 2021).

14. S. R. Lingampalli, M. M. Ayyub and C. N. R. Rao, *ACS Omega*, 2017, **2**, 2740−2748.

15. S. A. Crowe, L. N. Dossing, N. J. Beukes, M. Bau, S. J. Kruger, R. Frei and D. E. Canfield, *Nature*, 2013, **501**, 535–538.

16. B. Zhang and L. Sun, *Chem. Soc. Rev.*, 2019, **48**, 2216-2264.

17. A. Amunts, O. Drory and N. Nelson, *Nature*, 2007, **447**, 58–63.

18. Y. Umena, K. Kawakami, J. R. Shen and N. Kamiya, *Nature*, 2011, **473**, 55–60.

19. J. Schneider, H. Jia, J.T. Muckerman and E. Fujita, *Chem. Soc. Rev.*, **41**, 2036–2051.

20. C. Wang, Z. Sun, Y. Zheng and Y.H. Hu, *J. Mater. Chem. A*, 2019, **7**, 865–887.

21. Halmann M., *Nature*, 1978, **275**, 115–116.

22. T. Inoue, A. Fujishima, S. Konishi, and K. Honda, *Nature*, 1979, **277**, 637–638

23. A. Linsebigler, G. Lu and J. Yates Jr, *Chem Rev*, 1995, **95**, 735–758.

24. C. B. Hiragond, N. S. Powar, J. Lee and S.-I. In, *Small*, 2022, **18**, 2201428.

25. C. B. Hiragond, N. S. Powar and S.-I. In, *Nanomaterials*, 2020, **10**, 2569.

26. C. Hiragond, S. Ali and S. Sorcar, S.-I. In, *Catalysts*, 2019, **9**, 370.

27. X. Li, J. Wen, J. Low, Y. Fang and J. Yu, *Sci. China Mater.*, 2014, **57**, 70–100.

28. (a) T. Morimoto, C. Nishiura, M. Tanaka, J. Rohacova, Y. Nakagawa, Y. Funada, K. Koike, Y. Yamamoto, S. Shishido, T. Kojima, T. Saeki, T. Ozeki, and O. Ishitani, *J. Am. Chem. Soc.*, 2013, **135**, 13266; (b) K. Tanaka and D. Ooyama, *Coord. Chem.*

Rev. 2002, **226**, 211; (c) E. E. Benson, C. P. Kubiak, A. J. Sathrum and J. M. Smieja, *Chem. Soc. Rev.* 2009, **38**, 89; (d) S. Sato, T. Morikawa, S. Saeki, T. Kajino and T. Motohiro, *Angew. Chem. Int. Ed.*, 2010, **49**, 5101; (e) V. S. Thoi and C. J. Chang, *Chem. Commun.*, 2011, **47**, 6578.

29. T. Inoue, A. Fujishima, S. Konishi and K. Honda, *Nature*, 1979, **277**, 637 —638.

30. (a) V. P. Indrakanti, J. D. Kubicki and H. H. Schobert, *Energy Environ. Sci.*, 2009, **2**, 745 —758 ;(b) S. C. Roy, O. K. Varghese, M. Paulose and C. A. Grimes, *ACS Nano*, 2010, **4**, 1259 -1278; (c) K. Mori, H. Yamashita and M. Anpo, *RSC Adv.*, 2012, **2**, 3165 —3172; (d) A. Dhakshinamoorthy, S. Navalon, A. Corma and H. Garcia, *Energy Environ. Sci.*, 2012, **5**, 9217 —9233; (e) A. D. Handoko, K. Li and J. Tang, *Curr. Opin. Chem. Eng.*, 2013, **2**, 200 —206; (f) K. Li, X. An, K. H. Park, M. Khraisheh and J. Tang, *Catal. Today*, 2014, **224**, 3 —12 ;(g) W. Fan, Q. Zhang and Y. Wang, *Phys. Chem. Chem. Phys.*, 2013, **15**, 2632 —2649; (h) S. N. Habisreutinger, L. Schmidt-Mende and J. K. Stolarczyk, *Angew. Chem., Int. Ed.*, 2013, **52**, 7372 —7408; (i) J. Mao, K. Li and T. Peng, *Catal. Sci. Technol.*, 2013, **3**, 2481—2498; (j) S. Navalón, A. Dhakshinamoorthy, M. Álvaro and H. Garcia, *ChemSusChem*, 2013, **6**, 562 —577; (k) Y. Izumi, *Coord. Chem. Rev.*, 2013, **257**, 171 —186; (l) S. Das and W. M. A. Wan Daud, *RSC Adv.*, 2014, **4**, 20856 —2089; (m) W. Tu, Y. Zhou and Z. Zou, *Adv. Mater.*, 2014, **26**, 4607 —4626; (n) Y. Ma, X. Wang, Y. Jia, X. Chen, H. Han and C. Li, *Chem. Rev.*, 2014, **114**, 9987 —10043; (o) N. Zhang, R. Ciriminna, M. Pagliaro and Y. J. Xu, *Chem. Soc. Rev.*, 2014, **43**, 5276 —5287; (p) D. Chen, X. Zhang and A. F. Lee, *J. Mater. Chem. A*, 2015, **3**, 14487 —14516

31. S. Xie, Q. Zhang, G. Liu and Y. Wang, *Chem. Commun.*, 2016, **52**, 35–59.

32. S. N. Habisreutinger, L. Schmidt-Mende and J. K. Stolarczyk, *Angew. Chem. Int. Ed.*, 2013, **52**, 7372 7408.

33. „Stefan Neatu, J. A. Maciá-Agullò, P. Concepciòn and H. Garcia, *J. Am. Chem. Soc.*, 2014, **136**, 15969 15976.

34. X. Feng, J. D. Sloppy, T. J. LaTempa, M. Paulose, S. Komarneni, N. Bao and C. A. Grimes, *J. Mater. Chem.*, 2011, **21**, 13429.

35. X. Meng, S. Ouyang, T. Kako, P. Li, Q. Yu, T. Wang and J. Ye, *Chem. Commun.*, 2014, **50**, 11517–11519.

36. A. Sarkar, E. Gracia-Espino, T. Wågberg, A. Shchukarev, M. Mohl, A. R. Rautio, O. Pitkänen, T. Sharifi, K. Kordas and J. P. Mikkola, *Nano Res.*, 2016, **9**, 1956–1968.

37. C. Lin, Y. Song, L. Cao and S. Chen, *Nanoscale*, 2013, **5**, 4986.

38. Ş. Neaţu, J. A. Maciá-Agulló, P. Concepción and H. Garcia, *J. Am. Chem. Soc*., 2014, **136**, 15969–15976.

39. N. S. Lewis, *Inorg. Chem.,* 2005, ***44***, 6900.

40. H. Li, Y. Sun, Z. Y. Yuan, Y. P. Zhu and T. Y. Ma, *Angew. Chem. Int. Ed.*, 2018, **130**, 3276.

41. J. Ran, T. Y. Ma, G. Gao, X.-W. Du and S. Z. Qiao, *Energy Environ. Sci.,* 2015, **8**, 3708.

42. B. Han, X. W. Ou, Z. Q. Deng, Y. Song, C. Tian, H. Deng, Y. J. Xu and Z. Lin, *Angew. Chem., Int. Ed.,* 2018, **57**, 16811.

43. Q. Zhang, S. Gao, Y. Guo, H. Wang, J. Wei, X. Su, H. Zhang, Z. Liu and J. Wang, *Nat. Commun*, 2023, **14**, 1147.

44. Y.-C. Hao, L.-W. Chen, J. Li, Y. Guo, X. Su, M. Shu, Q. Zhang, W.-Y. Gao, S. Li, Z.-L. Yu, L. Gu, X. Feng, A.-X. Yin, R. Si, Y.-W. Zhang, B. Wang and C.-H. Yan, *Nat. Commun.*, 2021, **12**, 2682.

45. Y.-Z. Cheng, X. Ding and B.-H. Han, *ChemPhotoChem,* 2021, **5**, 406-417.

46. Q. Niu, Z. Cheng, Q. Chen, G. Huang, J. Lin, J. Bi and L. Wu, *ACS Sustainable Chem. Eng.,* 2021, **9**, 1333–1340

47. F. A. Rahimi, S. Dey, P. Verma and T. K. Maji, *ACS Catal.*, 2023, **13**, 5969–5978.

48. J. Low, B. Cheng, J. Yu and M. Jaroniec, *Energy Storage Mater.*, 2016, **3**, 24-35.

49. C. Hua, B. Chan, A. Rawal, F. Tuna, D. Collison, J. M. Hook and D. M. D’Alessandro, *J. Mater. Chem. C,* 2016, **4**, 2535-2544.

50. P. S. Liu and G. F. Chen, Butterworth-Heinemann, Elsevier B. V. Amsterdam: The Netherlands. 2014.

51. M. P. Singha, R. K. Singha and S. Chandra, *Prog. Mater. Sci.,* 2014, **64**, 73-120.

52. H. Nakajima and *Prog. Mater. Sci.,* 2007, **52**, 1091-1173.

53. F. Rouquerol, J. Rouquerol and S. King, *Academic Press*, 1999.

54. R. J. Hunter, *Oxford University Press Inc.,* New York, 1993.

55. S. Kitagawa, R. Kitaura and S.-i. Noro, *Angew. Chem., Int. Ed.,* 2004, **43**, 2334-2375.

56. S. Wei, F. Zhang, W. Zhang, P. Qiang, K. Yu, X. Fu, D. Wu, S. Bi and F. Zhang, *J. Am. Chem. Soc.,* 2019, ***141***, 14272−14279.

57. A. F. M. E. L-Mahdy, C.-H. Kuo, A. Alshehri, C. Young, Y. Yamauchi, J. Kim and S.-W. Kuo, *J. Mater. Chem. A*, 2018, **6**, 19532−19541.

58. A. Acharjya, P. Pachfule, J. Roeser, F.-J. Schmitt and A. Thomas, *Angew. Chem., Int. Ed.,* 2019, **58**, 14865−14870.

59. S.-Y. Jiang, S.-X. Gan, X. Zhang, H. Li, Q.-Y. Qi, F.-Z. Cui, J. Lu and X. Zhao, *J. Am. Chem. Soc.*, 2019, **141,** 14981−14986.

60. P. Puthiaraj, S.-M. Cho, Y.-R. Lee and W.-S. Ahn, *J. Mater. Chem. A*, 2015, **3**, 6792–6797.

61. J. Roeser, K. Kailasam and A. Thomas, *ChemSusChem*, 2012, **5**, 1793–1799.

62. Z. Z. Liang, R. C. Shen, Y. H. Ng, Y. Fu, T. Y. Ma, P. Zhang, Y. J. Li, X. Li, *Chem. Catal.*, 2022, **2**, 2157–2228.

63. S. S. Liu, M. F. Wang, Y. Z. He, Q. Y. Cheng, T. Qian, C. L. Yan, *Coord. Chem. Rev.*, 2023, **475**, 214882.

64. F. Nowsheenah, T. Abu, A. H. Athar, *J. Mater. Chem. A*, 2024, **12**, 10539–10553

65. S. Patial, V. Soni, A. Kumar, P. Raizada, T. Ahamad, X. M. Pham, Q. V. Le, V. H. Nguyen, S. Thakur, P. Singh, *Environ. Res.*, 2023, **218**, 114982.

66. P. Kuhn, M. Antonietti and A. Thomas, *Angew. Chem., Int. Ed.*, 2008, **47**, 3450–3453.

67. M. Liu, L. Guo, S. Jin and B. Tan, *J. Mater. Chem. A*, 2019, **7**, 5153−5172.

68. K. Kamiya, R. Kamai, K. Hashimoto and S. Nakanishi, *Nat. Commun.*, 2014, **5**, 5040.

69. P. Bhanja, K. Bhunia, S. K. Das, D. Pradhan, R. Kimura, Y. Hijikata, S. Irle and A. Bhaumik, *ChemSusChem*, 2017, **10**, 921−929.

70. T. Saida, O. Sekizawa, N. Ishiguro, M. Hoshino, K. Uesugi, T. Uruga, S. I. Ohkoshi, T. Yokoyama and M. Tada, *Angew. Chem., Int. Ed.*, 2012, **51**, 10311−10314.

71. R. Kamai, K. Kamiya, K. Hashimoto and S. Nakanishi, *Angew. Chem., Int. Ed.*, 2016, 55, 13184−13188.

72. C. E. Chan-Thaw, A. Villa, P. Katekomol, D. Su, A. Thomas and L. Prati, *Nano Lett.*, 2010, **10**, 537−541.

73. A. V. Bavykina, A. I. Olivos-Suarez, D. Osadchii, R. Valecha, R. Franz, M. Makkee, F. Kapteijn and J. Gascon, *ACS Appl. Mater. Interfaces*, 2017, **9**, 26060−26065.

74. L. Ma, W. Hu, B. Mei, H. Liu, B. Yuan, J. Zang, T. Chen, L. Zou, Z. Zou, B. Yang, Y. Yu, J. Ma, Z. Jiang, K. Wen and H. Yang, *ACS Catal.*, 2020, **10**, 4534−4542.

75. M. J. Bojdys, J. Jeromenok, A. Thomas and M. Antonietti, *Adv. Mater.*, 2010, **22**, 2202−2205.

76. P. Kuhn, A. Thomas and M. Antonietti, *Macromolecules*, 2009, **42**, 319−326.

77. K. Schwinghammer, S. Hug, M. B. Mesch, J. Senker and B. V. Lotsch, *Energy Environ. Sci.*, 2015, **8**, 3345−3353.

78. P. Katekomol, J. Roeser, M. Bojdys, J. Weber and A. Thomas, *Chem. Mater.*, 2013, **25**, 1542−1548.

79. X. Zhu, C. Tian, S. M. Mahurin, S. H. Chai, C. Wang, S. Brown, G. M. Veith, H. Luo, H. Liu and S. Dai, *J. Am. Chem. Soc.,* 2012, **134**, 10478−10484.

80. S.-Y. Yu, J. Mahmood, H.-J. Noh, J.-M. Seo, S.-M. Jung, S.-H. Shin, Y.-K. Im, I.-Y. Jeon and J.-B. Baek, *Angew.Chem., Int. Ed.,* 2018, **57**, 8438−8442.

81. S. Ren, M. J. Bojdys, R. Dawson, A. Laybourn, Y. Z. Khimyak, D. J. Adams and A. I. Cooper, *Adv. Mater.,* 2012, **24**, 2357−2361.

82. J. Xie, S. A. Shevlin, Q. Ruan, S. J. A. Moniz, Y. Liu, X. Liu, Y. Li, C. C. Lau, Z. X Guo and J. Tang, *Energy Environ. Sci.*, 2018, **11**, 1617− 1624.

83. K. Wang, L.-M. Yang, X. Wang, L. Guo, G. Cheng, C. Zhang, S. Jin, B. Tan and A. Cooper, *Angew. Chem., Int. Ed.,* 2017, **56,** 14149−14153.

84. S. Dey, A. Bhunia, D. Esquivel and C. Janiak, *J. Mater. Chem. A,* 2016, **4**, 6259−6263.

85. Y. Fu, W. Yu, W. Zhang, Q. Huang, J. Yan, C. Pan and G. Yu, *Polym. Chem.,* 2018, **9**, 4125−4131.

86. T. Geng, W. Zhang, Z. Zhu, G. Chen, L. Ma, S. Ye, Q. Niu, *Polym. Chem.,* 2018, **9**, 777−784.

87. S. H. Xiong, X. Fu, L. Xiang, G. Yu, J. P. Guan, Z. G. Wang, Y. Du, X. Xiong and C. Y. Pan, *Polym. Chem.*, 2014, **5**, 3424–3431.

88. Y. Luo, J. Liu, Y. Liu and Y. Lyu, *J. Polym. Sci., Part A: Polym. Chem.,* 2017, **55**, 2594–2600.

89. C. B. Meier, R. S. Sprick, A. Monti, P. Guiglion, J.-S. M. Lee, M. A. Zwijnenburg and A. I. Cooper, *Polymer,* 2017, **126**, 283−290.

90. C. Lu, J. Yang, S. Wei, S. Bi, Y. Xia, M. Chen, Y. Hou, M. Qiu, C. Yuan, Y. Su, F. Zhang, H. Liang and X. Zhuang, *Adv. Funct. Mater.*, 2019, **29**, 1806884.

91. S. Zhang, S. Wang, L. Guo, H. Chen, B. Tan, S. Jin, J. Mater. Chem. C 2020, 8, 192−200.

92. X. Zhu, C. Tian, S. M. Mahurin, S. H. Chai, C. Wang, S. Brown, G. M. Veith, H. Luo, H. Liu and S. Dai, *J. Am. Chem. Soc.,* 2012, **134**, 10478−10484.

93. R. Xu, X.-S. Wang, H. Zhao, H. Lin, Y.-B. Huang and R. Cao, *Catal. Sci. Technol.*, 2018, **8**, 2224.

94. (a) R. Xu, X.-S. Wang, H. Zhao, H. Lin, Y.-B. Huang and R. Cao, *Catal. Sci. Technol.,* 2018, **8**, 2224. (b) X. Hu, L. Zheng, S. Wang, X. Wang and B. Tan, *Chem. Commun.,* 2022, **58**, 8121. (c) L. Wang, L. Wang, S. Yuan, L. Song, H. Ren, Y. Xu, M. He, Y. Zhang, H. Wang, Y. Huang, T. Wei, J. Zhang, Y. Himeda and Z. Fan, *Appl. Catal. B.*, 2023, **322**, 122097. (d) L. Ran, Z. Li, B. Ran, J. Cao, Y. Zhao, T. Shao, Y. Song, M.K.H. Leung, L. Sun and J. Hou, *J. Am. Chem. Soc.*, 2022, **144**, 17097.

95. J. Tian, J. Zhang, B. Xu, Q. Chen, G. Huang and J. Bi, *ChemSusChem*, 2022, **15**, 202201107.

96. J. Di, J. Xia, H. Li, S. Guo and S. Dai, *Nano Energy*, 2017, **41**, 172.

97. X. Hu, L. Zheng, S. Wang, X. Wang and B. Tan, *Chem. Commun.*, 2022, **58**, 8121.

98. G. Huang, G. Lin, Q. Niu, J. Bi L. Wu, j. mater. Sci. Technol., 2022, 116, 41-49.

99. K. Sumida and J. Arnold, *J. Chem. Educ.*, 2011, **88**, 92-94.

100. O. M. Yaghi, M. O'Keeffe, N. W. Ockwig, H. K. Chae, M. Eddaoudi and J. Kim, *Nature*, 2003, **423**, 705.

101. H. Furukawa, K. E. Cordova, M. O'Keeffe and O. M. Yaghi, *Science*, 2013, **341**, 1230444.

102. H. C. Zhou, J. R. Long and O. M. Yaghi, *Chem. Rev.*, 2012, **112**, 673.

103. O. M. Yaghi, G. M. Li and H. L. Li, *Nature*, 1995, **378**, 703.

104. H. Li, M. Eddaoudi, T. L. Groy and O. M. Yaghi, *J. Am. Chem. Soc.*, 1998, **120**, 8571.

105. Z.H. Mai and D. X. Liu, *Cryst. Growth Des.*, 2019, **19**, 7439.

106. Z. Wang and S. M. Cohen, *Chemical Society Reviews*, 2009, **38**, 1315-1329.

107. L. E. Mphuthi, E. Erasmus, and E. H. G. Langner, *ACS Omega*, 2021, **6**, 31632−31645.

108. A. M. Shultz, A. A. Sarjeant, O. K. Farha, J. T. Hupp and S. T. Nguyen, *J. Am. Chem. Soc.*, 2011, **133**, 13252 —13255.

109. S. Pullen, H. Fei, A. Orthaber, S. M. Cohen and S. Ott, *J. Am. Chem. Soc.* 2013, **135**, 16997−17003.

110. M. B. Chambers, X. Wang, N. Elgrishi, C. H. Hendon, A. Walsh, J. Bonnefoy, J. Canivet, E. A. Quadrelli, D. Farrusseng, C. M.-Draznieks and M. Fontecave, *ChemSusChem*, 2015, **8**, 603–608.

111. (a) S. M. Cohen, *Chem. Rev.*, 2012, **112**, 970; (b) Z. Wang and S. M. Cohen, *Chem. Soc. Rev.*, 2009, **38**, 1315–1329.

112. C. Wang, Z. Xie, K. E. de Krafft and W. Lin, *J. Am. Chem. Soc.*, 2011, **133**, 13445–13454.

113. J.-L. Wang, C. Wang and W. Lin, *ACS Catal*., 2012, **2**, 2630–2640.

114. Y. Fu, D. Sun, Y. Chen, R. Huang, Z. Ding, X. Fu and Z. Li, *Angew. Chem., Int. Ed.,* 2012, **51**, 3364–3367.

115. D. Wang, R. Huang, W. Liu, D. Sun and Z. Li, *ACS Catal.*, 2014, 4254–4260.

116. X. Wu, L. Gagliardi and D. Truhlar, *J. Chem. Phys.*, 2019, **150**, 041701.

117. D. Sun, W. Liu, M. Qiu, Y. Zhang and Z. Li, *Chem. Commun.*, 2015, **51**, 2056.

118. T. Kajiwara, M. Fujii, M. Tsujimoto, K. Kobayashi, M. Higuchi, K. Tanaka and S. Kitagawa, *Angew. Chem., Int. Ed.*, 2016, **55**, 2697.

119. S. Karmakar, S. Barman, F. Rahimi and T. Maji, *Energy Environ. Sci.*, 2021, **14**, 2429.

120. E.X. Chen, M. Qiu, Y.F. Zhang, Y.S. Zhu, L.Y. Liu, Y.Y. Sun, X. Bu, J. Zhang and Q. Lin, *Adv. Mater.*, 2018, **30**, 1704388.

121. a) X. Sheng, H. Shi, L. Yang, P. Shao, K. Yu and X. Luo, *Sci. Total Environ.*, 2021, **750**, 141683; b) S. Luo, Z. Zeng, H. Wang, W. Xiong, B. Song, C. Zhou, A. Duan, X. Tan, Q. He, G. Zeng, Z. Liu and R. Xiao, *Prog. Polym. Sci.*, 2021, **115**, 101374; c) A. Hayat, M. Sohail, A. El Jery, K. M. Al-Zaydi, S. Raza, H. Ali, Y. Al-Hadeethi, T. A. Taha, I. Ud Din, M. Ali Khan, M. A. Amin, E. Ghasali, Y. Orooji, Z. Ajmal and M. Zahid Ansari, *Mater. Today*, 2023, **64**, 180–208; d) Q. Hao, Y. Tao, X. Ding, Y. Yang, J. Feng, R. L. Wang, X. M. Chen, G. L. Chen, X. Li, H. O. Yang, X. Hu, J. Tian, B. H. Han, G. Zhu, W. Wang, F. Zhang, B. Tan, Z. T. Li, D. Wang and L. J. Wan, *Sci China Chem*, 2023, **66**, 620–682.

122. J. X. Jiang, F. Su, A. Trewin, C. D. Wood, N. L. Campbell, H. Niu, C. Dickinson, A. Y. Ganin, M. J. Rosseinsky, Y. Z. Khimyak and A. I. Cooper, *Angew. Chem., Int. Ed.*, 2007, **46**, 8574–8578.

123. K. Müllen, J. R. Reynolds and T. Masuda, Conjugated Polymers, RSC: Cambridge, UK, 2014.

124. S. Zhang, S. Wang, L. Guo, H. Chen, B. Tan, S. Jin, *J. Mater. Chem. C*, 2020, **8**, 192−200.

125. a) Y. Xu, S. Jin, H. Xu, A. Nagai and D. Jiang, *Chem. Soc. Rev.*, 2013, **42**, 8012–8031; b) J. S. M. Lee and A. I. Cooper, *Chem. Rev.*, 2020, **120**, 2171-2214.

126. L. Sun, Z. Liang, J. Yu and R. Xu, *Polym. Chem.*, 2013, **4**, 1932–1938.

127. Y. Chen, G. Ji, S. Guo, B. Yu, Y. Zhao, Y. Wu, H. Zhang, Z. Liu, B. Han and Z. Liu, *Green Chem.*, 2017, **19**, 5777–5781.

128. S. Barman, A. Singh, F. A. Rahimi and T. K. Maji, *J. Am. Chem. Soc.*, 2021, **143**, 16284 16292.

129. F. A. Rahimi, S. Dey, P. Verma and T. K. Maji, *ACS Catal.*, 2023, **13**, 5969-5978.

130. W. Chen, P. Li, M. Xue, Z. Tang, N. Yin, Y. Hu, Y. Wang and Y. Yang, *Chem. Mater.*, 2023, **35**, 6754–6761.

131. W. Wu, Z. Dong, M. Chen, W. Li, A. Liao, Q. Liu, Y. Zhang, Z. Zhou, C. Zeng, X. Gong and C. Dai, *carbon energy*, 2025, **7**, e646.

Chapter 2

Single-site cobalt catalyst embedded in a covalent triazine-based framework (CTF) for photocatalytic CO_2 reduction

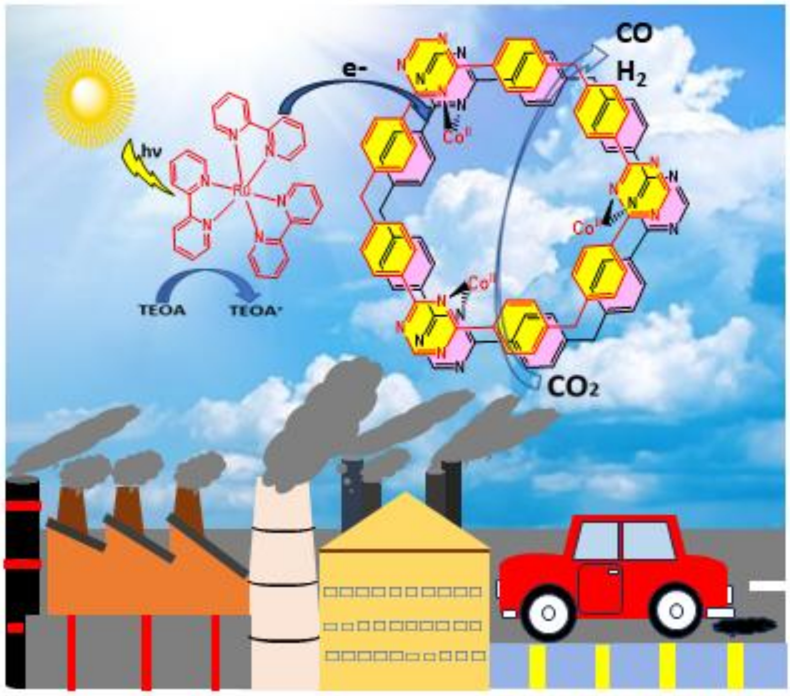

Paper published based on this work:

A. Jana, A. Maity, A. Sarkar, B. Show, P. A. Bhobe and A. Bhunia, *J. Mater. Chem. A*, 2024, **12**, 5244-5253

2.1 Introduction

The exponential growth in the world's population, industrialization, and urbanization leads to the overconsumption of the world's energy. Unfortunately, the majority of the present energy sources rely on non-renewable resources such as fossil fuels (e.g., coal, gas, oil, etc.). This over-exploitation of fossil fuels not only causes the depletion of natural resources but simultaneously leads to the excessive emission of CO_2 in the atmosphere, which is a primary driver of unprecedented global warming and other subsequent climate changes on a global scale over the past few decades.[1–3] This increase in CO_2 concentration at an alarming rate in the Earth's atmosphere will impact the natural carbon cycle, which will subsequently pose a threat to the entire human civilization. Certainly, it is accurate to anticipate that the era of oil will come to a close well before the Earth exhausts its oil reserves. This is due to the limitations imposed by emission regulations on the use of fossil fuels. Thus, there is an urgent need for the development of innovative, sustainable, and renewable technologies for mitigating climate change and promoting a sustainable environment. One of the effective strategies is the sequential adsorption and utilization of CO_2. In particular, the visible light-induced photocatalytic CO_2 reduction represents a promising and viable pathway as it has the capability to transform CO_2 into valuable chemicals such as CO, CH_4, CH_3OH, C_2H_5OH, etc. It addresses contemporary environmental concerns and the energy crisis. To date, numerous semiconductors such as CdS,[4] TiO_2,[5] and C_3N_4[6] have been utilized in the realm of photocatalytic carbon dioxide reduction. However, these materials have yet to demonstrate their efficiency as photocatalysts for CO_2 reduction, attributed to their manifestation of inadequate production yields and reaction product selectivity. This limited production and selectivity of products is attributed to the high recombination rate of photogenerated electron–hole pairs as well as the low adsorption capability of CO_2 on the surface of these inorganic photocatalysts.[7–9] Currently, various homogeneous[10,11] and heterogeneous[12–14] photocatalysts are being utilized in the photocatalytic CO_2 reduction reaction. Even though homogeneous catalysts demonstrate high photocatalytic activity and selectivity in CO_2 reduction,[15,16] heterogeneous catalysts are preferred for large-scale industrial applications. The preference for heterogeneous catalysts arise from their diverse benefits such as preventing dimerization or aggregation, addressing solubility issues, enabling reuse, easy product separation, maintaining stability in extended operation and offering costeffectiveness. Therefore, the pursuit of designing a novel photocatalyst for CO_2 photoreduction to conquer these challenges holds paramount importance.

In recent years, the development of single-atom catalysts (SACs), that feature single metal atoms embedded into solid supports, has emerged as a promising strategy that has garnered significant attention in the field of heterogeneous catalysis.[17,18] It combines the advantages of both heterogeneous and homogeneous catalysts and has shown great potential in the realm of CO_2 reduction owing to uniform active sites, excellent atom utilization efficiency, and highly unsaturated coordination environment.[19–22] Specifically, the distribution of individual atoms through coordination offers a sufficient number of unsaturated active sites. This arrangement facilitates the acceleration of charge separation and energy transfer, as well as the improved adsorption and activation of molecules. These characteristics prove advantageous to enhance the efficiency and selectivity of photocatalytic CO_2 reduction.

The essential factor for the preparation of stable SACs is the interaction between the solid support and single metal sites. Most importantly, the interaction between the metal and support has a noteworthy influence on both the adsorption and activation of CO_2 molecules, thereby enhancing the subsequent CO_2 conversion.[23,24] Therefore, it is crucial to design and develop robust solid supports to accommodate single metal atoms within the solid matrix by establishing strong interaction with the metal.[25] Recently, there has been growing significant interest in covalent triazine-based framework (CTFs), a novel subclass of covalent organic frameworks (COFs) consisting of triazine molecular units. These frameworks have emerged as promising contenders for solar-driven photocatalysts due to their specific physicochemical characteristics, which include a tunable porous structure with extreme surface area, high nitrogen content, unique electronic properties, and superior chemical and thermal stabilities.[21,26,27,28,29] The substantial surface area of CTFs along with their elevated N content and Lewis basicity empowers them to capture a significant surplus of CO_2 molecules activating them for subsequent transformation.[30,31] In recent years, CTFs have garnered much attention as solid supports for anchoring single metal atoms through the N-atom of a triazine ring to prepare robust single atom photocatalysts (SACs).[32] This incorporation of metal sites stands as a potent approach for enhancing photocatalytic activity by elevating active site numbers, facilitating efficient electron transfer into CTFs, and improving the separation efficiency of electron– hole pairs generated during photocatalysis.[33]

In our current investigation, a covalent triazine-based framework (CTF-TPE) has been synthesized from monomer tetra(4-cyanophenyl) ethylene under solvothermal conditions in the presence of CF_3SO_3H. The synthesized CTF has been used as a solid support for grafting the Co^{2+} atoms via coordination with the N-atom of the triazine moiety through a simple deposition method for photocatalytic

CO_2 reduction. The single Co^{2+} incorporated photocatalyst, CTF-TPE@Co-3 (3.1 wt% of Co), exhibits the highest photocatalytic efficiency and reaches CO evolution of 6616 mmol g^{-1} under a photocatalytic run of 7 hours, which is much higher than that exhibited by many earlier reported CTF-based photocatalysts (Table 2.2). Additionally, we have unveiled the presence of single Co sites via spectroscopic evidence, elucidating their pivotal contribution to the enhancement of photocatalytic CO_2 reduction. Furthermore, a plausible mechanism was explored for the enhancement of photocatalytic CO_2 reduction. Our study deepens insight into the fabrication and mechanism of single atom embedded CTFs in the context of photocatalytic CO_2 reduction.

2.2: Experimental section

2.2.1: Materials

Tetraphenyl ethylene, Bromine, CF_3SO_3H, and TEOA were purchased from Sigma-Aldrich. DCM, Acetone, Acetonitrile, THF, and Chloroform were purchased from Spectrochem. All solvents and chemicals were used without any further purification.

2.2.2: Synthesis of tetra(4-cyanophenyl) ethylene (2)

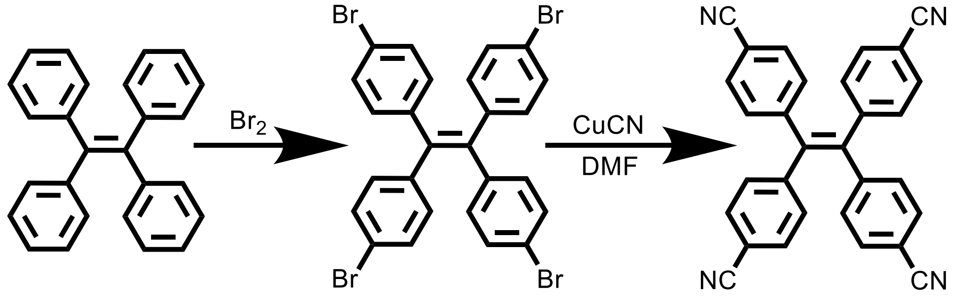

1 2

Figure 2.1: Systematic illustration for the synthesis of the nitrile monomer.

Synthesis of Tetra(4-bromophenyl) ethylene (1)

We have followed the previously reported procedure for the synthesis of the linker.[34] To a cooled solution of tetraphenylethylene (7.2 g, 21.7 mmol) in 40 mL of glacial acetic acid, bromine (8.8 mL, 170 mmol) was added dropwise over 10 minutes while maintaining an ice-water bath. Following the addition of dichloromethane (30 mL), the mixture was heated to 50 °C and stirred for approximately 30 minutes, with the reaction progress monitored by thin-layer chromatography (TLC). Upon completion, the reaction mixture was poured into 200 mL of ice water, resulting in the formation of a solid precipitate. The product was collected by filtration and thoroughly washed with water and ethanol. The crude product was obtained in an 87% yield (12.2 g) and used in subsequent steps without further purification. ^{1}H NMR ($CDCl_3$, 500 MHz): δ = 7.27 (d, J = 8.5 Hz, 8H), 6.85 (d, J = 8.5 Hz, 8H).

Synthesis of tetra(4-cyanophenyl) ethylene (2)

Then the tetra(4-bromophenyl) ethylene (6.5 g, 10.0 mmol), CuCN (5.0 g, 55.9 mmol), and DMF (50 mL) were placed in a 150 mL Schlenk flask. The mixture was heated at reflux for 60 h under a nitrogen atmosphere and then suspended in 300 mL water. Ethylenediamine (10 mL) was added, and the resulting mixture was stirred at 100 °C for 1 h and filtered. The precipitated solid was extracted with dichloromethane (3 × 150 mL each). The combined organic phase was dried with $MgSO_4$, filtered, and evaporated in a vacuum. The residue was repeatedly purified by chromatography on silica using a hexane/CH_2Cl_2 (1:1) as eluent, giving tetra(4-cyanophenyl) ethylene 3.2 g with a yield of 74%. ^{1}H NMR (CDCl3, 500 MHz) δ (ppm): 7.48 (t, J = 5.0 Hz, 8H) and 7.08 (t, J = 5.0 Hz, 8H).

2.2.3: Synthesis of the covalent triazine based framework (CTF-TPE)

To prepared the CTF-TPE, tetra(4-cyanophenyl) ethylene (200 mg) was added directly into the mixture of DCM (1.23 mL) and TFMS (0.47 mL) in a clean vial, followed by sonication for 10 minutes. Next, for the solvothermal synthesis of CTF, we placed the resulting solution in a preheated oven at 50°C for 24 h. The dark purple-colored product was quenched and washed with a mixed solvent of DCM and DMF (2:1 v/v). Finally, a yellow powder was obtained by filtration and washed it with H_2O (2 × 30mL), THF (2 × 30mL), DCM (2 × 30 mL), and acetone (2 × 30 mL), and the material was subsequently purified by Soxhlet extraction with acetone for 24h. The resulting product was then dried under vacuum conditions. The yield of the final product was 85%.

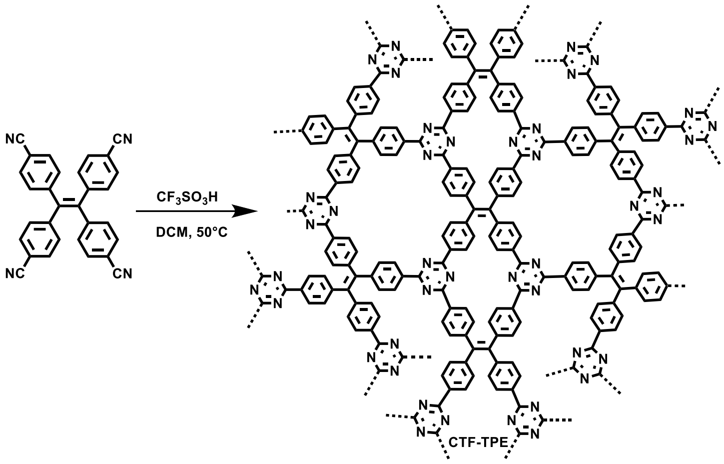

Figure 2.2: Synthesis scheme for the CTF-TPE.

2.2.4: Synthesis of CTF-TPE@Co

To deposit Co^{2+} on CTF-TPE, 25 mg of CTF-TPE was mixed with a specific amount of $CoCl_2$ in 2.5 mL acetonitrile. Then 65 µL TEA was added to the mixture, which was subsequently stirred for 1h. The mixture in a capped reaction vessel was placed in a CEM Discover single-mode microwave reactor and was heated to 80 °C for 120 min. After the microwave reaction, the resulting precipitate was recovered by centrifugation, and washed twice with chloroform, methanol, and acetonitrile, respectively. Following a similar procedure, a series of CTF-TPE@Co-n (n= 1 to 4; where, 1= 0.150 µmol of Co loading/mg, similarly, 2= 0.250 µmol/mg, 3=0.400 µmol/mg, 4= 0.700 µmol/mg) with different cobalt loading have been prepared to study the variation in photocatalytic CO_2 reduction.

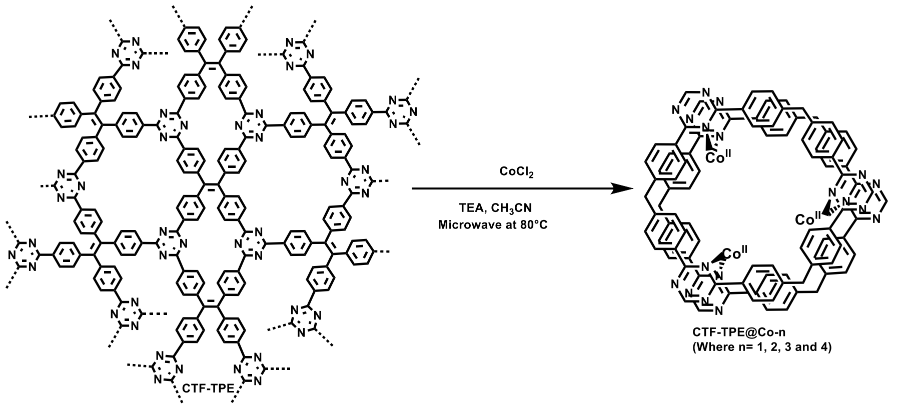

Figure 2.3: Synthesis scheme for CTF-TPE@Co-n

2.2.5: Characterization methods

Fourier transform–infrared (FT–IR) spectra of CTF-TPE and CTF-TPE@Co-n were collected on a Nicolet Magna IR 750 series-II FTIR spectrophotometer within the range of 400 cm^{-1} to

4000 cm^{-1} using KBr plates. The powder X-ray diffraction (PXRD) data of CTF-TPE and CTF-TPE@Co-n were collected with Bruker D8 Advance X-ray diffractometer (XRD) at room temperature using Cu Kα radiation (λ = 1.548 Å) in a 2θ range of 3–55°. Thermogravimetric analyses (TGA) were done at a ramp rate of 20 °C min^{-1} under air with Perkin Elmer Pyris Diamond TG–DTA instruments. UV absorption spectra were recorded using a Cary 60 UV–vis (Agilent Technologies) with a 1 cm path-length quartz cell. Fluorescence emission spectra were collected on a HORIBA Fluoromax-4 fluorometer. Nitrogen gas adsorption–desorption of the samples was performed to obtain BET-specific surface area (SBET) using Quanta chrome Autosorb iQ2 Instruments at liquid N_2 temperature (77 K). The samples were degassed under a high vacuum (10^{-6} torr) at 105 °C for 10 h. After degassing, the sample tube was then transferred to the analysis port of the sorption analyzer. Pore size distribution was calculated by quenched solid density functional theory (QSDFT) slit/cylindrical pore model. 1H and 13C NMR spectra were measured on Bruker-DRX 400 MHz instruments at room temperature in CDCl3. Field emission scanning electron microscope (FE-SEM) images with elemental mapping were obtained using a Carl Zeiss SUPRA 55VP FE-SEM instrument. Energy dispersive X-ray spectroscopy (EDS) was performed by Oxford Instruments X-Max with INCA software coupled to the FE-SEM. The Hitachi, S-4800, EDS detector was introduced to analyze the morphology and EDS of the samples. The Electron Paramagnetic Resonance (EPR) experiments were conducted with a JEOL JESFA200 ESR Spectrometer instrument having an X-band Microwave unit. The High-resolution transmission electron microscopy (HR-TEM) images were collected from the JEM, JEM-2100F instrument, operating at an accelerating voltage of 200 kV. Before the analysis, the 2-propanol solution of a small amount of sample was dispersed homogeneously in an ultrasonic cleaner for 2 h to ensure maximum dispersion of the sample, and then 2 µL of the solution was cast on a carbon-coated Cu-grid (300 mesh size), put in an airtight desiccator, and dried at ambient temperature for two days. HAADF-STEM and the corresponding EDS mapping were recorded using the same instrument. X-ray photoelectron spectroscopy (XPS) measurement was conducted by the Thermo Fisher ESCALAB Xi+ microProbe instrument with a monochromatic Al-Kα target, 1486.6 eV energy, and a maximum power of 15.0 KW. CoK-edge EXAFS measurement was carried out using the RIGAKU R-XAS laboratory spectrometer equipped with a 3 kW X-ray source and Ge (220) monochromator. Data was recorded in the transmission mode using a gas-filled ionization chamber before the sample and a scintillation detector after the sample. Inductively coupled plasma optical emission spectrometry (ICP-OES) results were obtained from an Icap 7000 ICP-OES (Thermo Scientific). After the photocatalysis, gaseous and liquid products were analyzed. The gaseous product was analyzed and quantified using TCD and FID detector in High-performance gas chromatography (Agilent 8860). GC was calibrated with known standard for H_2, CO and CH_4. Liquid products were analysed on a Metrohm Eco IC and 1H NMR. For the isotope labeling experiment, we purged the reaction mixture with $^{13}CO_2$. This product was detected using gas chromatography by MS detector (Perkin Elmer clarus 690).

Electrochemical characterization:

The Mott-Schottky analysis and impedance measurement were conducted using CHI760E workstation (CHI Instruments, USA) through a conventional three-electrode system immersed in a 0.2 M Na_2SO_4 aqueous solution.

Preparation of working electrode for Mott-Schottky measurement:

2.5 mg of respective CTF materials were dispersed in a solution of 250 μL water, 250 μL isopropyl alcohol (IPA), and 10 μL of Nafion to prepare a homogenous slurry. Subsequently, 12 μL of slurry was coated on a glassy carbon electrode and then dried at room temperature. The Ag/AgCl electrode was employed as the reference electrode, and the platinum plate was used as the counter electrode, respectively. The measurements were carried out under frequencies of 0.5, 1, and 1.5 kHz.

Preparation of working electrode for impedance measurement:

2.5 mg of respective CTF materials were dispersed in a solution of 250 μL water, 250 μL isopropyl alcohol (IPA), and 10 μL of Nafion to prepare a homogenous slurry. Subsequently, 12 μL of slurry was coated on a glassy carbon electrode and then dried at room temperature. The Ag/AgCl electrode was employed as the reference electrode, and the platinum plate was used as the counter electrode, respectively. A 0.2 M Na_2SO_4 solution was used as an electrolyte. The measurements were carried out with a bias potential of -0.4 V with a frequency range from 10^{-2} to 10^5 Hz under a nitrogen atmosphere.

Preparation of working electrode for transient photocurrent:

2.5 mg of respective CTF materials was dispersed in a solution of 250 μL water, 250 μL isopropyl alcohol (IPA), and 10 μL of Nafion to prepare a homogenous slurry. Subsequently, 300 μL of slurry was coated on an FTO glass plate (1 cm × 1 cm) and then dried at room temperature. The Ag/AgCl electrode was employed as the reference electrode, and the platinum plate was used as the counter electrode, respectively. The transient photocurrent responses were carried out under visible-light irradiation conditions (300 W Xenon arc lamp).

Photocatalytic testing:

Figure 2.4: Experimental set up of photocatalytic CO_2 reduction reaction.

The photocatalytic reactions were conducted with a 275 W Xe lamp with a 420 nm cut-off filter was used as the light source. In a typical process, a specific amount (2 mg) of catalyst, 2,2'-bipyridine (9.3 mg) as a cocatalyst, and $[Ru(bpy)_3]Cl_2 \cdot 6H_2O$ (10.4 mg) was dispersed into the solution of 3.0 mL acetonitrile solution containing TEOA and H_2O (acetonitrile: TEOA: H_2O= 3:1:1 v/v) in a quartz test tube. Before photocatalytic testing, the reaction solution was degassed with N_2 gas for 20 minutes followed by bubbling with CO_2 (99.999%, Airgas) in the dark for 30 min. The reaction solution was then irradiated at room temperature with stirring for photocatalytic CO_2 reduction. The headspace above the reaction solution was taken using a gas-tight syringe at different time intervals for product analysis using an Agilent 8860 equipped with a TCD and FID detector and a 60/80 Carboxen-1000 packed column (Supelco). The experimental component and amount of gas product were identified using the standard gas. Control experiments were conducted in the absence of light irradiation, photosensitizer, catalyst, sacrificial reagent, and CO_2. Isotope-labeled experiments were conducted with $^{13}CO_2$ instead of $^{12}CO_2$ under the same condition, and the obtained gaseous products were analyzed by gas chromatography−mass spectrometry (GC-MS). Liquid products were analysed using ion chromatography and ^1H NMR.

2.3 Result and discussions

2.3.1 Characterizations of CTF-TPE and CTF-TPE@Co-n

The polymerization of tetra(4-cyanophenyl) ethylene under solvothermal conditions in the presence of CF_3SO_3H resulted in the formation of CTF-TPE with a high yield (Figure 2.5). The FT-IR measurements provided valuable insights into the trimerization reaction. Upon examining the infrared (IR) spectra depicted in Fig.1a, it becomes apparent that a distinct and intense stretching band associated with –CN group is absent around 2226 cm^{-1}, which indicates the successful trimerization reaction of the monomer tetra(4-cyanophenyl) ethylene. Moreover, the characteristic absorption band at around 1504 cm^{-1}, and 1356 cm^{-1} is attributed to the C-N stretching bands of the triazine units (Figure 2.6a).[35]

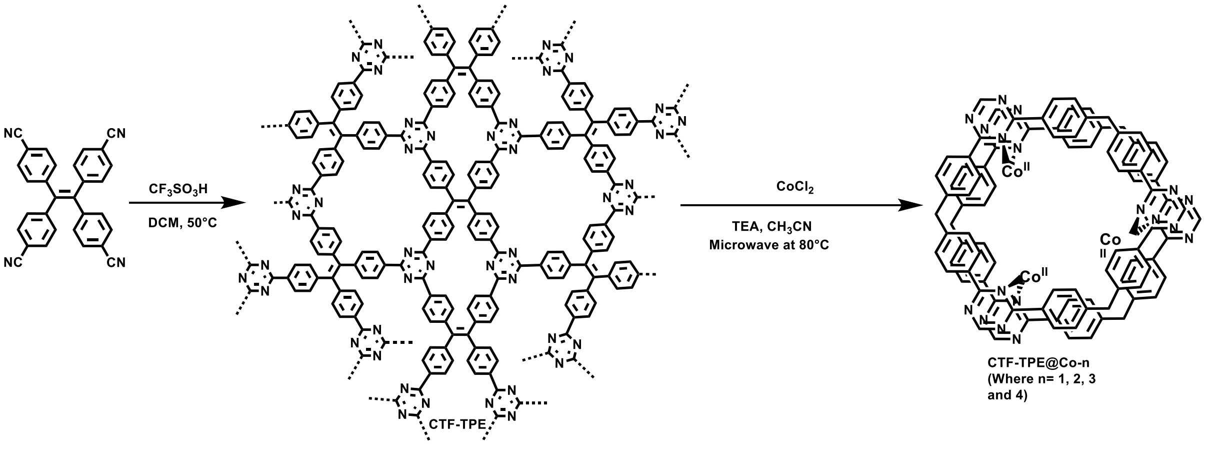

Figure 2.5. Schematic representation for the Synthesis of CTF-TPE and CTF-TPE@Co-n.

Additionally, CTF-TPE exhibits a peak around 806 cm^{-1}, which is associated with the triazine moiety (Figure 2.6a).[36] The synthesized CTF was additionally characterized using solid-state ^{13}C CP/MAS NMR spectroscopy, providing valuable insights into its structural composition (Figure 2.6b). The obtained spectra displayed three prominent resonances appearing at approximately 170, 144, and 130 ppm, which can be assigned to the carbon atom of the triazine ring (N=C-N), ethylene carbon atom (–C=C–), and aromatic carbon atoms, respectively. Remarkably, the absence of any peak corresponding to residual cyano end groups in the spectra confirms the complete trimerization reaction of all the monomers. The absence of residual cyano end groups further highlights the high conversion efficiency achieved during the trimerization process, indicating a successful transformation of the starting monomers

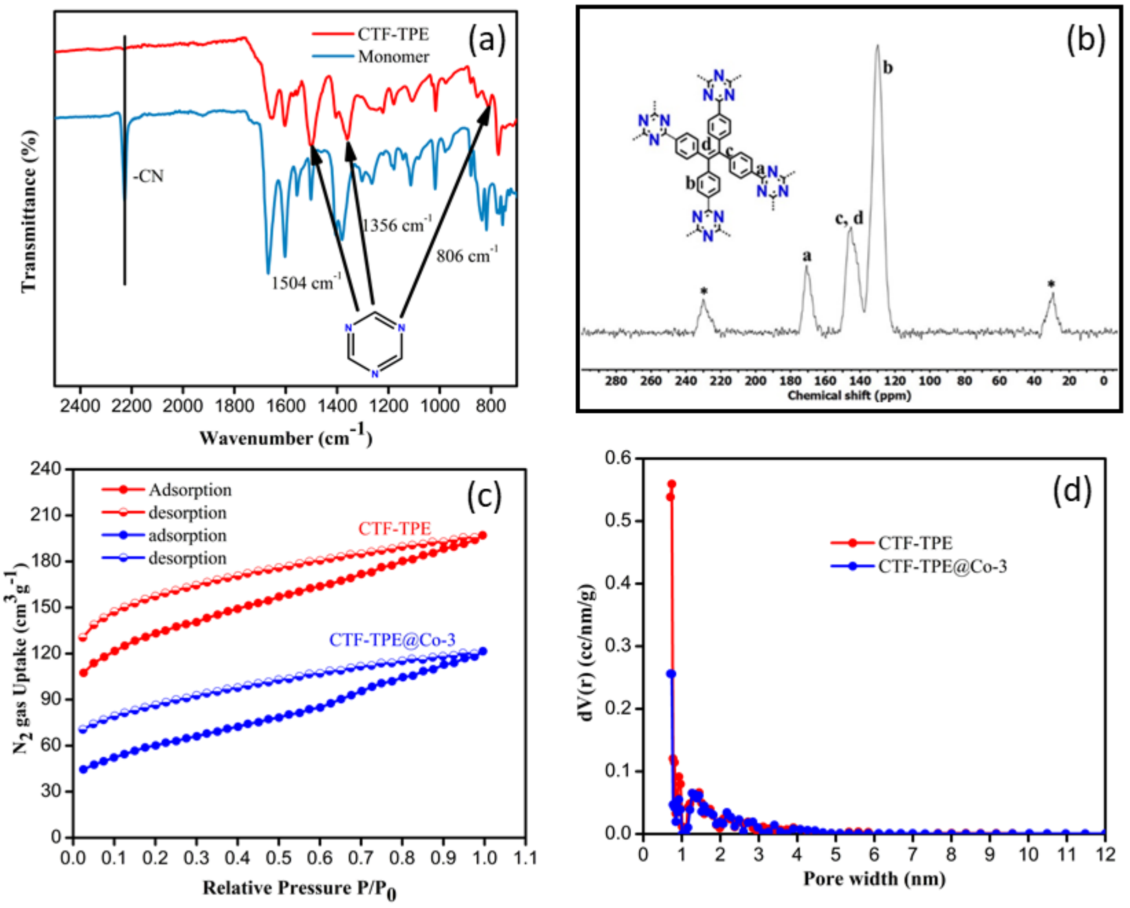

Figure 2.6: (a) IR spectra of monomer and CTF-TPE. (b) Solid-state ^{13}C CP/MAS NMR spectrum of CTF-TPE (* belongs to sidebands). (c) N_2 adsorption-desorption isotherm of CTF-TPE and CTF-TPE@Co-3. (d) Pore size distribution of CTF-TPE and CTF-TPE@Co-3 were evaluated using QSDFT method.

into the desired CTF structure. This finding aligns perfectly with the results obtained from the IR spectroscopy. The porosity of the CTF-TPE was calculated by N_2 adsorption study at 77 K. The calculated Brunauer– Emmett–Teller (BET) surface area and pore volume of the pristine CTF were found to be 434 m^2g^{-1} and 0.27 cm^3g^{-1}, respectively (Figure 2.6c, Table 2.1). Moreover, the assessment of the pore size in CTF-TPE was also conducted using the quenched solid density functional theory (QSDFT) slit/cylindrical pore model which exhibited a major pore at 0.4 nm with an additional pore at 0.8 and in the range of 1.2-1.5 nm (Figure 2.6d).

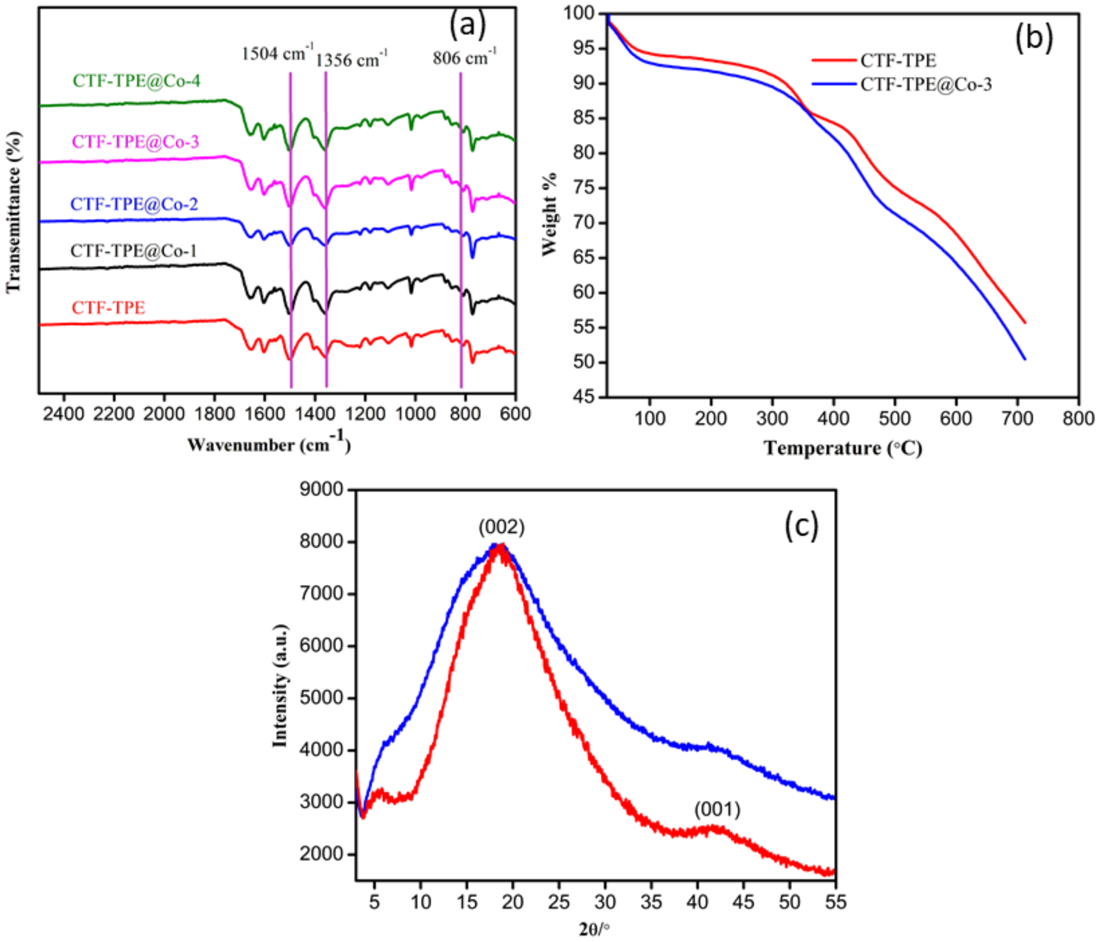

Figure 2.7: (a) Comparison of IR-spectra of different CTF-TPE@Co. (b) TGA for CTF-TPE and CTF-TPE@Co-3 in temperature range of 30 to 800 °C at the heating rate of 5 °C/min under N_2 atmosphere. (c) PXRD pattern of CTF-TPE and CTF-TPE@Co-3.

A series of Co-modified CTF-TPE including CTF-TPE@Co-1, CTF-TPE@Co-2, CTF-TPE@Co-3, and CTF-TPE@Co-4 have been synthesized using $CoCl_2$ in the presence of TEA and CH_3CN via a simple deposition method as reported previously (Figure 2.5).[37] The amount of cobalt (wt%) present in the synthesized CTF-TPE@Co-1 to-4 were, calculated by ICP-OES, found to be 0.8%, 1.5%, 3.1%, and 5.9%, respectively. However, no change in IR spectra has been observed for different cobalt-loaded CTF-TPE (Figure 2.7a) indicating the durability of the material. The thermal stability of both the CTF-TPE and CTF-TPE@Co were assessed through thermogravimetric analysis (TGA), which indicated that these materials remained stable up to a temperature of 320°C (Figure 2.7b). The initial weight loss observed in both cases can be attributed to the removal of water molecules and certain guest solvent molecules from the pores of the materials. However, as the temperature exceeded 400°C, a subsequent weight loss was observed, indicating the decomposition of the residual polymeric scaffold.[37] However, among all these cobalt-loaded samples, CTF-TPE@Co-3 is interesting because of its high catalytic activity under optimum conditions. Hence, a detailed structural analysis of CTF-TPE@Co-3 has performed. As predicted, the BET surface area of the CTF-TPE@Co-3, measured by N_2-sorption at 77 K after activation, decreased from 434 m^2g^{-1} to 243 m^2g^{-1} (Figure 2.6c). Also, pore volume was decreased from 0.27 cm^3g^{-1} to 0.17 cm^3g^{-1} (Table 2.1). However, the isotherm of CTF-TPE and CTF-TPE@Co-3 can be classified as a combination of isotherm type I(b) and type II in the lower and higher relative pressure region, respectively.[38] Typically, type I(b) isotherm indicates the characteristic for materials having microporous nature. Type II isotherm, observed for nonporous or macroporous materials, is for unrestricted monolayer multilayer adsorption. Both CTF-TPE and CTF-TPE@Co-3 exhibited H4 type hysteresis loop in the adsorption and desorption isotherms. This behaviour is analogous to that seen in other microporous polymers which is frequently attributed to framework swelling.[38,39 ,40 ,41 ,42] It demonstrates the softness of the framework. The PXRD profile of CTF-TPE and CTF-TPE@Co-3 show two broad peaks at 20° and 42°, indicating amorphous nature of the material (Figure 2.7c). These two peaks may arise from the (002) and (001) planes of carbon.[43,44] However, there is no noticeable change in the PXRD pattern before and after the loading of the cobalt has been observed. The PXRD analysis at a very high scan rate of cobalt-loaded CTF-TPE has been performed to confirm the presence of any cobalt oxide or cobalt nanoparticles within the framework (Figure 2.8). However, the data clearly indicates the absence of diffraction peak associated with cobalt nanoparticles or cobalt oxide, which further supports the existence of cobalt in the form of coordination structure rather than in the form of salt of metallic cobalt nanoparticles in the CTF matrix.[45]

Table 2.1: BET, Langmuir surface area, pore size and pore volume measurements:

SL No	Sample Name	BET surface area (m^2g^{-1})[a]	Langmuir surface area (m^2g^{-1})[b]	Pore size (nm)[c]	Pore volume (cm^3g^{-1})
1.	CTF-TPE	434	597	0.43	0.27
2.	CTF-TPE@Co-3	243	273	0.39	0.17

[a]BET surface area derived from the N_2 adsorption isotherm at 77 K over the relative pressure range p/p_0 = 0.01–0.05. [b]Langmuir surface area over the pressure range of 0–110 torr. [c]Pore size distribution measured by QSDFT.

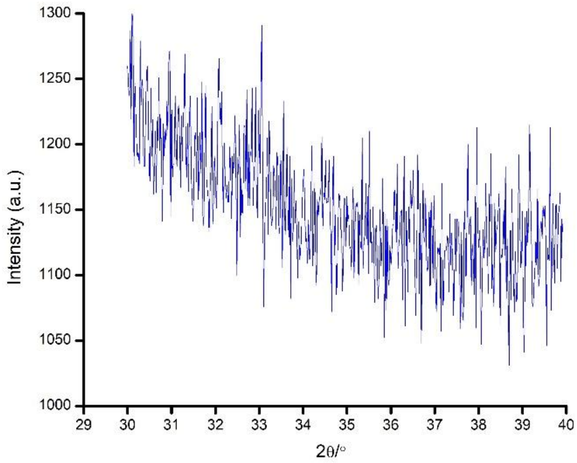

Figure 2.8: PXRD profile of CTF-TPE@Co-3 at a very high scan rate.

Further the solid-state electron paramagnetic resonance (EPR) spectra of CTF-TPE@Co-3 at room temperature was performed to deduce the formation of any metal nanoparticles or clusters (Figure 2.9). Generally, the ferromagnetic NPs or clusters give an intense broad EPR peak at g values ≈ 2.870.[46] However, there are no such EPR peaks observed at g values ≈ 2.870 for CTF-TPE@Co-3, which further reveals the absence of NPs or metal clusters within the CTF matrix. Additionally, the EPR spectroscopy shows the presence of a single Lorentzian line at a g value of 1.9997 for both CTF-TPE and CTF-TPE@Co-3, originated from the unpaired electrons on aromatic rings.[47] However, the EPR intensity of CTF-TPE has increased following the integration of Co^{2+} metal centers suggesting enhanced electron mobility in the π- conjugated CTF-TPE matrix and this observation aligns with the findings from the EIS analysis. Moreover, the EPR data do not reveal any detectable peak associated with ferromagnetic Co^{2+} single atom. This absence may be attributed to the short relaxation time, which is in close agreement with previous reports on Co–N_x–C SACs.[48]

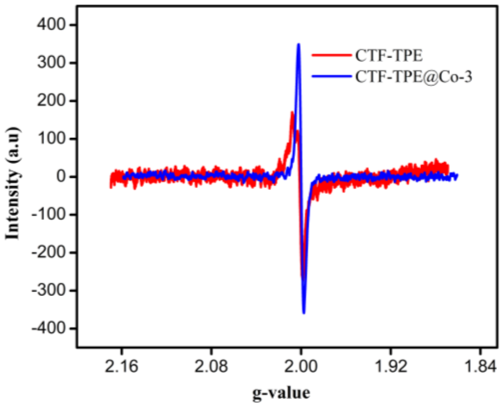

Figure 2.9: EPR spectra of CTF-TPE and CTF-TPE@Co-3.

In addition, the chemical structure analysis of N-containing CTF-TPE and CTF-TPE@Co-3 was conducted using photoelectron spectroscopy (XPS). High-resolution C 1s XPS analysis revealed two distinctive peaks at a binding energy of 284.8 eV and 286.2 eV, indicating the presence of distinct carbon atom types within the framework (Figure 2.10a). The peak at approximately 284.8 eV is associated with one type of carbon atom (C=C/C-C) and the broader peak at around 286.2 eV corresponds to the carbon atoms of triazine unit (N=C-N).[49] Similarly, the deconvolution of N 1s XPS spectra displayed a peak at a binding energy of 397.7 eV attributed to the N atom of the triazine unit (C=N-C) (Figure 2.10c).[50]

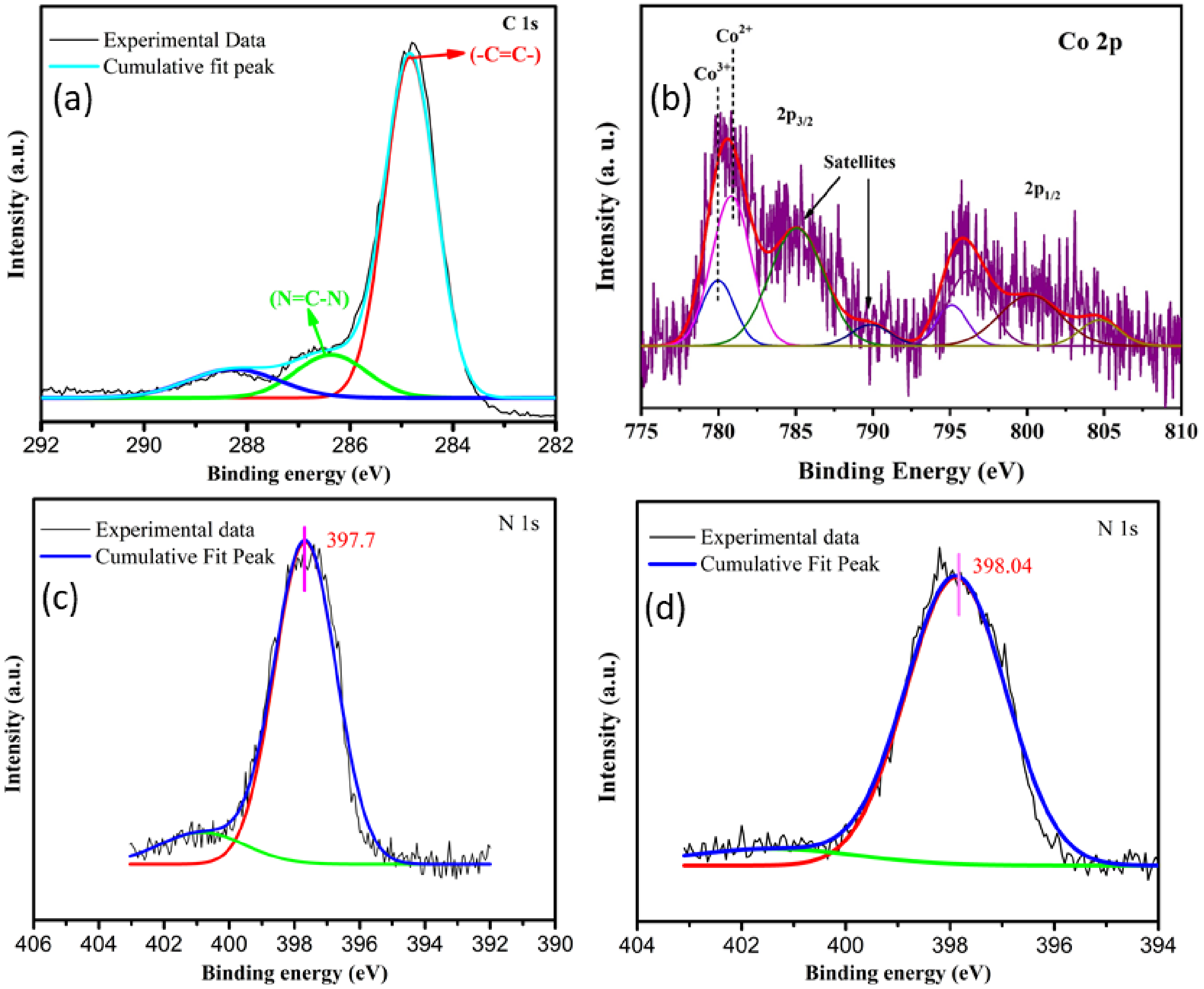

Figure 2.10: XPS spectra (C 1s) of CTF-TPE (a); Co 2p of CTF-TPE@Co-3 (b); N 1s of CTF-TPE (c) and N 1s of CTF-TPE@Co-3 (d).

More interestingly, in the case of Co-loaded CTF-TPE the binding energy of N 1s peak has been slightly shifted to 398.04 eV (Figure 2.10d). This shifting in binding energy is arising due to the coordination of Co to the N atom of triazine moiety.[51,52] The XPS analysis of cobalt in

CTF-TPE@Co-3 revealed major binding energy peaks at 780.8 eV ($2p_{3/2}$) and 796.2 eV ($2p_{1/2}$) with a 15.4 eV spin-orbit separation (Figure 2.10b).[53,54] These peaks provide a clear indication of the +2-oxidation state of the cobalt ion. The minor peaks with 15.2 eV spin-orbit separation observed at 779.9 eV and 795.1 eV, suggests the presence of a minimal amount of Co^{3+}.[53,54] However, it is challenging to identify the Co^{2+} and Co^{3+} using the primary 2p peaks due to their slight variation in peak positions ranging from 0.1 to 1.5 eV. The Co 2p core level spectra of the CTF-TPE@Co-3 can be differentiated by their distinct satellite peaks. The prominent satellite peaks of Co^{2+} occur at 785.03 eV and 800.21 eV. Hence, the binding energy difference of cobalt $2p_{3/2}$ peak and its corresponding satellite peaks come around 4-6 eV assigned to Co^{2+}, whereas the peak difference for Co^{3+} falls in the range of 9-10 eV (Figure 2.10b). The relative concentrations of Co^{2+} is found to be 90% compare to Co^{3+} in the CTF-TPE@Co-3. The presence of small amount of Co^{3+} may be ascribed to the surface oxidation or aerial oxidation of the sample.[55] Notably, Co 2p spectrum do not reveal any peaks corresponding to Co^0 (typically at around 778.5 eV). This observation excludes the presence of any Co-Co metallic bond.[56] The XPS study does not reveal any other cobalt species corresponding to CoO or cobalt metal.

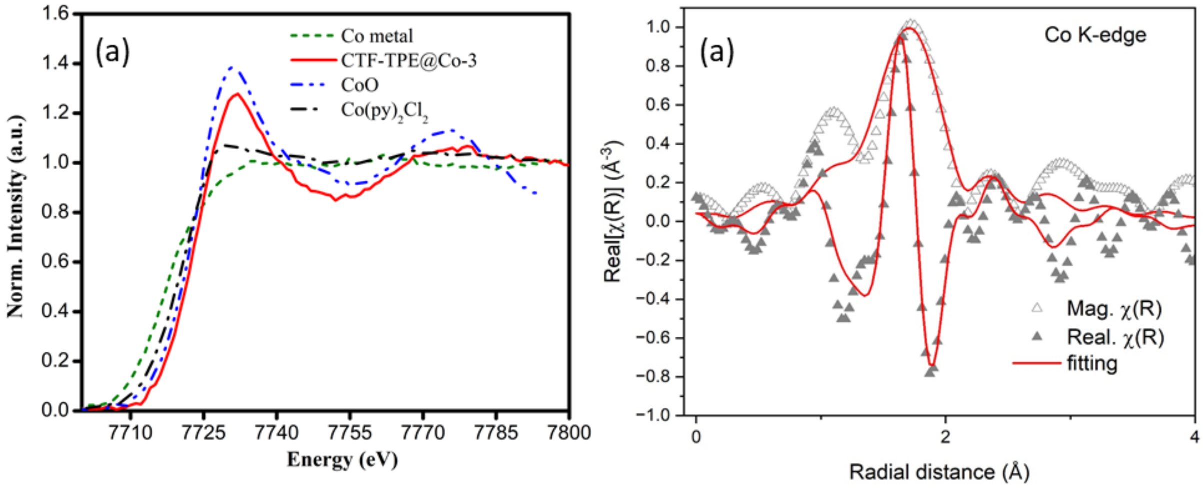

Figure 2.11: (a) XANES spectra recorded at Co-k edge for Co metal, CTF-TPE@Co-3, CoO, and $Co(py)_2Cl_2$, (b) EXAFS spectra of CTF-TPE@Co-3.

Furthermore, to investigate more about the coordination number and the electronic environment of the cobalt single sites in the CTF-TPE, extended X-ray absorption near-edge structure (XANES) spectra at the Co K-edge, referenced to the model compound $Co(py)_2Cl_2$, CoO, Co-metal was thoroughly investigated. Also, the Co K-edge Fourier transformed extended absorption fine structure (EXAFS) was extracted from the absorption spectrum of

CTF-TPE@Co-3 in the *k*-range of (3 – 10) Å^{-1} and fitting was carried out roughly in the *R*-range of (1 – 3) Å. The Co K-edge XANES spectra CTF-TPE@Co-3 with the reference compound Co(py)$_2$Cl$_2$, CoO, and Co-metal were shown in Figure 2.11b. The XANES curves

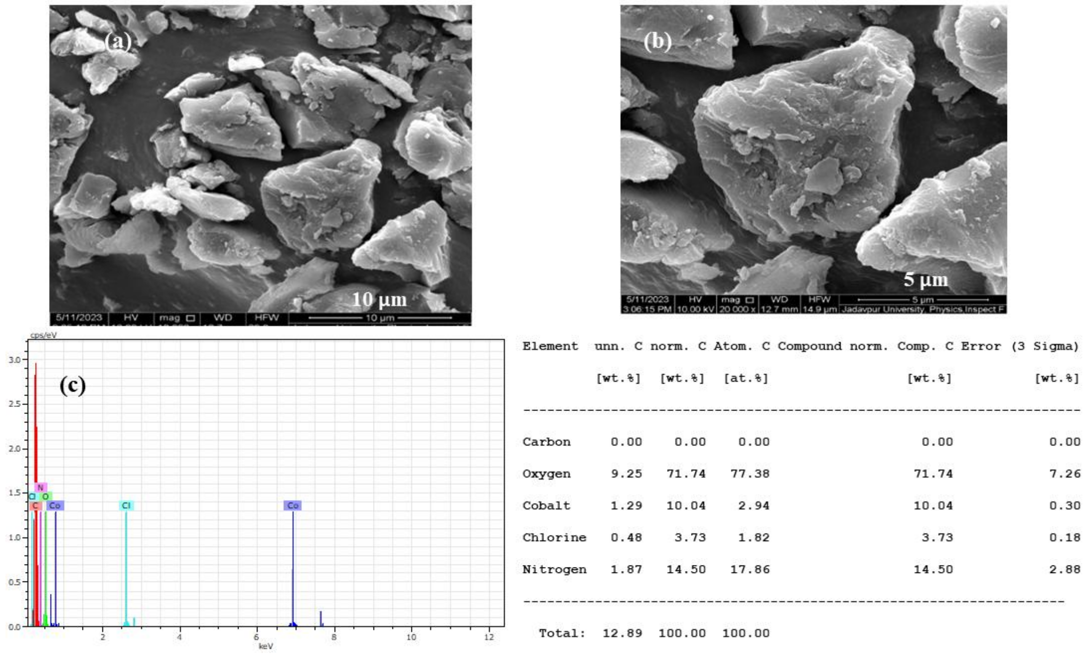

```
Element   unn. C norm. C Atom. C Compound norm. Comp. C Error (3 Sigma)
          [wt.%]  [wt.%]  [at.%]              [wt.%]          [wt.%]
-----------------------------------------------------------------------
Carbon     0.00    0.00    0.00                0.00            0.00
Oxygen     9.25   71.74   77.38               71.74            7.26
Cobalt     1.29   10.04    2.94               10.04            0.30
Chlorine   0.48    3.73    1.82                3.73            0.18
Nitrogen   1.87   14.50   17.86               14.50            2.88
-----------------------------------------------------------------------
  Total:  12.89  100.00  100.00
```

Figure 2.12: SEM image of CTF-TPE@Co-3 (a, b), EDX profile of CTF-TPE@Co-3 (c).

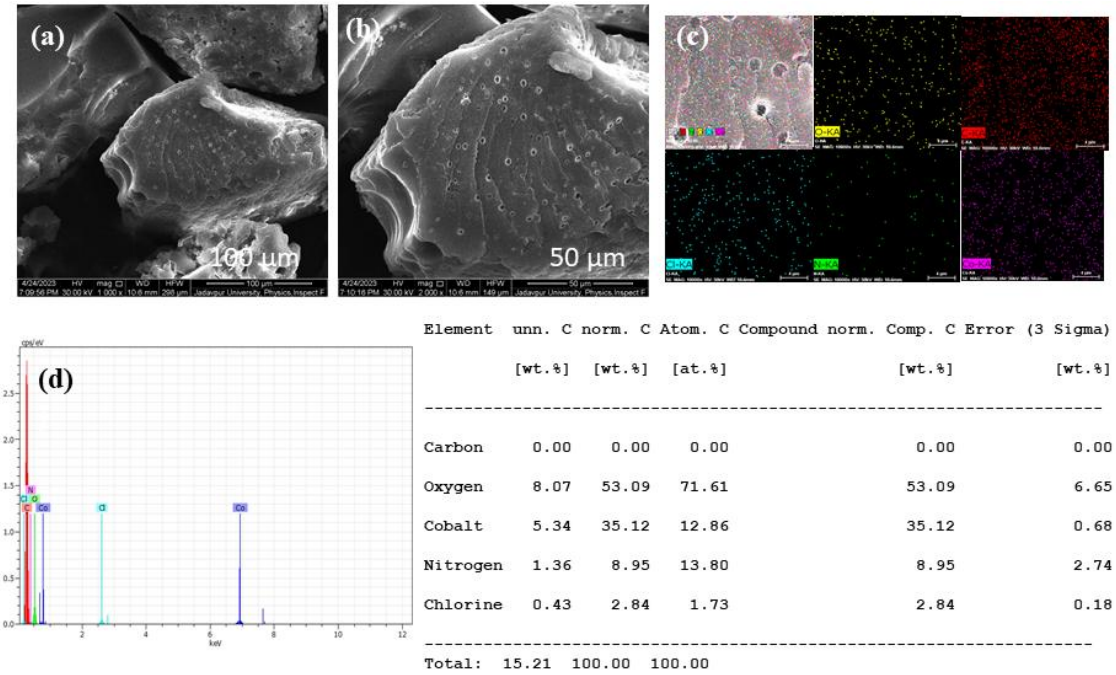

```
Element    unn. C norm. C Atom. C Compound norm. Comp. C Error (3 Sigma)
           [wt.%]  [wt.%]  [at.%]              [wt.%]          [wt.%]
------------------------------------------------------------------------
Carbon      0.00    0.00    0.00                0.00            0.00
Oxygen      8.07   53.09   71.61               53.09            6.65
Cobalt      5.34   35.12   12.86               35.12            0.68
Nitrogen    1.36    8.95   13.80                8.95            2.74
Chlorine    0.43    2.84    1.73                2.84            0.18
------------------------------------------------------------------------
Total:     15.21  100.00  100.00
```

Figure 2.13: (a, b) SEM images, (c) Elemental mapping and (d) EDX profile of CTF-TPE@Co-4.

Show that the absorption threshold peak position of CTF-TPE@Co-3 and reference compound $CoPy_2Cl_2$, CoO are look-alike indicating a 2+ valence state of the Co atoms in the CTF-TPE@Co-3 compound, which is consistent with the XPS data. The Fourier-transformed EXAFS spectrum (Figure 2.11a) of CTF-TPE@Co-3 demonstrates a prominent sharp peak around 1.56 Å, which can be attributed to the Co^{2+} and nitrogen atom bond distance.[21,25] No Co-Co peaks at 2.17 Å or larger bond distances were detected, confirming atomically dispersed Co species in CTF-TPE@Co-3.[57,44]

The morphology and textural study of the sample was investigated using a scanning electron microscope (SEM) and transmission electron microscope (TEM) for CTF-TPE@Co-3. The SEM images indicate the disordered structure of the CTF-TPE@Co-n (n=3, 4) (Figure 2.12a-b and 2.13a-b). The SEM-EDX mapping confirms the presence of Co, N, C, and Cl which are homogenously distributed within the CTF framework (Figure 2.12c and 2.13d). Further, the elemental mapping acquired by the high-angle annular dark field scanning transmission electron microscope (HAADF-STEM) indicates the uniform distribution of Co, N, C within the CTF framework (Figure 2.14a). Notably, no images associated with CoO or

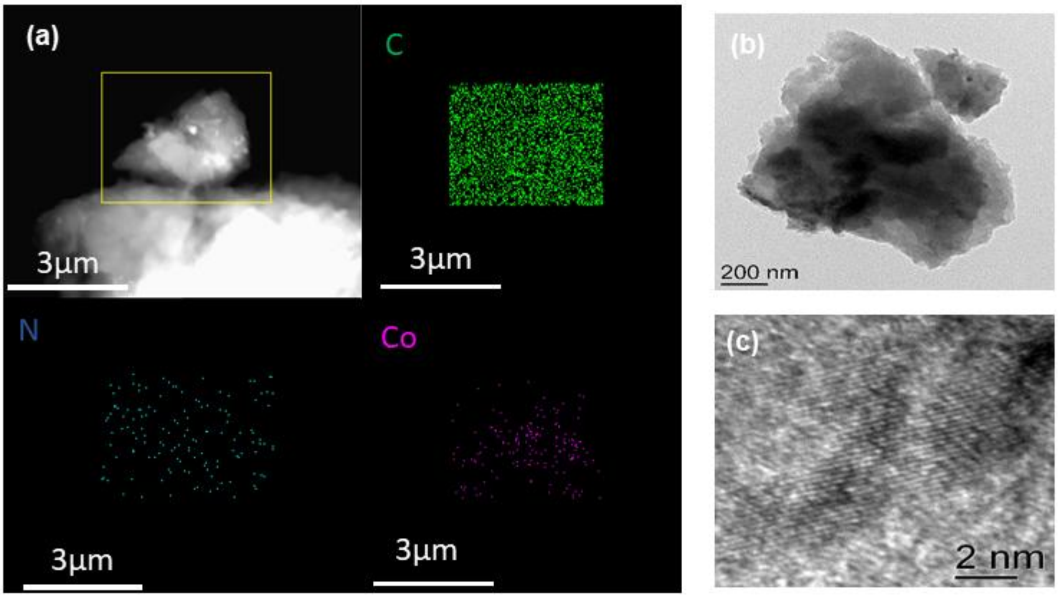

Figure 2.14: (a) EDX mapping images of C, N, Co elements in the CTF-TPE@Co-3. (b, c) HR-TEM images of CTF-TPE@Co-3.

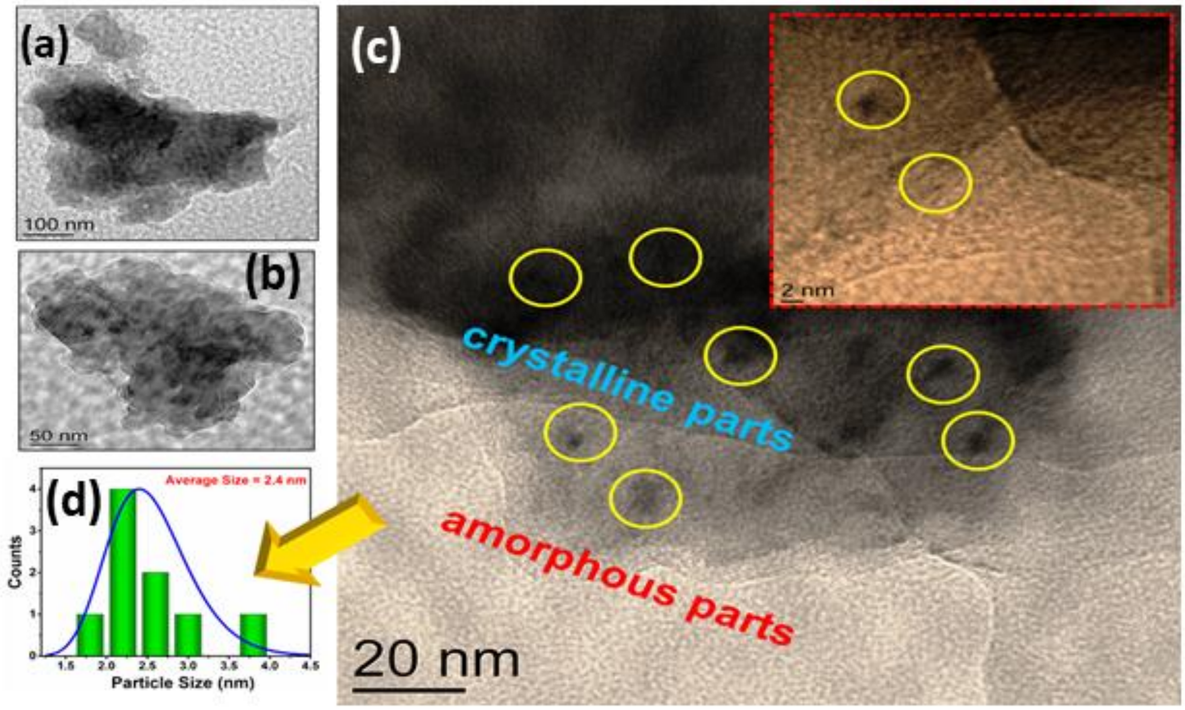

Figure 2.15: Fig.4 (a and b) Low-magnification TEM images of CTF-TPE@Co-3, (c) TEM image displaying both crystalline and amorphous nature of the sample (inset shows the its HRTEM image), (d) particle size distribution (PSD) of the crystallite parts.

metal clusters were identified in the high-resolution transmission electron microscope (HR-TEM) images (Figure 2.14b-c). This observation serves as additional confirmation of the effective incorporation of single atomic Co sites embedded in the CTF scaffold. TEM images shows that crystalline and amorphous components are well dispersed throughout the solid matrix. Moreover, low and high magnification indicates that the smaller crystallites are embedded in the amorphous matrix; particles size distribution curve indicates the particles have around 2.5 nm (Figure 2.15a-d); these tiniest crystallites are craped in the stacked flexible structure on C and N controlled by dopant Co^{2+} ion, this fact supports the selective site photocatalytic reductions. Figure 2.16a-b and Figure 2.16d-e characterize the different lattice fringes of (001) plane and distorted lattice class of the (002) plane (also existing in the XRD graph, Figure 2.7c), SAED pattern (Figure 2.16c), revealing that similar type of fringe distortions are dispersed throughout the metal doped CTF-TPE which enhances the photochemical performances.

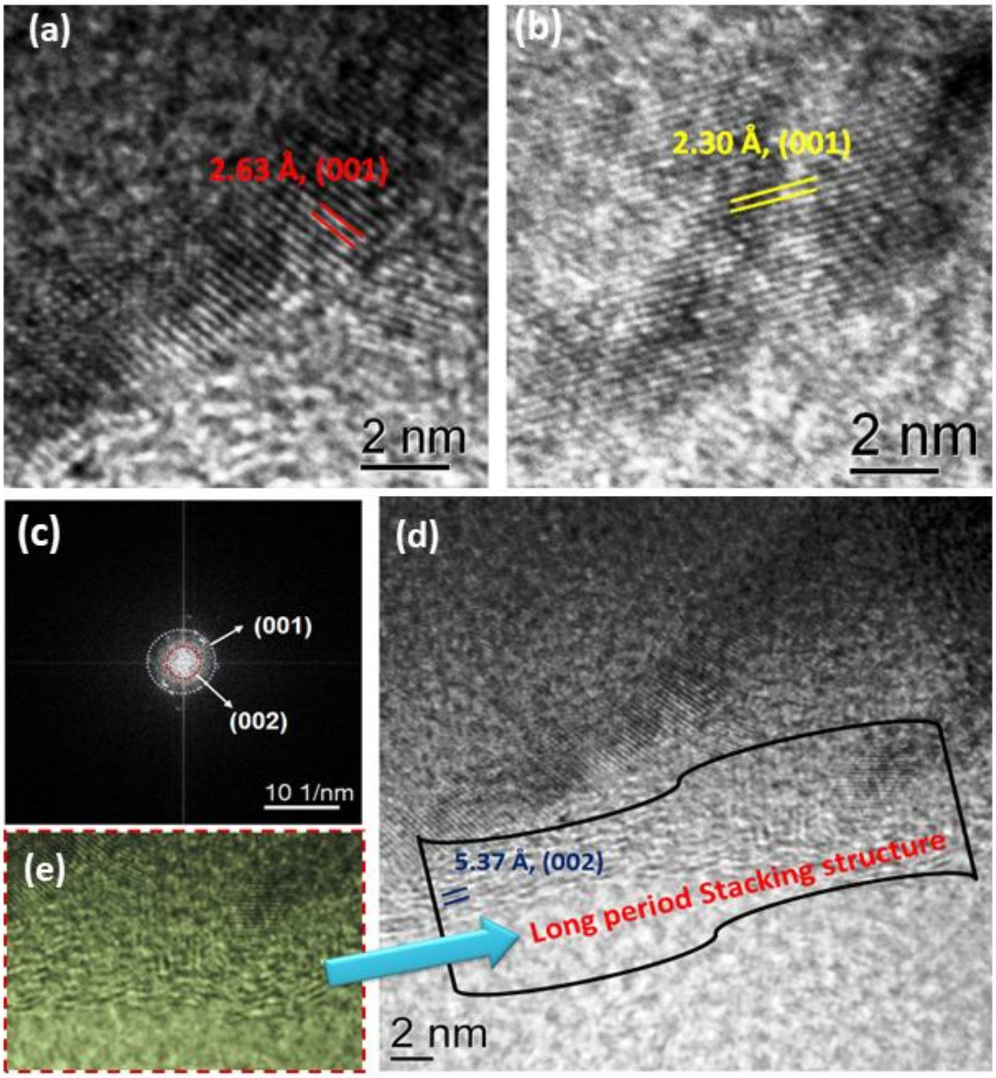

Figure 2.16: (a-b) High-magnification TEM images of CTF-TPE@Co-3 showing different lattice fringes of (001) plane, (c) corresponding SAED pattern, (d) HRTEM image of CTF-TPE@Co-3 exhibiting distorted (002) plane, (e) corresponding magnified view.

Photophysical and electrochemical study: In the last decade, it has been observed that CTFs are well-known for high CO_2 adsorption. Motivated by the high CO_2 adsorption in the CTF-TPE material, photochemical CO_2 reduction was studied. Indeed, the efficacy of the catalyst's photoreduction activity relies on two additional factors: the optical absorption properties and the efficiency of feasible transfer and separation of photoinduced charge. These two factors play a pivotal role in shaping the catalyst’s ability to absorb light and effectively

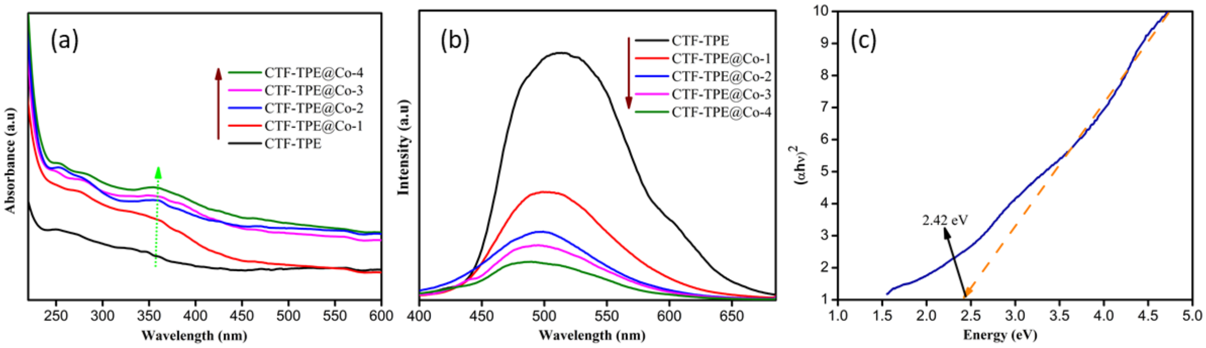

Figure 2.17: (a) UV-VIS absorption spectra of CTF and CTF-TPE@Co-n (n= 1 to 4); (b)Fluorescence spectra of CTF-TPE and CTF-TPE@Co-n (n= 1 to 4); (c)Tauc plot for CTF-TPE@Co-3.

utilize it to induce and separate charges. The UV-VIS spectroscopy of the synthesized catalysts has been investigated (Figure 2.17a). Both CTF-TPE and CTF-TPE@Co-n (n=1 to 4) exhibited a wide absorption peak ranging from 350-450 nm with a maximum absorption (λ_{max}) occurring at 355 nm. Notably, the inclusion of Co in the CTF-TPE resulted in higher photo absorption in the region (350-450 nm) compared to the pristine CTF-TPE (Figure 2.17a). This observation suggests a strong interaction between metal and the framework, indicating promising host-guest interaction.[58,59] The band gap for the CTF-TPE@Co-3 has been calculated from UV-vis absorption spectra using the Tauc formula and found to be 2.42 eV (Figure 2.17c). Further, the photoluminescence experiments were performed for CTF-TPE and CTF-TPE@Co-n (n=1 to 4) by exciting the materials at a wavelength of 360 nm. The materials CTF-TPE and CTF-TPE@Co-n (n=1 to 4) exhibited maximum fluorescence intensity at 520 nm. But, more importantly, the fluorescence intensity of CTF-TPE@Co-n gets quenched dramatically by many folds as compared to its counterpart, CTF-TPE (Figure 2.17b) as the metal loading increases. This observation implies a probability of higher charge separation thereby promoting a lower recombination rate of photoinduced electrons and holes within CTF-TPE@Co.[60] In addition, the transient photocurrent response shows a higher current density of cobalt-incorporated CTF than the pristine CTF when illuminated with visible light. This finding provides additional confirmation of the enhanced electrical conductifity and prolonged lifetime of charge carriers (Figure 2.18a). Moreover, the electrochemical impedance spectroscopy (EIS) was performed to assess the charge transfer proficiency. The EIS Nyquist plot of CTF-TPE and

CTF-TPE@Co-n exhibited a semicircle with a much smaller radius for cobalt-loaded CTF-TPE compared to bare CTF (Figure 2.18b). Smaller semicircles reveal the lower charge transfer resistance in the CTF-TPE@Co-3 thereby accelerating the electron transfer process. This phenomenon is likely a contributing factor to the enhanced photocatalytic activity observed in CTF-TPE@Co-3.[61]

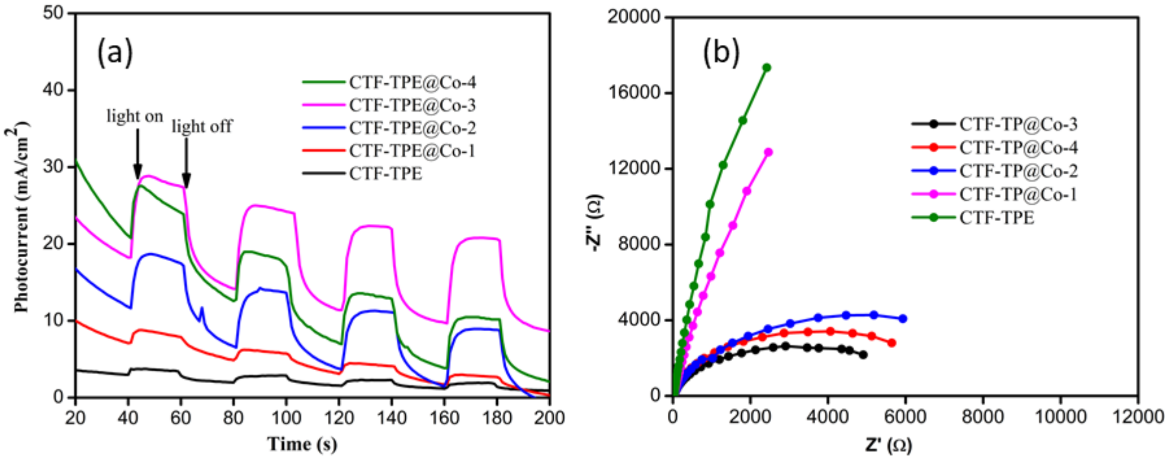

Figure 2.18: (a) EIS Nyquist plot and (e) Transient photocurrent response of CTF-TPE@Co-n (n= 1 to 4).

2.3.2: Photocatalytic CO_2 reduction

Taking into account the catalytic characteristics of the Co-ligand complex in CO_2 reduction reaction[62] combined with the strong affinity of CTF-TPE for CO_2[37] as well as its excellent chemical stability of CTF-TPE, we have examined the efficacy of the synthesized single-site cobalt-embedded CTF-TPE towards photocatalytic CO_2 reduction. The photocatalytic CO_2 reduction reaction has been carried out in a mixture of CH_3CN and H_2O solvents under visible light irradiation (λ= 420 nm) using TEOA as sacrificial electron donor, $[Ru(bpy)_3]^{2+}$ as a photosensitizer and 2,2’-bipyridine as cocatalyst (Fig. S22, ESI). All the components involved in this CO_2 reduction reaction, including sacrificial electron donor, photosensitizer, catalyst, and cocatalyst, are essential for an efficient photocatalytic CO_2 reduction reaction. The photocatalytic activity of CTF-TPE@Co materials towards CO_2 reduction has been optimized by varying the quantity of introduced Co species in the CTF-TPE scaffold (Figure 2.19a). In the absence of Co metal sites, CTF-TPE has shown poor catalytic activity, yielding a total CO production of only 40 $\mu molg^{-1}$ in 2h under optimal conditions. This poor performance of CTF-

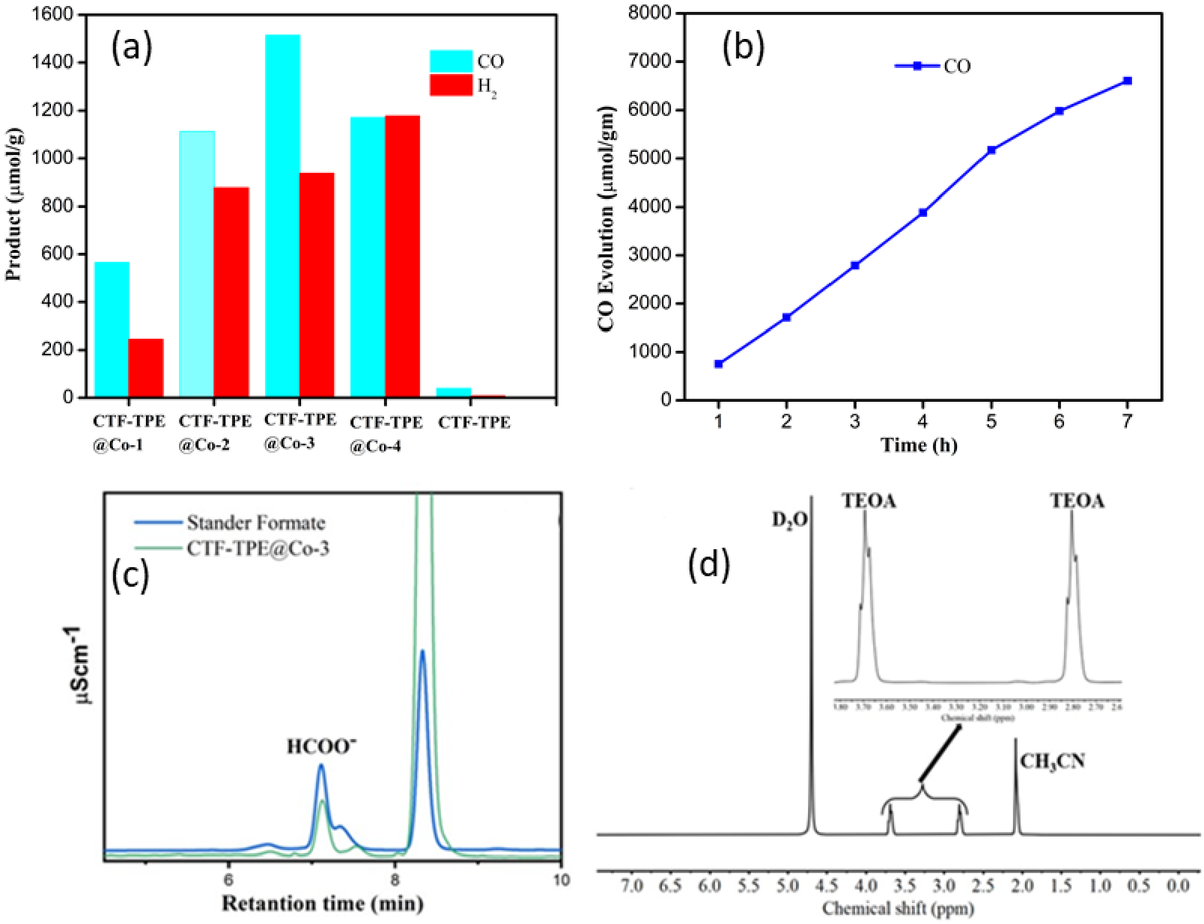

Figure 2.19: (a) CO evolution by different Co-loaded CTF-n (n=1, 2, 3, 4), negligible amount of format not shown. (b) 7h long photocatalytic run using CTF-TPE@Co-3. (c) ion chromatography and (d) ^{1}H NMR spectra of liquid product after CO_2 reduction.

TPE towards CO evolution may be ascribed to the higher recombination rate of electron-hole pairs during photocatalysis. However, the incorporation of single Co^{2+} metal centers into the CTF-TPE boosts its photocatalytic activity, which is consistent with the findings from the photoelectrochemical analysis. The outcomes of the photocatalytic carbon dioxide reduction experiments demonstrate that as the cobalt loading rises, the production of CO also increases (Figure 2.19a). Notably, among all the prepared photocatalysts, the optimal catalytic efficiency is achieved with a cobalt loading of 3.1 wt% (CTF-TPE@Co-3). The CTF-TPE@Co-3 shows the highest photocatalytic efficiency with CO and H_2 generation of 1515 $\mu molg^{-1}$ and 938 $\mu molg^{-1}$ within 2h, respectively. A negligible amount of formate also detected. Additionally, CTF-TPE@Co-3 has been employed for long-run photocatalytic experiments demonstrating CO evolution of 6616 $\mu molg^{-1}$ over 7h (Figure 2.19b), which is higher than the many previously reported CTF-based photocatalyst (Table 2.2).

The turnover number of CO evolution by CTF-TP@Co-3 is 13.32 after 7h of irradiation. However, a minute quantity of $HCOO^-$ (0.016 μmolg^{-1}) has been detected after analysing the liquid phase through ion chromatography (Figure 2.19c). No other liquid hydrocarbon products including CH_3OH and C_2H_5OH have been found in the ^1H NMR spectroscopy (Figure 2.19d). But at higher concentrations of cobalt (5.9 wt% Co loading), the catalytic efficiency of CTF-TPE@Co-4 declined with CO and H_2 production of 1172 μmolg^{-1} and 1178 μmolg^{-1}, respectively (Figure 2.19a). The reason behind this phenomenon may be attributed to the possibility that a higher concentration of Co can result in the formation of cobalt aggregates or clusters (Figure 2.20). This highlights the pivotal role of cobalt concentration in driving CO generation and underscores the optimal conditions for catalytic efficiency.

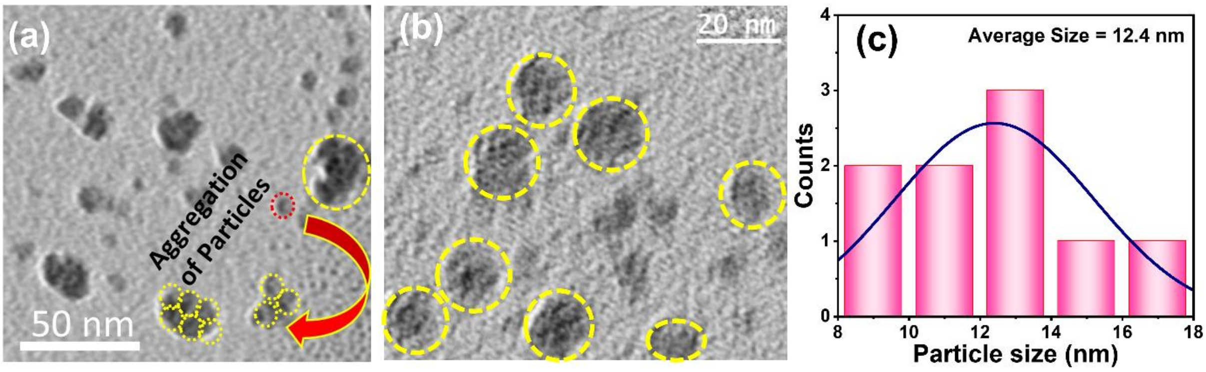

Figure 2.20: (a,b) HR-TEM image of CTF-TPE@Co-4. Highlighted parts are showing the formation of cobalt clusters through agglomeration. (c) The average size of the particle is found to be 12.4 nm.

Table 2.2. Comparison performance of photocatalytic CO evolution

Photocatalyst	Illumination range	SA	PS	Product	Production rate[a]	Reference
Ni-TpBpy-COF	λ > 420 nm	TEOA	$[Ru(bpy)_3]Cl_2$	CO	966	63
TTCOF-Zn	420 nm	H_2O	-	CO	2.06	64
ACOF-1	420 nm	H_2O	-	CH_3OH	60	65
N_3-COF	420 nm	H_2O	-	CH_3OH	98.3	66
Co-FPy-CON	420 nm	TEOA	$(Ir[dF(CF_3)ppy]_2(dtbpy))PF_6$	CO	1681	67
Co/CTF-1	λ > 420 nm	TEOA	$[Ru(bpy)_3]Cl_2$	CO	50	68
Re-CTF-py	200 nm	TEOA	-	CO	353.05	69
CTF-TPN	λ > 420 nm	TEOA	-	CO	330.3	70

NCTF-1	$\lambda > 420$ nm	TEA	-	CH_4	11.48	71
$ZnFe_2O_4$/FeP-CTFs	$\lambda > 420$ nm	TEOA	$[Ru(bpy)_3]Cl_2$	CH_4	178	72
Pt-SA/CTF-1	$\lambda > 420$ nm	TEA	-	CH_4	4.5	73
TiO_2@CTF-Py	$\lambda > 320$ nm	H_2O	-	CO	43.34	74
$Ni(OH)_2$/CTF-1	$\lambda > 420$ nm	TEOA	$[Ru(bpy)_3]Cl_2$	CO	38.66	75
CPB/CTF-1-Ni	$\lambda > 420$ nm	EA	-	CO	86.5	76
Fe_2O_3@Por-CTF10	$\lambda > 420$ nm	TEOA	$[Ru(bpy)_3]Cl_2$	CO	400	78
CTF-TPE@Co-3	**$\lambda > 420$ nm**	**TEOA**	**$[Ru(bpy)_3]Cl_2$**	**CO**	**750**	**This work**

In addition, a set of controlled experiments were conducted to know the key role of all the elements for this high CO production over CTF-TPE@Co-3(Figure 2.21a). The significant reduction in photocatalytic H_2 evolution to 254.03 µmolg^{-1} without the presence of H_2O suggests that the H_2 production may originate either from TEOA or H_2O sources. However, the removal of TEOA from the reaction mixture resulted in photocatalytic inactivity of CTF-TPE@Co-3 for CO_2 reduction. These findings suggest that the H_2O acts as a proton source and TEOA can serve as sacrificial electron donors for this CO_2 conversion system. More interestingly, we have achieved to generate a CO evolution of 1515 µmolg^{-1} only when 2,2'-bipyridine have been added in the reaction mixture (Figure 2.21a). However, in its absence, the CO evolution was lesser, measuring only 564 µmolg^{-1}. Hence, 2,2'-bipyridine, TEOA, and H_2O are crucial for high-efficiency photocatalytic CO_2 reduction. Moreover, no CO has been

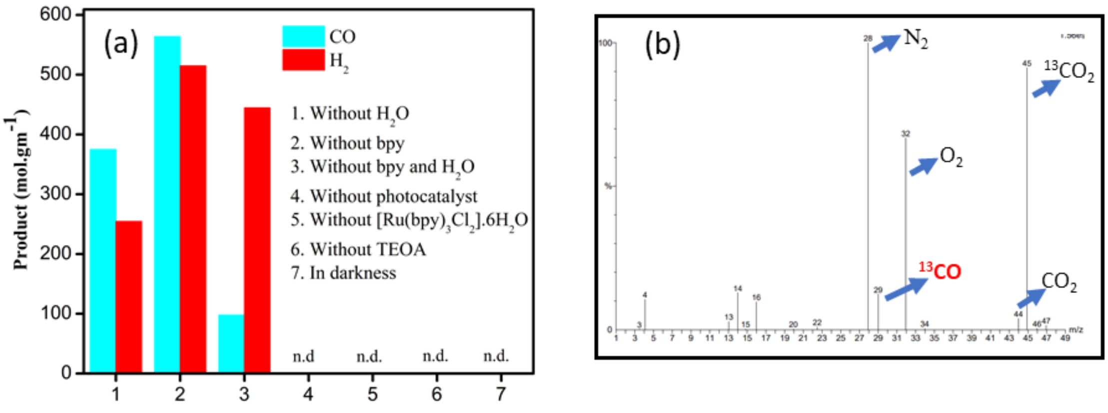

Figure 2.21: (a) reaction conditions for CO_2 reduction. (b) Isotope labeling experiment in presence of $^{13}CO_2$.

detected in the absence of light or photocatalyst revealing the photocatalytic nature of the reaction. No carbonaceous products have been noticed under the Ar atmosphere, which confirms that the CO is coming from the CO_2 rather than the organic solvent used in the reaction. Additionally, an isotope labeling experiment was conducted in the presence of $^{13}CO_2$ to confirm the origin of CO generation. The gaseous product was analyzed using gas chromatography-mass spectrometry (GC-MS), revealing a distinct peak at m/z = 29. This supports the production of CO from CO_2 gas, rather than from any other organic compounds (Figure 2.21b).[79] Moreover, the catalytic performance of the CTF-TPE@Co-3 has been investigated by direct sun light to mimic the natural photosynthesis and it gives 170 $\mu molg^{-1}$ CO and 8.0 $\mu molg^{-1}$ in 3h in a cloudy environment. Additionally, the heterogeneous nature of the CO_2 reduction reaction was further established by performing the recyclability and reusability tests (Figure 2.23a). The photocatalytic stability of CTF TPE@Co-3 was assessed through a 2h illumination cycle. As illustrated in Figure 2.23a, the rates of CO and H_2 production from CTF-TPE@Co-3 remained nearly constant even after five cycles run under the same experimental conditions. This observation confirms the excellent long-term stability of CTF-TPE@Co-3 for CO_2 reduction

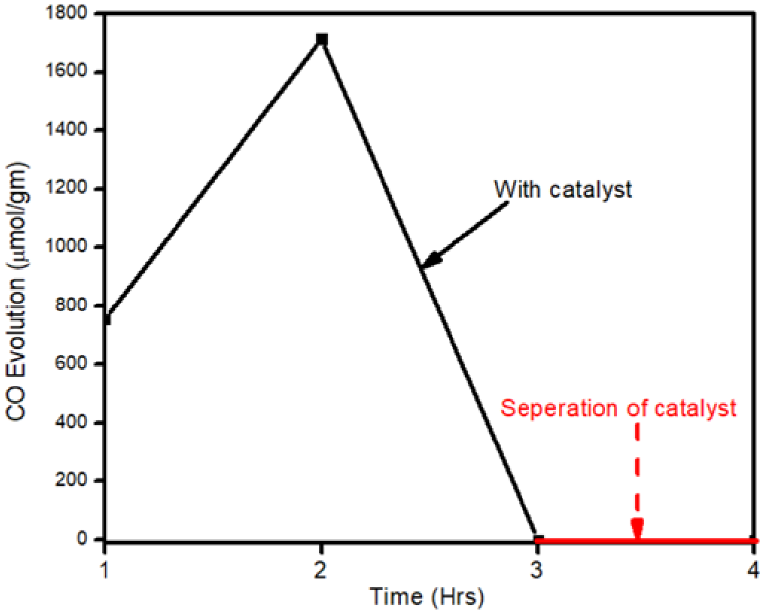

Figure 2.22: Leaching test over CTF-TPE@Co-3.

Furthermore, a leaching test was conducted to verify the heterogeneous nature of the photocatalyst in the context of photocatalytic CO_2 reduction reaction (Figure 2.22). In this experimental procedure, the catalyst was isolated after 2 hours photocatalytic run, and subsequently, the CO_2 reduction reaction was executed using the filtrate from the reaction mixture. Significantly, no CO evolution was observed in the GC chromatogram after the removal of the catalyst, affirming that no metal atoms had leached out from the CTF-TPE@Co-3 moiety. Thus, it demonstrates the pronounced heterogeneity of the CTF-TPE@Co-3.Further, no noticeable change has been observed in the FT-IR peaks and PXRD pattern of CTF-TPE@Co-3 after photocatalysis, demonstrating its stability during the reaction (Figure 2.23b-c). Also, the XPS analysis of recovered samples exhibited that the oxidation state of Co remains unchanged from its precatalysis state which shows the stability of the photocatalyst (Figure 2.23d). These results highlight the significant advantages of employing CTF-TPE for embedding single Co atoms, resulting in enhanced activity and outstanding durability.

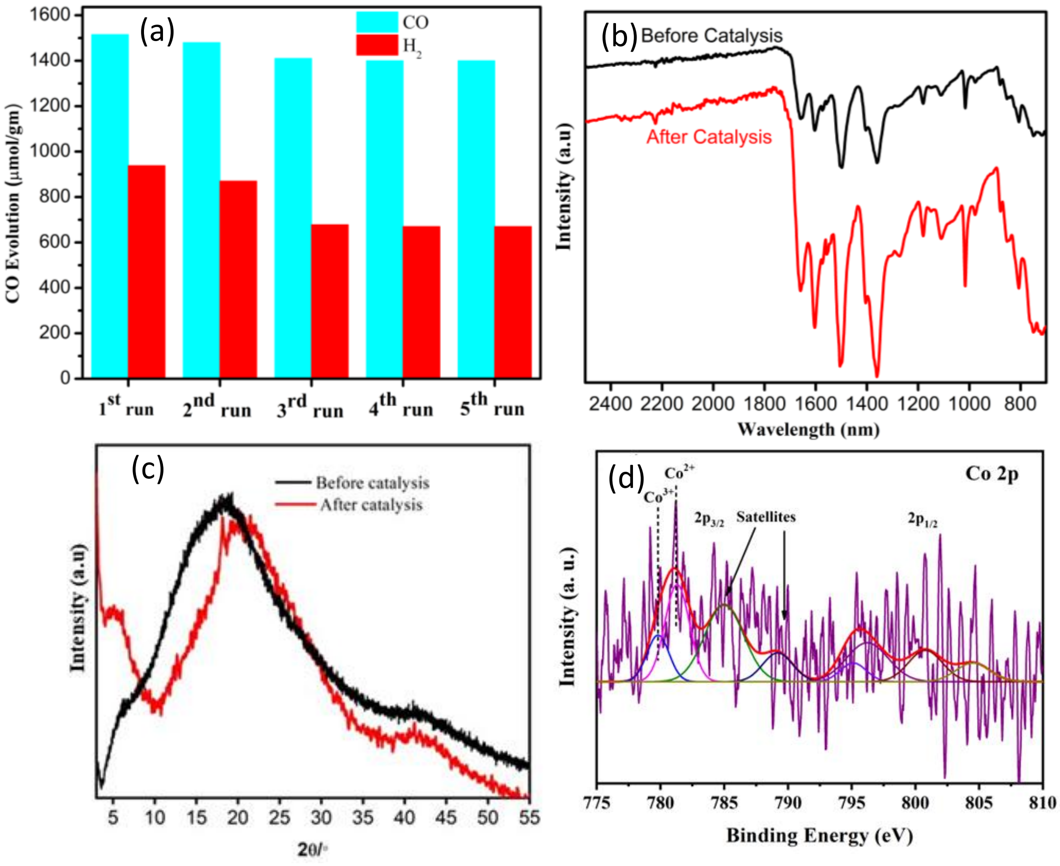

Figure 2.23: (a) recyclability test of CTF-TPE@Co-3. (b) FT-IR spectra and; (c) PXRD profile of CTF-TPE@Co-3 before and after photocatalysis. (d) XPS spectra of CTF-TPE@Co-3 after photocatalysis.

2.3.3 Photocatalytic CO_2 reduction mechanism: Now, to understand the CO_2 reduction mechanism, we have carried out photophysical and electrochemical studies. Firstly, we have investigated whether the photoexcited $Ru(bpy)_3]^{2+*}$ underwent oxidative or reductive quenching for initiating CO_2RR cycles. The emission intensity of $Ru(bpy)_3]^{2+}$ has been gradually quenched with the incremental addition of TEOA (Figure 2.24a). In contrast, there is no decrease in emission intensity observed upon the addition of CTF-TPE@Co-3 (Figure 2.24b).

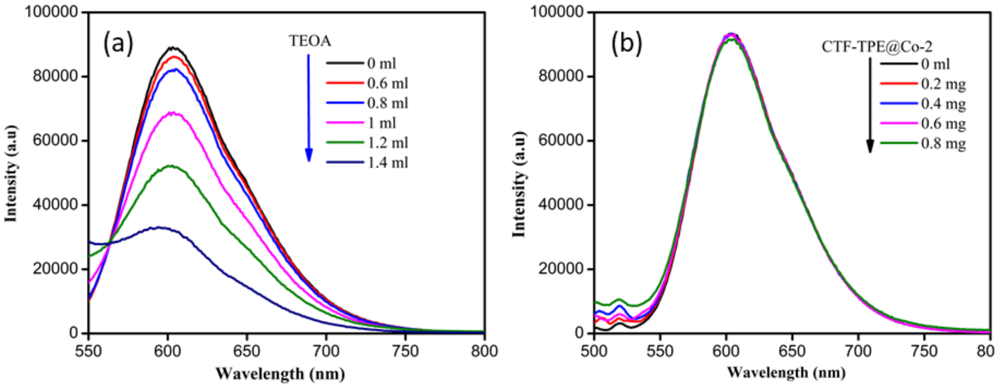

Figure 2.24: (a) Fluorescence spectra of $Ru(bpy)_3]^{2+}$ in presence of TEOA. (b) Fluorescence spectra of $Ru(bpy)_3]^{2+}$ in presence of CTF-TPE@Co-3.

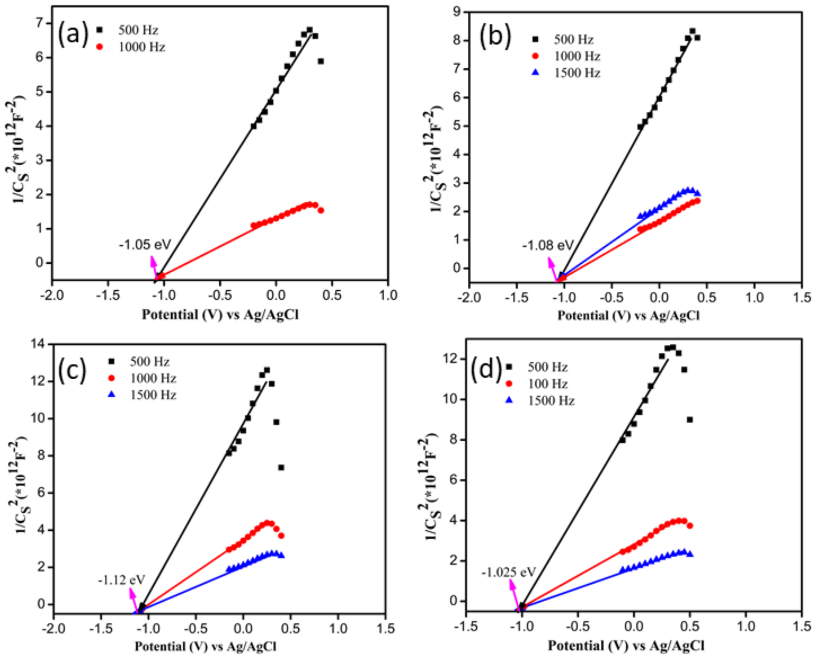

Figure 2.25: Mott-Schottky plots of CTF-TPE@Co-1 (a), CTF-TPE@Co-2 (b), CTF-TPE@Co-3 (c), and CTF-TPE@Co-4 (d) at different frequency.

This suggests a reductive quenching mechanism for CO_2RR, wherein electron transfer occurrs from TEOA to photoexcited $Ru(bpy)_3]^{2+*}$ to generate $Ru(bpy)_3]^{+}$, and then finally $Ru(bpy)_3]^{+}$ inject electrons into the cobalt center (Figure 2.26 (top)). The flat band potential of the photocatalyst CTF-TPE@Co-3 is found to be -1.12 V vs Ag/AgCl (-0.92 V vs NHE) using Mott Schottky measurements at different frequencies in 2 M Na_2SO_4 electrolyte (Figure 2.25c). Hence, its valence band was calculated to be 1.5 V (Figure 2.26 (bottom)). The Mott-Schottky plot of all the CTF-TPE@Co-n (1 to 4) shows a positive slope demonstrating the n-type nature of the semiconductors (Figure 2.25).[80] The reduction potential of LUMO of CTF-TPE@Co-n (n= 1,2,4) is found to be -0.851V, -0.881V, and -0.826V, respectively from the Mott-Schottky plot (Figure 2.25).

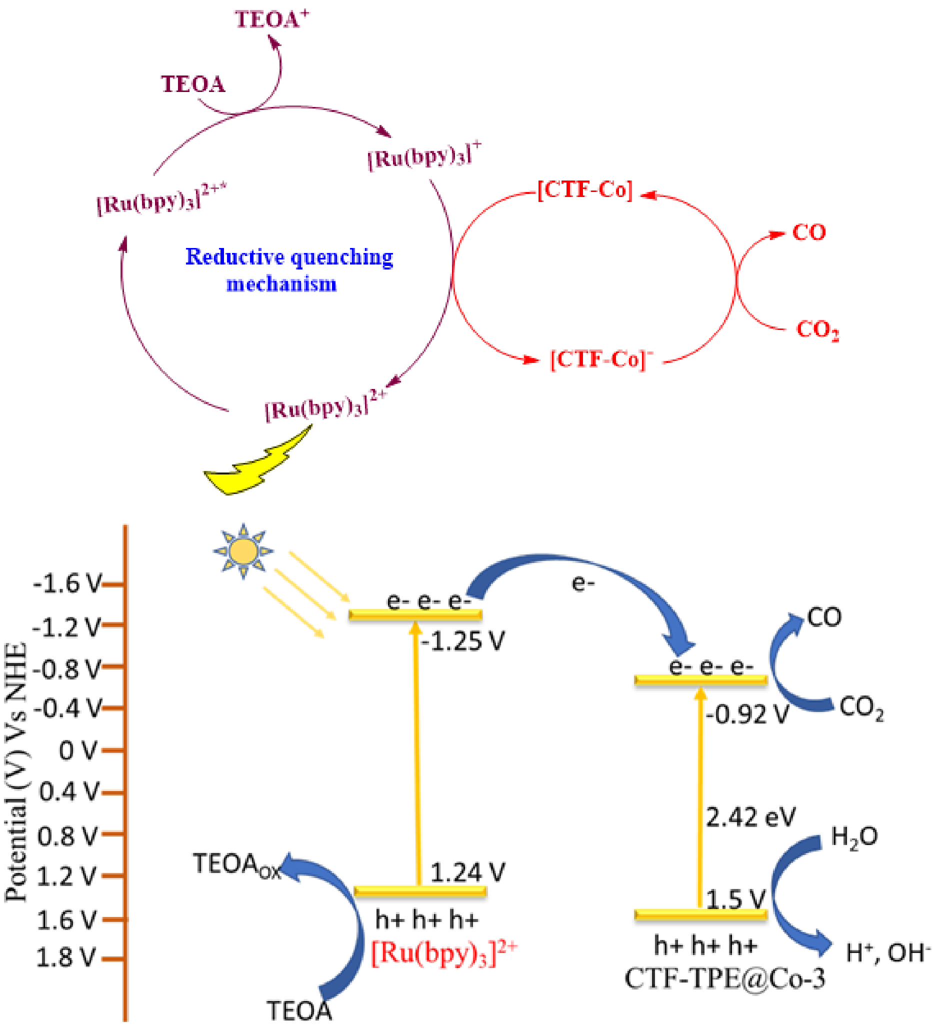

Figure 2.26: Reductive or oxidative quenching pathway of Ru(bpy)3]$^{2+}$ during photocatalytic reaction (top); possible potential diagram for CO_2 reduction by CTF-TPE@Co-3 (bottom).

Now, it is evident that the reduction potential of CTF-TPE@Co-3 is less negative than the $Ru(bpy)_3]^{2+}$ $(E(Ru(bpy)_3]^{2+}*/Ru(bpy)_3]^{+}) = -1.25$ V vs. NHE), but more negative than the reduction potential of CO_2 to CO ($E(CO_2/CO) = -0.52$ V vs. NHE)[22] (Figure 2.26 (bottom)). This suggests an electron transfer from photosensitizer to CTF-TPE@Co-3, facilitating electron injection from catalyst to CO_2 and driving the photocatalytic conversion of CO_2 to CO (Figure 2.26 (bottom)). Based on the aforementioned results and discussions, we have proposed a plausible mechanism for photocatalytic CO_2 reduction reaction as depicted in Fig. 8. Under light irradiation, the $Ru(bpy)_3]^{2+}$ and CTF-TPE@Co-3, creating excited electron-hole pairs and promote the electrons to the excited state $Ru(bpy)_3]^{2+}*$. Subsequently, TEOA reductively quenched $Ru(bpy)_3]^{2+}*$ to generate the reduced photosensitizer $Ru(bpy)_3]^{+}*$. The $Ru(bpy)_3]^{+}*$ transfer the photogenerated electrons to the Co active sites for the CO_2 reduction to CO. On the other hand the valence band location of CTF-TPE@Co-3 readily overcomes the water oxidation threshold potential.[81] Thus, the photogenerated holes in the VB of the CTF-TPE@Co-3 oxidize H_2O to give H^+ and HO^- which is a crucial step in photocatalytic CO_2 reduction process.[82] The holes selectively react with $OH^–$ species to prevent electron–hole recombination, and simultaneously, H^+ unite to generate H_2, which is detected in GC This also supports the proposed mechanism.

2.4 Conclusions

In summary, we have showcased the successful preparation of an effective CTF-based photocatalyst by anchoring single Co^{2+} active sites within the triazine framework for CO_2 reduction under visible light irradiation. The synthesized CTF-TPE material, featuring isolated cobalt single sites, demonstrated remarkable efficiency in photocatalytic CO_2 reduction in the presence of a dye and sacrificial electron donor. It achieved a CO generation of 6616 $\mu molg^{–1}$ for a continuous 7h run. This photocatalytic activity is on par with the performance of other state-of-the-art heterogeneous catalysts documented in the literature under analogous conditions (Table 2.2). This superior photocatalytic activity of CTF-TPE@Co-3 may be attributed to the coordination of Co^{2+} sites within the CTF-TPE scaffold, which facilitates the electron transfer from the photosensitizer to the catalyst and enhances the system’s CO_2 adsorption capacity, thereby increasing its overall photocatalytic activity. The results suggest that the CTF-TPE is a potential support to stabilize the single Co atom through strongcoordination of metals and nitrogen atoms of triazine rings. This study unveils a promising strategy for the fabrication of an effective triazine-based photocatalyst based on earth-abundant transition metals and we believe that our work will open a new avenue for designing and constructing next-generation photocatalyst in the realm of solar fuels.

2.5 References:

1. C. R. Timothy, D. K. Dilek, R. Y. Steven, S. Yogesh, T. S. Thomas and N. G. Daniel, *Chem. Rev.,* 2010, **110**, 6474–6502.

2. S. Das and W. M. A. Wan Daud, *RSC Adv.*, 2014, **4**, 20856–20893.

3. D. Li, M. Kassymova, X. Cai, S.-Q. Zang and H.-L. Jiang, *Coord. Chem. Rev.*, 2020, **412**, 213262.

4. L. Cheng, Q. J. Xiang, Y. L. Liao and H. W. Zhang, *Energy Environ. Sci.*, 2018, **11**, 1362–1391.

5. S. N. Habisreutinger, L. Schmidt Mende and J. K. Stolarczyk, *Angew. Chem., Int. Ed.,* 2013, **52**, 7372–7408.

6. S. W. Cao, J. X. Low, J. G. Yu and M. Jaroniec, *Adv. Mater.*, 2015, **27**, 2150–2176.

7. J. Fu, B. Zhu, C. Jiang, B. Cheng, W. You and J. Yu, *Small*, 2017, **13**, 1603938.

8. Q. Lang, W. Hu, P. Zhou, T. Huang, S. Zhong, L. Yang, J. Chen and S. Bai, *Nanotechnology*, 2017, **28**, 484003.

9. M. Zhou, S. Wang, P. Yang, Z. Luo, R. Yuan, A. M. Asiri, M. Wakeel and X. Wang, *Eur. J. Chem.,* 2018, **24**, 18529–18534.

10. H. Rao, L. C. Schmidt, J. Bonin and M. Robert, *Nature*, 2017, **548**, 74–77.

11. H. Takeda, K. Ohashi, A. Sekine and O. Ishitani, *J. Am. Chem. Soc.*, 2016, **138**, 4354–4357.

12. Y. Wang, X. Liu, X. Han, R. Godin, J. Chen, W. Zhou, C. Jiang, J. Thompson, K. Mustafa, S. Shevlin, J. Durrant, Z. Guo and J. Tang, *Nat. Commun.*, 2020, **11**, 2531.

13. M. F. Kuehnel, C. D. Sahm, G. Neri, J. R. Lee, K. L. Orchard, A. J. Cowan and E. Reisner, *Chem. Sci.*, 2018, **9**, 2501–2509.

14. S. Roy and E. Reisner, *Angew. Chem., Int. Ed.*, 2019, **58**, 12180–12184.

15. Y. Kuramochi, O. Ishitani and H. Ishida, *Coord. Chem. Rev*., 2018, **373**, 333.

16. J. Bonin, A. Maurin and M. Robert, *Coord. Chem. Rev.,* 2017, **334**, 184.

17. J. J. Mao, C. T. He, J. J. Pei, W. X. Chen, D. S. He, Y. Q. He, Z. B. Zhuang, C. Chen, Q. Peng and D. S. Wang, *Nat. Commun*., 2018, **9**, 4958.

18. S. Paul, S. Sarkar, A. Adalder, S. Kapse, R. Thapa and U. K. Ghorai, *ACS Sustainable Chem. Eng.*, 2023, **11**, 6191–6200.

19. W. Zhong, R. Sa, L. Li, Y. He, L. Li, J. Bi, Z. Zhuang, Y. Yu and Z. Zou, *J. Am. Chem. Soc*., 2019, **141**, 7615–7621.

20. X. Wang, Z. Fu, L. Zheng, C. Zhao, X. Wang, S. Y. Chong, F. McBride, R. Raval, M. Bilton, L. Liu, X. Wu, L. Chen, R. S. Sprick and A. I. Cooper, *Chem. Mater.*, 2020, **32**, 9107–9114.

21. X. Hu, L. Zheng, S. Wang, X. Wang and B. Tan, *Chem. Commun.*, 2022, **58**, 8121.

22. J. Wang, W. Zhu, F. Meng, G. Bai, Q. Zhang and X. Lan, *ACS Catal*., 2023, **13**, 4316–4329.

23. J. L. Liang, Q. Q. Song, J. H. Wu, Q. Lei, J. Li, W. Zhang, Z. M. Huang, T. X. Kang, H. Xu and P. Wang, *ACS Nano*, 2022, **16**, 4152–4161.

24. Z. J. Li, D. H. Wang, Y. E. Wu and Y. D. Li, *Natl. Sci. Rev*., 2018, **5**, 673–689.

25. P. Huang, J. Huang, S. A. Pantovich, A. D. Carl, T. G. Fenton, C. A. Caputo, R. L. Grimm, A. I. Frenkel and G. Li, *J. Am. Chem. Soc.*, 2018, **140**, 16042.

26. (a) W. Huang, Z. J. Wang, B. C. Ma, S. Ghasimi, D. Gehrig, F. Laquai, K. Landfester and K. A. I. Zhang, *J. Mater. Chem. A*, 2016, **4**, 7555–7559; (b) Z. Cheng, H. Pan, H. Zhong Z. Xiao, X. Li and R. Wang, *Adv. Funct. Mater.*, 2018, **28**, 1707597.

27. S. Kuecken, A. Acharjya, L. Zhi, M. Schwarze, R. Schomaecker and A. Thomas, *Chem. Commun.*, 2017, **53**, 5854–5857.

28. J. Xie, S. A. Shevlin, Q. Ruan, S. J. A. Moniz, Y. Liu, X. Liu, Y. Li, C. C. Lau, Z. X. Guo and J. Tang, *Energy Environ. Sci.*, 2018, **11**, 1617–1624.

29. S. Zhang, G. Cheng, L. Guo, N. Wang, B. Tan and S. Jin, *Angew. Chem., Int. Ed.*, 2019, **59**, 6007–6014.

30. G. C. Huang, Q. Niu, J. W. Zhang, H. M. Huang, Q. S. Chen, J. H. Bi and L. Wu, *Chem. Eng. J.*, 2022, **427**, 131018.

31. G. C. Huang, G. Y. Lin, Q. Niu, J. H. Bi and L. Wu, *J. Mater. Sci. Technol*., 2022, **116**, 41–49.

32. C. Lu, J. Yang, S. Wei, S. Bi, Y. Xia, M. Chen, Y. Hou, M. Qiu, C. Yuan, Y. Su, F. Zhang, H. Liang and X. Zhuang, *Adv. Funct. Mater*., 2019, **29**, 1806884.

33. S. Yang, R. Sa, H. Zhong, H. Lv, D. Yuan and R. Wang, *Adv. Funct. Mater*., 2022, **32,** 2110694.

34. H. Wang, B. Li, H. Wu, T.-L. Hu, Z. Yao, W. Zhou, S. Xiang, and B. Chen, *J. Am. Chem. Soc*., 2015, **137**, 9963−9970.

35. P. Kuhn, M. Antonietti and A. Thomas, *Angew. Chem., Int. Ed.*, 2008, **47**, 3450–3453.

36. H. A. Patel, F. Karadas, A. Canlier, J. Park, E. Deniz, Y. Jung, M. Atilhan and C. T. Yavuz, *J. Mater. Chem.*, 2012, **22**, 8431-8437.

37. A. Bhunia, I. Boldog, A. Möller and C. Janiak, *J. Mater. Chem. A*, 2013, **1**, 14990–14999.

38. (a) I. D. Wessely, A. M. Schade, S. Dey, A. Bhunia, A. Nuhnen, C. Janiak and S. Br¨ ase, *Materials*, 2021, **14**, 3214; (b) S. Dey, A. Bhunia, I. Boldog and C. Janiak, *Microporous Mesoporous Mater.*, 2017, **241**, 303–315; (c) S. Dey, A. Bhunia, H. Breitzke, P. B. Groszewicz, G. Buntkowsky and C. Janiak, *J. Mater. Chem.* A, 2017, **5**, 3609–3620.

39. J. Weber, M. Antonietti and A. Thomas, *Macromolecules,* 2008, **41**, 2880–2885.

40. N. Ritter, I. Senkovska, S. Kaskel and J. Weber, *Macromol. Rapid Commun*., 2011, **32**, 438–443.

41. R. Dawson, L. A. Stevens, T. C. Drage, C. E. Snape, M. W. Smith, D. J. Adams and A. I. Cooper, *J. Am. Chem. soc*., 2012, **134**, 10741–10744.

42. X. Zhu, C. Tian, S. M. Mahurin, S.-H. Chai, C. Wang, S. Brown, G. M. Veith, H. Luoll, H. Liu and S. Dai, *J. Am. Chem. Soc.*, 2012, **134**, 10478–10484.

43. D.N.Li, Y. K. Fan, H. R. Yuan, L. F. Deng, J. Z. Yang, Y. Chen and B. Luo, *Energy Fuels*, 2020, **34**, 13089–13095.

44. H. Jin, P. Li, P. Cui, J. Shi, W. Zhou, X. Yu, W. Song and C. Cao, *Nat. Commun*., 2022, **13**, 723.

45. X.-Y. Dong,Y.-N. Si, Q.-Y. Wang,S.WangandS.-Q.Zang, *Adv. Mater*., 2021, **33**, 2101568.

46. P. Kumar, K. Kannimuthu, A. S. Zeraati, S. Roy, X. Wang, X. Wang, S. Samanta, K. A. Miller, M. Molina, D. Trivedi, J. Abed, M. A. C. Mata, H. A. Mahayni, J. Baltrusaitis, G. Shimizu, Y. A. Wu, A. Seiftokaldani, E. H. Sargent, P. M. Ajayan, J. Hu and Md G. Kibria, *J. Am. Chem. Soc.*, 2023, **145**, 8052–8063.

47. G. G. Zhang, M. W. Zhang, X. X. Ye, X. Q. Qiu, S. Lin and X. C. Wang, *Adv. Mater*., 2014, **26**, 805–809.

48. X.Li, A. E. Surkus, J. Rabeah, M. Anwar, S. Dastigir, H. Junge, A. Brückner and M. Beller, *Angew. Chem., Int. Ed.*, 2020, **59**, 15849–15854.

49. G. G. Zhang, J. S. Zhang, M. W. Zhang and X. C Wang, *J. Mater. Chem*., 2012, **22**, 8083-8091.

50. Z. Q. Luo, S. Lim, Z. Q. Tian, J. Z. Shang, L. F. Lai, B. MacDonald, C. Fu, Z. X. Shen, T. Yu and J. Y. Lin, *J. Mater. Chem*., 2011, **21**, 8038–8044.

51. X. Zhu, C. C. Tian, S. M. Mahurin, S. H. Chai, C. M. Wang, S. Brown, G. M. Veith, H. M. Luo, H. L. Liu and S. Dai, *J. Am. Chem. Soc*., 2012, **134**, 10478.

52. L. S. Ma, W. B. Hu, B. B. Mei, H. Liu, B. Yuan, J. Zang, T. Chen, L. L. Zou, Z. Q. Zou, B. Yang, Y. Yu, J. Y. Ma, Z. Jiang, K. Wen and H. Yang, *ACS Catal*., 2020, **10**, 4534.

53. T. Baidya, T. Murayama, S. Nellaiappan, N. K. Katiyar, P. Bera, O. Safonova, M. Lin, K. R. Priolkar, S. Kundu, B. S. Rao, P. Steiger, S. Sharma, K. Biswas, S. K. Pradhan, N. Lingaiah, K. D. Malviya and M. Haruta, *J. Phys. Chem*. C, 2019, **123**, 19557–19571.

54. T. Baidya, T. Murayama, P. Bera, O. V. Safonova, P. Steiger, N. K. Katiyar, K. Biswas and M. Haruta, *J. Phys. Chem*. C, 2017, **121**, 15256–15265.

55. M. Liu, Z. Wang, J. Liu, G. Wei, J. Du, Y. Li, C. An and J. Zhang, *J. Mater. Chem. A,* 2017, **5**, 1035–1042.

56. R. Ma, X. Cui, Y. Wang, Z. Xiao, R. Luo, L. Gao, Z. Weie and Y. Yang, *J. Mater. Chem. A*, 2022, **10,** 5918.

57. C. Gao, S. Chen, Y. Wang, J. Wang, X. Zheng, J. Zhu, L. Song, W. Zhang and Y. Xiong, *Adv. Mater.*, 2018, **30**, 1704624.

58. Q. Huang, J. Yu, S. Cao, C. Cui and B. Cheng, *Appl. Surf. Sci*.,2015, **358**, 350–355.

59. P. Xia, B. Zhu, J. Yu, S. Cao and M.Jaroniec, *J.Mater.Chem.*A, 2016, **5,** 3230.

60. W. K. Jo, S. Kumar, S. Eslava and S. Tonda, *Appl. Catal., B*, 2018, **239**, 586–598.

61. M.E. Khan, M. M. Khanand M. H. Cho, *New J. Chem*., 2015, **39**, 8121–8129.

62. S. Fernandez, F. Franco, C. Casadevail, V. M. Diaconescu, J. M. Luis and J. L. Fillol, *J. Am. Chem. Soc*., 2020, **142**, 120–133.

63. W. Zhong, R. Sa, L. Li, Y. He, L. Li, J. Bi, Z. Zhuang, Y. Yu and Z. Zou, *J. Am. Chem. Soc.* 2019, **141**, 7615–7621.

64. M. Lu, J. Liu, Q. Li, M. Zhang, M. Liu, J.-L. Wang, D.-Q. Yuan and Y.-n. Lan, *Angew. Chem. Int. Ed.* 2019, **58**, 12392-12397.

65. Y. Fu, X. Zhu, L. Huang, X. Zhang, F. Zhang and W. Zhu, *Applied Catalysis B: Environmental*, 2018, **239**, 46-51.

66. A. F. M. EL-Mahdy, H. A. E. Omr, Z. A. Alothman and H. Lee, J. Colloid Interface Sci., 2023, **633**, 775-785.

67. X. Wang, Z. Fu, L. Zheng, C. Zhao, X. Wang, S. Y. Chong, F. McBride, R. Raval, M. Bilton, L. Liu, X. Wu, L. Chen, R. S. Sprick and A. I. Cooper, *Chem. Mater.* 2020, **32**, 9107–9114

68. J. Bi, B. Xu, L. Sun, H. Huang, S. Fang, L. Li and L. Wu, *ChemPlusChem*, 2019, **84**, 1149-1154

69. R. Xu, X.-S. Wang, H. Zhao, H. Lin, Y.-B. Huang and R. Cao, *Catal. Sci. Technol.*, 2018, **8**, 2224-2230.

70. Y. He, X. Chen, C. Huang, L. Li, C. Yang and Y. Yu, *Chin. J. Catal.*, 2021, **42**, 123-130.

71. Q. Niu, Z. Cheng, Q. Chen, G. Huang, J. Lin, J. Bi and L. Wu, *ACS Sustainable Chem. Eng.*, 2021, **9**, 1333-1340.

72. Y. Yan, Q. Fang, J. Pan, J. Yang, L. Zhang, W. Zhang, G. Zhuang, X. Zhong, S. Deng and J. Wang, *Chem. Eng. J.*, 2021, **408**, 127358.

73. G. Huang, Q. Niu, J. Zhang, H. Huang, Q. Chen, J. Bi and L. Wu, *Chem. Eng. J.*, 2022, **427**, 131018.

74. Z. Xu, Y. Cui, D. Young, J. Wang, H. Li, G. Bian and H. Li, *J. CO_2 Util.*, 2021, **49**, 101561

75. T. Zhao, Q. Niu, G. Huang, Q. Chen, Y. Gao, J. Bi and L. Wu, *J. Colloid Interface Sci.*, 2021, **602**, 23-31.

76. H. Zhong, Z. Hong, C. Yang, L. Li, Y. Xu, X. Wang and R. Wang, *ChemSusChem*, 2019, **12**, 4493-4499.

78. S. Zhang, S. Wang, L. Guo, H. Chen, B. Tan and S. Jin, J. *Mater. Chem. C*, 2020, **8**, 192-200.

79. X. H. Lin, Z. D. Xie, B. Su, M. Zheng, W. X. Dai, Y. D. Hou, Z. X. Ding, W. Lin, Y. X. Fang and S. B. Wang, Nanoscale, 2021, **13**, 18070.

80. J.-S. Qin, S. Yuan, L. Zhang, B. Li, D.-Y. Du, N. Huang, W. Guan, H. F. Drake, J. Pang, Y.-Q. Lan, A. Alsalme and H.-C. Zhou, *J. Am. Chem. Soc.*, 2019, **141**, 2054–2060.

81. B. M. Hunter, H. B. Gray and A. M. Müller, *Chem. Rev.*, 2016, **116**, 14120–14136.

82. C. B. Hiragond, N. S. Powar, J. Lee and S.-I. In, *Small*, 2022, **18**, 2201428.

Chapter 3

Visible-Light-Driven CO_2 Reduction Using Imidazole-Based Metal–Organic Frameworks as Heterogeneous Photocatalysts

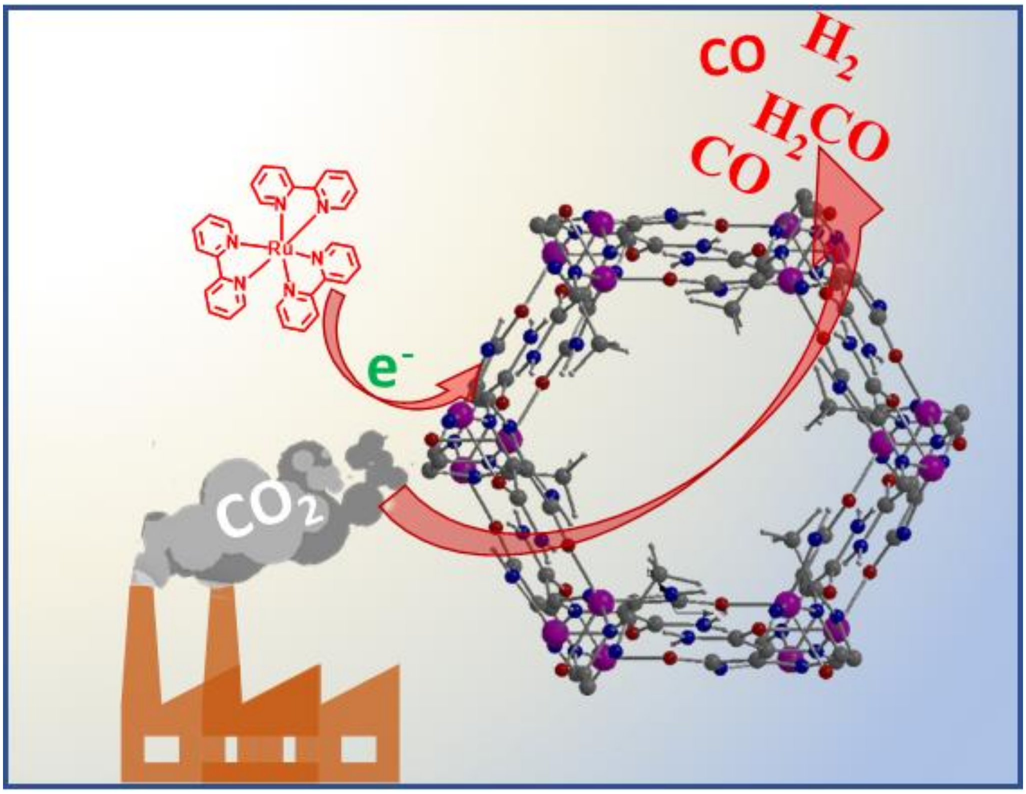

Paper published based on this work:

A. Jana, Sinthia Saha, Suvendu Sekhar Mondal, Navjot Kaur, Asamanjoy Bhunia, *Chem Asian J.*, 2025, **20**, e202401401.

3.1 Introduction

Solar-driven CO_2 reduction is an innovative approach for tackling climate change and enhancing energy sustainability, drawing inspiration from the natural process of photosynthesis.[1] Just as plants convert CO_2 and sunlight into energy and biomass, solar-driven technologies aim to mimic this process by transforming CO_2 into valuable fuels or chemicals (i.e. CO, HCOOH, HCHO, CH_3OH, CH_4).[2,3] This method not only helps to mitigate atmospheric CO_2 levels but also utilizes solar energy, which is a clean, abundant, and cost-effective resource. In this context, this process is particularly appealing for large-scale applications. However, CO_2, being a linear molecule, possesses enhanced chemical stability and high bond dissociation energy, which complicates its conversion into useful chemicals.[4] This can be overcome by using a photosensitizer, suitable catalyst, and sacrificial reducing agent. In this context, since the landmark study on heterogeneous CO_2 photoreduction using TiO_2 as a catalyst, the focus has been increasingly shifted towards inorganic semiconductors.[5] However, despite significant advancements, many inorganic photocatalysts still face critical challenges such as limited tunability, potential heavy metal toxicity, and wide band gaps, which hinder their practical application. This highlights the pressing need for alternative materials. Currently most of the molecular photocatalysts are primarily based on second- and third-row transition metals like ruthenium (Ru) and rhenium (Re), which have set performance benchmarks in artificial CO_2 reduction.[6,7,8 ,9,10] Considering, the high production costs, toxicity, and scarcity of these transition metal complexes, the use of such catalysts for large-scale solar energy conversion systems may be less favourable or sustainable.[10] In contrast, from both economic and sustainability perspectives, catalysts based on earth-abundant, first-row transition metals are more desirable. However, these artificial molecular photocatalytic systems suffer from limited long-term stability.[4] Therefore, developing heterogeneous photocatalysts made from earth-abundant transition metals that exhibit high stability remains a significant challenge.

In this context, since the past two decades Metal–organic frameworks (MOFs), a class of crystalline and porous materials made up of metal-containing clusters and organic linkers have attracted much admiration due to their large-scale applicability such as in gas sorption, gas separation and catalysis.[11-14] These reticular materials offer a high density of catalytically active sites, and their porous structures facilitate efficient charge and mass transfer, making them highly suitable for photocatalytic CO_2 reduction. In recent years, a variety of MOFs have been specifically developed for this purpose.[15,16,17] Among these, zeolitic imidazolate frameworks (ZIFs), which are composed of imidazolate ligands and transition metal cations, have become prominent as effective heterogeneous cocatalysts for CO_2 reduction due to their adjustable morphology, uniform pore size, and excellent chemical and thermal stability.[18,19] In addition to their high CO_2 adsorption capacity, ZIFs are made from earth-abundant, inexpensive, and non-toxic transition metals. They are also easy to synthesize and replicate, making them promising candidates for large-scale solar energy conversion systems.

Herein, we chose the imidazolate framework Potsdam (IFP) as the platform because of their extraordinary chemical stability and readily reachable sites for functionalization.[20,21,22] This work emphasised on the synthesis of transition metal based photocatalysts using the IFP model which is a sub type of the ZIF, comprising of pentacoordinated Zn (IFP-1(Zn))[23] or Co (IFP-5(Co))[24] secondary binding units and 2-methylimidazolate-4-amide-5-imidate (MIAI) linkers. Comparative study was performed between the synthesised IFP-1(Zn), IFP-5(Co) and the bimetallic IFP-1(Zn/Co) system to examine their photocatalytic activity in the CO_2 reduction. To elucidate the potential mechanism of the catalytic cycle involved in CO_2 reduction, we conducted photophysical and electrochemical investigations, along with Density Functional Theory (DFT) calculations.

3.2 Experimental section

3.2.1 Materials

Tetraethylammonium chloride, (≥98.0%), triethanolamine (TEOA), and were purchased from Sigma-Aldrich. triethyl orthoacetate, $[Ru(bpy)_3]Cl_2\cdot 6H_2O$ and 1,3-dimethyl-2-phenyl-2,3-dihydro-1H-benzo[d]imidazole (BIH) were purchased from BLD pharm. Diaminomaleonitrile (>96%) were purchased from TCI. Xylene was purchased from spectrochem, India. Na_2SO_4 (≥98.0%), Cobalt (II) nitrate hexahydrate (≥98.0%), Methanol (MeOH), dimethyl formamide (DMF), acetonitrile, glacial acetic acid was procured from Merck, India. All of the chemicals were commercially available and used without further purification.

3.2.2 Synthesis of 4,5-dicyano-2-methylimidazole

The ligand 4,5-dicyano-2-methylimidazole has been synthesized by adapting a reported procedure.[25] Diaminomaleonitrile (4.38 g, 40.56 mmol) was dissolved in 20 mL of acetonitrile, followed by the addition of triethyl orthoacetate (TOA, 8.10 mL, 7.17 g, 44.30 mmol). The reaction mixture was then stirred under reflux for 24 hours. Once thin-layer chromatography (TLC) confirmed the complete consumption of the starting material, the solvent was removed under reduced pressure. The resulting dark residue was diluted in xylene and heated at reflux for an additional 24 hours, after which the solvent was again evaporated under reduced pressure. The crude product was dissolved in ethanol, treated with 500 mg of activated charcoal, and stirred at reflux for 24 hours. After filtering off the charcoal, the solvent was removed under reduced pressure, yielding 4,5-dicyano-2-methyl-1H-imidazole as a white powder.

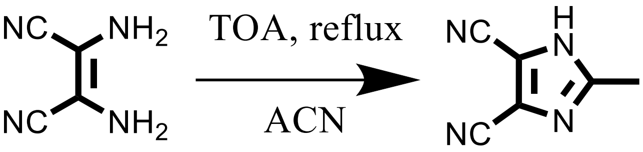

3.2.3 Ionic liquid synthesis

Ionic liquid has been synthesized following a reported procedure.[26] Anhydrous potassium carbonate (1.33 g, 9.6 mmol) was added to a solution of 4,5-dicyano-2-methylimidazole (0.85 g, 6.4 mmol) in 50 mL of acetone at room temperature, and the mixture was stirred for 6-7 hours. Following this, a dichloromethane solution (50 mL) containing tetraethylammonium chloride (1.06 g, 6.4 mmol) was added for the synthesis of the ionic liquid, and the reaction mixture was stirred for an additional 3-4 hours. The mixture was then filtered and concentrated under vacuum. The product was extracted with acetone, the extract was filtered, and the solvent was evaporated to yield the ionic liquid.

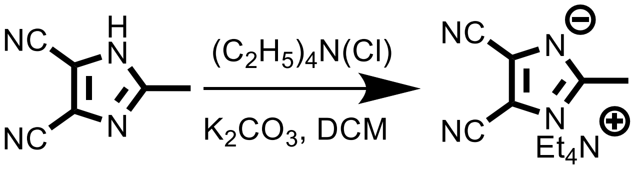

3.2.4 Synthesis of IFP-1(Zn)

In a pyrex tube, $Zn(NO_3)_2·4H_2O$ (198 mg, 0.76 mmol) and 4,5-dicyano-2-methylimidazole (100 mg, 0.76 mmol) were combined in 6 mL of DMF.[23] The Pyrex tube was heated to 120°C for 48 hours. After cooling to room temperature, the pale-yellow precipitate was collected by centrifugation and washed three times with DMF and acetone. The synthesized MOF was activated at 120 °C for 10 h.

3.2.5 Synthesis of IFP-1(Zn/Co)

Co-exchanged IFP-1(Zn) was synthesized via ion exchange process. IFP-1 (100 mg) was dispersed in 5 mL methanolic solution caontaining $CoCl_2.6H_2O$ (100 mg). Then, the resulting mixture was placed in oven at 60 °C temperature for 5 days. After the reaction the ion exchange MOF was was obtained by filtration and washed with MeOH extensively until the supernatant was colorless and then the resulting formed MOF was soaked in MeOH for 3 days. Exchange with fresh MeOH three times each day was carried out. The synthezed ion-exchanged materials designated as IFP-1(Zn/Co). The resulted MOF was activated at120 °C for 10 h.

3.2.6 Synthesis of IFP-5(Co)

The synthesis was adapted from a known procedure.[22] In a pyrex tube , tetraethylammonium 4,5-dicyano-2-methylimidazolate (0.07 g, 0.26 mmol) and $Co(NO_3)_2{\cdot}6H_2O$ (0.08 g, 0.26 mmol) were dissolved in 3 mL of DMF. The tube was sealed, and the mixture was heated to 130°C for 48 hours. After cooling to room temperature, fine purple microcrystals were obtained by filtration and air-dried. IFP-5(Co) was then activated at 120 °C for 10 h.

3.2.7 Characterization methods

The Fourier transform–infrared (FT–IR) spectra of IFP-1(Zn), IFP-1(Zn/Co), and IFP-5(Co) were collected on a Bruker FTIR 4000 instrument equipped with a zinc selenide (ZnSe) ATR. The powder X-ray diffraction (PXRD) data of IFP-1(Zn), IFP-1(Zn/Co), and IFP-5(Co) were collected with Bruker D8 Advance X-ray diffractometer (XRD) at room temperature using Cu Kα radiation ($\lambda = 1.548$ Å) in a 2θ range of 3–55°. Thermogravimetric analyses (TGA) were done at a ramp rate of 10 °C min^{-1} under N_2 atmosphere and air atmosphere with Perkin Elmer Pyris Diamond TG–DTA instruments. UV absorption spectra were recorded using a Cary 60 UV–vis (Agilent Technologies) with a 1 cm path-length quartz cell. Fluorescence emission spectra were collected on a HORIBA Fluoromax-4 fluorometer. Nitrogen gas adsorption–desorption of the samples was performed to obtain BET-specific surface area (S_{BET}) using Quanta chrome Autosorb iQ2 Instruments at liquid N_2 temperature (77 K). The samples were degassed under a high vacuum (10^{-6} torr) at 185 °C for 10 h. After degassing, the sample tube was then transferred to the analysis port of the sorption analyzer. Pore size distribution was calculated by non-local density functional theory (NLDFT) using the ‘carbon slit pore’ model. Field emission scanning electron microscope (FE-SEM) images were obtained using a Carl Zeiss SUPRA 55VP FESEM instrument. Energy dispersive X-ray spectroscopy (EDS) was performed by Oxford Instruments X-Max with INCA software coupled to the FE-SEM. The Hitachi, S-4800, EDS detector was introduced to analyze the morphology and EDS of the samples. X-ray photoelectron spectroscopy (XPS) measurement was conducted by the Thermo Fisher ESCALAB Xi+ microProbe instrument with a monochromatic Al-Kα target, 1486.6 eV energy, and a maximum power of 15.0 KW. Inductively coupled plasma optical emission spectrometry (ICP-OES) results were obtained from an Icap 7000 ICP-OES (Thermo Scientific). After the photocatalysis, gaseous and liquid products were analyzed. The gaseous products were analyzed and quantified using TCD and FID detector in High-performance gas chromatography (Agilent 8860). GC was calibrated with known standard for H_2, CO. Liquid products were analysed through ^{1}H NMR. The gaseous products from isotope labeling experiment were detected using gas chromatography by MS detector (Perkin Elmer clarus 690).

Electrochemical characterization

The Mott-Schottky analysis and impedance measurement were conducted using CHI760E workstation (CHI Instruments, USA) through a conventional three-electrode system immersed in a 0.2 M Na_2SO_4 aqueous solution.

Preparation of working electrode for Mott-Schottky measurement

2.5 mg of respective materials were dispersed in a solution of 250 μL water, 250 μL isopropyl alcohol (IPA), and 10 μL of Nafion to prepare a homogenous slurry. Subsequently, 12 μL of slurry was coated on a glassy carbon electrode and then dried at room temperature. The Ag/AgCl electrode was employed as the reference electrode, and the platinum plate was used as the counter electrode, respectively. The measurements were carried out under frequencies of 0.5, 1, and 1.5 kHz.

Preparation of working electrode for impedance measurement

2.5 mg of respective materials were dispersed in a solution of 250 μL water, 250 μL isopropyl alcohol (IPA), and 10 μL of Nafion to prepare a homogenous slurry. Subsequently, 12 μL of slurry was coated on a glassy carbon electrode and then dried at room temperature. The Ag/AgCl electrode was employed as the reference electrode, and the platinum plate was used as the counter electrode, respectively. A 0.2 M Na_2SO_4 solution was used as an electrolyte. The measurements were carried out with a bias potential of -0.2 V with a frequency range from 10^{-2} to 10^5 Hz under a nitrogen atmosphere.

Photocatalytic testing:

As reported previously[27,28,29] the photocatalytic reactions were conducted with a 300 W Xe lamp with a 420 nm cut-off filter. In a typical process, activated catalyst (1 mg), BIH (20 mg) and $[Ru(bpy)_3]Cl_2\cdot6H_2O$ (12 mg) was dispersed into the solution of 3.0 mL acetonitrile solution containing 1 mL TEOA and 1 mL H_2O in a quartz tube. Before photocatalytic testing, the reaction solution was degassed with N_2 gas for 20 minutes followed by bubbling with CO_2 (99.999%, Airgas) in the dark for 30 minutes. The reaction solution was then irradiated at room temperature with stirring for photocatalytic CO_2 reduction (See photocatalytic set-up below). The headspace above the reaction solution was taken using a gas-tight syringe at different time intervals for product analysis using an Agilent 8860 equipped with a TCD and FID detector and a 60/80 Carboxen-1000 packed column (Supelco). Liquid products were analysed using ion chromatography and ^1H NMR. Control experiments were conducted in the absence of light irradiation, photosensitizer, catalyst, sacrificial reagent, and CO_2.

Isotope-labelling experiments: 1 mg of catalyst, BIH (20 mg) and $[Ru(bpy)_3]Cl_2\cdot6H_2O$ (12 mg) was dispersed into the solution of 3.0 mL acetonitrile and 1 mL H_2O mix solvent solution containing 1 mL TEOA in a quartz tube. Before photocatalytic testing, the reaction solution was degassed with N_2 gas for 20 minutes followed by bubbling with $^{13}CO_2$ for a few seconds, as it is expensive. The reaction solution was then illuminated with a 300 W Xe lamp. The obtained gaseous products were analyzed by gas chromatography−mass spectrometry (GC-MS).

Figure 3.1: Photocatalytic set up.

3.3 Result and discussions

3.3.1 Characterization of the synthesized MOFs

The crystalline imidazolate based MOFs, IFP-1(Zn) and IFP-5(Co), were synthesized under solvothermal condition by previously reported methods.[23,24] IFP-1(Zn) is a three-dimensional porous material with the empirical formula {[Zn(L1)]·$3H_2O$}, where L1 = 2-methylimidazolate-4-amide-5-imidate. It is isostructural to IFP-5(Co), which has the empirical formula [Co(L1)]·0.5 DMF. During the synthesis of these IFPs, partial hydrolysis of the ligands resulted in the formation of 2-methylimidazolate-4-amide-5-imidate, which serves as the actual linker in the IFP (Figure 3.2). In the IFP-1 structure, a distorted trigonal–bipyramidal environment is formed around the zinc ion.[23] In contrast, the Co^{2+} is penta-coordinated by the linkers to form a similar distorted trigonal–bipyramidal geometry (Figure 3.3a).[24] Such five-fold and unsaturated coordination environment around the Co^{2+} centre, which might increase the affinity of the guest molecules. The structure has 1D hexagonal channels running along

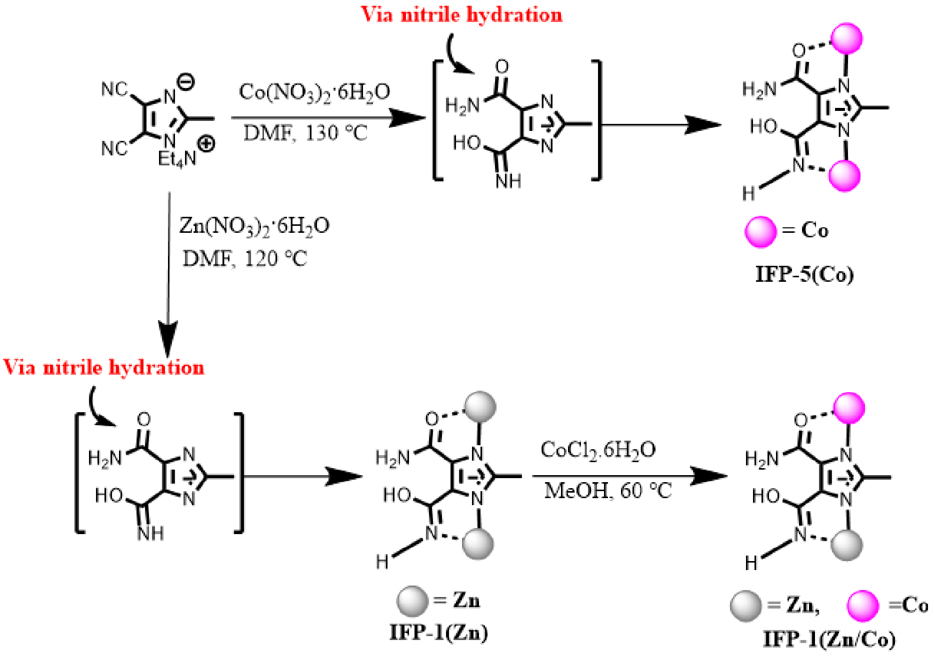

Figure 3.2: Schematic representation of synthesis route for preparation of IFP-1(Zn), IFP-5(Co), and IFP-1(Zn/Co).

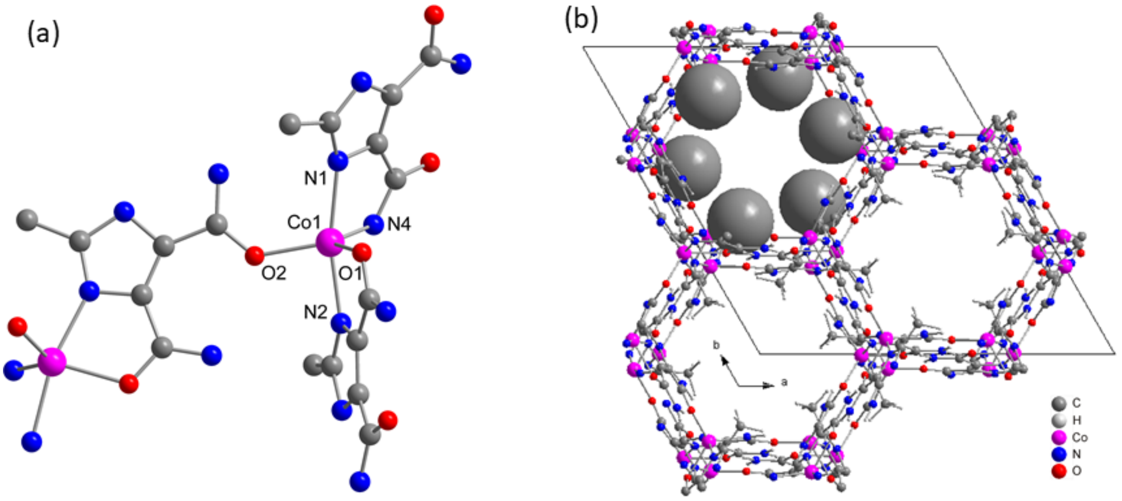

Figure 3.3: a) Section of the crystal structure of IFP-5, showing the coordination environment of Co^{2+} the bridging mode of imidazolate-4-amide-5-imidate linkers linker (L1). (b) Hexagonal channels in IFP-5 and the methyl groups at the linker are presented in a space filling mode.

c axis. The accessible diameter of the channels in IFP-5 was estimated to be 3.8 Å (considering the van der Waals radii). The walls of the hexagonal channel are principally built by the rigid and planar imidazolate-4-amide-5-imidate linkers. The Co^{2+} ions are situated at the edges of the hexagonal channels. The methyl groups project into the open channels (Figure 3.3b).

In addition, we have demonstrated for the first time the incorporation of Co^{2+} metal centre into IFP-1(Zn) MOF through metal ion exchange to prepare a bimetallic imidazolate based MOF, IFP-1(Zn/Co) (Figure 3.2). For the metal ion exchange of IFP-1(Zn) with Co^{2+}, we immersed IFP-1(Zn) in a methanolic solution of $CoCl_2{\cdot}6H_2O$ for 5 days at 60 °C. Upon completion of the reaction, the exchanged IFP-1(Zn) was extensively washed with methanol and then re-immersed in fresh methanol for 3 days to remove any excess Co^{2+} ions. The IFP MOFs were activated by thermal treatment at 120 °C under vacuum for 10 h. All the prepared materials were characterized using FTIR, PXRD, N_2 adsorption-desorption isotherm, inductively coupled plasma-optical emission spectroscopy (ICP-OES). In addition, the incorporation of CO^{2+} was validated through scanning electron microscopy−energy-dispersive X-ray spectroscopy (SEM−EDX) and X-ray photoelectron spectroscopy (XPS).

The PXRD data of the activated IFP-1(Zn), IFP-5(Co), and IFP-1(Zn/Co) exhibited patterns consistent with the simulated data, confirming the successful formation of crystalline MOFs (Figure 3.4a). Furthermore, the comparable PXRD patterns of pristine IFP-1(Zn) and its cobalt-exchanged counterpart, IFP-1(Zn/Co), demonstrate the retention of structural integrity in IFP-1(Zn/Co) throughout the metal exchange process with Co^{2+} (Figure 3.4a). The FTIR spectra of IFP-1(Zn) and IFP-5(Co) showed characteristic bands at around 1560 cm^{-1} and 1660 cm^{-1}, indicating the presence of amide and imidate groups (Figure 3.4b).[21]

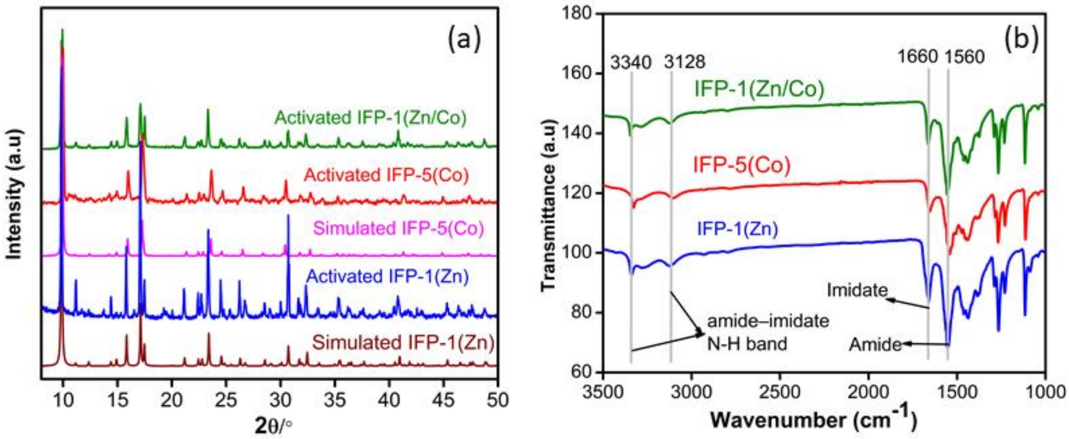

Figure 3.4: (a) PXRD profile of synthesized materials along with their simulated PXRD data. (b) FT-IR spectra of IFP-1(Zn), IFP-5(Co), IFP-1(Zn/Co).

Furthermore, absorption band was noticed at around 3128 cm^{-1} and 3340 cm^{-1} which appeared for a typical amide–imidate N−H band. Notably, in the FTIR spectrum there was no noticeable peak at around 2226 cm^{-1}, indicating the absence of CN groups in the reactants (i.e., 4,5-dicyano-2-methylimidazole) after the reaction demonstrating the complete conversion of the reactants.[30] The FTIR spectrum of the Co-exchanged MOF, IFP-1(Zn/Co), displayed characteristic bands similar to that of the pristine IFP-1(Zn), suggesting no additional bond formation occurred during the metal exchange process.

We have conducted the TGA experiments for IFP-1(Zn) and IFP-1(Zn/Co) MOFs under a nitrogen (N_2) atmosphere after activating the samples at 120 °C (Figure 3.5a). The thermal profiles reveal that both IFP-1(Zn) and IFP-1(Zn/Co) exhibit no significant weight loss up to 430 °C, indicating exceptional thermal stability under the given conditions. On the other hand, the TGA experiment for IFP-5(Co) has been performed under air atmosphere. The IFP-5(Co) demonstrates thermal stability up to 330 °C (Figure 3.5b). The TGA profile of IFP-5(Co) shows a weight loss of 13.7 % (calculated 13.97 %) before decomposition, which can be attributed to the removal of guest DMF solvent molecules from the pore.

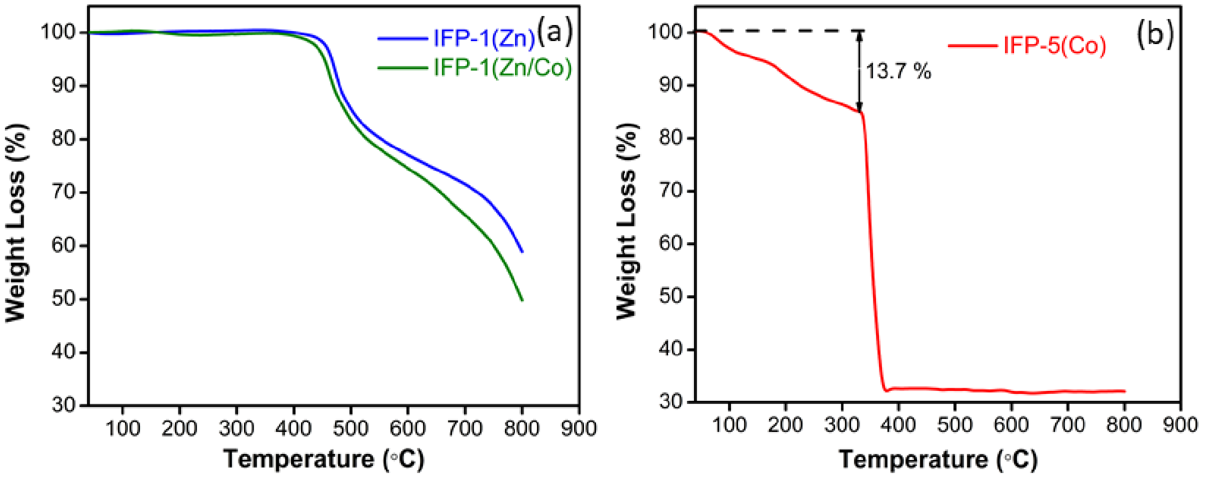

Figure 3.5: (a) Thermogravimetric analysis of (a) IFP-1(Zn) and IFP-1(Zn/Co) under N_2 atmosphere, and (b) IFP-5(Co) under air atmosphere.

The BET surface area of IFP-1(Zn) and IFP-(Zn/Co) was found to be 701 m^2 g^{-1} and 675 m^2 g^{-1}, respectively (Figure 3.6a, Table 3.1). The BET surface area of exchanged IFP-1(Zn/Co) was similar to pristine IFP-1(Zn). Further the pore volume and half pore width of both the materials were almost similar i.e., 0.292 cc g^{-1} and ~7 Å, respectively (Figure 3.6b). The BET surface area for IFP-5(Co) was 773 m^2 g^{-1} and the pore size distribution indicated the half pore width of ~7 Å.

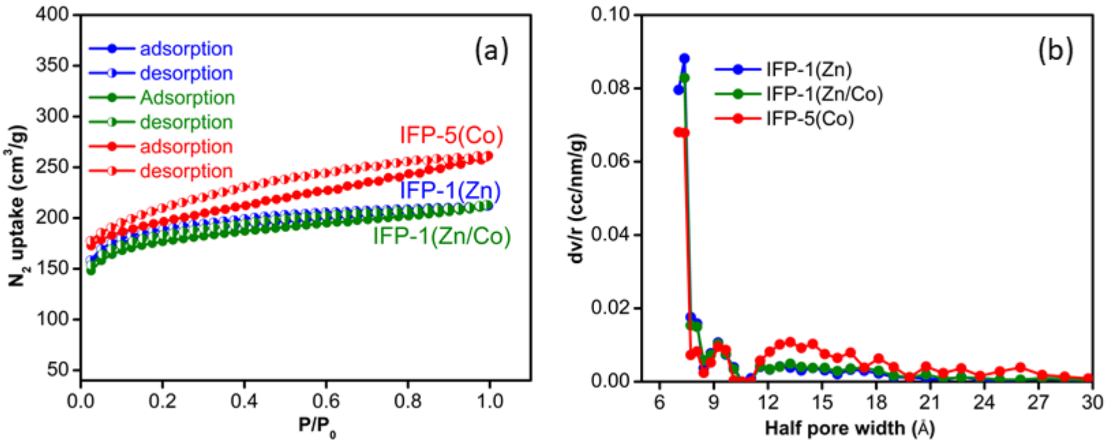

Figure 3.6: (a) N_2 sorption of all prepared MOFs. (b) pore size distribution of all prepared materials.

Table 3.1: BET surface area, C constant and correlation coefficient (r) of IFPs

Synthesized MOFs	**BET surface area (m^2/g)***	**C Constant**	**Correlation coefficient, r**
IFP-1(Zn)	701	719.605	0.999984
IFP-1(Zn/Co)	675	537.545	0.999996
IFP-5(Co)	773	1409.221	0.999996

* For BET, the uncertainty is ± 50.

ICP-OES analysis of IFP-1(Zn) and IFP-5(Co) demonstrated the presence of 27.32 wt % of Zn and 21.60 wt % of Co, respectively. The ICP-OES analysis of IFP-1(Zn/Co) confirmed the presence of Co metal with 2.77 wt % and 24.43 wt % of Zn indicating the successful metal ion exchange process (Table 3.2).

Table 3.2: Amount of Co and Zn present in the prepared materials

Catalyst	Zn (wt%)		Co (wt%)	
	Calculated	Found	Calculated	Found
IFP-1(Zn)	28.24	27.32	-	-
IFP-1(Zn/Co)	-	24.43	-	2.77
IFP-5(Co)	-	-	22.53	21.06

Further, the SEM image of Co^{2+}-exchanged MOF and pristine IFP-1(Zn) revealed no change in particle size and morphology of the MOF confirming its retention of the structural integrity before and after the metal ion exchange reaction (Figure 3.7a-b). Further, the SEM-EDX data shows the presence of Co in the exchanged MOF which further validates the successful preparation of bimetallic MOF, IFP-1(Zn/Co) (Figure 3.7c). The chemical structure and oxidation state of the metals in the synthesized metal-exchanged MOF, IFP-1(Zn/Co) was further assessed using XPS measurements.

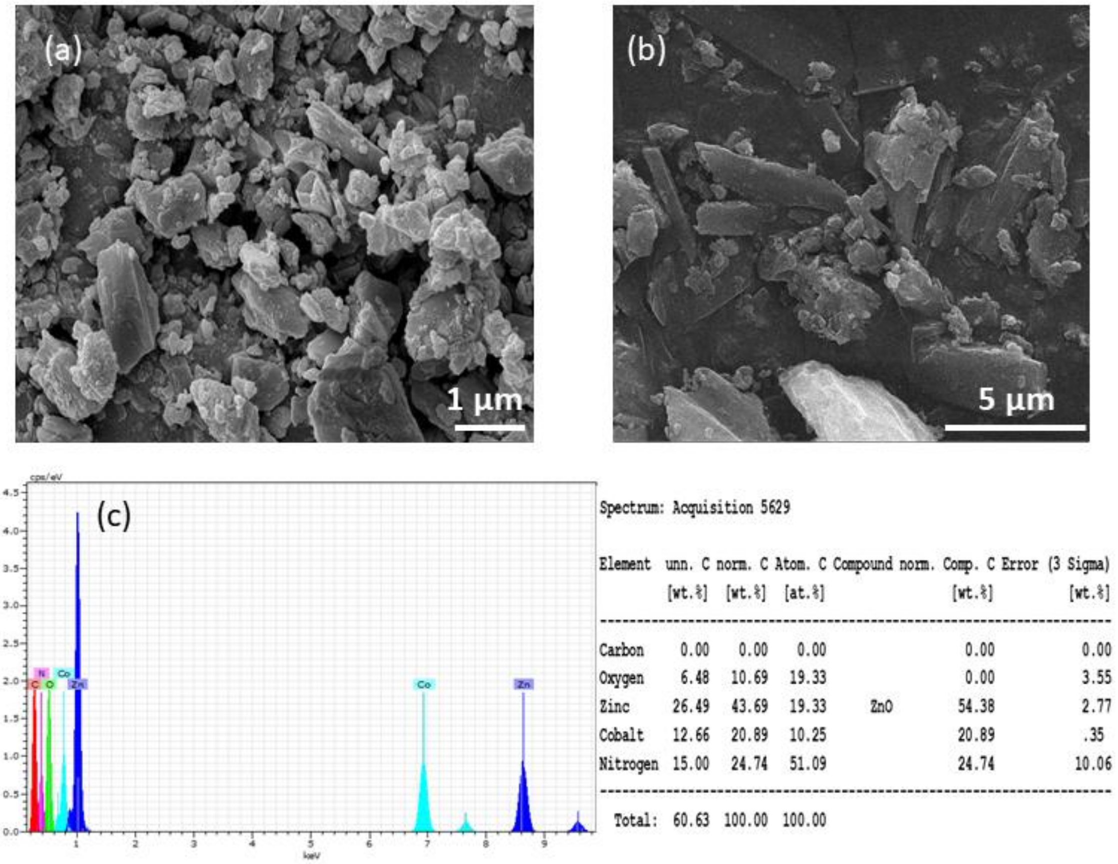

```
Spectrum: Acquisition 5629

Element  unn. C norm. C Atom. C Compound norm. Comp. C Error (3 Sigma)
         [wt.%]  [wt.%]  [at.%]                [wt.%]          [wt.%]
----------------------------------------------------------------------
Carbon     0.00    0.00    0.00                  0.00            0.00
Oxygen     6.48   10.69   19.33                  0.00            3.55
Zinc      26.49   43.69   19.33     ZnO         54.38            2.77
Cobalt    12.66   20.89   10.25                 20.89             .35
Nitrogen  15.00   24.74   51.09                 24.74           10.06
----------------------------------------------------------------------
  Total:  60.63  100.00  100.00
```

Figure 3.7: (a) SEM image of IFP-1(Zn). (b) SEM image of IFP-1(Zn/Co). (c) SEM-EDX data of IFP-1(Zn/Co).

The Co-exchanged MOF, exhibited a Zn $2p_{3/2}$ photoelectron peak at a binding energy of approximately 1021.5 eV, and 1044.5 eV for Zn $2p_{1/2}$ with a spin-orbit splitting of around 23.0 eV between the Zn $2p_{3/2}$ and Zn $2p_{1/2}$ (Figure 3.8b). These binding energies are consistent with those reported for Zn^{2+} in previous studies.[31,32,33] No peaks other than these two were observed, ruling out the presence of Zn in any other oxidation state. The XPS analysis of IFP-1(Zn/Co) also showed major binding peaks at 781.2 eV ($2p_{3/2}$) and 797 eV ($2p_{1/2}$) with a spin orbit separation of 15.8 eV. Prominent satellite peaks were observed at 786.7 eV and 802.3 eV, corresponding to the 2p core level spectra for Co (Figure 3.8a). The difference in the binding

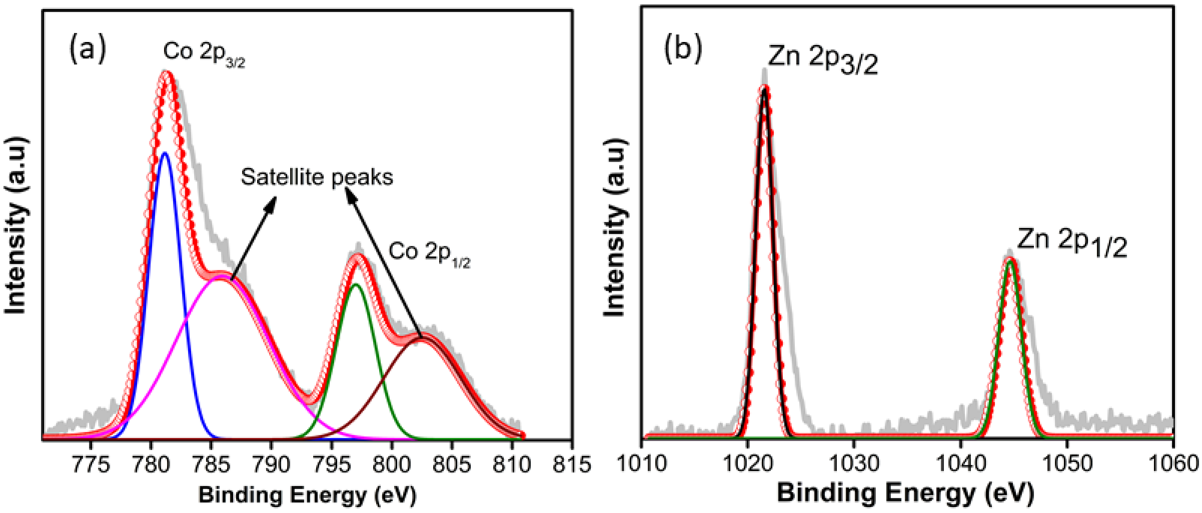

Figure 3.8: (a) Co 2p XPS spectrum of IFP-1(Zn/Co). (b) Zn 2p XPS spectrum of IFP-1(Zn/Co).

energies of the Co $2p_{3/2}$ peak and Co $2p_{1/2}$ with their corresponding satellite peaks was falls between 4-6 eV.[34,35,36] This XPS study confirmed the presence of cobalt in the +2 oxidation state within the IFP-1(Zn) matrix, with no cobalt species associated with CoO or metallic cobalt was detected.[36]

3.3.2 Photocatalytic CO_2 reduction

Considering their high chemical and thermal stability, large surface area and high CO_2 adsorption, we have employed the synthesized materials as photocatalysts to study their photocatalytic CO_2 reduction performance under visible light irradiation. Following the previously reported procedure[37,38,39] the photocatalytic experiments were carried out for each activate photocatalyst in a mixed solvent of acetonitrile and H_2O (3:1) containing $[Ru(bpy)_3]Cl_2\cdot 6H_2O$, BIH (20 mg), and TEOA (1 mL) as sacrificial agents under visible light irradiation (λ= 420 nm) . In this photocatalytic system, BIH acting as potent sacrificial electron donor, capable to quench the excited state of photosensitizer, $[Ru(bpy)_3]Cl_2\cdot 6H_2O$. Meanwhile, TEOA primarily serves as proton acceptor for $BIH^{+\cdot}$ intermediate.[40] The successful execution of the photocatalytic CO_2 reduction reaction relies on the integration of all the key components, including the sacrificial electron donor, photosensitizer, H_2O and catalyst. Each component play a vital role and collectively contributing to the overall efficiency of the photocatalytic CO_2 reduction process. Based on the photocatalytic tests, it was found that the reduction of CO_2 resulted in the formation of two

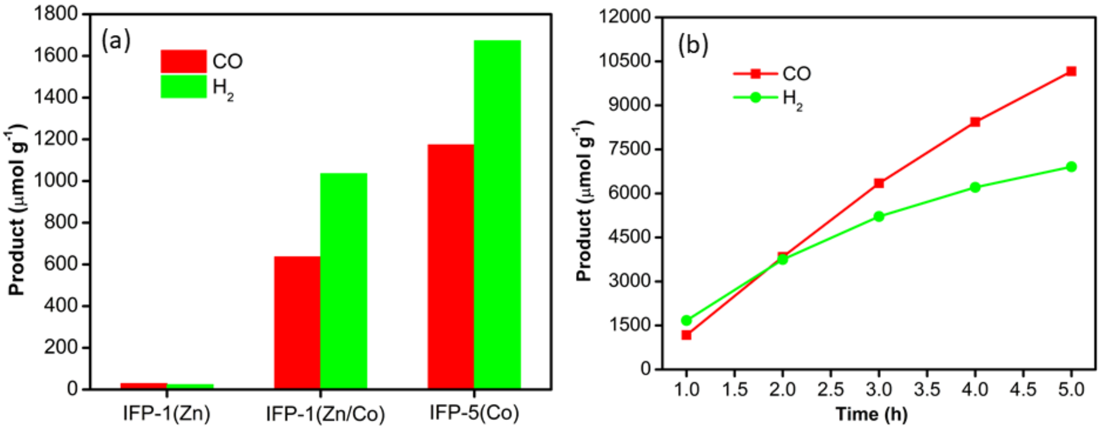

Figure 3.9: (a) Photocatalytic activities of IFP-based photocatalysts (1 h run). (b) 5 h long photocatalytic run over IFP-5(Co).

electron reduction products, CO and H_2, as illustrated in Figure 3.9a. The photocatalytic CO_2 reduction efficiency of the prepared photocatalysts followed the trend: IFP-1(Zn) < IFP-1(Zn/Co) < IFP-5(Co). IFP-1(Zn) exhibited poor photocatalytic efficiency, producing only 29 μmol g^{-1} of CO and 24 μmol g^{-1} of H_2 (Figure 3.9a). The low photocatalytic efficiency indicates that IFP-1(Zn) is unfavourable for photocatalytic CO_2 reduction. The low CO evolution observed for IFP-1(Zn) can likely be attributed to the higher recombination rate of electron-hole pairs during the photocatalytic process. However, the introduction of Co^{2+} metal centre into this IFP-1(Zn) through partial metal ion exchange method, has improved the overall catalytic performance of the photocatalyst, IFP-1(Zn/Co), which showed CO evolution of 636 μmol g^{-1} and H_2 evolution of 1036 μmol g^{-1} in 1 hour. Notably, IFP-5(Co) exhibited a significant enhancement in photocatalytic activity, achieving CO and H_2 evolution rates of 1174 μmol g^{-1} and 1673 μmol g^{-1}, respectively, within just 1 hour of the photocatalytic process. These values far surpass the performance of both IFP-1(Zn) and IFP-1(Zn/Co) catalysts which may be attributed to the high concentration of Co active sites as determined by the ICP-OES analysis. These findings highlighted that the Co sites function as the primary catalytic centres, driving the superior photocatalytic performance. In addition, we also examined the photocatalytic activity of IFP-5(Co) for 5 h long photocatalytic run revealing CO generation of 10301 μmol g^{-1} and H_2 generation of 6868 μmol g^{-1} with a production rate of 2060 μmol g^{-1} h^{-1} and 1373 μmol g^{-1} h^{-1} (Figure 3.9b) which is highly comparable to various other MOF-based photocatalysts reported to date (Table 3.3). The 5 h long run photocatalytic experiment initially

Table 3.3: Photocatalytic activity of different heterogenous photocatalyst towards CO_2 reduction

Photocatalyst	**Illumination range**	**SA**	**PS**	**Product**	**Production rate**[a]	**Selectivity**	**Reference**
MOF-Ni	420–800 nm	TIPA	$[Ru(bpy)_3]Cl_2$	CO	371.6	97.7%	41
Cd-PMOFs	>420 nm	TEOA	$[Ru(bpy)_3]Cl_2$	CO	139	N.R	42
Cd(II)PMOF	>420 nm	TEA	$[Ru(bpy)_3]Cl_2$	CO	56	N.R	43
Co-UiO-67	400–800 nm	N.R	$[Ru(bpy)_3]Cl_2$	CO	3292.5	NR	44
Zr-DMBD-Co MOF	450 nm	TEOA	$[Ru(phen)_3](PF_6)_2$	CO	33.3	98%	45
MOF-525-Co	$\lambda \geq 400$	TEOA		CO	210	84 %	46
Zr-MBA-TET-Re-MOF	>420	H_2O		CO	80.5	99.9	47
Ni-MOL-100	>420 nm	TEOA	$Ru(phen)_3(PF_6)_2$	CO	2972	96 %	48
66-IS-Ni	>420 nm	TEOA	$[Ru(bpy)_3]Cl_2$	CO	1352	87%	49
Zr-MBA-Ru/Re-MOF	>400 nm			CO	440	99%	50
PCN-250-Fe2Mn	>420 nm	TIPA	$[Ru(bpy)_3]Cl_2$	CO	21.51	82.5%	51
IFP-5(Co)	**>420 nm**	**TEOA + BIH**	$[Ru(bpy)_3]Cl_2$	**CO**	**2060**	**N.R**	**THIS WORK**

[a] Unit: $\mu mol\ g^{-1}\ h^{-1}$

demonstrated the higher production of H_2, however as the irradiation time progressed the selectivity towards CO production increases (Figure 3.9b). Subsequently, we have also investigated the catalytic performance of the IFP-5(Co) under irradiation by direct sun light from 10:00 am to 3:00 am on 09/10/2024 (Cloudy sky) to mimic the natural photosynthesis and we found 2615 $\mu mol\ g^{-1}$ CO and 1161 $\mu mol\ g^{-1}$ H_2. No other liquid products such as CH_3OH, HCHO, C_2H_5OH, HCOOH were detected in the ^{1}H-NMR analysis of the reaction mixture (Figure 3.10).

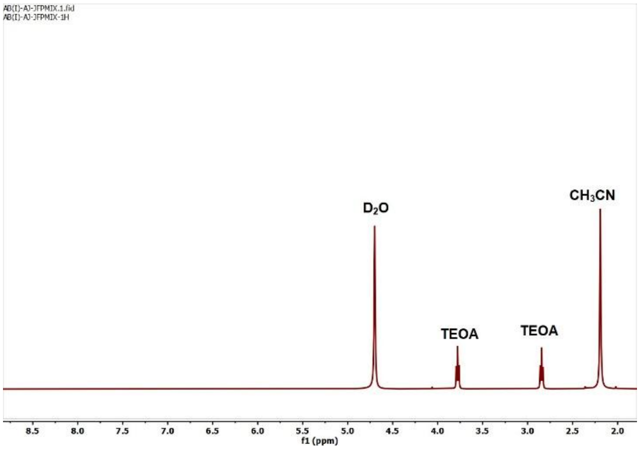

Figure 3.10: ^{1}H-NMR spectroscopy of the reaction mixture after photocatalytic CO_2 reduction.

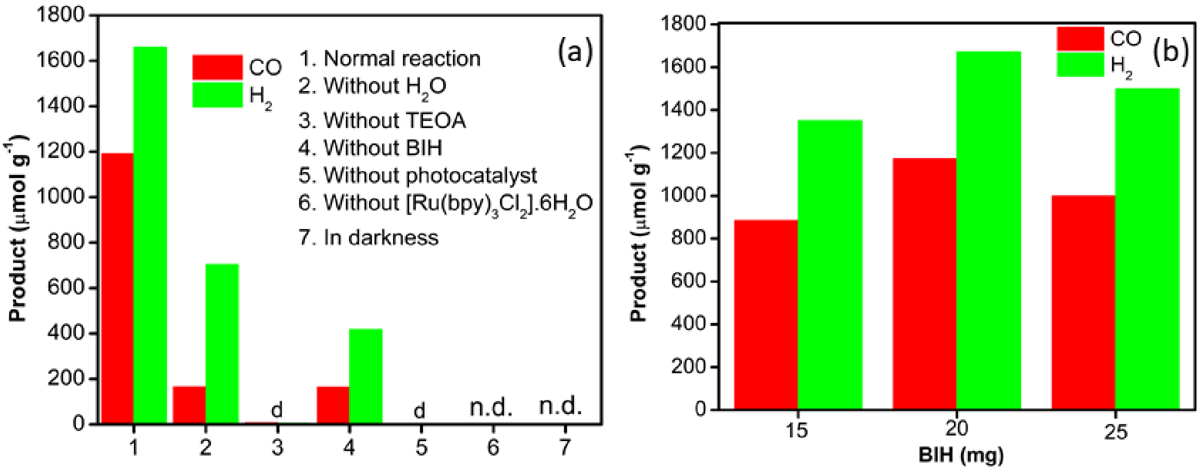

Figure 3.11: (a) Photocatalytic activities of IFP-5(Co) under different conditions (1 h run). (b) Photocatalytic CO evolution over IFP-5(Co) with different loading of BIH for 1 h run.

Furthermore, a set of control experiments were conducted over IFP-5(Co) to investigate the key factors influencing the photocatalytic CO_2 reduction and H_2 evolution processes (Figure 3.11a). The photocatalytic experiment without using H_2O resulted in a slight decrease in H_2 production. These results indicated the protons for H_2 production may originate either from TEOA or H_2O. However, when TEOA was removed, the overall photocatalytic performance was drastically reduced (Figure 3.11a). This observation suggests that TEOA can act as proton source as well as sacrificial electron donor, indicating its decisive role in facilitating the overall performance of the photocatalyst.[52] In this photocatalytic reaction system, the addition of BIH significantly enhanced the catalytic activity for CO_2 reduction due to its high reductive capability, rapid deprotonation of the oxidized BIH species ($BIH^{+\cdot}$), and ability to donate two electrons during the reaction.[53] Thus, we have studied the photocatalytic activity by varying different amount of BIH and observed highest CO generation at a loading of 20 mg BIH (Figure 3.11b). Moreover, the removal of BIH from reaction reduced the CO production to 164 μmol g^{-1} and H_2 evolution to 417 μmol g^{-1} (Figure 3.11a). No photocatalytic activity was observed in the absence of the photosensitizer and light, revealing that the electrons taking part in the CO_2 conversion were transferred from the photosensitizer under visible light irradiation (Figure 3.11a). However, a trace amount of CO (0.096 μmol) and H_2 (0.105 μmol) was detected in absence of the catalyst IFP-5(Co). These results collectively underscored the indispensability of all the components within this system. The photocatalytic CO_2 reduction experiment using N_2 gas instead of CO_2 did not show any CO evolution. This result suggested that the CO_2

reduction is the sole source for the CO formation rather than the degradation of the catalyst or the organic solvents TEOA, CH_3CN.[36] Additionally, an isotope labelling experiment with $^{13}CO_2$ was performed to verify the source of CO production. The gaseous products were analysed via gas chromatography-mass spectrometry (GC-MS), which showed a characteristic peak at m/z = 29. This confirms that the CO originated from CO_2 rather than from any other organic compounds (Figure 3.12a). Further, the catalytic stability of IFP-5(Co) for CO_2 reduction was evaluated over four 1 h illumination cycles (Figure 3.12b).

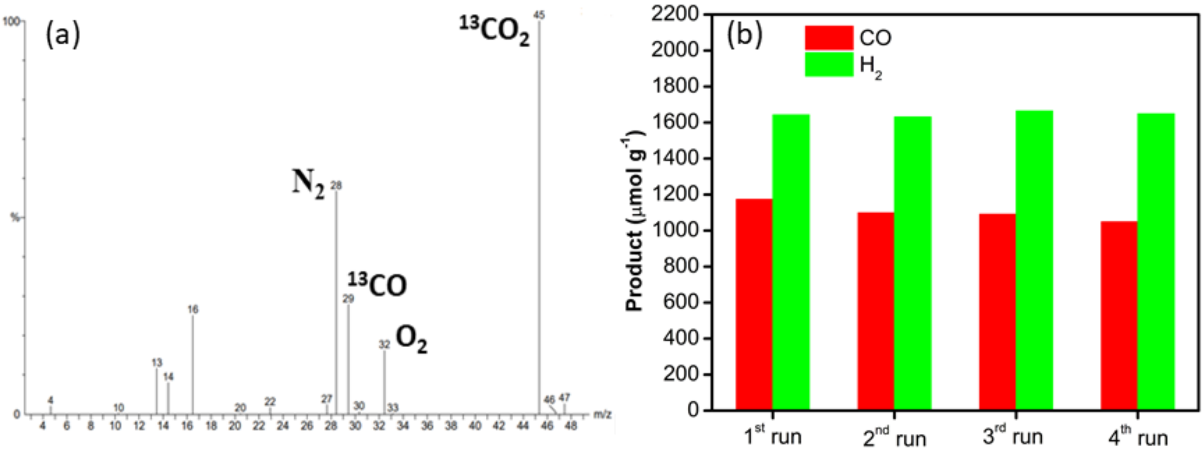

Figure 3.12: (a) ^{13}C isotope labelling experiment for CO generation by using $^{13}CO_2$ as carbon source. (b) Recyclability test of IFP-5(Co).

Recycle test for IFP-5(Co) in photocatalytic CO_2 reduction:

Recycle tests on IFP-5(Co) for photocatalytic CO_2 reduction were conducted to demonstrate the heterogenous nature of the photocatalyst as reported previously.[39] The CO_2 reduction reaction was performed using 5 mg of IFP-5(Co), 20 mg of BIH, 12 mg of $[Ru(bpy)_3]Cl_2\cdot 6H_2O$, in a 4 mL acetonitrile and water mixture (3:1) containing 1 mL of TEOA. The solution was purged with CO_2 for 30 minutes. The reaction was irradiated using a 300 W Xenon lamp equipped with a 420 nm cut-off filter. After each 1-hour recycling run, we have filtered the photocatalyst and washed with acetonitrile. Then again, the recovered catalysts employed for the next photocatalytic cycle under the same condition as mentioned above. The photocatalytic performance of IFP-5(Co) over all the four cycles exhibited no significant loss in production of CO and H_2 confirming its excellent long-term stability and cycling durability for CO_2 reduction. After 4 recycle tests, we have characterized the reused and fresh IFP-5(Co) samples through PXRD and FT-IR spectroscopy, where no such change had been observed demonstrating the stability of the catalyst IFP-5(Co) in the photocatalytic reaction medium (Figure 3.13a-b).

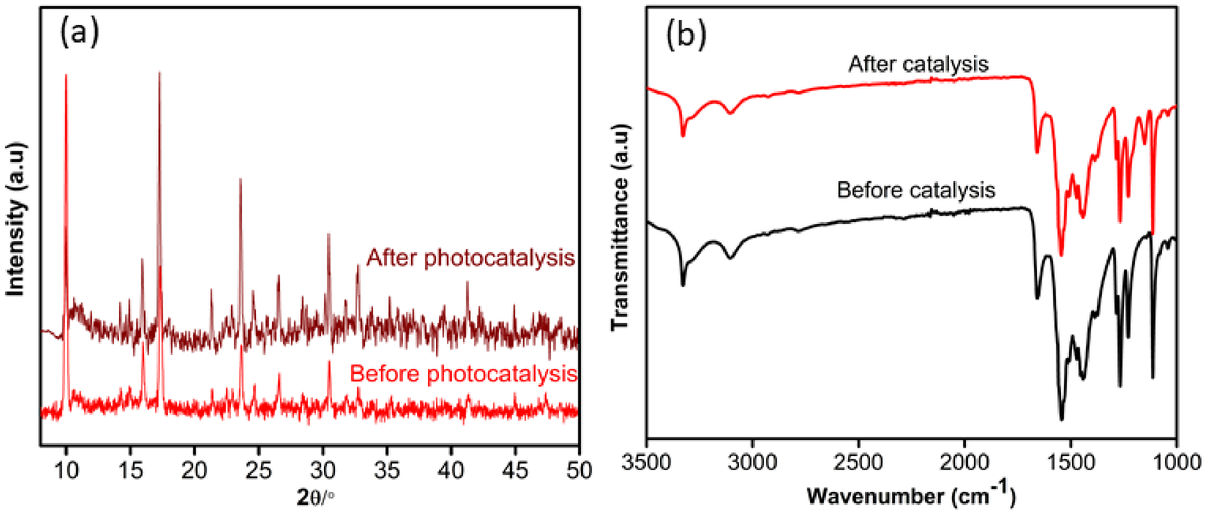

Figure 3.13: (a) PXRD profile, and (b) FT-IR spectra of IFP-5(Co) after and before photocatalysis.

Leaching Test: To further confirm the heterogeneous nature of the photocatalyst, a leaching test was performed (Figure 3.14). A photocatalytic CO_2 reduction experiment was conducted for 1 hour under the same conditions as described previously. Following this, the reaction mixture was filtered to separate the catalyst, IFP-5(Co). The filtrate, containing only the reaction solution, was then used for an additional 2-hour photocatalytic CO_2 reduction experiment (the gaseous product was collected in 1 h interval).

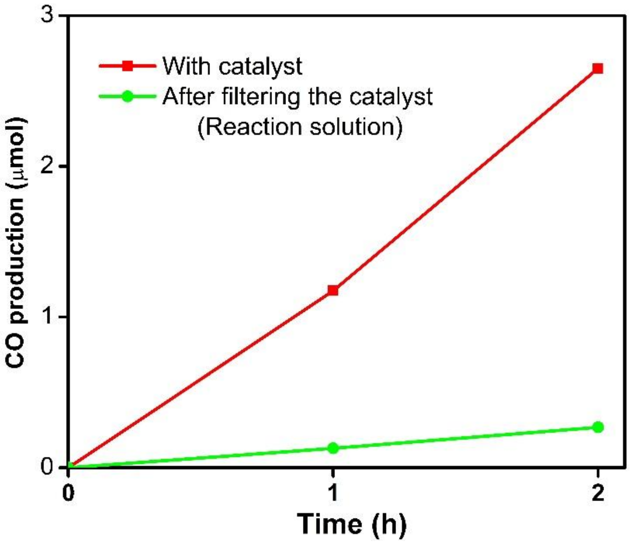

Figure 3.14: Photocatalytic test after separating the catalyst (2 h run).

The photocatalytic activity of the filtrate showed CO generation comparable to that observed in the blank test (using $[Ru(bpy)_3]Cl_2{\cdot}6H_2O$, BIH, and TEOA). The experiment indicated that there was no Co leaching from the IFP-5(Co) catalyst into the solution occurred during the reaction.

3.3.3 Plausible photocatalytic CO_2 reduction mechanism

Photophysical and electrochemical studies were conducted to elucidate the potential photocatalytic CO_2 reduction mechanism of IFP-5(Co) within this system. First, UV-Vis spectroscopy was performed to analyse the optical properties of the synthesized catalysts (Figure 3.15a). Both IFP-1(Zn) and IFP-1(Zn/Co) exhibited a maximum absorption peak at 300 nm. In contrast, IFP-5(Co) showed a slight red shift, with the maximum absorption peak observed at 328 nm. These absorption peaks can be attributed to the presence of the electron-rich imidazole group, which facilitates the π–π* transition.[54]

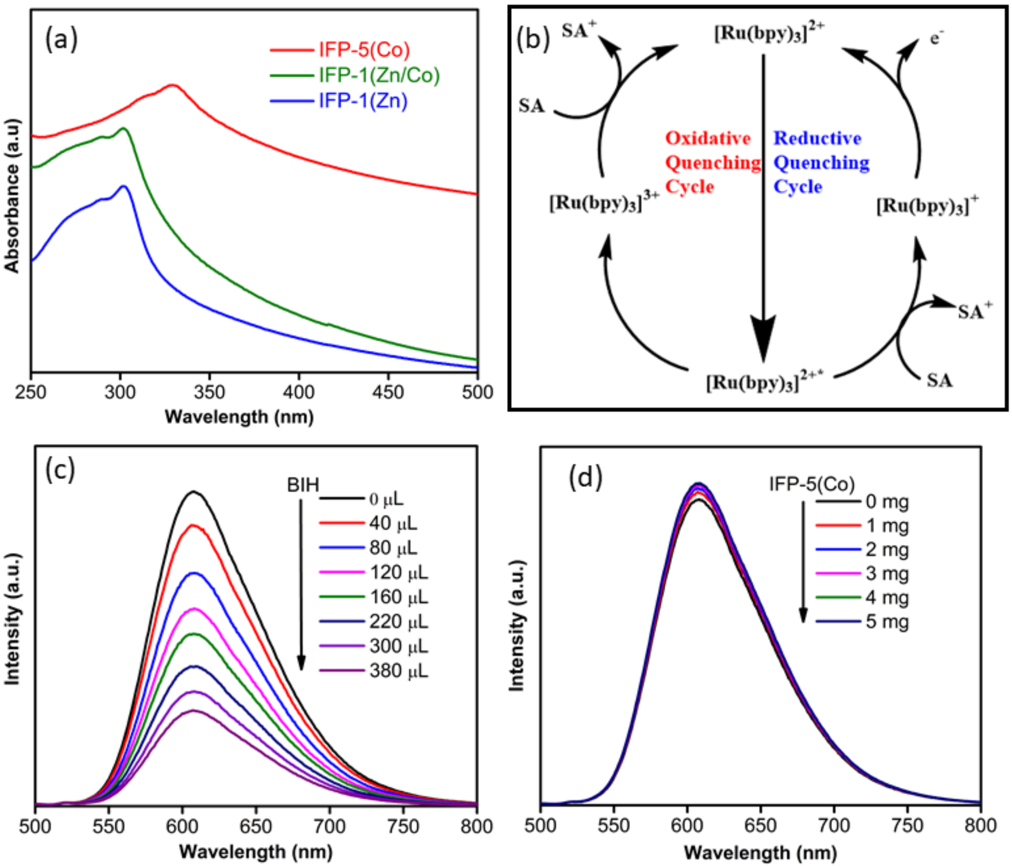

Figure 3.15: (a) UV-Vis spectra of IFP-1(Zn), IFP-1(Zn/Co) and IFP-5(Co) (b) Schematic oxidative and reductive pathways of Ru-PS (PS= photosensitizer). (c) Emission intensity of $[Ru(bpy)_3]^{2+}$ after incremental addition of BIH and (d) IFP-5(Co).

Then, to know, whether the photoexcited Ru^{II} PS underwent reductive quenching by BIH or oxidative quenching by the IFP-5(Co), initiating the catalytic cycle (Figure 3.15b), we conducted photoluminescence spectra of $[Ru(bpy)_3]^{2+}$ with varying amount of BIH and IFP-5(Co). As depicted in Figure 3.15c, the emission intensity of $[Ru(bpy)_3]^{2+}$ was effectively quenched by BIH, while no significant quenching was observed with IFP-5(Co) (Figure 3.15d). This outcome underscored that the photoexcited $[Ru(bpy)_3]^{2+*}$ underwent reductive quenching by BIH, leading to the generation of the $[Ru(bpy)_3]^{+*}$ which injects electrons to the Co catalytic sites for CO_2 reduction. Further, the electronic properties and band structures of the catalysts has been studied through Tauc plot, Mott-Schottky plot and electrochemical impedance spectroscopy. Electrochemical impedance spectroscopy (EIS) was utilized to assess the charge transfer resistance within the materials. As illustrated in Figure 3.16a, IFP-5(Co) displayed a smaller arc radius compared to the other materials, signifying reduced electronic resistance and more efficient electron transport. This lower charge transfer resistance contributed to the superior photocatalytic activity of IFP-5(Co) relative to the other catalysts.

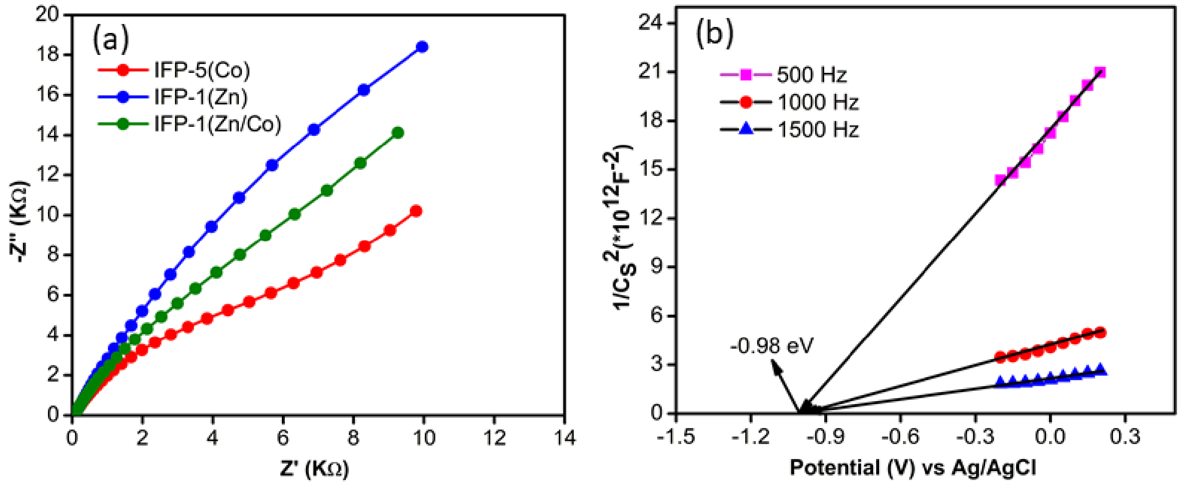

Figure 3.16: (a) EIS spectra of the prepared photocatalysts. (b) Mott-Schottky plot for IFP-5(Co).

The electronic structure of IFP-5(Co) was studied using Mott-Schottky and Tauc plots (Figure 3.16b, Figure 3.17a). The Mott-Schottky curve for IFP-5(Co) showed positive slope indicating IFP-5(Co) is a n-type semiconductor.[55] From the plot, the lowest unoccupied molecular orbital (LUMO) of IFP-5(Co) was determined to be -0.98 eV versus the Ag/AgCl electrode, equivalent to -0.78 eV versus NHE. The band gap of IFP-5(Co), derived from the Tauc plot using UV-Vis absorption spectra, was found to be 2.20 eV. Consequently, the highest occupied molecular orbital (HOMO) of IFP-5(Co) was calculated to be 1.42 eV. The band gap values and band

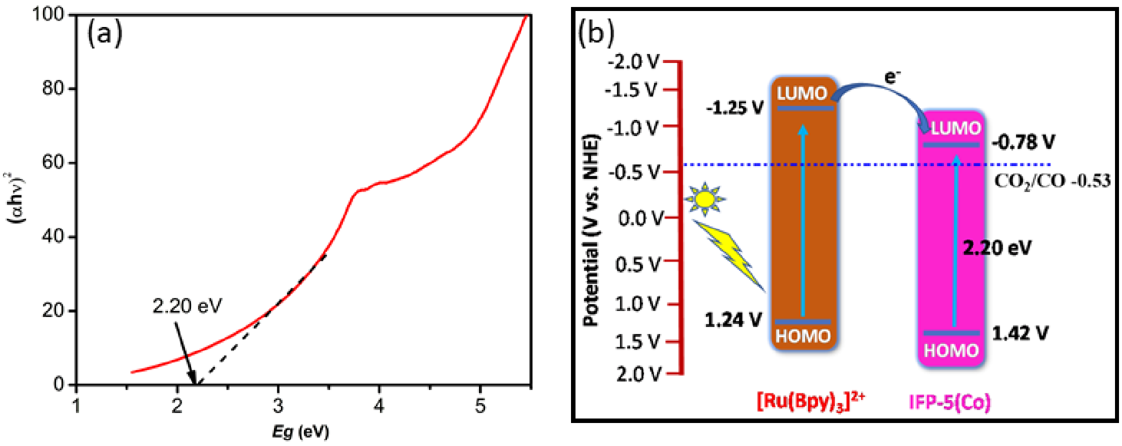

Figure 3.17: (a) Tauc plot of IFP-5(Co). (b) Potential diagram of $[Ru(bpy)_3]^{2+}$ and IFP-5(Co) showing feasible electron transfer.

positions indicated that the reduction potential of IFP-5(Co) was less negative than that of $[Ru(bpy)_3]^{2+}$ ($E([Ru(bpy)_3]^{2+*}/[Ru(bpy)_3]^{+}) = -1.25$ V vs. NHE) but more negative than the reduction potential for CO_2 to CO conversion ($E(CO_2/CO) = -0.52$ V vs. NHE) (Figure 3.17b). This suggested that electron transfer occurred from the photosensitizer to IFP-5(Co), which subsequently facilitated electron injection from the catalyst to CO_2, thereby promoting the photocatalytic reduction of CO_2 to CO.

Furthermore, the mechanism of CO_2 reduction catalysed by IFP-5(Co) and IFP-1(Zn) was thoroughly examined using Density Functional Theory (DFT) calculations. The molecular structure of IFP-5(Co) was constructed and optimized at the B3LYP/LANL2DZ[56,57,58] level of theory, as implemented in Gaussian 16.[59]

The widely accepted reaction pathway proposes that CO_2 adsorbs onto the catalyst surface and undergoes an initial hydrogenation step, leading to the formation of *COOH intermediate. This intermediate is then transformed into *CO. *COOH and *CO serving as the key intermediates in the photocatalytic conversion of CO_2 to CO.[60,61] The resulting energy profile, depicted in Figure 3.18, provides valuable insights into the reaction pathway. The process initiates with the formation of the IFP-5($Co^{2+}\ldots CO_2^{2-}$) complex. As depicted in Figure 3.18, CO_2 adsorbs onto the Co site, where it undergoes activation and subsequent hydrogenation, forming a -COOH intermediate through the first transition state (TS1) i.e., *COOH formation with an energy barrier of 10.72 eV. Further hydrogenation propels the reaction forward, leading to dehydration via a second transition state (TS2) i.e., formation of *CO and culminating in the production of CO and H_2O. Hence the results showed that the step of forming *CO from

*COOH requires the maximum free energy of 16.59 eV indicating the formation of *CO is the rate-determining step of the overall CO_2 to CO reaction.

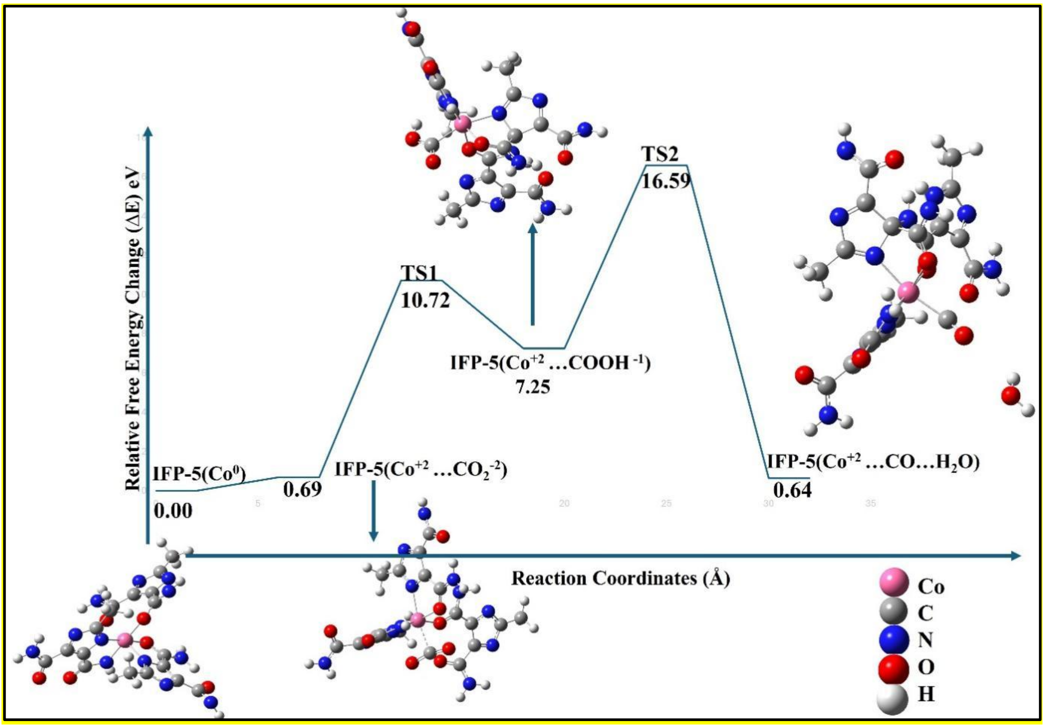

Figure 3.18: The relative energy profile of CO_2 reduction catalyzed by IFP-5(Co).

The energy profile revealed that IFP-5(Co) demonstrating that the Co sites are thermodynamically more favourable for CO_2 to CO formation under visible light irradiation. Therefore, IFP-5(Co) has superior catalytic activity for CO evolution, which can be ascribed to the low energy barrier in the reaction process.

In addition to investigating CO_2 reduction catalysed by IFP-5(Co), a similar study was conducted using Zn as the metal centre.

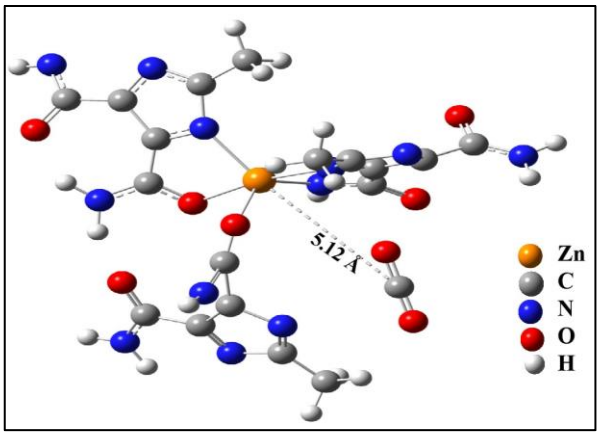

Figure 3.19: Optimized geometry of IFP-1(Zn) with CO_2 linkage.

However, in this case, no bonding interaction with CO_2 was observed. The optimized geometry, shown in Figure 3.19, reveals that CO_2 does not adsorb onto the Zn site; instead, it moves away, as indicated by the significant Zn-CO_2 distance (Figure 3.19). The calculated DFT results aligning well with the aforementioned experimental observations, where IFP-1(Zn) demonstrated very poor photocatalytic efficiency, yielding only 29 μmol g^{-1} of CO and 24 μmol g^{-1} of H_2 (Figure 3.11a). In contrast, IFP-5(Co) exhibited the highest photocatalytic reduction efficiency among all the prepared catalysts, likely due to the higher concentration of Co^{2+} centres, as verified by ICP-OES analysis. The DFT calculations support this, showing that the Co active site plays a critical role in the CO_2 reduction mechanism, facilitating key hydrogenation and dehydration steps with a moderate energy barrier of 16.59 eV for the rate-determining step. Together, these findings underscore the essential role of the Co^{2+} metal centre in the catalytic performance of IFP-5(Co), both experimentally and computationally, highlighting its superiority over Zn-based catalysts for CO_2 reduction.

Now, based on the above mentioned experimental and theoretical results we have proposed a plausible mechanism for the photocatalytic CO_2 reduction as depicted in Figure 3.20.

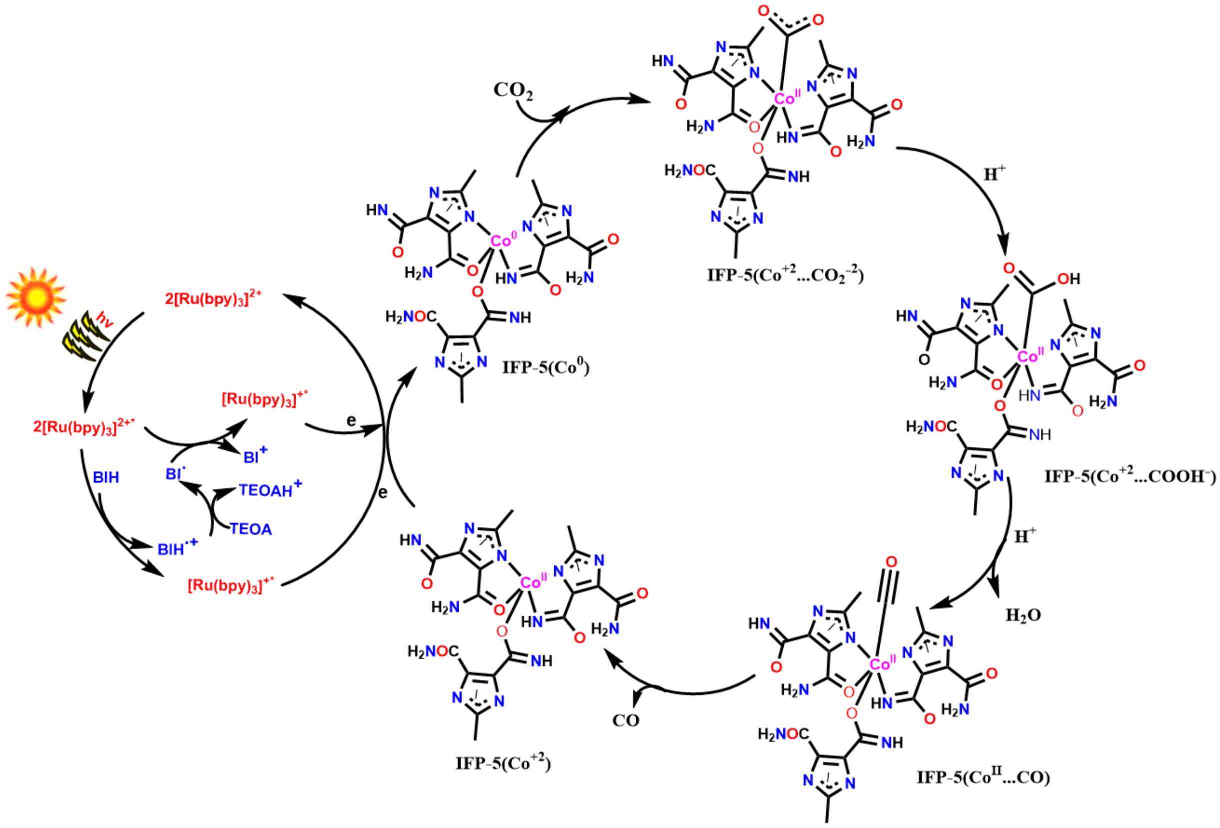

Figure 3.20: Mechanism for photocatalytic cycle for CO_2 reduction over IFP-5(Co).

The reaction begins with the photoexcitation of the photosensitizer $[Ru(bpy)_3]Cl_2$, forming the triplet MLCT excited state $^3[Ru(bpy)_3]^{2+*}$ upon visible light irradiation. This excited state is then reductively quenched by one-electron transfer from BIH, as demonstrated in the photoluminescence experiment (Figure 3.15c), generating the reduced photosensitizer $[Ru(bpy)_3]^+$. The resulting oxidized BIH ($BIH^{+\bullet}$) is readily deprotonated by TEOA, producing the strongly reducing $BI^\bullet$ species, which further reduces another molecule of $^3[Ru(bpy)_3]^{2+*}$, yielding two equivalents of $[Ru(bpy)_3]^+$ in the overall photoinduced process. Subsequently, the two reduced photosensitizers, $[Ru(bpy)_3]^+$, facilitate the reduction of the Co^{II} center in IFP-5(Co) to Co^0 by transferring two electrons. The reduced photosensitizer subsequently returns to its original $[Ru(bpy)_3]^{2+}$ state, thereby completing the catalytic cycle. CO_2 molecules then coordinate to the reduced, unsaturated Co^0 sites through the carbon atom, forming a $Co^{II}–CO_2^{2-}$ adduct. This adduct undergoes protonation, yielding a $Co^{II}–COOH^-$ intermediate. Further protonation of this intermediate results in the elimination of an H_2O molecule, generating the $Co^{II}–CO$ species. Following the desorption of CO, the catalyst IFP-5(Co) is regenerated, initiating a new catalytic cycle. Simultaneously, During the photocatalytic CO_2 reduction process, water splitting occurs simultaneously, producing protons (H^+), which play a crucial role in facilitating the reaction.[62]

Additionally, the protons are also supplied by TEOA which can act as sacrificial electron donor as well as proton donor. The CO_2 molecules bound to the catalyst surface are subsequently hydrogenated with two equivalents of protons (H^+), resulting in the formation of CO (Figure 3.20). On the other hand, the available excess protons coming from H_2O, TEOA and BIH in the reaction system can readily reduce to generate H_2 by induced photoexcited electrons.[63,36] Hence, these two competitive reactions lead to the formation of syngas (CO and H_2). We can summarise the two competitive reactions as follows:

$$CO_2 + 2H^+ + 2e^- \longrightarrow CO + H_2O$$
$$2H^+ + 2e^- \longrightarrow H_2$$

However, it is crucial to note that the absence of TEOA significantly reduces the overall photocatalytic activity of IFP-5(Co). TEOA functions as a base for $BIH^{\bullet+}$, preventing back electron transfer from IFP-5(Co) to $BIH^{\bullet+}$, thereby sustaining the photocatalytic cycle.[64]

3.4 Conclusion

In conclusion, we successfully introduced imidazolate-based metal-organic frameworks (IFP-1(Zn) and IFP-5(Co)) as effective photocatalysts for CO_2 reduction. Post-synthetic modification of IFP-1(Zn) via partial metal ion exchange with Co(II) produced a bimetallic framework, IFP-1(Zn/Co), which significantly enhanced photocatalytic performance compared to its pristine counterpart, IFP-1(Zn). Photocatalytic experiments revealed that the metal-exchanged IFP-1(Zn/Co) demonstrated improved CO_2 reduction efficiency. However, IFP-5(Co) exhibited the highest catalytic activity, highlighting the pivotal role of cobalt in driving superior photocatalytic performance. Notably, IFP-5(Co) achieved exceptional CO and H_2 evolution of 10,160 μmol g^{-1} and 6,908 μmol g^{-1}, respectively, over a 5-hour photocatalytic run. In addition, through a combination of photophysical, electrochemical, and DFT studies, a plausible mechanism for CO_2 reduction was proposed. This work underscores the potential of IFP-based MOFs and metal ion substitution strategies in developing advanced photocatalysts for sustainable CO_2 conversion.

3.5 References

1. J. Barbar, *Chem.Soc.Rev.,* 2008, **38**,185.
2. A.S. Agarwal, Y.Zhai, D. Hill, and N. Sridhar, *ChemSusChem*, 2011, **4**, 1301.
3. K.S.Lackner, *Eur. Phys. J. Spec. Top.,* 2009, **176**, 93.
4. H. Fei, M. D. Sampson, Y. Lee, C.P. Kubiak, and S. M. Cohen, *Inorg. Chem.,* 2015, ***54***, 6821.
5. S. N. Habisreutinger, L. Schmidt Mende and J. K. Stolarczyk, *Angew. Chem. Int. Ed.,* 2013, **52**, 7372.
6. T. Morimoto, C. Nishiura, M. Tanaka, J. Rohacova, Y. Nakagawa, Y. Funada, K. Koike, Y. Yamamoto, S. Shishido, T. Kojima, T. Saeki, T. Ozeki, and O. Ishitani, *J. Am. Chem. Soc.,* 2013, **135**, 13266.
7. K. Tanaka, and D. Ooyama, *Coord. Chem. Rev.,* 2002, **226**, 211.
8. E. E. Benson, C. P. Kubiak, A. J. Sathrum, and J. M. Smieja, *Chem. Soc. Rev.,* 2009, **38**, 89.
9. S. Sato, T. Morikawa, S. Saeki, T. Kajino, and T. Motohiro, *Angew. Chem. Int. Ed.,* 2010, **49**, 5101.
10. V. S. Thoi, and C. J. Chang, *Chem. Commun.,* 2011, **47**, 6578.

11. K. Sumida, D. L. Rogow, J. A. Mason, T. M. McDonald, E. D. Bloch, Z. R. Herm, T. H. Bae, and J. R. Long, *Chem. Rev*., 2012, **112,** 724.

12. P. Deria, D. A. Gomez-Gualdron, I. Hod, R. Q. Snurr, J. T. Hupp, and O. K. Farha, *J. Am. Chem. Soc.*, 2016, **43**, 14449.

13. N. S. Bobbitt, M. L. Mendonca, A. J. Howarth, T. Islamoglu, J. Y. Hupp, O. K. Farha, and R. Q. Snurr, *Chem. Soc. Rev.,* 2017,**46**, 3357.

14. S. Goswami, M. Chen, M. R. Wasielewski, O. K. Farha, and J. T. Hupp, *ACS Appl. Mater. Interfaces,* 2018**, 40,** 34409.

15. L. Shi, T. Wang, H. Zhang, K. Chang and J. Ye, *Adv. Funct. Mater.*, 2015, **25**, 5360.

16. J. T. Barmanbek, A. S. Alshammari, P. Yang, and O. M. Yaghi, *J. Am. Chem. Soc.*, 2017, **139**, 356.

17. C. Wang, Z. Xie, K. E. deKrafft, and W. Lin, *J. Am. Chem. Soc.*, 2011, **133**, 13445.

18. R. Banerjee, A. Phan, B. Wang, C. Knobler, H. Furukawa, M. O'Keeffe, and O. M. Yaghi, *Science*, 2008, **319**, 939.

19. A. Phan, C. J. Doonan, F. J. Uribe-Romo, C. B. Knobler, M. O'Keeffe and O. M. Yaghi, *Acc. Chem. Res*., 2010, **43**,58.

20. F. Debatin, K. Behrens, J. Weber, I.A. Baburin, A. Thomas, J. Schmidt, I. Senkovska, S. Kaskel, A. Kelling, N. Hedin, Z. Bacsik, S. Leoni, G. Seifert, C. Jager, C. Gunter, U. Schilde, A. Friedrich, and H.J.Holdt, *Chem.Eur.J.*, 2012, **18,** 11630.

21. K. Behrens, S. S. Mondal, R. Nöske, I. A. Baburin, S. Leoni, C. Günter, J. Weber, and H.-J. Holdt, *Inorg. Chem.*, 2015, **54**, 10073.

22. S. S. Mondal, A. Bhunia, S. Demeshko, A. Kelling, U. Schilde, C. Janiak, and H.-J. Holdt, *CrystEngComm,* 2014, ***16***, 39.

23. F. Debatin, A. Thomas, A. Kelling, N. Hedin, Z. Bascik, I. Senkovska, S. Kaskel, M. Junginger, H. Müller, U. Shilde, C. Jäger, A. Friedrich, and H. J. Holdt, *Angew. Chem. Int. Ed.,* 2010, ***8,*** 1258.

24. F. Debatin, J. Möllmer, S. S. Mondal, K. Behrens, A. Möller, R. Staudt, A. Thomas, H.-J. Holdt, *J. Mater. Chem.,* 2012, ***22,*** 10221-10227.

25. H. Yanagisawa, Y. Amemiya, T. Kanazaki, Y. Shimoji, K. Fujimoto, Y. Kitahara, T. Sada, M. Mizuno, M. Ikeda, S. Miyamoto, Y. Furukawa, H. Koike, *J. Med. Chem.,* 1996, **39**, 323–338.

26. A. Bucci, S. S. Mondal, V. Martin-Diaconescu, A. Shafir, and J. Lloret-Fillol, *ACS Appl. Energy Mater.* **2019**, *2*, 8930−8938.

27. X. Wang, Z. Fu, L. Zheng, C. Zhao, X. Wang, S. Y. Chong, F. McBride, R. Raval, M. Bilton, L. Liu, X. Wu, L. Chen, R. S. Sprick, A. I. Cooper, *Chem. Mater.,* 2020, **32,** 9107-9114.

28. M. Wang, J. Liu, Y. Wang, B. Liu, C. Guo, X. Gao, C. Gong, X. Li, G. G. Gurzadyana and L. Sun, *J. Mater. Chem. A,* 2018, ***6***, 4768.

29. J. Wang, W. Zhu, F. Meng, G. Bai, Q. Zhang, and X. Lan, *ACS Catal.,* 2023, **13**, 4316−4329.

30. A. Jana, J. Mandal, S. S. Mondal, R. Patra, and A. Bhunia, *Inorg. Chim. Acta*, 2023, **549,** 121409.

31. M. Thanh, T. Thien, P. Du, N. Hung, D. Khieu, *J. Porous Mater*., 2018, **25**, 857.

32. M. R. A. Amid, S. Park, J. S. Kim, Y. M. Lee, and H. Jeong, *J. Mater. Chem. A,* 2019, 7, 9680.

33. L. E. Mphuthi, E. Erasmus and E.H.G. Langner, *ACS Omega*, 2021, **6**, 31632.

34. T. Baidya, T. Murayama, S. Nellaiappan, N.K. Katiyar, P. Bera, O. Safonova, M. Lin, K. R. Priolkar, S. Kundu,B. S. Rao, P. Steiger, S. Sharma, K. Biswas, S.K. Pradhan,N. Lingaiah, K. D. Malviya and M. Haruta, *J. Phys. Chem. C,* 2019, **123,** 19557.

35. T. Baidya, T. Murayama, P. Bera, O. V. Safonova, P. Steiger, N. K. Katiyar, K. Biswas and M. Haruta, *J. Phys. Chem. C*, 2017, **121**, 15256.

36. A. Jana, A. Maity, A. Sarkar, B. Show, Preeti A. Bhobe and A. Bhunia, *J. Mater. Chem. A*, 2024, **12**, 5244.

37. X. Wang, Z. Fu, L. Zheng, C. Zhao, X. Wang, S. Y. Chong, F. McBride, R. Raval, M. Bilton, L. Liu, X. Wu, L. Chen, R. S. Sprick and A. I. Cooper, *Chem. Mater.,* 2020, **32**, 9107.

38. M. Wang, J. Liu, Y. Wang, B. Liu, C. Guo, X. Gao, C. Gong, X. Li, G. G. Gurzadyanand, and L. Sun, *J. Mater. Chem. A,* 2018, **6**, 4768.

39. J. Wang, W. Zhu, F. Meng, G. Bai, Q. Zhang, and X. Lan, *ACS Catal*., 2023, **13**, 4316.

40. Y. Tamaki, and O. Ishitani, *ACS Catal*., 2017, **7**, 3394.

41. X.-K. Wang, J. Liu, L. Zhang, L.-Z. Dong, S.-L. Li, Y. -H. Kan, D.-S. Lan, and Y.-Q Li, *ACS Catal.,* 2019, **9**, 1726.

42. J. Ding, Y. Wu, S. Jia, Y. Feng, K. Li, M. Fang, J. Bao, and Y. Wu, *J. Solid State Chem.,* 2020, **292**, 121690.

43. Q. Li, Y. Luo, Y. Ding, Y. Wang, Y. Wang, H. Du, R. Yuan, J. Bao, M. Fang, and Y. Wu, *Dalton Trans.,* 2019, **48**, 8678.

44. X. Gao, B. Guo, C. Guo, Q. Meng, J. Liang, and J. Liu, *ACS Appl. Mater. Interfaces.,* 2020, **12**, 24059–24065.

45. D.-C. Liu, T. Ouyang, R. Xiao, W.-J. Liu, D.-C. Zhong, Z. Xu, and T.-B. Lu, *ChemSusChem.*, 2019, **12,** 2166-2170.

46. H. B. Zhang, J. Wei, J. C. Dong, G. G. Liu, L. Shi, P. F. An, G. X. Zhao, J. T. Kong, X. J. Wang, X. G. Meng, J. Zhang, and J. H. Ye, *Angew. Chem. Int. Ed.*, 2016, **55**, 14310-14314.

47. S. R. V. Parambil, F. A. Rahimi, R. Ghosh, S. Nath, and T. K. Maji, *Inorg. Chem.*, 2023**, 62,** 19312–19322.

48. W. Yang, H.J. Wang, R. R. Liu, J. W. Wang, C. Zhang, C. Li, D.C. Zhong, and T.B. Lu, *Angew. Chem. Int. Ed.*, 2021, **60**, 409-414.

49. Y.-L Dong, H.-R. Liu, S.-M. Wang, G. W. Guan, and Q.Y. Yang, *ACS Catal.*, 2023, **13**, 2547–2554.

50. S. Karmakar, S. Barman, F. A. Rahimi, and T. K. Majhi, *Energy Environ. Sci.,* 2021, **14**, 2429-2440.

51. H. Dong, X. Zhang, Y. Lu, Y. Yang, Y.P. Zhang, H.L. Tang, F.M. Zhang, Z.D. Yang, X. Sun, and Y. Feng, *Appl. Catal. B Environ.*, 2020, **276**, 119173.

52. J. Lin, Z. Pan, and X. Wang, *ACS Sustain Chem. Eng*., 2013, **2**, 353.

53. Y. Tamaki, K. Koike, and T. Morimoto, *J. Catal.*, 2013, **304**, 22.

54. M. Thanh, T. Thien, P. Du, N. Hung, and D. Khieu, *J. Porous Mater.*, 2018, **25**, 857–869.

55. J.-S. Qin, S. Yuan, L. Zhang, B. Li, D.-Y. Du, N. Huang, W. Guan, H. F.Drake, J. Pang, Y.-Q. Lan, A. Alsalme, and H.-C. Zhou, *J. Am. Chem. Soc.*, 2019, **141**, 2054.

56. A. D. Becke, *J. Chem. Phys.*, 1992, **96**, 2155.

57. C. Lee, W. Yang, and R. G. Parr, *Phys. Rev. B*, 1988, **37**, 785.

58. P. J. Hay, and W. R. Wadt, *J. Chem. Phys.*, 1985, **82**, 270.

59. M. J. Frisch, G. W. Trucks, H. B. Schlegel, G. E. Scuseria, M. A. Robb, J. R. Cheeseman, G. Scalmani, V. Barone, B. Mennucci, G. A. Petersson, H. Nakatsuji, M. Caricato, X. Li, H. P. Hratchian, A. F. Izmaylov, J. Bloino, G. Zheng, J. L. Sonnenberg, M. Hada, M. Ehara, K. Toyota, R. Fukuda, J. Hasegawa, M. Ishida, T. Nakajima, Y. Honda, O. Kitao, R. Nakai, T. Vreven, J. A. Montgomery Jr., J. E. Peralta, F. Ogliaro, M. J. Bearpark, J. J. Heyd, E. Brothers, K. N. Kudin, V. N. Staroverov, T. A. Keith, R. Kobayashi, J. Normand, K. Raghavachari, A. Rendell, J. C. Burant, S. S. Iyengar, J. Tomasi, M. Cossi, N. Rega, J. M. Millam, M. Klene, C. Adamo, R. Cammi, J. W. Ochterski, R. L. Martin, K. Morokuma, O. Farkas, J. B. Foresman, D. J. Fox, *Gaussian 16, Revision C.01*, Gaussian, Inc., Wallingford CT, 2016.

60. W. Yang, H. J. Wang, R. R. Liu, J. W. Wang, C. Zhang, C. Li, D. C. Zhong, and T. B. Lu, *Angew. Chem. Int. Ed.*, 2021, **60,** 409.

61. E. Karamian, and S. Sharifnia, *J. CO_2 Util.*, 2016, **16**, 194.

62. C. B. Hiragond, N. S. Powar, J. Lee, and S.-I. In, *Small*, 2022, **18**, 2201428.

63. M. Wang, J. Liu, C. Guo, X. Gao, C. Gong, Y. Wang, B. Liu, X. Li, G. G. Gurzadyana, and L. Sun, *J. Mater. Chem. A*, 2018, **6**, 4768.

64. T. Nakajima, Y. Tamaki, and K. Ueno, *J. Am. Chem. Soc*., 2016, **138**, 13818

Chapter 4

Molecularly Engineered MOF Photocatalyst For CO Production from Visible Light-driven CO_2 Reduction

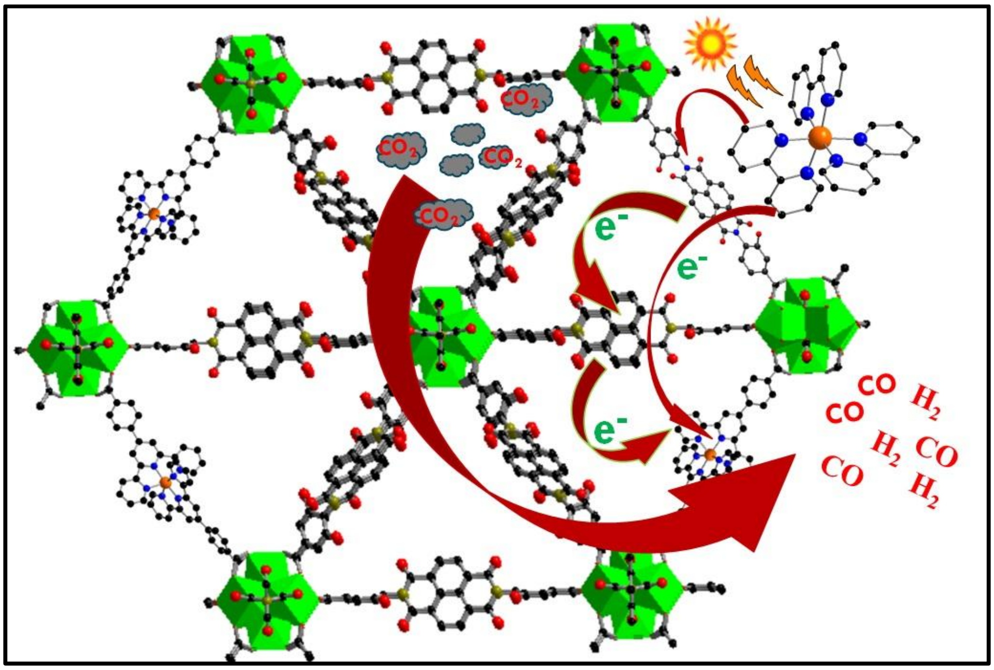

Paper published based on this work:

<u>A. Jana</u>, A. Maity, A. Adalder, S. Saha and A. Bhunia, *Nanoscale*, 2025,

4.1 Introduction

Utilizing clean and sustainable energy sources, especially the abundant solar energy, for the photocatalytic reduction of CO_2 to efficiently generate value-added chemicals and fuels such as CO, CH_4, HCOOH, CH_3OH, and C_2H_5OH holds promise in addressing environmental concerns and energy shortages.[1,2,3,4,5,6] The activity of a photocatalyst is controlled by the kinetics and thermodynamics of the catalyst such as light absorption, charge separation, charge migration and surface redox reaction. Therefore, significant efforts have been devoted towards the design and development of new potential photocatalysts for the efficient conversion of CO_2 through photocatalysis. Till now, various inorganic semiconductors catalysts have been investigated for their applicability in the photochemical transformation of CO_2 into carbon-based products.[7,8,9] However, these catalysts have some limitations, including deficient surface-active site densities, limited tailorability, wide band gap, low CO_2 adsorption capability, and unavoidable e^-/h^+ recombination phenomenon.[10,11] These shortcomings collectively contribute to the restricted photocatalytic efficiencies. On the other hand, since Lehn and his team first reported the photochemical reduction of CO_2 utilizing Re^I complexes as both photosensitizers and catalysts.[12] The utilization of molecular metal-based complexes in homogeneous photocatalytic CO_2 reduction has garnered significant attention due to their remarkable efficiency and selectivity in converting CO_2 to C1 feedstocks, specifically CO and formic acid.[13,14,15] However, despite their promising performance, these catalysts suffer from some drawbacks including difficulty in separating the catalyst from the reaction system and their lack of recyclability, as well as potential issues related to catalyst deactivation, hindering their large-scale industrial application.[16] Hence, it is highly desirable to design and synthesize a novel photocatalyst that is efficient, stable, and recyclable for CO_2 reduction.

A novel approach to overcome the drawbacks associated with both homogeneous and heterogeneous catalytic systems is by integrating their respective advantages to develop an efficient and versatile catalytic platform. This can be achieved by installation of homogeneous catalysts onto a solid support i.e., heterogeneous matrix to develop a hybrid heterogeneous catalytic system. In context to this, MOF has emerged as suitable solid support to heterogenized catalytically active centres for many important reactions.[17,18,19,20]

MOFs are gaining much attention as a promising catalytic material due to their exceptional attributes such as remarkable chemical stability, higher surface area, tunable pore structure, uniformity of active sites, diverse functionalities, easy modification, etc.[21,22,23,24] All these characteristics collectively establish MOF materials as an ideal class of host matrices for immobilizing molecular catalysts. The integration of the desired molecular catalyst into pre-synthesized MOFs can be effectively accomplished through a technique known as PSE, alternatively referred to as SALE.[25,26,27] This method has demonstrated significant efficacy in fabricating single-site MOF catalysts, particularly notable for their restricted accessibility when employing direct solvothermal approaches. Among various MOFs, Zr-MOFs family have regularly been applied in SALE due to its special chemical and thermal stability.[28,29,30] Therefore, we selected a Zr-based MOF (Zr-NDI-MOF) as heterogenous matrices, made up of naphthalene diimide (NDI) redox-active organic linker.[31] This framework offers the potential for facilitating charge transport to catalytic sites, enhancing efficiency in photocatalytic processes.

Metal complexes based on 2,2':6',2"-terpyridine (tpy) and its derivatives have emerged as effective molecular homogeneous catalysts for various energy-related applications.[32,33] Sato *et al*. demonstrated the efficacy of an IrIII complex, [Ir(tpy)(R-ppy)Cl], for photocatalytic CO2 reduction, indicating the potential of metal complexes in this process.[34] Similarly, ruthenium-polypyridyl complexes are known for their visible light absorption, high excited state lifetime, and potent oxidizing and reducing capabilities, making them ideal candidates for water splitting[35] and CO_2 reduction.[36,37] Another bis-terpyridine based Ru(II) complex, $[Ru(ttpy)_2]^{2+}$ (ttpy = 4′-p tolyl-2,2′:6′:2″-terpyridine) reported by Chao *et al*. in 2022 which exhibited a trace amount of CO in presence of $[Ru(bpy)_3]^{2+}$.[38] However, this complex with proper functionality can be heterogenized into a suitable porous support.[39] In this study, we have employed $[Ru(cptpy)_2]$ complex (cptpy= 4′-(4 carboxylphenyl)- 2.2′:6′,2″terpyridine)) to be heterogenized into the Zr-NDI MOF via SALE. As per the previous studies, the size of the linkers plays a crucial role in ensuring the successful SALE process. The size of $[Ru(cptpy)_2]$ (22.2 A) is nearly matched in length with the NDI linker. This similarity in size, combined with the synthetic accessibility of NDI, further supports the choice of the Zr-NDI MOF.

Based on these considerations, for the first time we have incorporated the $[Ru(cptpy)_2]$ complex into Zr-NDI MOF by substituting NDI linker through SALE process or mixed ligands solvothermal synthesis strategy to develop a robust mix ligand MOF, Zr-NDI@Ru-tpy or Zr-NDI@Ru-tpy-m respectively. The Zr NDI@Ru-tpy showed an enhanced photocatalytic activity towards CO_2 reduction, giving a CO production of 14698 μmol g^{-1} of CO and 606 μmol g^{-1} of H_2 in a 6 h reaction period in the presence of BIH and TEOA as the sacrificial electron donor and $[Ru(bpy)_3]^{2+}$ as photosensitizer in the DMF solvent system. The catalyst also exhibited high selectivity of ~97% towards CO production. On the other hand, the parent

MOF (Zr-NDI MOF) as a photocatalyst is totally inactive towards CO_2 reduction. In situ DRIFT spectroscopic studies indicate that Zr-NDI@Ru-tpy could adsorb and activate the CO_2, generating the key intermediate COOH* species during the photocatalysis. In addition to this, a comprehensive study on photophysical and electrochemical studies supported the proposed mechanism.

4.2 Experimental section

4.2.1 Materials

$ZrCl_4$ (99.99%), $RuCl_3 \cdot xH_2O$ (≥99.98), naphthalene-1,4,5,8-tetracarboxylic dianhydride (≥98.0%), 2-acetylpyridine, tetrabutylammonium hexafluorophosphate (n-Bu_4NPF_6, for electrochemical analysis, ≥99.0%), potassium hexafluorophosphate (KPF_6, ≥99.0%), 4-amino-3-hydroxybenzoic acid (97%), triethanolamine (TEOA), and fluorine-doped tin oxide (FTO) substrates (7 Ω/sq) were purchased from Sigma-Aldrich. $[Ru(bpy)_3]Cl_2 \cdot 6H_2O$ and 1,3-dimethyl-2-phenyl-2,3-dihydro-1H-benzo[d]imidazole (BIH) were purchased from BLD pharma. 4-methoxycarbonylbenzaldehyde (>98%) was purchased from TCI. Methanol (MeOH), dimethyl formamide (DMF), acetonitrile, glacial acetic acid was procured from Merck, India. All of the chemicals were commercially available and used without further purification.

4.2.2 Synthesis of 3-Hydroxy-2-[7-(4-carboxy-2-hydroxyphenyl)-1,3,6,8-tetraoxo-3,6,7,8-tetrahydro-1H-benzo[lmn][3,8] phenanthrolin-2-yl]benzoic acid (NDI)

NDI ligand has been synthesized following a reported procedure.[40] 4-amino-3-hydroxybenzoic acid (1.01 g, 6.6 mmol) and naphthalene-1,4,5,8-tetracarboxylic dianhydride (0.804g, 3 mmol) were charged in a round bottom flask in 20 mL DMF and the resulting dark red solution reflux overnight under argon atmosphere. The reaction mixture was cooled down to room temperature and 5 mL of 1M HCl solution was added to it and then the resulting solution was added to 250 mL of ice-cold water to get the desired product as a precipitate. The pale-yellow precipitate was collected by centrifugation, washed with 25 mL ethanol, 25 mL water, and 25 mL ether, and dried under a vacuum. ^1H NMR (400 MHz, DMSO-d_6) δ ppm: 7.5−7.60 (m, 6 H), 8.59−8.88 (s, 4 H), 10.17 (s, 2 H).

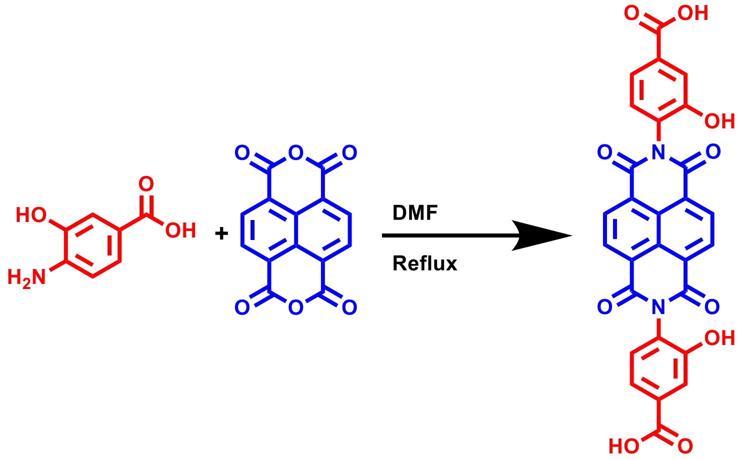

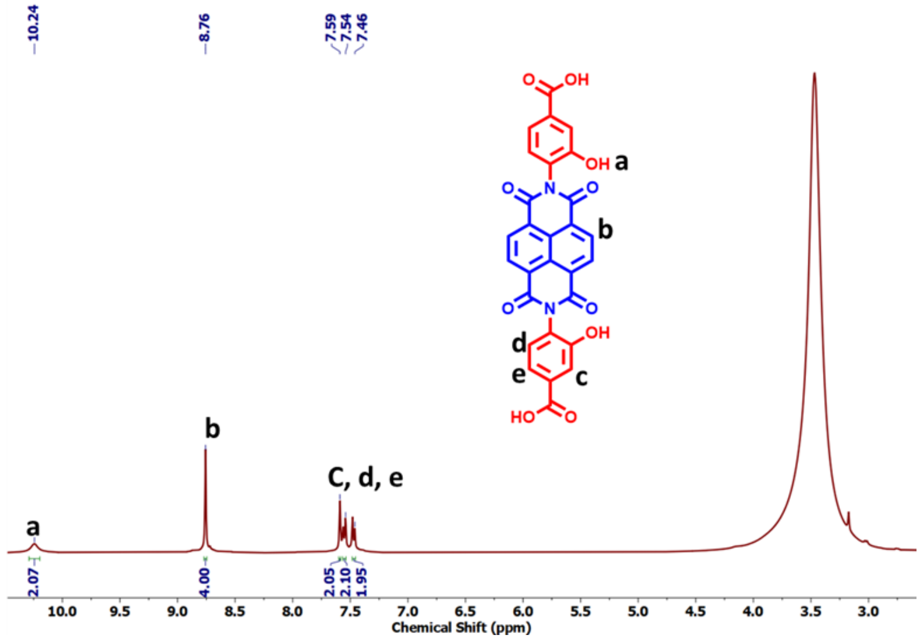

Figure 4.1: ^{1}H NMR spectrum of NDI linker.

4.2.3 Synthesis of ptpy-COOH (cptpy)

The ligand ptpy-OMe has been synthesized according to a reported procedure.[41] KOH (2.5g, 44 mmol), 4-methoxycarbonylbenzaldehyde (6.82 g, 42 mmol), and 2-acetylpyridine (9.2 mL, 82 mmol) were ground together for 15 minutes in a pestle and mortar to give a sticky yellow solid, which was left standing for 30 minutes, ground again and dispersed in water. The solid was collected by filtration, washed with water, and dried in air for 1 h. The off-white precipitate was dispersed in a suspension of ammonium acetate (16.0 g, 208 mmol) in ethanol (125 mL) and the mixture was stirred for 8 days at room temperature in a flask open to air and the resulting precipitate was isolated by filtration and recrystallized twice from hot ethanol to give ptpy-OMe as very pale-yellow fibers. ^{1}H NMR (400 MHz, $CDCl_3$) δ ppm: 8.79 (2H, s), 8.75 (2H, d), 8.70 (2H, d), 8.20 (2H, d), 8.00 (2 H, d), 7.93 (2H, dt), 7.41 (2H, t), 3.98 (3H, s). The ptpy-OMe ligand was mixed with 50% HCl solution under stirring. The resulting solution was refluxed overnight. The slightly brown precipitate was filtered off and washed with water and cold ethanol to get a pure product, ptpy-COOH (cptpy). ^{1}H NMR (400 MHz, DMSO-d_6) δ ppm: 8.94-8.96 (2H, d), 8.88-8.89 (4H, s), 8.34-8.37 (2H, t), 8.15 (4H, s), 7.79-7.82 (2H, t).

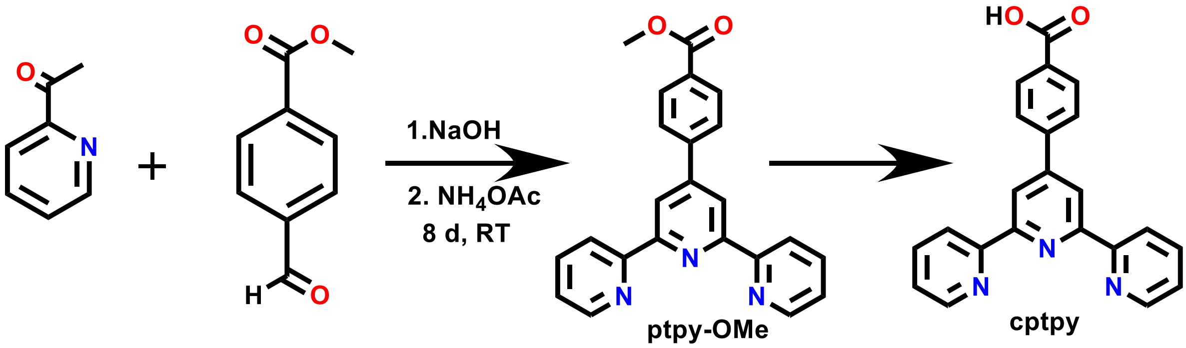

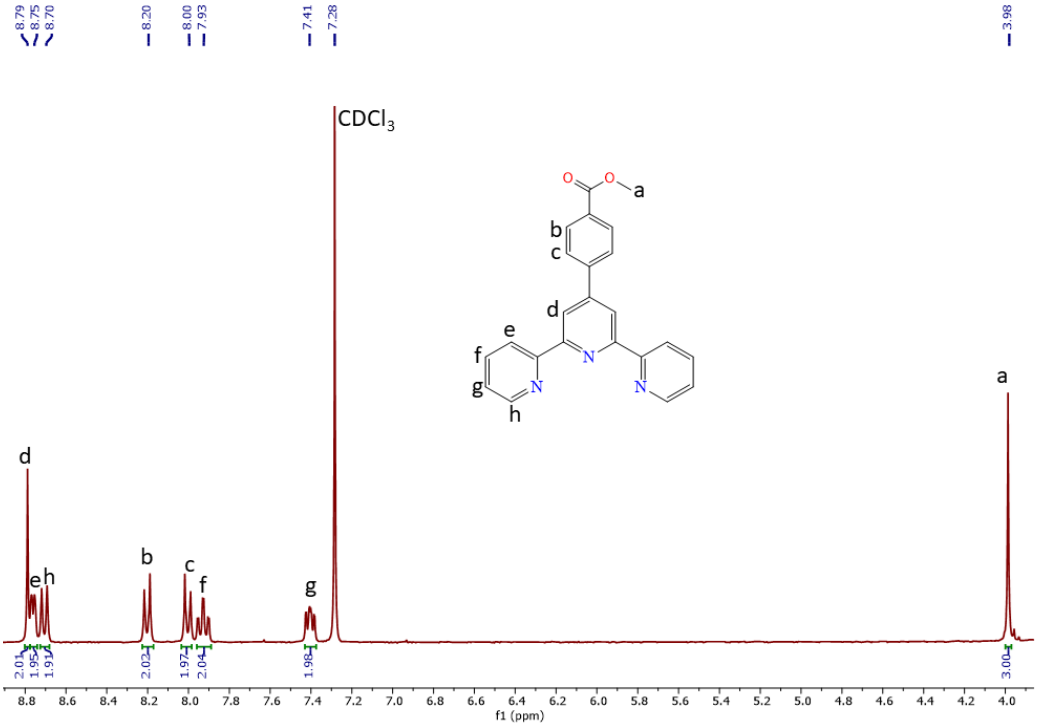

Figure 4.2: ^{1}H NMR spectrum of ptpy-OMe.

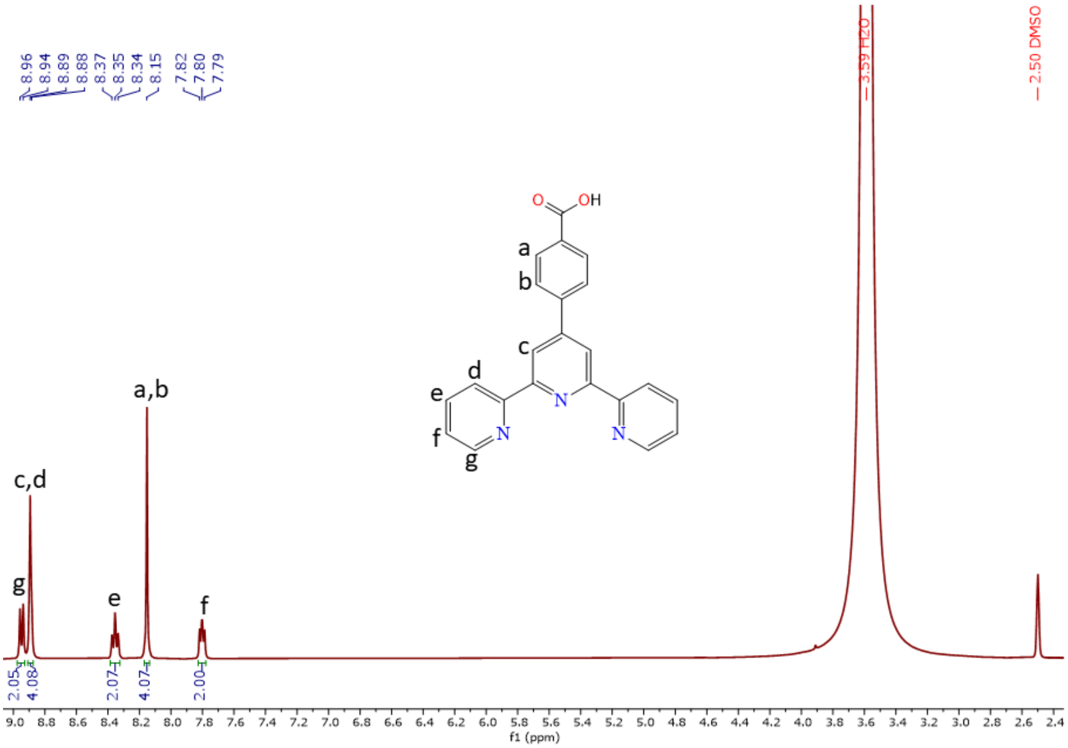

Figure 4.3: ^{1}H NMR spectrum of ptpy-COOH.

4.2.4 Synthesis of Preparation of [Ru(cptpy)$_2$]

This complex has been synthesized following a modified reported procedure.[42] The cptpy (0.8 mmol, 0.285 gm) and $RuCl_3.xH_2O$ (0.4 mmol, 0.0829) were added to 15 mL of ethylene glycol and heated the resulting solution overnight at 180°C in an argon atmosphere. Then the mixture was cooled down to room temperature and poured into 30 mL H_2O. After that 15 mL of saturated KPF_6 in methanol was added dropwise into the solution under stirring then let the solution to stir for 30 minutes. Then the orange precipitate was filtered off and washed with water and dried in vacuum. The resulted dark red solid was dissolved in 15 mL EtOH, 15 mL THF and 15 mL 3M NaOH. This solution was refluxed overnight and then the reaction mixture was allowed to stand to cool down to room temperature. Then this reaction mixture was adjusted to pH=1. The formed red precipitate was filtered off and washed with water. ^{1}H NMR (400 MHz, $CDCl_3$) δ ppm: 9.57 (2H, s), 9.14-9.16 (2H, d), 8.57-8.59 (2H, d), 8.30-8.32 (2H, d), 8.07-8.11 (2H, t), 7.57-7.58 (2H, d), 7.28-7.32 (2H, t).

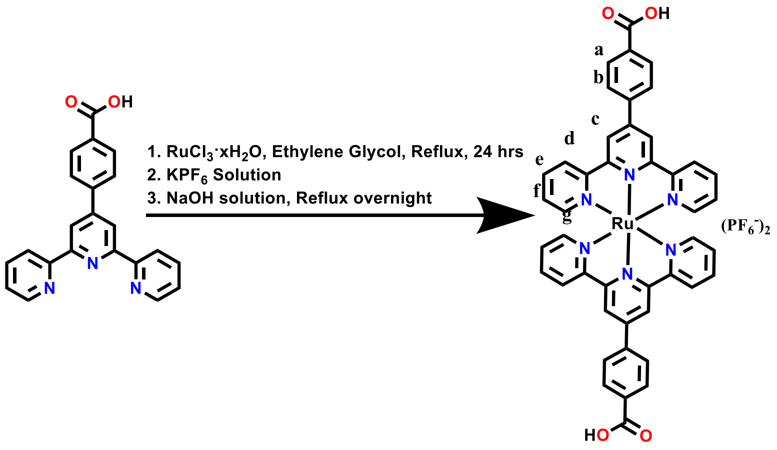

[Ru(cptpy)$_2$]

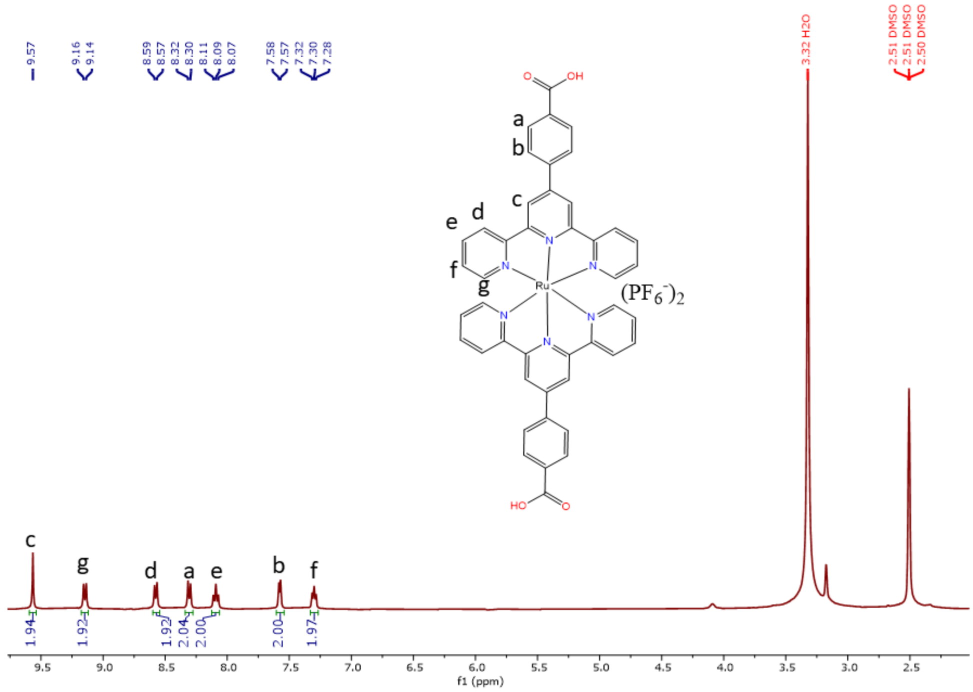

Figure 4.4: ^{1}H NMR spectrum of [Ru(cptpy)$_2$].

4.2.5 Synthesis of [Ru(tpy)$_2$]

The preparation of [Ru(tpy)$_2$] was carried out by modifying a previouly reported procedure.[43] The tpy (0.4 mmol, 0.0933g), $RuCl_3 \cdot xH_2O$ (0.2 mmol, 0.041 g) along with $AgNO_3$ (0.6 mmol, 0.102 g) was refluxed for 24 h using 100 mL of ethanol solvent. The solution was then filtered over celite to remove the AgCl precipitate. The filtrate was collected and dried. Then the resulting product was dissolved in 15 mL of acetonitrile. A small amount of KPF_6 (4 - 5 mg) was added and the solution was filtered again and dried off. Finally, the product was dissolved in 20 mL of DCM, filtered, and dried. It was then eluted using a DCM/MeOH mixture containing a pinch of KPF_6. ^1H NMR (300 MHz, DMSO-d_6) δ ppm: 9.10 (d, 4H), 8.84 (d, 4H), 8.55 (t, 2H), 8.03 (td, 4H), 7.48 – 7.39 (m, 4H), 7.27 (ddd, 4H).

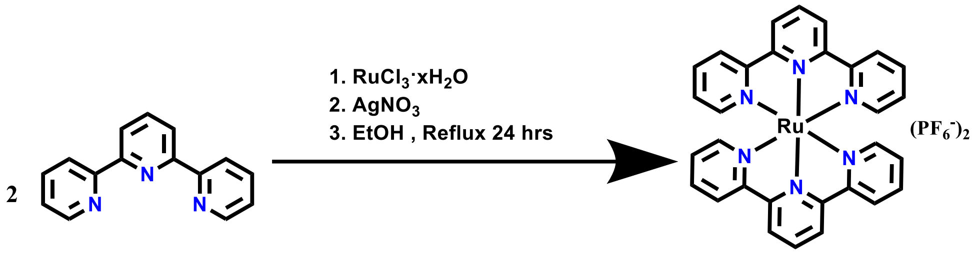

[Ru(tpy)$_2$]

4.2.6 Synthesis of Zr-NDI MOF

Zr-NDI MOF has been synthesized by using $ZrCl_4$ (82 mg, 0.35 mmol), NDI ligand (177.3 mg, 0.35 mmol), and 0.602 mL (10.5 mmol) of glacial acetic acid in 4 mL of DMF.[40] After 10 minutes of sonication, the reaction mixture in autoclave was placed in a preheated 120 °C oven for 72 h. After cooling down the reaction mixture to room temperature, the yellow precipitate product was centrifuged off and washed three times with DMF and then the precipitate was incubated in MeOH for solvent exchange. At last, the Zr-NDI MOF was activated at 85°C for 12 h.

4.2.7 Synthesis of Zr-NDI@Ru-tpy via SALE

[Ru(cptpy)$_2$] complex was incorporated in Zr-NDI-MOF via solvent assisted ligand exchange (SALE). [Ru(cptpy)$_2$] (30 mg) was immersed in 4 mL DMF solvent. The red solution was added to solid Zr-NDI MOF (15 mg). Then, the resulting mixture was placed in oven at 100 °C temperature for 5 days. The ligand exchange MOF was centrifuged and washed with DMF extensively until the supernatant was colorless and then the resulting formed MOF was soaked in DMF for 3 days. Then the MOF was exchanged with fresh MeOH three times daily for three consecutive days. Then the MOF was activated at 85 °C for 12 h.

4.2.8 Synthesis of Zr-NDI@Ru-tpy-m via mixed ligand solvothermal method

The mixed linker MOF, Zr-NDI@Ru-tpy-m was prepared through direct solvothermal method by following the same experimental procedure as that for Zr-NDI MOF.[40] For this mixed linker MOF synthesis, $ZrCl_4$ (21 mg), NDI ligand (44 mg), $Ru(cptpy)_2$ (24 mg), glacial acetic acid (0.150 mL) and 1 mL DMF were added to autoclave. The autoclave was placed in the preheated oven at 120 °C for 72 h. The red precipitate was collected by centrifugation and washed with DMF and MeOH. The final product was activated under vacuum at 85 °C for 12 h.

4.2.9 Digestion, ^1H NMR and ligand exchange (%) for Zr-NDI@Ru-tpy

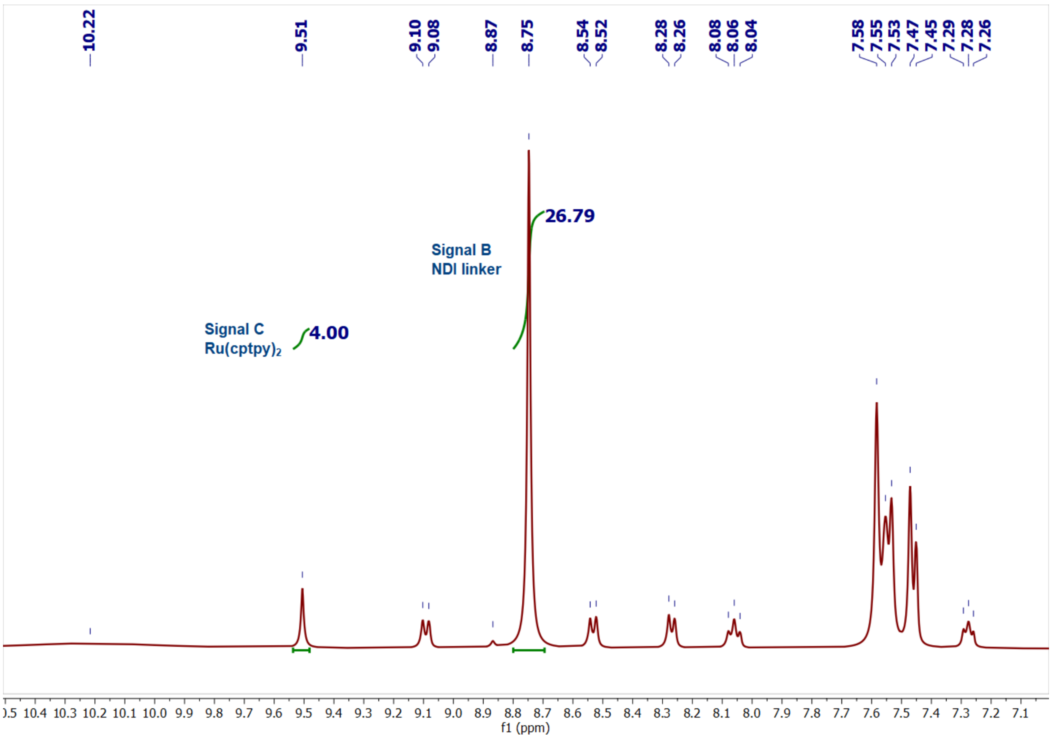

Figure 4.5: ^1H NMR spectra of digested Zr-NDI@Ru-tpy.

The percentage of linker incorporation into the Zr-NDI MOF was determined through ^1H NMR analysis of the digested MOF in a solution of 590 µL DMSO-d_6 and 10 µL of 40% HF. The analysis revealed that approximately 15% of $Ru(cptpy)_2$ was incorporated into the MOF. This percentage was calculated using the integrals of specific signals corresponding to the two linkers. For the NDI linker, the protons on the naphthalene core (signal B) at around 8.75 ppm were chosen. For the $[Ru(cptpy)_2]$ linker, the terpyridine group protons (signal C) at 9.5 ppm were selected, as these signals do not overlap, are easily identifiable, and distinguishable (Figure S6). The integrals of these signals were normalized by dividing by their respective number of protons, consistent with those in the free linker, as shown in equation 1 of the acetic acid modulated MOF. This normalization process provided the percentage of each linker present within the MOF.

$$\frac{Integral\ (4)}{Corresponding\ protons\ (4)} = 1$$

$$\frac{Integral\ (26.97)}{Corresponding\ protons\ (4)} = 6.74$$

$$\frac{1}{6.74} \times 100 \ = 14.83\ \%$$

4.2.10 Digestion, ^{1}H NMR and ligand exchange (%) for Zr-NDI@Ru-tpy-m (prepared via mixed ligands solvothermal method)

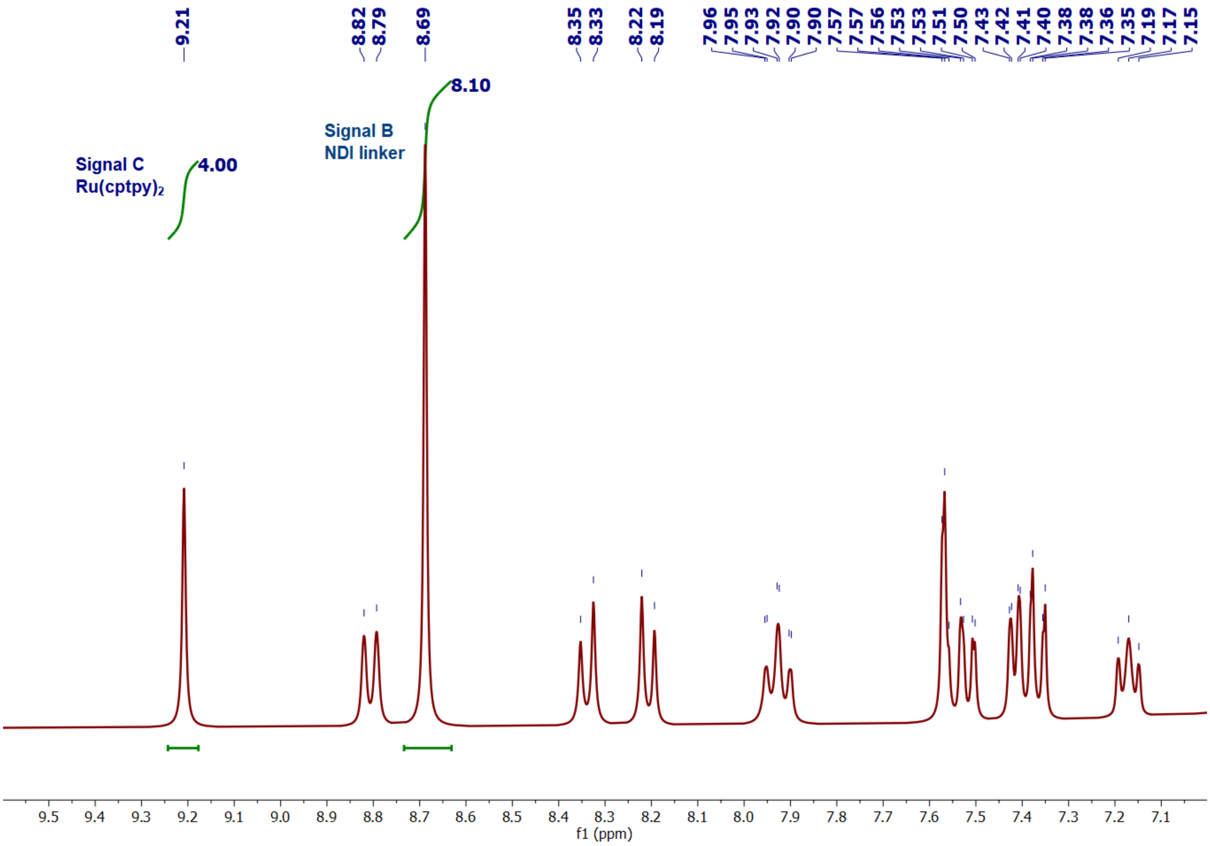

Figure 4.6: ^{1}H NMR spectra of digested Zr-NDI@Ru-tpy-m (prepared by mixed ligand solvothermal method).

Similarly, we have also calculated the percentage of [Ru(cptpy)$_2$] incorporated in the Zr-NDI@Ru-tpy-m, obtained by mixed ligand solvothermal method. We have found approximately 50% of [Ru(cptpy)$_2$] in the mixed linker MOF.

$$\frac{Integral\ (4)}{Corresponding\ protons\ (4)} = 1$$

$$\frac{Integral\ (8.10)}{Corresponding\ protons\ (4)} = 2.025$$

$$\frac{1}{2.0254} \times 100\ = 49.38\ \%$$

4.2.11 Apparent Quantum Efficiency Calculation:

Apparent quantum efficiency (AQE) is defined as the following equation

$$\text{AQE} = \frac{Number\ of\ reacted\ electrons}{Number\ of\ incident\ photons} \times 100$$

Two electrons are required to convert CO_2 to CO. So, AQE for CO can be calculated using the following equation

$$\text{AQE} = \frac{2 \times the\ number\ of\ evolved\ CO\ molecules}{the\ number\ of\ incident\ photons} \times 100 \text{ ………. equation 1}$$

Below, we described the AQE determination at 420 nm for Zr-NDI@Ru-tpy.

1) The amounts of CO produced were measured by applying a 420 nm band-pass filter for 6 hours. The amounts of CO evolved in 6 hours were 14.69 μmol.
2) The average intensity of irradiation after the 420 nm band pass filter was determined to be 34.13 Mw cm^{-1} at room temperature.
3) The irradiation area was determined to be 3.14 cm^2.
4) The number of incident photons (N) is 4.89 × 10^{21} as calculated below:

$$N = \frac{AE\lambda}{hc} = \frac{3.14 \times 34.13 \times 10^{-3} \times 3600 \times 6 \times 420 \times 10^{-9}}{6.626 \times 10^{-34} \times 3 \times 10^{8}}$$

$$= 4.89 \times 10^{21}$$

5) The AQE for CO was calculated based on equation 1

$$\text{AQE} = \frac{2 \times the\ number\ of\ evolved\ CO\ molecules}{the\ number\ of\ incident\ photons} \times 100$$

$$= \frac{2 \times N_A \times [CO]}{N} \times 100$$

$$= \frac{2 \times 14.69 \times 10^{-6} \times 6.02 \times 10^{23}}{4.89 \times 10^{21}} \times 100 = 0.362\ \%$$

Therefore, the total AQE of Zr-NDI@Ru-tpy at 420 nm was 0.362 %.

Where:

N is the number of incident photons

E is the total incident energy on the photocatalyst (J)

A is the irradiation area

λ is the light wavelength (m)

h is Planck's constant (J s)

c is the speed of light (m s^{-1})

N_A is Avogadro's number (mol^{-1})

[CO] the amounts of CO (mol), after 6 hours.

4.2.12 Characterization methods

The Fourier transform–infrared (FT–IR) spectra of Zr-NDI and Zr-NDI@Ru-tpy were collected on a Bruker FTIR 4000 instrument equipped with a zinc selenide (ZnSe) ATR. The powder X-ray diffraction (PXRD) data of Zr-NDI, Zr-NDI@Ru-tpy and Zr-NDI@Ru-tpy-m were collected with Bruker D8 Advance X-ray diffractometer (XRD) at room temperature using Cu K_α radiation (λ = 1.548 Å) in a 2 θ range of 3–55°. Thermogravimetric analyses (TGA) were done at a ramp rate of 10 °C min^{-1} under nitrogen with Perkin Elmer Pyris Diamond TG–DTA instruments. UV absorption spectra for $[Ru(cptpy)_2]$ dissolved in DMF solvent, were recorded using a Cary 60 UV–vis (Agilent Technologies) with a 1 cm path-length quartz cell. The solid-state UV/Vis spectra of Zr-NDI MOF and Zr-NDI@Ru-tpy were measured using Lamda 750, Make perkin elmer. Fluorescence emission spectra were collected on a HORIBA Fluoromax-4 fluorometer. Nitrogen gas adsorption–desorption of the samples was performed to obtain BET-specific surface area (S_{BET}) using Quanta chrome Autosorb iQ2 Instruments at liquid N_2 temperature (77 K). The samples were degassed under a high vacuum (10^{-6} torr) at 85 °C for 10 h. After degassing, the sample tube was then transferred to the analysis port of the sorption analyzer. Pore size distribution was calculated by non-local density functional theory (NLDFT) using the ‘carbon slit pore’ model. ^{1}H NMR spectra were measured on Bruker Ascend 400 instruments at room temperature in $CDCl_3$ and DMSO-d_6. Field emission scanning electron microscope (FE-SEM) images were obtained using a Carl Zeiss SUPRA 55VP FE-SEM instrument. Energy dispersive X-ray spectroscopy (EDS) was performed by Oxford Instruments X-Max with INCA software coupled to the FE-SEM. The Hitachi, S-4800, EDS detector was introduced to analyze the morphology and EDS of the samples. X-ray photoelectron spectroscopy (XPS) measurement was conducted by the Thermo Fisher ESCALAB Xi+ microProbe instrument with a monochromatic Al-Kα target, 1486.6 eV energy, and a maximum power of 15.0 kW. Inductively coupled plasma optical emission spectrometry (ICP-OES) results were obtained by the Perkin Elmer Optima 8000. After the photocatalysis, gaseous and liquid products were analyzed. The gaseous products were analyzed and quantified using TCD and FID detector in High-performance gas chromatography (Agilent 8860). GC was calibrated with known standard for H_2, CO and CH_4. Liquid products were analysed on a Metrohm Eco IC and ^{1}H NMR. Concentration of formate ion was quantified using ion chromatography technique (Eco IC Metrohm). The gaseous products from isotope labelling experiment were detected using gas chromatography by MS detector (Perkin Elmer clarus 690).

General procedure of photocatalytic CO_2 reduction

As reported previously[44,45] the photocatalytic reactions were conducted with a 300 W Xe lamp with a 420 nm cut-off filter. In a typical photocatalytic process, 1 mg of catalysts, BIH (12 mg) and $[Ru(bpy)_3]Cl_2\cdot 6H_2O$ (12 mg) was dispersed into the solution of 3.0 mL DMF solution containing 1 mL TEOA in a quartz vial. Before photocatalytic testing, the reaction solution was degassed with N_2 gas for 20 minutes followed by bubbling with CO_2 (99.999%, Airgas) in the dark for 30 minutes. The reaction solution was then irradiated with 300 W Xe light source equipped with $\lambda > 420$ nm at room temperature with stirring for photocatalytic CO_2 reduction. The headspace above the reaction solution was taken using a gas-tight syringe at different time intervals for product analysis using an Agilent 8860 equipped with a TCD and FID detector and a 60/80 Carboxen-1000 packed column (Supelco). Liquid products were analysed using ion chromatography and ^{1}H NMR. Control experiments were conducted in the absence of light irradiation, photosensitizer, catalyst, sacrificial reagent, and CO_2.

Isotope-labelled experiments

1 mg of catalyst, BIH (12 mg) and $[Ru(bpy)_3]Cl_2 \cdot 6H_2O$ (12 mg) was dispersed into the solution of 3.0 mL DMF solution containing 1 mL TEOA in a quartz vial. Before photocatalytic testing, the reaction solution was degassed with Ar gas for 20 minutes followed by bubbling with $^{13}CO_2$ for a very short time of 120 seconds only because of its high cost. The reaction solution was then illuminated with a 300 W Xe lamp. The obtained gaseous products were analysed by gas chromatography−mass spectrometry (GC-MS).

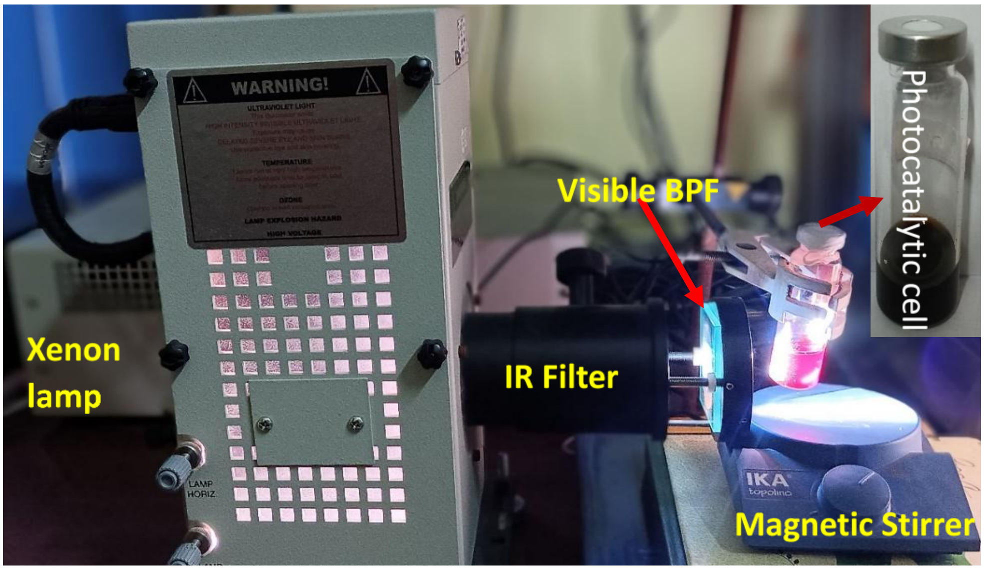

Figure 4.7: Setup for photocatalysis under laboratory condition in presence of Zr-NDI@Ru-tpy.

In Situ DRIFT Studies:

In situ diffuse reflectance Fourier Transform Infrared (FTIR) spectroscopy was employed to investigate the photocatalytic reactions of Zr-NDI@Ru-tpy catalysts. The experiments were conducted using a BRUKER Vertex 70V IR spectrometer equipped with a mercury cadmium telluride (MCT) detector for enhanced sensitivity. A slurry consisting of 3 mg of Zr-NDI@Ru-tpy catalyst and 5 mg of BIH in DMF solvent was uniformly coated onto a glass slide, followed by the addition of a few drops of TEOA. The prepared sample was then placed at the center of the reaction cell. A high-vacuum pump was used to evacuate all gasses from the reaction cell, after which pure CO_2 (99.99%) was introduced into the reactor for 15 minutes. Finally, the catalyst was exposed to visible light, and in-situ FTIR spectra were collected at regular intervals using the MCT detector to monitor the photocatalytic process.

Electrochemical characterization

The Mott-Schottky analysis and impedance measurement were conducted using CHI760E workstation (CHI Instruments, USA) through a conventional three-electrode system immersed in a 0.1 M TBAF DMF solution.

Mott-Schottky measurement[46]

2.5 mg of respective MOF materials were dispersed in a solution of 250 µL water, 250 µL isopropyl alcohol (IPA), and 10 µL of Nafion to prepare a homogenous slurry. Subsequently, the final slurry was coated on a glassy carbon electrode and then dried at room temperature. The Ag/AgCl electrode was employed as the reference electrode, and the platinum plate was used as the counter electrode. The measurements were carried out under frequencies of 0.5, 1, and 1.5 kHz (from -1.5 V to +1.5 V). The curve was plotted using Eq. 1.

$1/C^2 = (2/\ \varepsilon\ \varepsilon_0\ A^2\ e\ N_D)\ (V - V_{fb} - k_B T/e)$ ------------------Eq.1

Where, C and A are the interfacial capacitance and area, respectively. The ε, ε_0, k_B, T, e, N_D and V are the dielectric constant of the semiconductor, permittivity of free space, Boltzmann constant, absolute temperature, electronic charge, number of donors and applied voltage, respectively. A plot of $1/C^2$ against V should yield a straight line from which V_{fb} can be determined from the intercept on the V axis.

Calculation of Conduction Band (E_{CB}) and Valance Band (E_{VB}) w.r.t. NHE:

The conduction band (E_{CB}) potentials for Zr-NDI@Ru-tpy is calculated by equation 2.

E_{CB} (NHE)= V_{fb} --------------------------------------Eq. 2

The valance band (E_{VB}) position was calculated by using equation 3.

$E_{VB} = E_{CB}$ + Band Gap-------------------------Eq. 3

Preparation of working electrode for impedance measurement

2.5 mg of respective MOF materials were dispersed in a solution of 250 μL water, 250 μL isopropyl alcohol (IPA), and 10 μL of Nafion to prepare a homogenous slurry. Subsequently, the final slurry was coated on a glassy carbon electrode and then dried at room temperature. The Ag/AgCl electrode was employed as the reference electrode, and the platinum plate was used as the counter electrode. A 0.1 M TBAF DMF solution was used as an electrolyte. The measurements were carried out with a bias potential of 0.4 V with a frequency range (10^{-2} to 10^{5} Hz) under a nitrogen atmosphere.

Preparation of working electrode for transient photocurrent

2.5 mg of respective MOF material was dispersed in a solution of 250 μL water, 250 μL isopropyl alcohol (IPA), and 10 μL of Nafion to prepare a homogenous slurry. Subsequently, the final slurry was coated on an FTO glass plate (1 cm × 1 cm) and then dried at room temperature. The Ag/AgCl electrode was employed as the reference electrode, and the platinum plate was used as the counter electrode, respectively. The transient photocurrent responses were carried out under visible-light irradiation conditions (300 W Xenon arc lamp).

4.3 Result and Discussion

4.3.1 Characterization of the synthesized MOFs

In 2018, Ott and co-workers reported the preparation of the NDI linker (length ∼19.5 Å) containing UiO-type framework [Zr(dcphOH-NDI)] which has similar structural topology to Zr-L6 (where, L_6 (length 20.5 Å) = 4,4′-[1,4-naphthalenebis(ethyne 2,1-diyl)]dibenzoate)) MOF.[31,47] As observed previously, Zr(dcphOH-NDI), termed as Zr-NDI, adopts a 12-c fcu net with 2 fold interpenetration. It consists of $[Zr_6(\mu_3\text{-}O)_4(\mu_3\text{-}OH)_4]$ secondary building unit (SBU) and NDI linker.[31] The donor acceptor hydrogen bonding and rigidity of the NDI linker facilitates the high chemical stability and high porosity of the MOF material, which is essential in catalysis.[48] To use this MOF in catalysis, we have installed the $[Ru(cptpy)_2]$ moiety into the Zr-NDI MOF. However, we first attempted to synthesize the $[Ru(cptpy)_2]$ complex (length ∼22.2 Å; cptpy= 4′-(4 carboxylphenyl)- 2.2′:6′,2″terpyridine)) based UiO –family MOFs with porous interpenetrated Zr−organic frameworks (PIZOFs) topology. Since, we were unable to make PIZOFs MOFs, therefore, we were motivated to explore ligand exchange strategy of Zr(dcphOH-NDI) and mixed ligand in-situ solvothermal synthesis. The photocatalyst Zr-NDI@Ru-tpy was prepared via well-known PSLE between UiO-type MOF, [Zr(dcphOH-NDI)] (Zr-NDI) and [Ru(cptpy)2].[19] The [Ru(cptpy)$_2$] complex was incorporated into the Zr-NDI framework using SALE method, as shown in Figure 4.8 (see more details of both the linkers (NDI, Ru(cptpy)$_2$ and Ru(tpy)$_2$), ^{1}H NMR data in Figure 4.1- 4.4). The best exchange results were observed using DMF as solvent at 100 °C for 5 days.

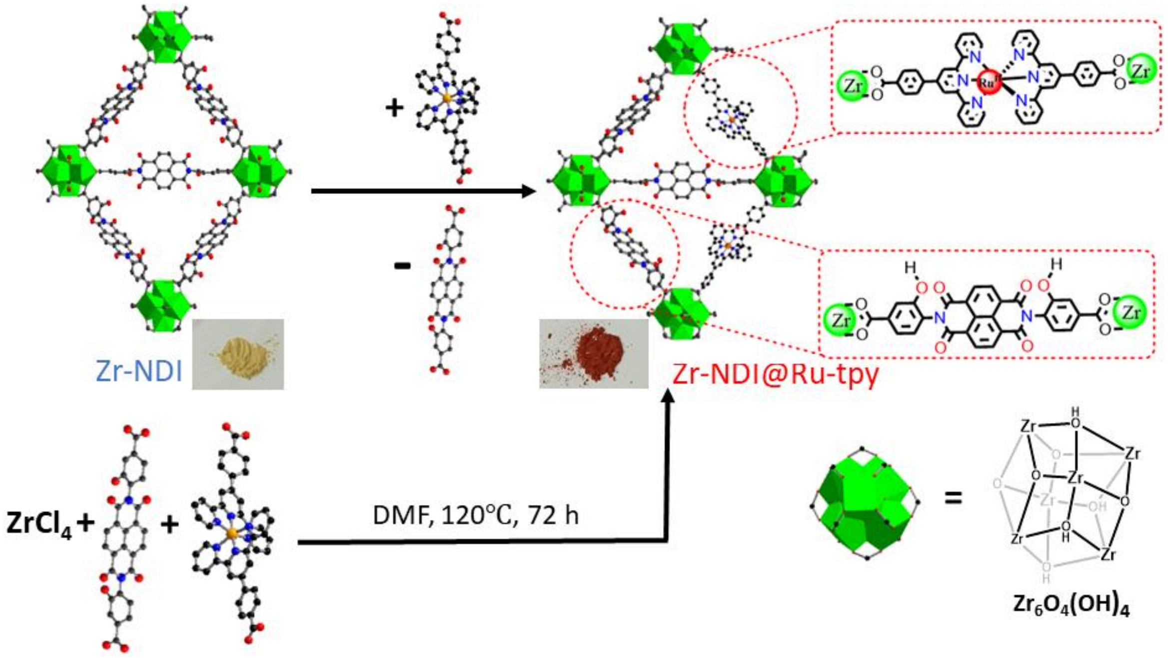

Figure 4.8: Schematic representation for synthesis of Zr-NDI@Ru-tpy or Zr-NDI@Ru-tpy-m using SALE or mixed ligand solvothermal strategy, respectively.

The final product of the linker exchange process, Zr-NDI@Ru tpy, was isolated as reddish microcrystalline powder after washing extensively with fresh DMF followed by activation under vacuum. This visually reddish appearance from pale yellow colour further indicated the incorporation of [Ru(cptpy)$_2$] into the the Zr-NDI MOF (Figure 4.8). We have also assisted the successful incorporation of [Ru(cptpy)$_2$] via SALE process by performing control experiments with [Ru(tpy)$_2$] (tpy= 2,2':6',2"-terpyridine) having no coordinating carboxylate groups on the terpyridine ligand. We have immersed the Zr-NDI MOF into the [Ru(tpy)$_2$] solution applying identical reaction condition, showing no substantial incorporation of [Ru(tpy)$_2$] after extensive washing with DMF and MeOH (Figure 4.9). The absence of NMR peaks corresponding to the [Ru(tpy)$_2$] in the 1H NMR spectrum of the digested Zr-NDI MOF signified that the [Ru(cptpy)$_2$] complex was coordinated into the Zr-NDI MOF through SALE method rather than getting trapped within the MOF pores (Figure 4.9).

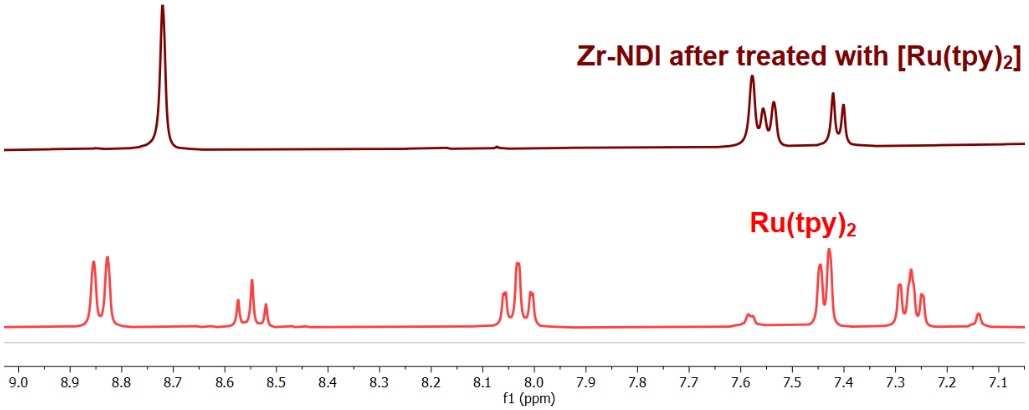

Figure 4.9: ^{1}H NMR of [Ru(tpy)$_2$] and digested Zr-NDI MOF (after treating with [Ru(tpy)$_2$]).

The powder X-ray diffraction (PXRD) characterizations were performed to analyze the crystalline phase of the synthesized Zr-NDI and Zr-NDI@Ru-tpy (Figure 4.10a). The PXRD patterns before and after SALE confirmed the preservation of crystallinity as well as gross structure of the framework. The successful SALE in the MOF has further confirmed by ^{1}H NMR characterization. For this analysis, Zr-NDI@Ru-tpy was digested in DMSO-d$_6$/HF solution. The ^{1}H NMR spectroscopic analysis provided detailed insights into the structure of the digested Zr-NDI@Ru-tpy MOF. It exhibited all the corresponding protons of NDI linker and the [Ru(cptpy)$_2$] complex (Fig. 4.10b). The protons of the naphthalene core and the phenyl ring of the NDI linker exhibited peaks at 8.75 ppm and 7.58-7.45 ppm, respectively. Additionally, a peak corresponding to the phenolic protons of the NDI linker was observed at 10.22 ppm. The protons of the terpyridine core in the [Ru(cptpy)$_2$] complex showed chemical shifts at 9.51 ppm, 9.10-9.08 ppm, 8.52-8.54 ppm, 8.04-8.08 ppm and 7.26-7.29 ppm. Furthermore, the protons of the phenyl ring of the [Ru(cptpy)$_2$] complex appeared at 8.26-8.28 ppm (Figure 4.5). These results confirmed the successful incorporation of the [Ru(cptpy)$_2$] complex into the Zr-NDI framework.

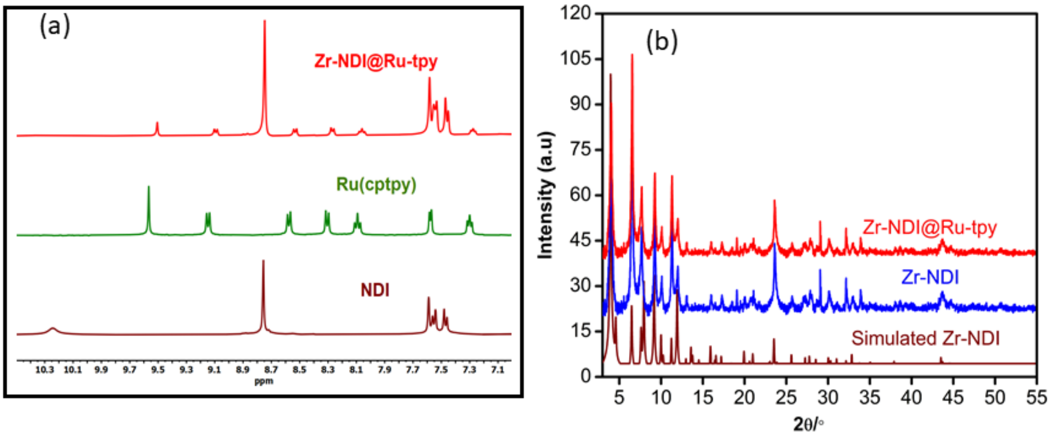

Figure 4.10: (a) PXRD pattern of Simulated Zr-NDI MOF,[48] Zr-NDI and Zr-NDI@Ru-tpy. (b) ^{1}H NMR spectra of NDI linker, [Ru(cptpy)$_2$] complex and digested Zr-NDI@Ru-tpy.

The percentage of ligand incorporation was calculated through the proton resonance integrals of the NDI linker and the [Ru(cptpy)$_2$] complex in the digested Zr-NDI@Ru-tpy, indicating that approximately ~15% of the [Ru(cptpy)$_2$] complex was incorporated into the MOF framework (see details in section 4.2.9). The FTIR spectroscopy of the Zr-NDI MOF and Zr-NDI@Ru-tpy showed substantial agreement, with no significant changes in band positions. This indicated that the bonding environment and molecular structure of the Zr-NDI MOF were retained after post-synthetic modification. Notably, we observed peaks around 1630 cm^{-1} and 1710 cm^{-1} corresponding to C=O stretching, and a broad peak centered at 3325 cm–^{1} indicative of the presence of -OH groups (Figure 4.11a). Further, we have studied the thermogravimetric analysis (TGA) of Zr-NDI and Zr-NDI@Ru tpy which showed thermal stability upto 450 ℃ for both the materials (Figure 4.11b). However, an initial weight loss of approximately 8% was observed in the TGA profile up to 100 ℃, which can be ascribed to the removal of the solvent molecule trapped in the pore of the framework.

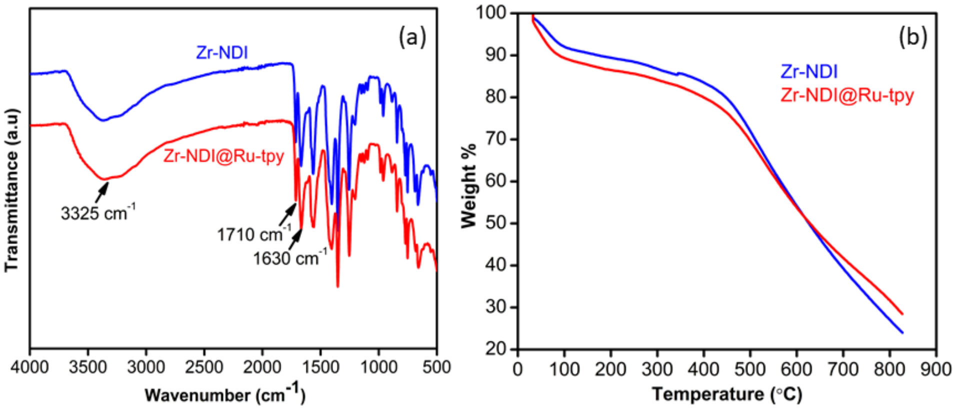

Figure 4.11: (a) FT-IR spectra of Zr-NDI and Zr-NDI@Ru-tpy. (b) TGA analysis of Zr-NDI and Zr-NDI@Ru-tpy.

The N_2 adsorption-desorption isotherm analysis of activated Zr-NDI@Ru-tpy revealed a BET surface area of 1016 m^2 g^{-1}, which closely aligned with the BET surface area of pristine Zr NDI (1340 m^2 g^{-1}) (Figure 4.12b). Additionally, the pore size distribution for both the pristine MOF and the $[Ru(cptpy)_2]$ incorporated MOF revealed identical pore diameters (Fig. 4.12c).

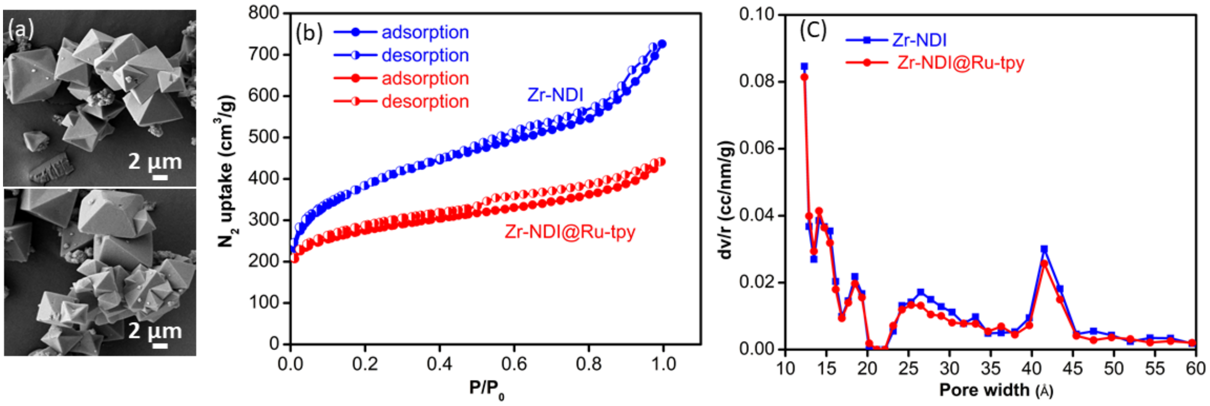

Figure 4.12: (a) SEM image of Zr-NDI (top) and Zr-NDI@Ru-tpy (bottom). (b) N_2 adsorption-desorption isotherm of Zr-NDI and Zr-NDI@Ru-tpy measured at 77 K. (c) Pore size distribution of Zr-NDI and Zr-NDI@Ru-tpy.

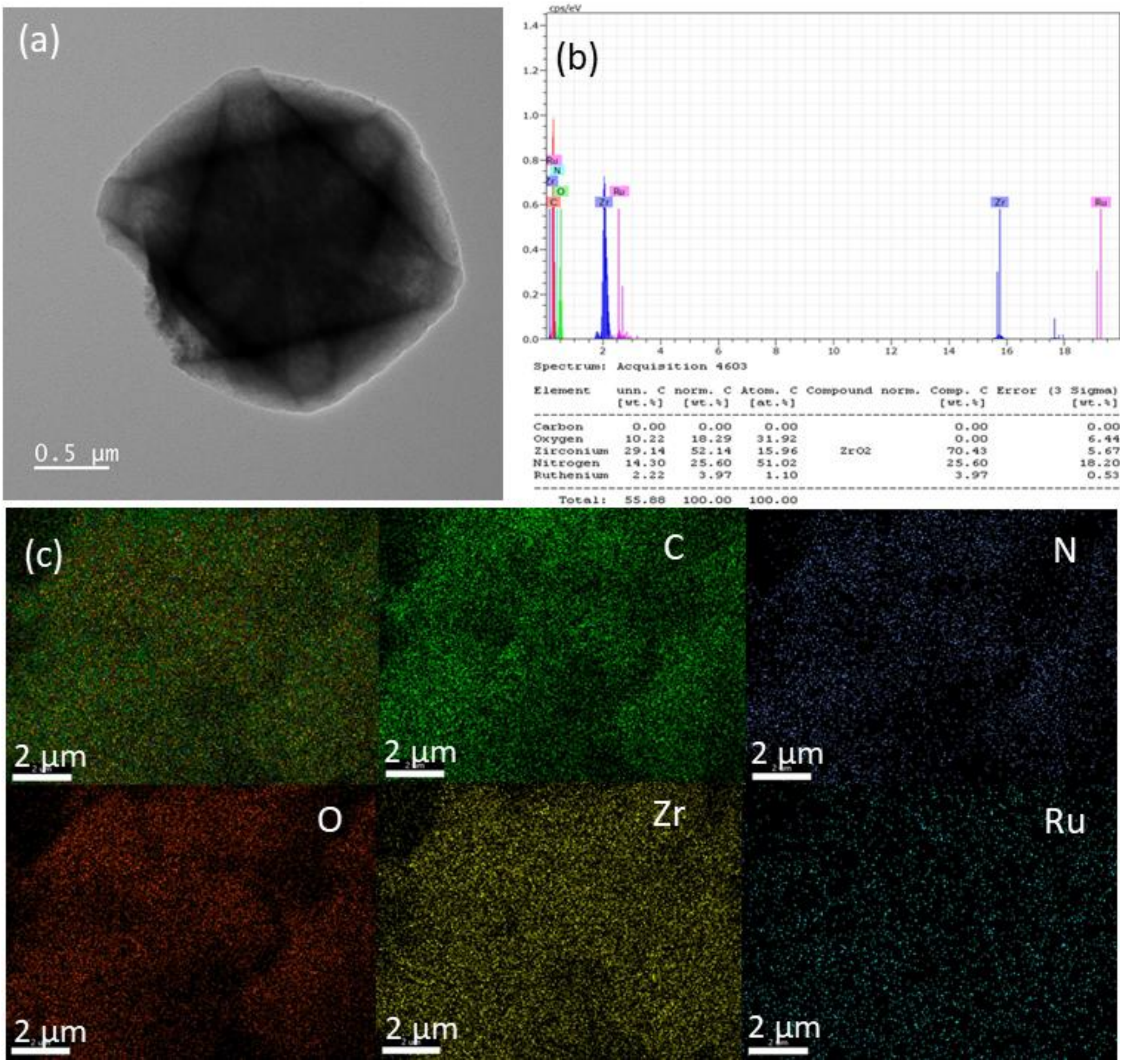

```
Spectrum: Acquisition 4603

Element     unn. C  norm. C  Atom. C  Compound norm.  Comp. C  Error (3 Sigma)
            [wt.%]  [wt.%]   [at.%]                   [wt.%]            [wt.%]
-------------------------------------------------------------------------------
Carbon       0.00    0.00     0.00                      0.00              0.00
Oxygen      10.22   18.29    31.92                      0.00              6.44
Zirconium   29.14   52.14    15.96       ZrO2          70.43              5.67
Nitrogen    14.30   25.60    51.02                     25.60             18.20
Ruthenium    2.22    3.97     1.10                      3.97              0.53
-------------------------------------------------------------------------------
   Total:   55.88  100.00   100.00
```

Figure 4.13: (a) TEM image of Zr-NDI@Ru-tpy (b) SEM-EDX profile and (c) elemental mapping of Zr-NDI@Ru-tpy.

The field emission scanning microscopy (FE-SEM) images depicted that Zr-NDI@Ru-tpy maintained an identical morphology to pristine Zr-NDI (Figure 12a (top, Zr-NDI; bottom, Zr NDI@Ru-tpy)).

Additionally, the morphology of Zr-NDI@Ru-tpy was investigated using transmission electron microscopy (TEM), which revealed well-defined octahedral shapes with a size of ~2–3 µm (Figure 4.13a). Moreover, energy-dispersive X-ray spectroscopy (EDX) analysis revealed the presence of intact [Ru(cptpy)$_2$] within the framework. The EDX data showed the presence of Zr and Ru elements in the ligand-exchanged MOF (Figure 4.13b). The SEM elemental mapping demonstrated the uniform distribution of C, N, O, Zr and Ru (Figure 4.13c). These findings strongly support the successful realization of the PSLE approach.

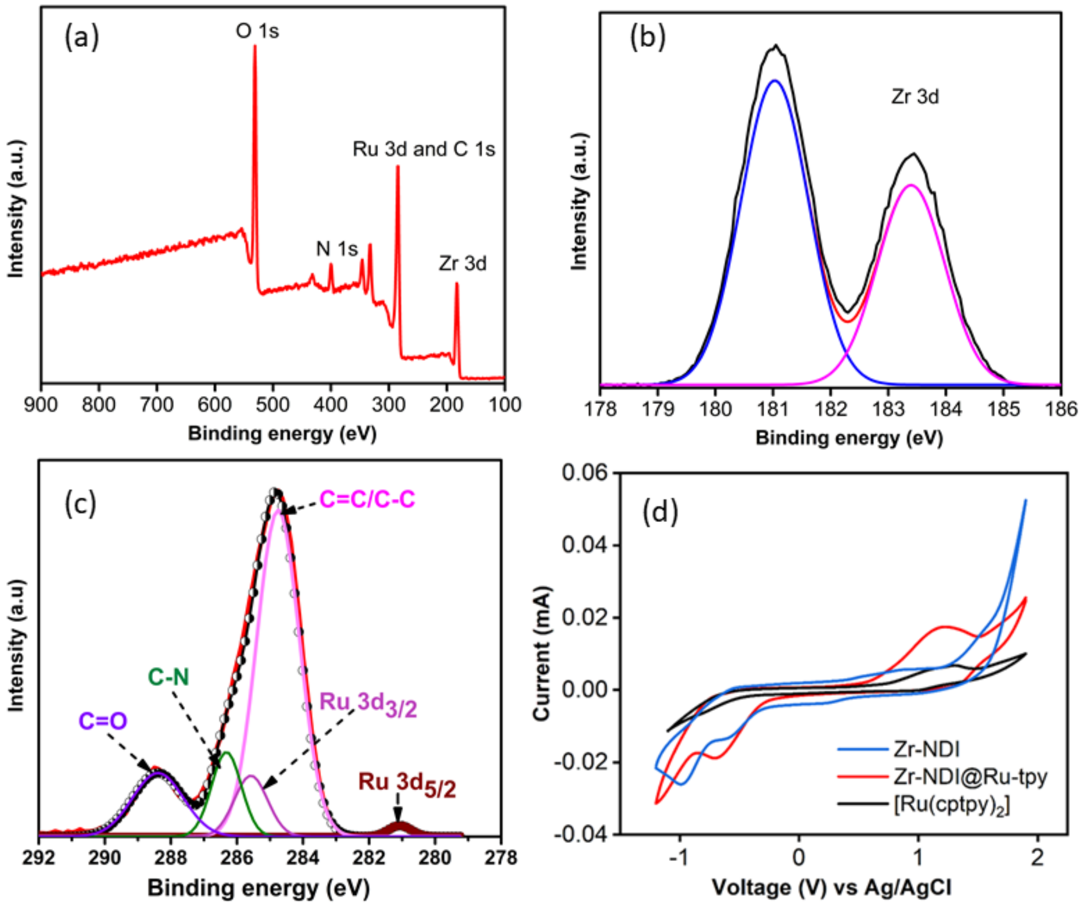

Figure 4.14: (a) Long range XPS survey of Zr-NDI@Ru-tpy. (b) Zr 3d of Zr-NDI@Ru-tpy. (c) XPS spectra of Ru 3d and C 1s. (d) CV of Zr-NDI, Zr-NDI@Ru-tpy, and [Ru(cptpy)$_2$] at a scan rate of 100 mVs^{-1} in DMF with 0.1 M tetrabutylammonium hexafluorophosphate as supporting electrolyte.

Further, X-ray photoelectron spectroscopy (XPS) analysis has been performed to confirm the oxidation state of ruthenium atom and their successful installation within the MOF framework. The XPS survey revealed the presence of peaks associated with O, N, C and Ru elements (Fig. 4.14a). Two new peaks at binding energy 181.5 eV and 183.4 eV assigned to the Zr 3d of the Zr-NDI@Ru-tpy framework (Figure 4.14b). Figure 4.14c illustrated the presence of Ru 3d and C 1s spectra where Ru 3d3/2 and C 1s overlapped. The deconvolution of Ru 3d spectra gives two peaks at around 285.4 and 281.2 eV corresponds to Ru 3d3/2 and Ru 3d5/2 states, respectively. The values mentioned are consistent with the findings of previous reports on the hexacoordinated [RuII–N6] system.[49,50] The analysis of high-resolution C 1s spectra revealed three distinct peaks at approximately 284.4 eV, 286.4 eV, and 288.6 eV, corresponding to the C 1s core signals of C–C, C–N, and C=O bonds, respectively (Figure 4.14c).[51] Additionally, UV-Vis spectroscopy of both the Zr NDI@Ru-tpy MOF and the molecular complex,

$[Ru(cptpy)_2]$ shows an absorbance band at 500 nm, attributed to the metal to-ligand charge transfer of the ruthenium complex (Figure 4.15a and Fig. 4.15b). The UV-Vis spectra further affirmed the successful incorporation of $[Ru(cptpy)_2]$ into the MOF structure. The integrity of the molecular complex $[Ru(cptpy)_2]$ incorporated into the Zr-NDI MOF was further confirmed through cyclic voltammetry analysis (CV) (Figure 4.14d). The inductively coupled plasma optical emission spectrometry (ICP-OES) of digested Zr NDI@Ru-tpy showed that the wt % of Ru is 1.2 %.

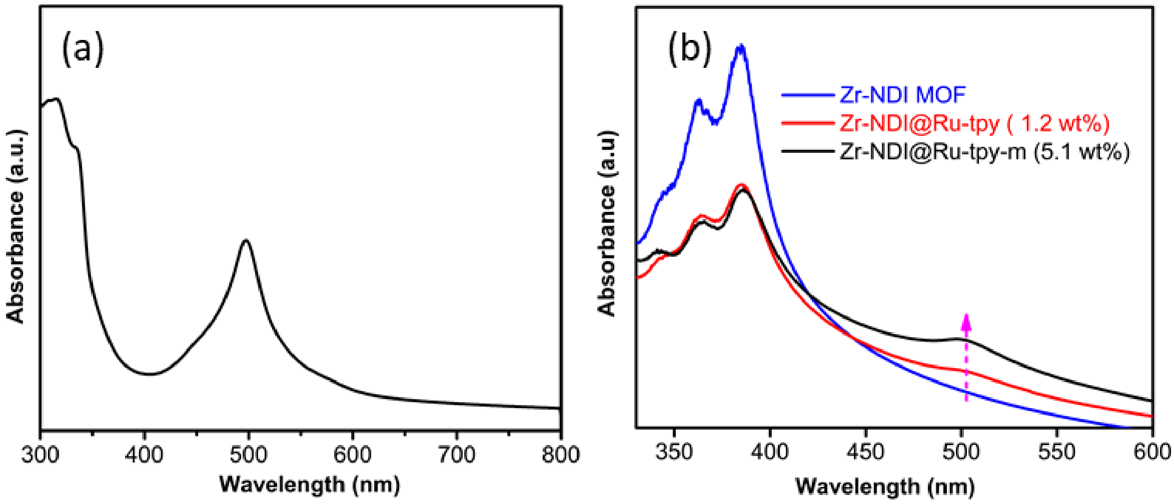

Figure 4.15: (a) UV-Vis spectrum of $[Ru(cptpy)_2]$ dissolved in DMF solvent. (b) UV-Vis spectra of Zr-NDI MOF, Zr-NDI@Ru-tpy and Zr-NDI@Ru-tpy-m (experiment carried out by dispersing 1 mg catalyst in 3 ml DMF).

Moreover, we have also able to incorporate $[Ru(cptpy)_2]$ in the Zr-NDI MOF, by applying the mixed ligands solvothermal synthesis protocol[52] as follows: Zr-NDI@Ru-tpy-m has been prepared by employing $[Ru(cptpy)_2]$ and NDI linker with $ZrCl_4$ and acetic acid in a DMF solution at 120°C for 72 h (Figure 4.8). The crystallinity of the synthesized Zr-NDI@Ru tpy-m was retained, as the PXRD pattern remained consistent with the simulated Zr-NDI MOF (Figure 4.16a). The ^1H NMR spectroscopy of digested Zr-NDI@Ru-tpy-m showed that approximately 50% incorporation of $[Ru(cptpy)_2]$ was achieved (for details see section 4.2.10). ICP-OES analysis confirmed the material contained 5.1 wt % Ru. Additionally, Zr-NDI@Ru-tpy-m exhibited a BET surface area of 720 m^2/g and a pore diameter of ~12 Å (Figure 4.16b-c). The comparison of the optical absorption properties of Zr-MOFs, Zr NDI@Ru-tpy and Zr-NDI@Ru-tpy-m, was assessed before being utilized in photocatalytic CO_2 reduction. The UV-Vis spectroscopy of Zr-NDI@Ru-tpy and Zr-NDI@Ru-tpy-m exhibited enhanced absorption in the visible light region (400-700 nm), which was absent in the pristine Zr-NDI MOF (Figure 4.15b). Notably, the absorption intensity increases with higher Ru-loading, signifying an improved light-harvesting capability. This extended visible light absorption is attributed to efficient charge transfer from donor Ru-terpyridine moieties to acceptor NDI moieties.

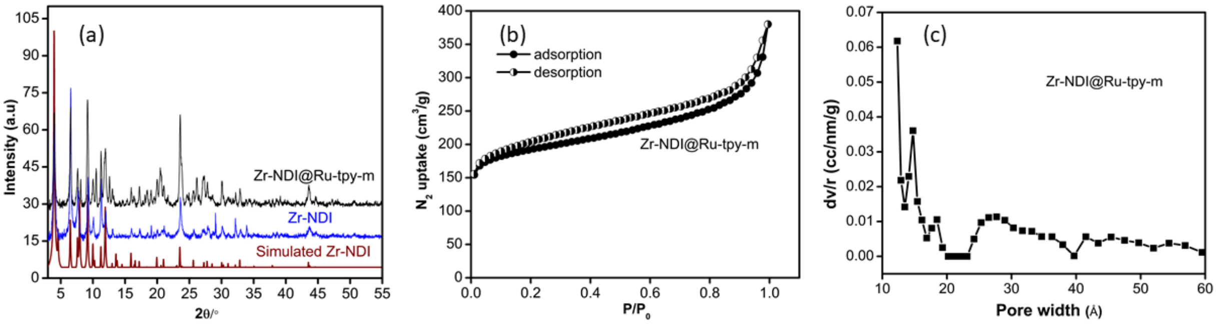

Figure 4.16: (a) PXRD profile of simulated Zr-NDI MOF, synthesized Zr-NDI, and Zr-NDI @Ru-tpy-m (prepared by mixed ligands solvothermal method). (b) N_2 adsorption-desorption isotherm of Zr-NDI@Ru-tpy-m measured at 77 K. (c) Pore size distribution of Zr-NDI@Ru-tpy-m.

To investigate this, we performed also CV (Figure 4.17a-b) and estimated the free energy change (ΔG_{et}) for the photoinduced electron transfer using the Rehm Weller equation: $\Delta G_{et} = E^{ox}_{1/2}$ ($Ru^{2+/3+}$) - $E^{red}_{1/2}$ ($NDI^{0/\bullet-}$) − E_{exc} (NDI)= -0.73 eV (where $E^{ox}_{1/2}$ is the half –wave oxidation potential of [$Ru(cptpy)_2$] (1.11 V), $E^{red}_{1/2}$ is the half-wave reduction potential of NDI (-0.62 V), and E_{exc} is the singlet excited state energy of NDI (2.46 eV, (Figure 4.17c))).[53] The negative ΔGet value confirms a thermodynamically favourable electron transfer process from [$Ru(cptpy)_2$] to the NDI moiety. Further, the band gaps of the photocatalysts were measured from their corresponding UV-Vis spectroscopy using Tauc plots and observed a reduced band gap of Zr-NDI@Ru-tpy (2.18 eV) than the pristine Zr-ND MOF (2.73 eV) (Figure 4.18a-b). This reduction may be attributed to the facile electron delocalization facilitated by the D-A charge transfer within the Zr-NDI@Ru-tpy framework.[54]

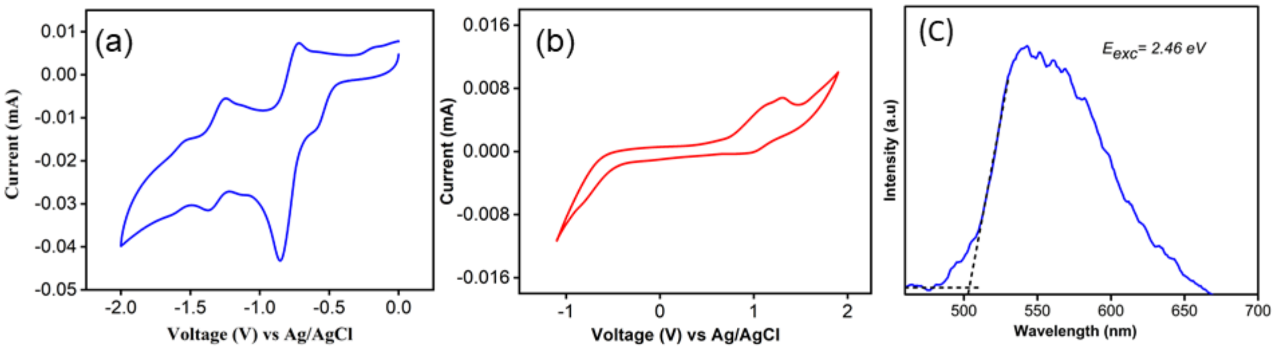

Figure 4.17: (a) CV of NDI linker and (b) [Ru(cptpy)$_2$] complex at a scan rate of 100 mVs^{-1} in DMF with 0.1 M tetrabutylammonium hexafluorophosphate as supporting electrolyte. (c) Fluorescence emission spectrum of NDI linker ((λ_{exc}= 380 nm) in DMF solvent.

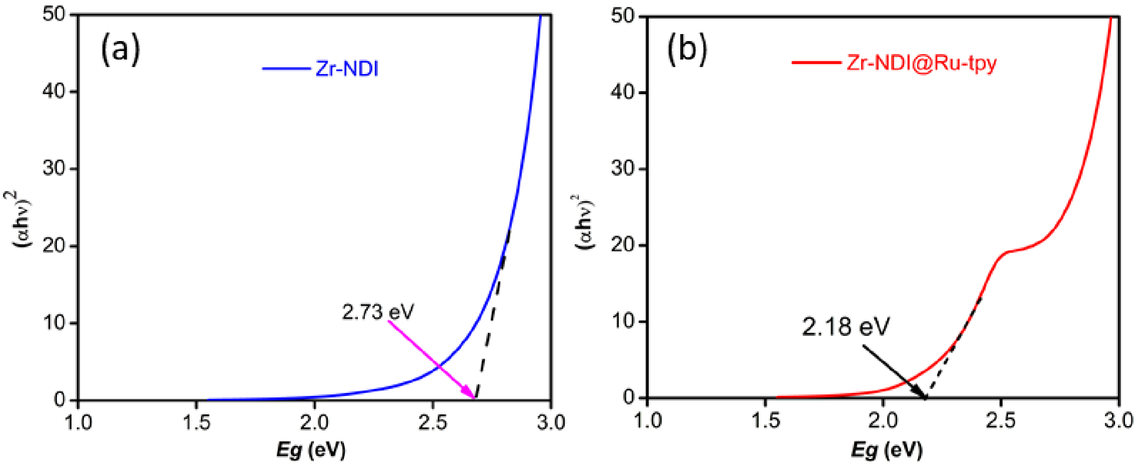

Figure 4.18: a) Tauc plot of Zr-NDI MOF and (b) Zr-NDI@Ru-tpy.

4.3.2 Photocatalytic CO$_2$ reduction

Following the successful integration of [Ru(cptpy)$_2$], we have investigated its photocatalytic efficacy as a photocatalyst for CO$_2$ reduction in different reactions conditions under visible light irradiation. The photocatalytic CO$_2$ reduction of Zr NDI@Ru-tpy under visible light (λ>420 nm) in the presence of [Ru(bpy)$_3$]$^{2+}$ as a photosensitizer was conducted in oxygen free DMF solvent saturated with CO$_2$, utilizing triethanolamine (TEOA), and 1,3-dimethyl-2-

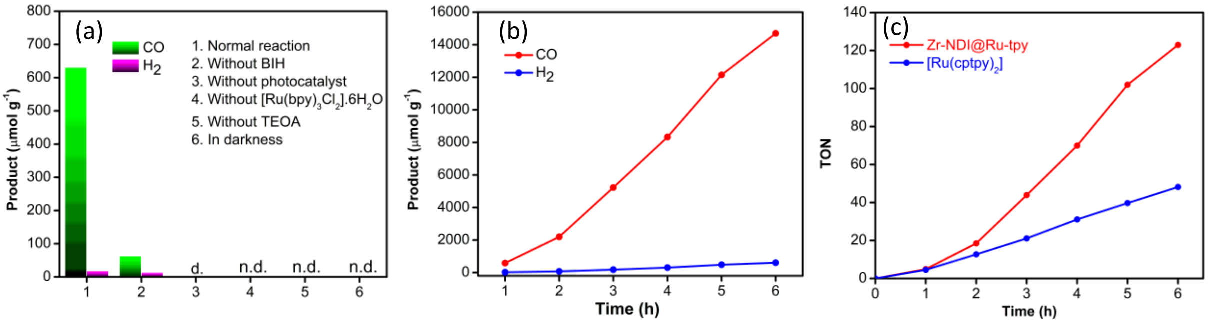

Figure 4.19: (a) Control experiments over Zr-NDI@Ru-tpy for 1 h. (b) CO and H_2 production using Zr-NDI@Ru-tpy as catalyst over 6 h photocatalytic run. (c) TONs of CO production by Zr-NDI@Ru-tpy and [Ru(cptpy)$_2$] under visible light irradiation.

phenyl-2,3-dihydro-1H benzo[d]imidazole (BIH) as sacrificial electron donors. The gas chromatography analysis of the headspace gas showed the evolution of CO and H_2 gas by Zr-NDI@Ru-tpy in photocatalytic reaction.

It was observed that Zr-NDI@Ru-tpy produced 631 μmol g^{-1} of CO and 18 μmol g^{-1} of H_2 within 1 h with high selectivity of 97 % (Figure 4.19a). However, the parent Zr-NDI MOFs was totally inactive towards CO evolution. During the 6 h long photocatalytic experiment, Zr-NDI@Ru-tpy produced 14,698 μmol g^{-1} of CO (Figure 4.19b). This corresponds to an impressive production rate of 2,449 μmol g^{-1} h^{-1}, which is highly comparable to various other MOF-based photocatalysts reported to date (Table 4.1). A minimal amount of H_2 has also been noticed after 6 h long photocatalytic run demonstrating that Zr-NDI@Ru-tpy is highly selective towards CO production. Zr-NDI@Ru-tpy catalyzed CO production achieved a turnover number (TON) of 123 over 6 h run (Figure 4.19c). On the other hand, we have carried out photocatalytic CO_2 reduction reaction using homogenous counterpart [Ru(cptpy)$_2$] keeping all the other condition unaltered and found a TON of only 48.2 after 6 h visible light irradiation (Figure 4.19c). The lower activity of the homogeneous counterpart was likely attributed to complex deactivation. This suggested that the Zr-NDI-MOF matrix stabilizes the [Ru(cptpy)$_2$] complex, thereby enhancing its performance. The high catalytic efficiency is also due to facile electron transfer from the donor [Ru(cptpy)$_2$] chromophore to the NDI acceptor. Furthermore, the apparent quantum yield (AQY) for CO production was determined to be 0.362% under irradiation at 420 nm which is comparable to the other reported photocatalysts (Table 4.1, for details calculation see section 4.2.11).

Table 4.1: Photocatalytic activity of different photocatalyst towards CO_2 reduction

Photocatalyst	**Illumination range**	**SA**	**PS**	**Product**	**Production[a]**	**Selectivity**	**QY (%)**	**Reference**
MOF-Ni	420–800 nm	TIPA	$[Ru(bpy)_3]Cl_2$	CO	371.6	97.7%	0.0053	55
Cd-PMOFs	>420 nm	TEOA	$[Ru(bpy)_3]Cl_2$	CO	139	N.R	N.R	56
Cd(II)PMOF	>420 nm	TEA	$[Ru(bpy)_3]Cl_2$	CO	56	N.R	N.R	57
Co-UiO-67	400–800 nm	N.R	$[Ru(bpy)_3]Cl_2$	CO	3292.5	N.R	N.R	58
Zr-DMBD-Co MOF	450 nm	TEOA	$[Ru(phen)_3](PF_6)_2$	CO	33.3[c]	98%	0.06	59
PMOF/Re	>500 nm	BIH		CO	1893	NR	$1.97 \pm 0.07 \times 10^{-2}$	60
Ni-MOL-100	>420 nm	TEOA	$Ru(phen)_3(PF_6)_2$	CO	2972	96 %	NR	61
66-IS-Ni	>420 nm	TEOA	$Ru(bpy)_3Cl_2$	CO	1352	87%	0.14	62
Zr-MBA-Ru/Re-MOF	>400 nm			CO	440	99%	0.11	63
PCN-250-Fe_2Mn	>450 nm	TIPA	$[Ru(bpy)_3]Cl_2$	CO	21.51[b]	>80 %	2.60	64
PCN-250- Fe_2Ni	>450 nm	TIPA	$[Ru(bpy)3]Cl_2$	CO	15.86[b]	>80 %	0.85	64
MOF-525-Co	400-800 nm	TEOA		CO	200.6	N.R	N.R	65
Zn-MOF nanosheets / ZIF-67	>420 nm	TEOA		CO		89.5 %	0.69	66
Zr-MBA-Ru/Mn-MOF	450	H_2O		CO	1027	99	0.24	67
Re@TEB-BPY	400	TEA		CO	91.7	~68%	0.22	68
Zr-NDI@Ru-TPY	**>420 nm**	**TEOA + BIH**	**$[Ru(bpy)_3]Cl_2$**	**CO**	**2249**	**97 %**	**0.362**	**THIS WORK**

[a]Unit: μmol g^{-1} h^{-1}; [b]Unit: mmol g^{-1} h^{-1}; [c] Unit: μmol

We have also investigated the photocatalyst Zr-NDI@Ru tpy-m, with a higher Ru loading of 5.1 wt% for CO_2 reduction under identical reaction conditions. It exhibited a enhanced CO production of 6750 μmol g^{-1} whereas Zr-NDI@Ru-tpy, with a lower Ru loading of 1.2 wt%, produced 2183 μmol g^{-1} of CO within 2 h. Interestingly, when the rate of CO formation was normalized to the total catalyst content, the low loading Zr-NDI@Ru-tpy demonstrated a higher rate of CO evolution compared to that of high loading Zr-NDI@Ru-tpy-m. This indicated that the photocatalytic activity of the catalyst is influenced by the photosensitizer to catalyst ratio, as previously reported.[69] The superior CO generation observed for the low Ru-loading Zr-NDI@Ru-tpy than the high loading material can be attributed to the use of higher photosensitizer-to-catalyst ratio ($[Ru(bpy)_3]$: [Ru in MOFs] = 80:1) in Zr-NDI@Ru-tpy experiment compared to those in Zr-NDI@Ru-tpy-m ($[Ru(bpy)_3]$: [Ru in MOFs] = 32:1).

We also conducted an ion chromatography analysis of the reaction solvent to investigate the formation of liquid products, such as formic acid (HCOOH). The ion chromatography results showed the production of formate (24 μmol) for 1 h (Figure 4.20a). However, it is noteworthy that photocatalysis experiments conducted without Zr-NDI@Ru-tpy (using only the photosensitizer, BIH and TEOA) still facilitated the production of formate, achieving a formate generation of 34 μmol within 1 h (Figure 4.20a). Hence, the result clearly demonstrated that the $[Ru(bpy)_3]^{2+}$ acts as a catalyst for CO_2 reduction to formate, not Zr-NDI@Ru-tpy. The observed formate production without Zr-NDI@Ru-tpy are expected, as Hawecker *et al*. demonstrated in 1985 that $[Ru(bpy)_3]^{2+}$ acts as a homogeneous catalyst for the photochemical reduction of CO_2 to formate.[70] ^{1}H NMR spectroscopy has been utilized to check the other liquid hydrocarbon products derived from CO_2 such as CH_3OH and C_2H_5OH. This experiment showed that there was no production of CH_3OH and C_2H_5OH (Figure 4.20b).

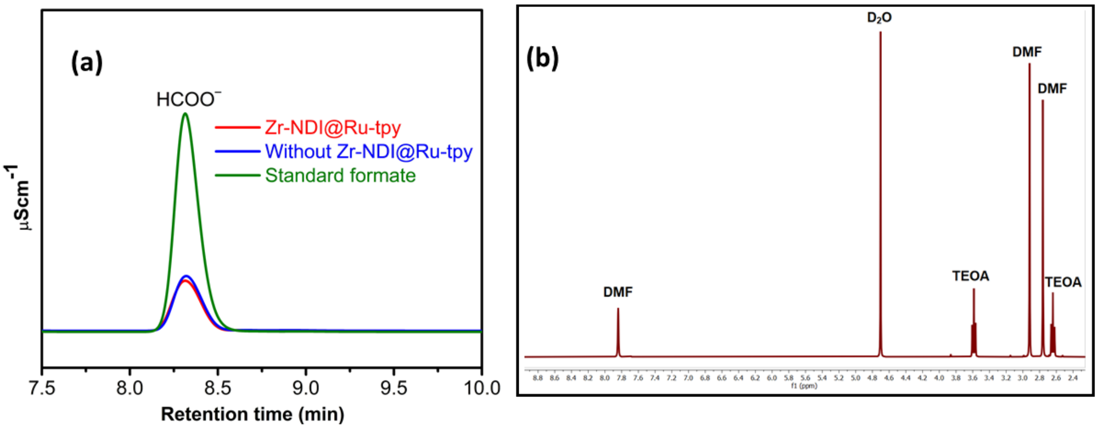

Figure 4.20: (a) Ion chromatography curve for formate detection. (b) ^{1}H NMR spectroscopy of the reaction mixture after photocatalytic CO_2 reduction.

Subsequently, a set of control experiments were conducted to understand the primary factors influencing the photoreduction of CO_2 (Figure 4.19a). There is an optimum concentration for BIH at which photocatalyst showed the highest catalytic activity (Figure 4.21a). Moreover, the removal of BIH from reaction reduced the CO production to 63 μmol g^{-1} (Figure 4.19a). Absence of TEOA also resulted in photocatalytic inactivity towards CO evolution (Figure 4.19a). In the absence of the Zr-NDI@Ru-tpy as the catalyst (using only the photosensitizer, BIH and TEOA), a negligible amount of CO and H_2 was detected which is 2.8 μmol g^{-1} and 3.1 μmol g^{-1} respectively. Additionally, the absence of light or photosensitizer yielded no CO evolution, affirming the photocatalytic nature of the reaction. These results collectively underscored the indispensability of all the components within this system. Subsequently, we have also investigated the catalytic performance of the Zr-NDI@Ru-tpy under irradiation by direct sun light from 11:00 am to 3:00 pm on 17/05/2024 to mimic the natural photosynthesis and we found 1430 μmol g^{-1} CO and 88 μmol g^{-1} H_2. Now, in order to understand the source of CO, we have performed the photocatalytic reaction in presence of N_2 instead of CO_2. After 1 h, there was no detectable CO gas. This indicated that CO was not coming from catalyst's decomposition or solvent decomposition. Further, to verify the source of the produced CO through the photoreduction of dissolved CO_2, we conducted isotope labelling experiment utilizing $^{13}CO_2$ (Figure 4.21b). The presence of peaks at m/z = 29 provided indications that the evolved ^{13}CO originated from the photoreduction of $^{13}CO_2$. This finding also served to confirm

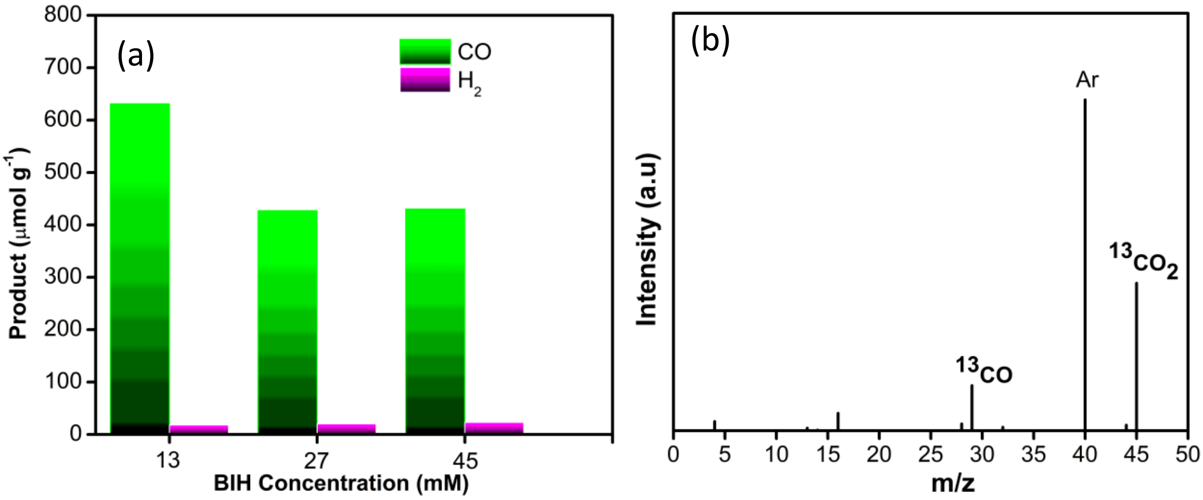

Figure 4.21: (a) Control experiments over Zr-NDI@Ru-tpy for 1 h. (b) Photocatalytic CO evolution over Zr-NDI@Ru-tpy with different BIH concentration for 1 h. (c) ^{13}C isotope labelling experiment for CO generation by using $^{13}CO_2$ as carbon source.

that the CO originated from the dissolved CO_2 rather than from the decomposition of any organic compound within the photocatalytic medium. To further assess the stability of the Zr-NDI@Ru-tpy catalyst, recyclability studies were conducted (Figure 4.22a). The catalyst was analyzed through five 1h recycling experiment. A slight decrease in production of CO was observed after each cycle (Figure 4.22a). The yield decreased in the 4th and 5th runs, which was attributed to the loss of the Ru metal as the ICP-OES analysis of Zr-NDI@Ru-tpy after 5 cycles run shows the presence of 0.8 wt% Ru, compared to 1.2 wt% initially. The PXRD pattern (Figure 4.22b) and FT-IR spectra (Figure 4.22c) of Zr-NDI@Ru-tpy remains unaltered suggesting its stability during the course of the photocatalytic run. In addition, we have also investigated the SEM image of Zr-NDI@Ru-tpy after photocatalysis which demonstrated the retainment of crystallinity (Figure 4.22d).

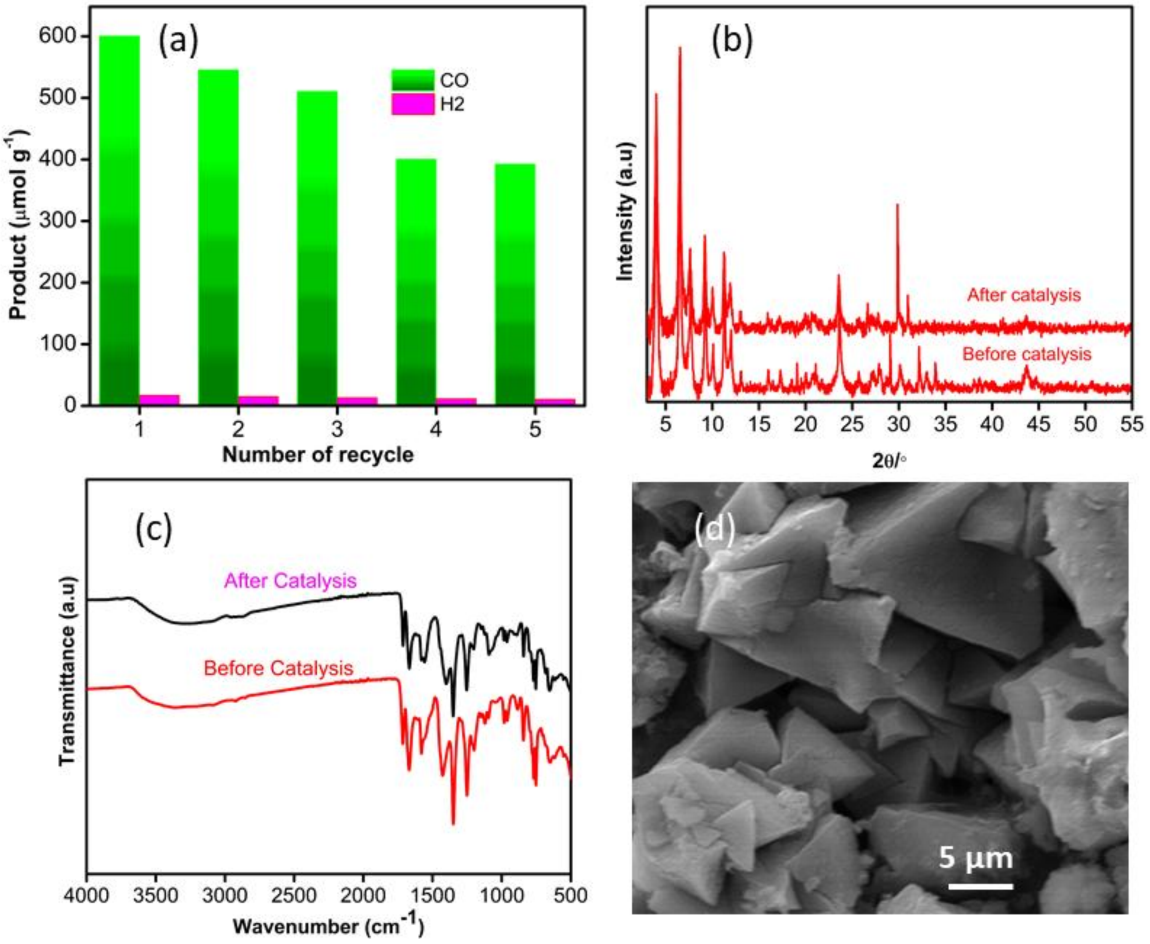

Figure 4.22: (a) Recyclability test of Zr-NDI@Ru-tpy. (b) PXRD profile of as prepared Zr-NDI@Ru-tpy and after photocatalysis. (c) FT-IR spectra of Zr-NDI@Ru-tpy after and before photocatalysis. (d) SEM image of Zr-NDI@Ru-tpy after photocatalytic reaction.

4.3.3 Photocatalytic CO_2 reduction mechanism

To understand the potential photocatalytic mechanism of Zr NDI@Ru-tpy within the system, we conducted transient photocurrent responses and photoluminescence spectra analysis at room temperature, aiming to elucidate the charge transfer behaviour and photoinduced charge separation efficiency. In Figure 4.23a, Zr-NDI@Ru-tpy demonstrated higher photocurrent density than the pristine Zr-NDI upon exposure to light indicating enhanced photoinduced electron mobility in Zr NDI@Ru-tpy and thereby exhibiting high photocatalytic activity. Further, the effectiveness of charge transfer was elucidated through electrochemical impedance spectroscopy (EIS) (Figure 4.23b). An electric circuit (or equivalent circuit) was extracted from the Nyquist plot to understand the electrochemical processes. As depicted in Figure 4.23b (inset), the equivalent circuit consists of the resistance of solution (R_S), bulk resistance (R_{Bulk}), a bulk capacitance (C_{Bulk}), charge transfer resistance (R_{ct}), space charge capacitance (C_{SC}), Warburg element (W). The R_{CT} values of Zr-NDI and Zr-NDI@Ru-tpy were 2.2 KΩ and 1.6 KΩ, respectively, which were calculated from the diameter of the semicircle. The low R_{CT} value of Zr-NDI@Ru-tpy indicates that ions could rapidly transfer at the interface between the electrode and electrolyte solution, which results in a better catalytic performance.[71] Apart from possessing a suitable conduction band (CB) potential with reduction capacity, the photocatalytic activity of Zr NDI@Ru-tpy is attributed to the enhanced electron mobility and separation efficiency of photoinduced charges compared to the pristine Zr-NDI MOF.

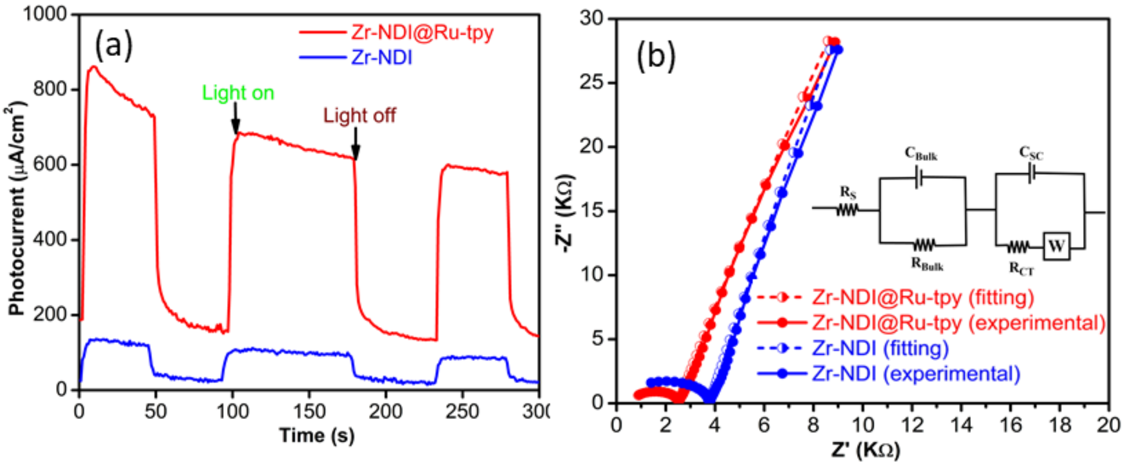

Figure 4.23: (a) Transient photocurrent response, and (b) electrochemical impedance spectra of Zr-NDI and Zr-NDI@Ru-tpy.

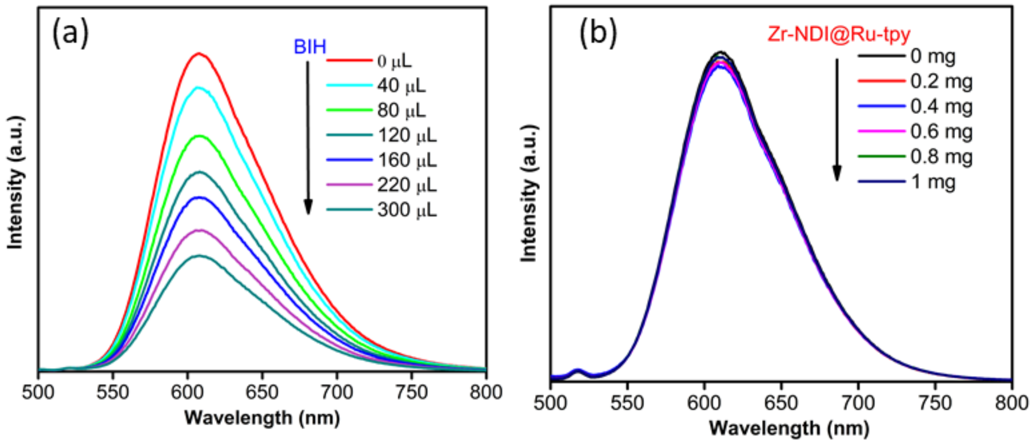

Figure 4.24: (a) Emission intensity of $[Ru(bpy)_3]^{2+}$ after incremental addition of BIH, and (b) Zr-NDI@Ru-tpy.

Now, to know, whether the photoexcited Ru^{II} PS undergoes reductive quenching by BIH or oxidative quenching by the Zr-NDI@Ru-tpy, initiating the catalytic cycle, we conducted luminescence spectra of $[Ru(bpy)_3]^{2+}$ with varying amount of BIH and Zr-NDI@Ru-tpy. As depicted in Figure 4.24a, the emission intensity of $[Ru(bpy)_3]^{2+}$ was effectively quenched by BIH, while no significant quenching was observed with Zr-NDI@Ru-tpy (Figure 4.24b). This outcome underscored that the photoexcited $[Ru(bpy)_3]^{2+}$* undergoes reductive quenching by BIH, leading to the generation of the $[Ru(bpy)_3]^{+}$*. In addition, Mott-Schottky analysis was conducted to evaluate the flat-band potential and assess the feasibility of effective CO_2 reduction for Zr-NDI@Ru-tpy (Figure 4.25a). The analysis revealed a positive slope in the plot of C^{-2} versus the applied potential, confirming the n type semiconductor characteristics.[51]

The flat-band potential of Zr-NDI@Ru-tpy was determined from the intersection point of the Mott-Schottky plot, found to be -0.91 V versus the Ag/AgCl reference electrode (i.e., -0.71 V vs normal hydrogen electrode (NHE).[44a] Generally, in n-type semiconductors, the bottom of the conduction band is usually approximated to be nearly equal to the flat-band potential.[72,73] According to this, the conduction band level was estimated to be positioned at -0.71 V vs NHE. Now, using the relationship $E_{VB}=E_{CB}+E_g$, the valence band potential of Zr-NDI@Ru-tpy was calculated to be 1.47 V vs NHE. The results showed the more positive potential of the conduction band in Zr-NDI@Ru-tpy, relative to -1.25 V vs. NHE ($E[Ru(bpy)_3]^{2+}*/[Ru(bpy)_3]^{+}$),[74] demonstrated the thermodynamic feasibility of photoexcited electron transfer from the photosensitizer to the catalyst. Furthermore, the more negative conduction band potential of Zr-NDI@Ru-tpy compared to the reduction potential for the conversion of CO_2 to CO (-0.52 V vs. NHE)[75] indicated the theoretical viability of using Zr-NDI@Ru-tpy as a catalyst for photocatalytic CO_2 reduction to CO (Figure 4.25b).

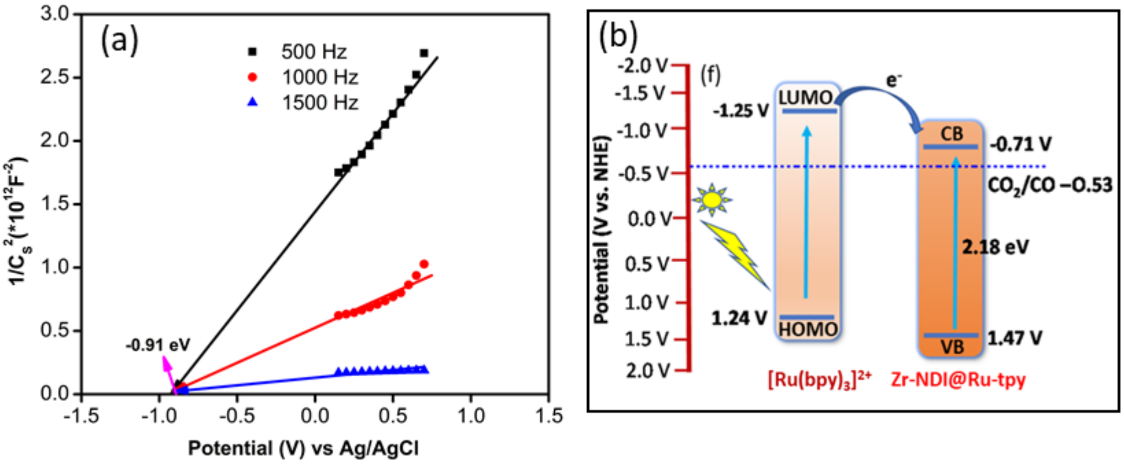

Figure 4.25: (a) Mott-Schottky plot for Zr-NDI@Ru-tpy. (b) Potential diagram of $[Ru(bpy)_3]^{2+}$ and Zr-NDI@Ru-tpy showing feasible electron transfer.

Furthermore, we have employed in situ DRIFT to analyse the reaction intermediates generated during the photocatalytic CO_2 reduction and hence aid in elucidating the mechanism behind the photocatalytic CO_2 reduction process associated with Zr NDI@Ru-tpy.[76] Figure 4.26 depicted the absence of peaks prior to photo-irradiation. However, as the irradiation time increased, a gradual emergence of several peaks was observed between 1200-2200 cm^{-1} in the in situ FTIR spectra. The emergence of new peaks at 1273 and 1316 cm^{-1} may be attributed to the presence of the monodentate carbonate group (m-CO_3^{2-}), while the peak around 1348 cm^{-1} suggested the formation of the bidentate carbonate group (b-CO_3^{2-}) which probably formed due to the dissolved CO_2 in the CO_2 conversion system.[6,77,78,79] Notably, two new infrared peaks were observed at 1532 and 1631 cm^{-1} for Zr-NDI@Ru-tpy which gradually increased with prolonged visible light irradiation. They are likely to indicate the symmetric and asymmetric stretching of the carboxylate group (COOH*) attached to Ru^{II}, which is an important intermediate species in the photocatalytic reduction of CO_2 to CO.[80] The formed COOH* intermediates could further protonate to generate CO* which is revealed by the appearance of IR peak at around 2020 cm^{-1}.[81] This confirmed the production of CO during photocatalytic CO_2 reduction. However, peaks in the 1800–2000 cm^{-1} range were also observed, which may result from the formation of different CO species coordinated to Ru sites as reported previouly.[82,83,84,85] The peak appeared at 1957 cm^{-1} and 1834 cm^{-1} may be ascribed to the linear and bridged CO adsorption on Ru-sites.[82,83,84,85]

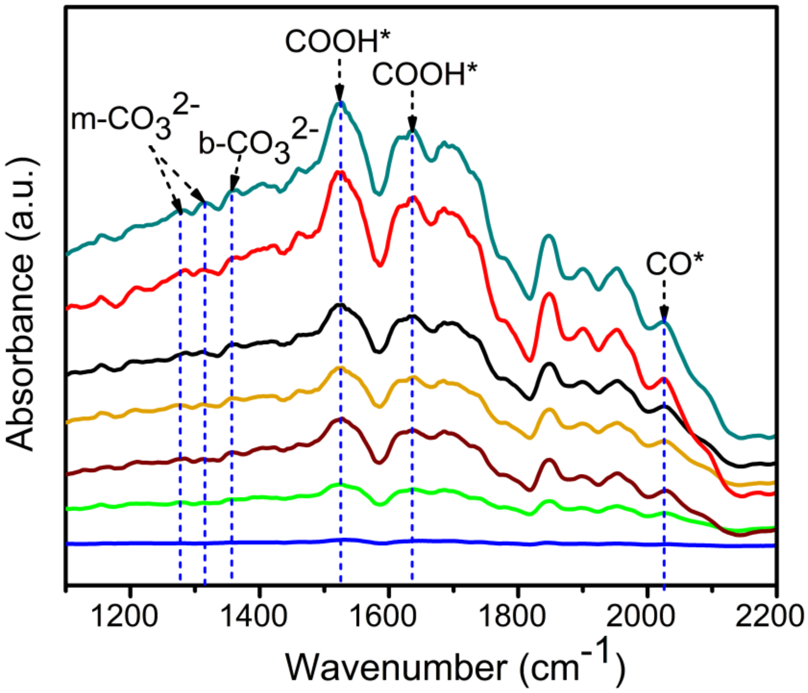

Figure 4.26: *In situ* DRIFT spectra of Zr-NDI@Ru-tpy under visible light irradiation (1 h).

Taking into account the findings and discussions outlined above, we presented a plausible photocatalytic CO_2 reduction mechanism over Zr-NDI@Ru-tpy, as depicted in Fig. 4.27. Upon illumination, the photosensitizer $[Ru(bpy)_3]^{2+}$ absorbs photons, leading to the excitation of electrons and their subsequent transition to the excited state $[Ru(bpy)_3]^{2+*}$. As the CO_2 reduction reaction is occurring through reductive quenching mechanism, hence the excited $[Ru(bpy)_3]^{2+*}$ will be reduced by accepting electron from BIH affording $[Ru(bpy)_3]^{+*}$ and oxidized BIH ($BIH^{\cdot+}$). Nevertheless, $BIH^{\cdot+}$ readily undergoes deprotonation, yielding deprotonated $BI^{\cdot}$ that can provide an additional electron to reduce another $[Ru(bpy)_3]^{2+*}$ species, thereby generating 2 equivalents of reduced $[Ru(bpy)_3]^{+*}$ during the photoinduced process. Subsequently, two reduced $[Ru(bpy)_3]^{+*}$ species transfer two electrons consecutively to the catalytic centre $[Ru^{II}(cptpy)_2]$ and generates $[Ru^{I}(cptpy^{\cdot})(cptpy)]$. Next, CO_2 get attached with the reduced metal center through carbon atom with the substitution of one pyridine nitrogen atom in tpy moiety,[80b,86] forming the intermediate species $[Ru^{II}(cptpy)(\eta^2\text{-}cptpy)(COO^{2-})]$ which further undergoes protonation to form $[Ru^{II}(cptpy)(\eta^2\text{-}cptpy)(COOH^{-})]^{+}$.

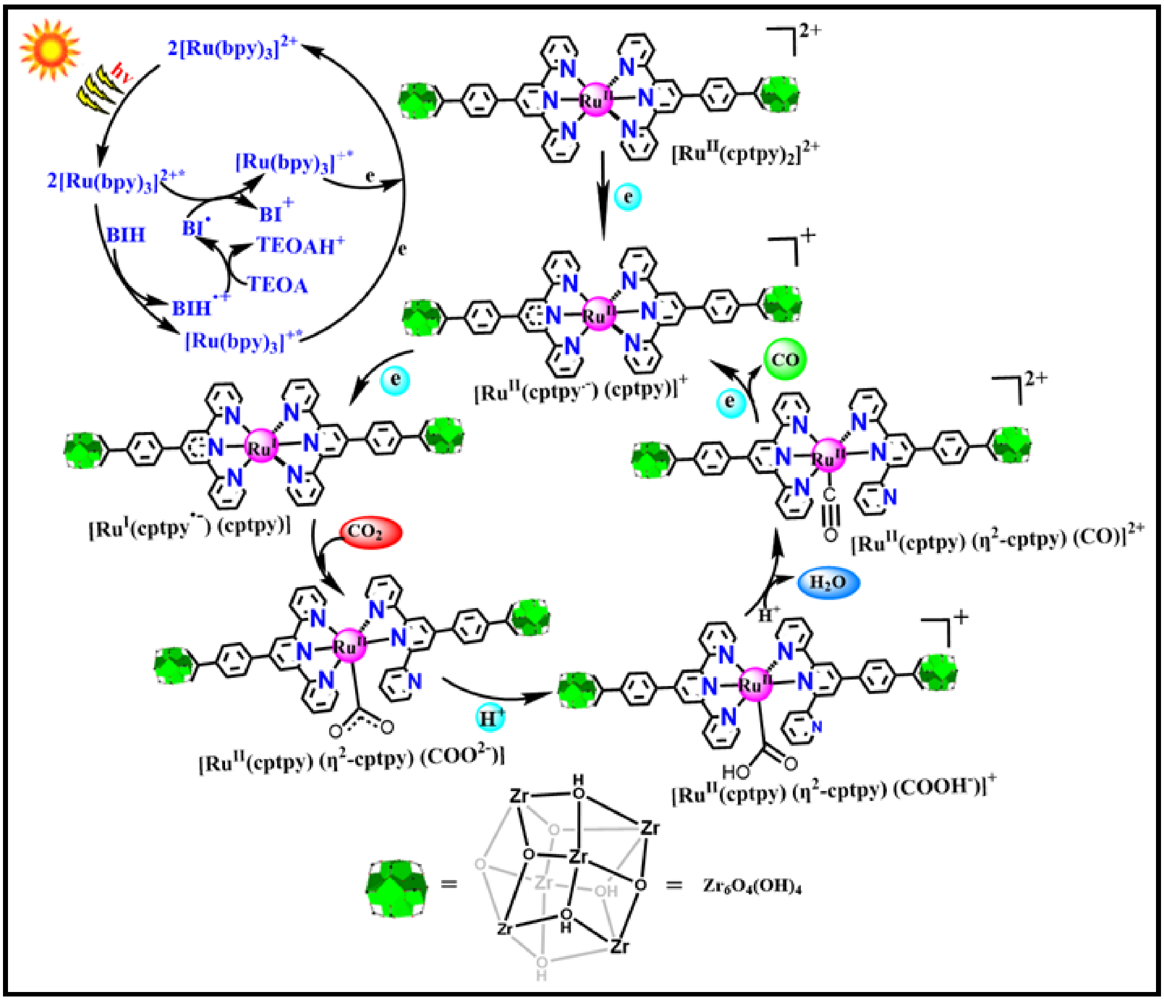

Figure 4.27: Plausible mechanism pathway for photocatalytic CO_2 reduction by Zr-NDI@Ru-tpy.

Then, further protonation of intermediate species $[Ru^{II}(cptpy)(\eta^2\text{-}cptpy)(COOH^-)]^+$ and subsequent elimination of H_2O result in the formation of $[Ru^{II}(cptpy)((\eta^2\ cptpy)(CO)]^{2+}$ which undergo reduction and removal of CO, regenerating $[Ru^{II}(cptpy^{\cdot-})(cptpy)]^+$ and thus complete the photocatalytic cycle. It is worth mentioning that without TEOA, the photocatalytic system is totally inactive to generate CO this is because in absence of TEOA, $BIH^{\cdot+}$ may readily reduce by ruthenium complex in the MOF and inhibits the photocatalytic cycle. When TEOA added in the reaction medium, TEOA acts as a base for $BIH^{\cdot+}$. This led to the suppression of the back electron transfer from ruthenium in the MOF (Figure 4.28).

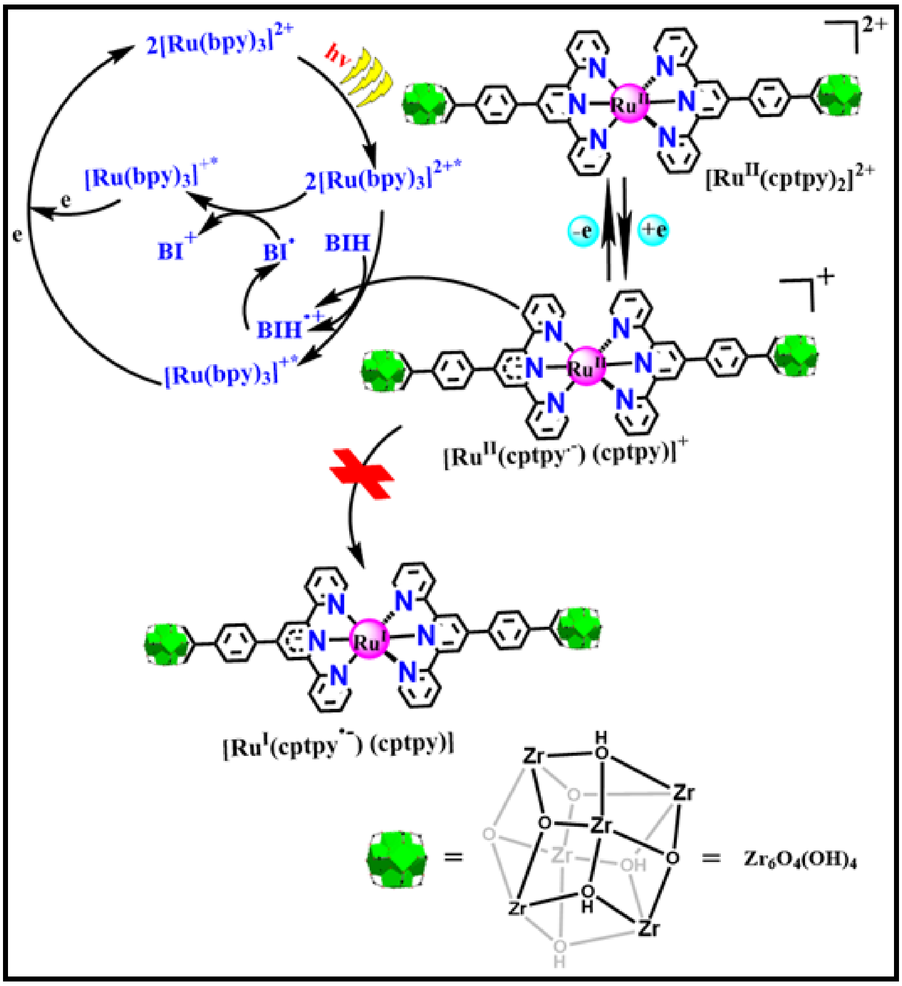

Figure 4.28: Possible mechanism of photocatalytic CO_2 reduction in absence of TEOA.

4.4 Conclusion

We have presented a successful design strategy to develop redox-active mixed linker MOF through SALE and mixed ligands solvothermal strategy for photocatalytic CO_2 reduction. We have accommodated a redox metal complex, [Ru(cptpy)$_2$] as a catalytic centre into the robust ZrIV-MOF by replacing the existing linker through SALE and mixed ligands solvothermal strategy. The findings have confirmed the successful incorporation of [Ru(cptpy)$_2$] into the MOF and making it a highly suitable candidate for CO_2 reduction. The resulting MOF exhibited efficient photocatalytic performance with the enhanced stability of the solid-state MOF host. This Zr-NDI@Ru tpy MOF shows an efficient conversion of CO_2 to CO under visible light irradiation. It reveals a CO production of 14698 μmol g^{-1} with a TON of 123 in 6 h photocatalytic run, which stands on par with numerous previously reported photocatalysts. The Zr NDI@Ru-tpy catalyst is not only highly efficient in generating CO, but also exhibits a high selectivity for producing CO (97%) over H_2. Additionally, we have proposed a plausible mechanism for the photocatalytic reduction of CO_2 over Zr-NDI@Ru-tpy through in situ

DRIFTS analysis, along with photophysical and electrochemical studies. However, a detail mechanistic study through DFT calculation is underway for mixed linker MOF, which contains tpy based first row transition metal complex. Hence, our work focused on the innovative integration of homogeneous and heterogeneous catalytic systems to overcome existing limitations. Thus, we anticipate that it will provide a new avenue for developing efficient, sustainable, stable, and recyclable photocatalysts.

4.5 References

1. X. Li, Y. Sun, J. Xu, Y. Shao, J. Wu, X. Xu, Y. Pan, H. Ju, J. Zhu, and Y. Xie, *Nat. Energy,* 2019, **4**, 690–699.

2. Z. J. Zhang, and E. Reisner, *Nat. Chem. Rev*., 2020, **4**, 6–21.

3. Y. Bai, L. Wilbraham, B. J. Slater, A. M. Zwijnenburg, S. R. Sprick, and I. A. Cooper, *J. Am. Chem. Soc.,* 2019, **141**, 9063–9071.

4. R. Kuriki, T. Ichibha, and K. Hongo*, J. Am. Chem. Soc*., 2018, **140**, 6648–55.

5. J. Albero, Y. Peng, and H. García, *ACS Catal*., 2020, **10**, 5734– 5749.

6. S. Barman, A. Singh, A. F. Rahimi, and T. K. Maji, *J. Am. Chem. Soc*., 2021, **143**, 16284–16292.

7. S. N. Habisreutinger, L. Schmidt-Mende, and J. K. Stolarczyk, *Angew. Chem. Int. Ed*., 2013, **52**, 7372–408.

8. Q. Liu, Y. Zhou, and J. Kou, *J. Am. Chem. Soc*., 2010, **132**, 14385–7.

9. L. Cheng, Q. J. Xiang, Y. L. Liao, and H. W. Zhang, *Energy Environ. Sci*., 2018, **11**, 1362–1391.

10. M. Zhou, S. Wang, P. Yang, Z. Luo, R. Yuan, A. M. Asiri, M. Wakeel, and X. Wang, *Chem. Eur. J.*, 2018, **24**, 18529–18534.

11. J. Fu, B. Zhu, C. Jiang, B. Cheng, W. You and J. Yu, *Small*, 2017, 1603938.

12. J. Hawecker, J.-M. Lehn, and R. Ziessel, *Helv Chim. Acta*., 1986, **69**, 1990-2012.

13. E. E. Benson, C. P. Kubiak, A. J. Sathruma, and J. M. Smieja, *Chem. Soc. Rev*., 2009, **38**, 89-99.

14. T. Ouyang, H. H. Huang, and J. W. Wang, *Angew. Chem. Int. Ed*., 2017, **56**, 738–43.

15. D. Hong, Y. Tsukakoshi, and H. Kotani, *J. Am. Chem. Soc*., 2017, **139**, 6538–6541.

16. W. Wang, S. Wang, X. Ma, and J. Gong, *Chem. Soc. Rev*., 2011, **40**, 3703–3727.

17. R. C. Klet, S. Tussupbayev, J. Borycz, J. R. Gallagher, M. M. Stalzer, J. T. Miller, L. Gagliardi, J. T. Hupp, T. J. Marks, C. J. Cramer, M. Delferro, and O. K. Farha, *J. Am. Chem. Soc.*, 2015, **137**, 15680−15683.

18. S. A. Burgess, A. Kassie, S. A. Baranowski, K. J. Fritzsching, K. Schmidt-Rohr, C. M. Brown, and C. R. Wade, *J. Am. Chem. Soc.*, 2016, **138**, 1780−1783.

19. C. Tan, X. Han, Z. Li, Y. Liu, and Y. Cui, *J. Am. Chem. Soc.*, 2018, **140,** 47, 16229–16236.

20. N. F. Suremann, B. D. McCarthy, W. Gschwind, A. Kumar, B. A. Johnson, L. Hammarström, and S. Ott, *Chem. Rev.*, 2023, **123**, 6545-6611.

21. L. Chen, J.-W. Ye, H.-P. Wang, M. Pan, S.-Y. Yin, Z.-W. Wei, L.-Y. Zhang, K. Wu, and C.-Y. Fan Su, *Nat. Commun*., 2017, **8**, 15985.

22. Y. B. Huang, J. Liang, and Cao Wang, *Chem. Soc. Rev*., 2017, **46**, 126–157.

23. S. M. Cohen, Z. Zhang, and J. A. Boissonnault, *Inorg. Chem*., 2016, **55**, 7281–7290.

24. A. Jana, S. Saha, S. S. Mondal, N. Kaur, and A. Bhunia, *Chem. Asian J*., 2024, **20**, e202401401.

25. S. M. Cohen, *J. Am. Chem. Soc*., 2017, **139**, 2855−2863.

26. S. Yuan, P. Zhang, L. Zhang, A. T. Garcia-Esparza, D. Sokaras, J. S. Qin, L. Feng, G. S. Day, W. Chen, H. F. Drake, P. Elumalai, S. T. Madrahimov, D. Sun, and H. C. Zhou, *J. Am. Chem. Soc.,* 2018, **140**, 10814−10819.

27. M. Taddei, R. J. Wakeham, A. Koutsianos, E. Andreoli, and A. R. Barron, *Angew. Chem. Int. Ed*., 2018, **57**, 11706−11710.

28. Y. Bai, Y. Dou, L.-H. Xie, W. Rutledge, J.-R. Li, and H.-C. Zhou, *Chem. Soc. Rev*., 2016, **45**, 2327-236.

29. F. Xiao, X. Hu, Y. Chen, and Y. Zhang, *ACS Appl. Mater. Interfaces*, 2019, **11**, 47390–47403.

30. J. H. Cavka, S. Jakobsen, U. Olsbye, N. Guillou, C. Lamberti, S. Bordiga, and K. P. Lillerud, *J. Am. Chem. Soc*., 2008, **130**, 13850-13851.

31. B. A. Johnson, A. Bhunia, H. Fei, S. M. Cohen, and S. Ott, *J. Am. Chem. Soc*., 2018, **140**, 2985–2994.

32. A. Winter, G. R. Newkome, and U. S. Schubert, *ChemCatChem,* 2011, **3**, 1384−1406.

33. A. Winter, and U. S. Schubert, *ChemCatChem*, 2020, **12**, 2890−2941.

34. S. Sato, T. Morikawa, T. Kajino, and O. Ishitani, *Angew. Chem. Int. Ed*., 2013, **52**, 988−992.

35. R. Gueret, L. Poulard, M. Oshinowo, J. Chauvin, M. Dahmane, G. Dupeyre, P. P. Laine, J.

Fortage, and M. N. Collomb, *ACS Catal.,* 2018, **8**, 3792–3802.

36. D. C. Fabry, H. Koizumi, D. Ghosh, Y. Yamazaki, H. Takeda, Y. Tamaki, and O. A Ishitani, *Organometallics,* 2020, **39**, 1511–1518.

37. Y. Kuramochi, O. Ishitani, and H. Ishida, *Coord. Chem. Rev*., 2018, **373**, 333–356.

38. Y. Fang,T. Liu, L. Chen, and D. Chao, Chem. Commun., 2022, **58**, 7972-7975.

39. (a) D. Kim, S. Bhattacharjee, E. Lam, C. Casadevall, S. Rodríguez Jiménez, and E. Reisner, Small, 2024, 2400057. (b) W.-J. Xu, B.-X. Huang, G. Li, F. Yang, W. Lin, J.-X. Gu, H.-G. Deng, Z.-G. Gu, and H.-G. Jin, *ACS Catal*., 2023, **13**, 5723–5732.

40. B. A. Johnson, A. Bhunia, H. A. Fei, S. M. Cohen, and S. Ott, *J. Am. Chem. Soc.*, 2018, **140**, 2985–2994.

41. E. C. Constable, E.L. Dunphy, C.E. Housecroft, M. Neuburger, S. Schaffner, F. Schapera, and S. R. Batten, *Dalton Trans.,* 2007, 4323–4332.

42. Z.-H Yan, M.-H Du, J. Liu, S. Jin, C. Wang, G.-L Zhuang, X. -J Kong, L. -S. Long, and L. -S. Zheng, *Nat. Commun.*, 2018**, 9**, 3353.

43. M. W. Cooke, P. Tremblay, and G. S. Hanan, *Inorg. Chim. Acta,* 2008, **361,** 2259-2269.

44. X. Wang, Z. Fu, L. Zheng, C. Zhao, X. Wang, S. Y. Chong, F. McBride, R. Raval, M. Bilton, L. Liu, X. Wu, L. Chen, R. S. Sprick, and A. I. Cooper, *Chem. Mater.,* 2020, **32**, 9107-9114.

45. M. Wang, J. Liu, Y. Wang, B. Liu, C. Guo, X. Gao, C. Gong, X. Li, G. G. Gurzadyana and L. Sun, *J. Mater. Chem. A,* 2018, **6**, 4768.

46. P. Verma, A. Singh, F. A. Rahimi, P. Sarkar, S. Nath, S. K. Pati and T. K. Maji, *Nat. Commun.,* 2021, **12**, 7313.

47. J. R. Marshall, Y. Kalinovskyy, L. S. Griffin, C. Wilson, A. B. Blight, and S. R. Forgan, *J. Am. Chem. Soc.,* 2017, **139**, 6253–6260.

48. Y. Kim, S. Lee, Y.-P. Chen, B. Lee, S. Lee, and J. Park, *Small*, 2024, **20**, 2305999.

49. C. Agne`s, J.-C. Arnault, F. Omne`s, B. Jousselme, M. Billon, G. Bidan, and P. Mailley, *Phys. Chem. Chem. Phys.,* 2009, **11**, 11647–11654.

50. X. Li, B. Zheng, J. Du, H. Yuan, and D. Xiao, *RSC Adv.,* 2014, **4**, 467–473.

51. (a) S. Karmakar, S. Barman, F. A. Rahimi, and T. K. Maji, *Energy Environ. Sci.*, 2021, **14**, 2429-2440. (b) X. Lin, S. Wang, W. Tu, H. Wang, Y. Hou, W. Dai, and R. Xu, *ACS Appl. Energy Mater.*, 2019, **2**, 7670–7678.

52. W.-J. Xu, B.-X. Huang, G. Li, F. Yang, W. Lin, J.-X. Gu, H.-G. Deng, Z.-G. Gu, and H.-G. Jin, *ACS Catal.*, **2023**, **13**, 5723–5732.

53.(a) Weller, A. *Pure Appl. Chem.*, 1968, **16**, 115– 124; (b) Z. Ji and Y. Wu, *J. Phys. Chem. C*, 2013, **117**, 18315−18324.

54. Z. Guo, D. K. Panda, M. A. Gordillo, A. Khatun, H. Wu, W. Zhou, and S. Saha, *ACS Appl. Mater. Interfaces*, 2017, **9**, 38, 32413–32417.

55. X.-K. Wang, J. Liu, L. Zhang, L.-Z. Dong, S.-L. Li, Y. -H. Kan, D.-S. Lan, and Y.-Q Li, *ACS Catal.*, 2019, ***9***, 1726.

56. J. Ding, Y. Wu, S. Jia, Y. Feng, K. Li, M. Fang, J. Bao, and Y. Wu, *J. Solid State Chem.*, 2020, **292**, 121690.

57. Q. Li, Y. Luo, Y. Ding, Y. Wang, Y. Wang, H. Du, R. Yuan, J. Bao, M. Fang, and Y. Wu, *Dalton Trans.*, 2019, **48**, 8678.

58. X. Gao, B. Guo, C. Guo, Q. Meng, J. Liang, and J. Liu, *ACS Appl. Mater. Interfaces*. 2020, **12**, 24059–24065.

59. D.-C. Liu, T. Ouyang, R. Xiao, W.-J. Liu, D.-C. Zhong, Z. Xu, and T.-B. Lu, *ChemSusChem*, 2019, **12**, 2166-2170.

60. S. Choi, W.-J. Jung, K. Park, S. -Y. Kim, J. -O. Baeg, C.H. Kim, H.-J. Son, C. Pac, and S. O. Kang, *ACS Appl. Mater. Interfaces*, 2021, **13**, 2710–2722.

61. W. Yang, H.J. Wang, R. R. Liu, J. W. Wang, C. Zhang, C. Li, D.C. Zhong, and T.B. Lu, *Angew. Chem. Int. Ed.*, 2021, **60**, 409-414.

62. Y.-L Dong, H.-R. Liu, S.-M. Wang, G. W. Guan, and Q.Y. Yang, *ACS Catal.*, 2023, **13**, 2547–2554.

63. S. Karmakar, S. Barman, F. A. Rahimi, and T. K. Majhi, *Energy Environ. Sci.*, 2021, **14,** 2429-2440.

64. H. Dong, X. Zhang, Y. Lu, Y. Yang, Y.P. Zhang, H.L. Tang, F.M. Zhang, Z.D. Yang, X. Sun, and Y. Feng, *Appl. Catal. B,* 2020**, 276**, 119173.

65. H. Zhang, J. Wei, J. Dong, G. Liu, L. Shi, P. An, G. Zhao, J. Kong, X. Wang, X. Meng, J. Zhang, and J. Ye, *Angew. Chem. Int. Ed.*, 2016**, 55**, 14310-14314.

66. L. Ye, Y. Gao, S. Cao, H. Chen, Y. Yao, J. Hou, and L. Sun, *Appl. Catal. B,* 2018, **227,** 54-60.

67. S. R. V. Parambil, S. Karmakar, F. A. Rahimi, and T. K. Maji, *ACS Appl. Mater. Interfaces*, 2023, **15**, 27821–27831.

68. F. A. Rahimi, S. Dey, P. Verma, and T. K. Maji, *ACS Catal.*, 2023, **13**, 5969–5978.

69. S. Roy, A. Bhunia, N. Schuth, M. Haumannb and S. Ott, *Sustainable Energy Fuels*, 2018, **2**, 1148-1152.

70. J. Hawecker, J.-M. Lehn, and R. Ziessel, *Chem. Commun.*, 1985, 56-58.

71. (a) A. Maity, M. Siebels, A. Jana, M. Eswaran, R. Dhanusuraman, C. Janiak, and A Bhunia, *ChemSusChem*, 2024, e202401716. (b) J. Su, J. Zhang, S. Chai, Y. Wang, S. Wang, and Y. Fang, *Acta Phys.-Chim. Sin.*, 2024, **40**, 2408012.

72. J.-S. Qin, S. Yuan, L. Zhang, B. Li, D.-Y. Du, N. Huang, W. Guan, H. F. Drake, J. Pang, Y.-Q. Lan, A. Alsalme and H.-C. Zhou, *J. Am. Chem. Soc.*, 2019, **141**, 2054–2060.

73. K. Maeda, K. Sekizawa, O. Ishitani, *Chem. Commun.*, 2013, **49**, 10127−10129.

74. S. Yang, R. Sa, H. Zhong, H. Lv, D. Yuan, R. Wang, *Adv. Funct. Mater.*, 2022, **32**, 2110694.

75. J. Wang, W. Zhu, F. Meng, G. Bai, Q. Zhang, and X. Lan, *ACS Catal.*, 2023, **13**, 4316−4329.

76. F. Liu, J. Deng, B. Su, K.-S. Peng, K. Liu, X. Lin, S.-F. Hung, X. Chen, X. F. Lu, Y. Fang, G. Zhang, and S. Wang. ACS Catal. 2025, 15, 1018–1026.

77. L. C. Grabow, and M. Mavrikakis, *ACS Catal.*, 2011, **1**, 365−384

78. X. Li, Y. Sun, J. Xu, Y. Shao, J. Wu, X. Xu, Y. Pan, H. Ju, J. Zhu, and Y. Xie, *Nat. Energy,* 2019, **4**, 690−699.

79. Y. Wang, T. Sun, T. Zheng, X. Ding, P. Zhang, Q. Xu, T. Li, S. Zhang, K. Wang, L. Xu, and J. Jiang, *ACS Materials Lett.,* 2024, **6**, 140–152.

80. (a) Y. Wang, T. Sun, T. Zheng, X. Ding, P. Zhang, Q. Xu, T. Li, S. Zhang, K. Wang, L. Xu, J. Jiang, *ACS Materials Lett.,* 2024, **6,** 140−152. (b) P. Verma, F. Ahamed Rahimi, D. Samanta, A. Kundu, J. Dasgupta, and T. K. Maji, *Angew. Chem. Int. Ed.*, 2022, **61**, e202116094.

81. (a) H. Agarwala, X. Chen, J. R. Lyonnet, B. A. Johnson, M. Ahlquist, S. Ott, *Angew. Chem. Int. Ed.*, 2023, **62**, e202218728. (b) F. A. Rahimi, S. Dey, P. Verma, and T.K. Majhi, *ACS Catal.*, 2023, **13**, 5969–5978. (c) S. R. V. Parambil, S. Karmakar, F. A. Rahimi, and T. K. Maji, *ACS Appl. Mater. Interfaces*, 2023, **15**, 27821–27831. (d) M. J. Hossain, M. M. Rahman, and Md. J. Sharif, *Nanoscale Adv*., 2020**, 2**, 1245-1252.

82. C. Mebrahtu, F. Krebs, G. Giorgianni, S. Abate, S. Perathoner, G. Centi, A. I. Large, G. Held, R. Arrigo, and R. Palkovits, *Chem. Eng. Res. Des.*, 2023, **193**, 320-339.

83. A. Comas-Vives, K. Furman, D. Gajan, M. C. Akatay, A. Lesage, F. H. Ribeiroc and C. Cope´ret, *Phys. Chem. Chem. Phys.*, 2016, **18**, 1969.

84. S. Y. Chin, C. T. Williams and M. D. Amiridis, *J. Phys. Chem. B,* 2006, **110**, 871–882.

85. M. R. Elahifard, M. Pe´rez Jigato and J. W. Niemantsverdriet, *Chem. Phys. Lett.*, 2012, **534**, 54–57.

86. J. J. Leung, J. Warnan, K. H. Ly, N. Heidary, D. H. Nam, M. F. Kuehnel and E. Reisner, *Nat. Catal.*, 2019, **2**, 354–365.

Chapter 5

Metallosalen-Integrated Conjugated Microporous Polymers for scalable Syngas Production from Visible-Light-Driven CO_2 Reduction

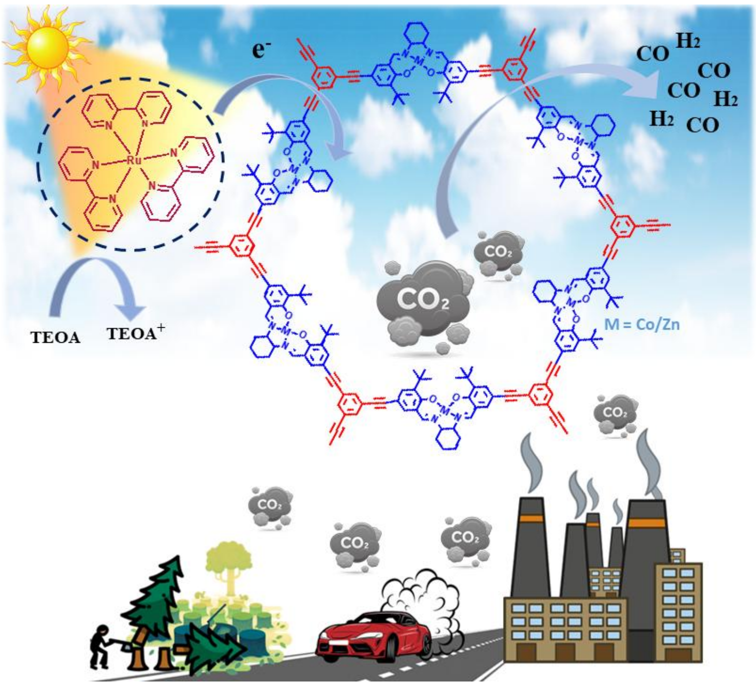

5.1 Introduction

The incessant use of fossil fuels and its catastrophic effect on the environment has arisen the need for the development of sustainable technologies which can administer these problems.[1] Since carbon dioxide emissions have only escalated lately, thus implementation of green chemistry concepts has gained considerable popularity. Therefore, using visible light to catalytically convert CO_2 into useful C1 chemical feedstocks (CO, HCOOH, CH_3OH, and CH_4) has emerged as a crucial strategy for diminishing carbon emissions to alleviate the impacts of global temperature rise..[2,3]Among the various technological approaches to CO_2 conversion, the visible-light-driven two-electron reduction of CO_2 to CO stands out due to its favourable kinetics and lower energy barrier compared to single-electron or multi-electron pathways.[4,5] CO, a key component of syngas (a mixture of H_2 and CO) plays a central role in the industrial synthesis of valuable hydrocarbons. Syngas serves as a crucial intermediate for the production of synthetic fuels and chemicals, with its effectiveness largely dependent on the tunability of the H_2/CO ratio to suit specific industrial processes.[6,7] At present, most syngas is produced through coal gasification or steam reforming of natural gas, both of which rely heavily on non-renewable fossil fuels and involve energy-intensive, harsh processing conditions. In contrast, photocatalytic CO_2 reduction under visible light offers a sustainable and mild alternative, particularly in aqueous systems where H_2 evolution naturally accompanies CO formation. This simultaneous generation of H_2 and CO offers a promising route for continuous syngas production.[8,9] Moreover, tailoring the H_2/CO ratio is essential for downstream applications—for instance, a 2:1 ratio is optimal for methanol synthesis and Fischer–Tropsch processes.[10] However, directly generating syngas with a tunable H_2/CO ratio from CO_2 reduction using solar energy represents a highly promising, yet underexplored strategy, largely due to the complex scientific and technical hurdles involved. In recent decades, a diverse array of photocatalytic materials such as graphitic carbon nitride (C_3N_4),[11,12] TiO_2,[13,14] CeO_2,[15] $CuInS_x$,[16] and CdS[17] have been extensively studied for their ability to drive CO_2 photoreduction (CO_2PR) toward syngas production. While these materials have shown considerable potential in promoting CO generation from CO_2, their overall efficiency remains limited. This is primarily due to their inadequate absorption of visible light and suboptimal charge separation and transfer properties, low surface area, low CO_2 adsorption capability which hinder their practical applicability in large-scale processes.[18] Consequently, the development of cost-effective photocatalysts with improved charge transport, and robust stability under reaction conditions remains a critical challenge for advancing CO_2-to-syngas conversion technologies. In recent years, microporous materials such as metal–organic frameworks (MOFs),[19,20] covalent organic frameworks (COFs),[21,22] and their derived heterostructures have been actively investigated as promising photo- and electrocatalysts for CO_2 reduction into various value-added products. In contrast, conjugated microporous polymers (CMPs), a distinct class of porous organic materials with extended π-conjugation have received comparatively little attention in this field.[23,24] Given their unique structural features, CMPs hold significant potential for heterogeneous photocatalytic CO_2 reduction. Their high surface area and intrinsic porosity facilitate efficient diffusion of reactants, while the extended π-conjugated networks enable effective charge transport to active sites.[25] Furthermore, the exceptional thermal and chemical stability of CMPs arises from their rigid backbones composed of robust C–C covalent bonds, allowing them to maintain structural integrity under harsh conditions and in diverse solvents. By carefully selecting photoactive building blocks with strong visible light absorption, CMPs can be rationally designed for enhanced photocatalytic performance, making them attractive candidates for next-generation CO_2 conversion systems.

In this study, we present the design and synthesis of a new class of metal-functionalized conjugated microporous polymers (CMPs), constructed from Salen-Co/Zn complexes and 1,3,5-triethynylbenzene as key building units. The resulting materials, termed salen-CMP@Co and salen-CMP@Zn, exhibit excellent photocatalytic performance for the visible-light-driven reduction of CO_2 to syngas. Benefiting from their extended π-conjugated frameworks and permanent porosity, these CMPs provide an ideal platform for efficient CO_2 capture, activation, and subsequent conversion. Importantly, the incorporation of Earth-abundant, low-toxicity transition metals such as cobalt and zinc enhances photocatalytic activity while also promoting environmental sustainability. Among the synthesized catalysts, salen-CMP@Co demonstrated superior performance, achieving CO and H_2 evolution rates of 1628 μmol g^{-1} and 5922 μmol g^{-1}, respectively. Moreover, we achieved tunable syngas production by adjusting the water content in the reaction system, enabling control over the CO/H_2 ratio from 1:6.6 to 1:1.7. Furthermore, Comprehensive photophysical and electrochemical characterizations provided valuable insights into the charge separation dynamics and reaction mechanism, further supporting the potential of these CMPs as efficient and versatile platforms for solar driven CO_2 conversion.

5.2: Experimental section

5.2.1: Materials

Tetrakis(triphenylphosphine)palladium (0), 3-tert-butyl-2-hydroxybenzaldehyde, copper(I) iodide, (R, R)-1,2-diaminocyclohexane, and various solvents were obtained from Aldrich and used without further purification. 1,3,5-Triethynylbenzene was purchased from Alfa Aesar and used as received. Cobalt (II) acetate, Zinc acetate tetrahydrate and triethanolamine (TEOA) were sourced from Sigma-Aldrich. The compound 5-bromo-3-tert-butyl-2 hydroxybenzaldehyde was synthesized following a modified literature procedure.

5.2.2 Synthesis of 5-bromo-3-tert-butyl-2-hydroxybenzaldehyde[26]

A solution of Br_2 (0.44 mL, 8.45 mmol) in acetic acid (2 mL) was added dropwise over 30 minutes at room temperature to a stirred solution of 3-tert-butyl-2-hydroxybenzaldehyde (1.50 g, 8.41 mmol) in acetic acid (5 mL). After stirring for an additional 2 hours, the reaction mixture was diluted with dichloromethane (50 mL) and sequentially washed with water (20 mL), saturated aqueous sodium metabisulfite (20 mL), saturated sodium bicarbonate solution (10 mL), and brine (20 mL). The organic layer was dried over anhydrous sodium sulfate, and the solvent was removed under reduced pressure to yield a yellow solid. The crude product was purified by recrystallization from methanol (10 mL), affording the analytically pure compound as a yellow powder (m.p. 64–65 °C). The product was characterized by ^1H NMR spectroscopy (500 MHz, CDCl3). 1H NMR (500 MHz, CDCl3): δ 11.73 (s, 1H), 9.82 (s, 1H), 7.58 (d, J = 2.5 Hz, 1H), 7.51 (d, J = 2.5 Hz, 1H), 1.41 (s, 9H); 13C NMR (125 MHz, CDCl3): δ 196.0, 160.2, 141.6, 137.3, 133.6, 124.5, 122.0, 35.6, 29.4.

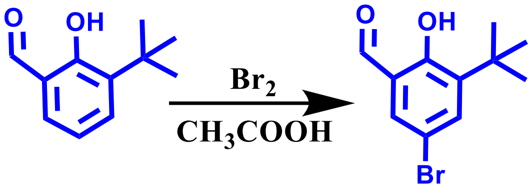

5.2.3 Synthesis of Salen[26]

[Salen = (R, R)-N, N'-bis(5-bromo-3-tert-butyl-salicylidene)-1,2-cyclohexanediamine]

A solution of (R, R)-1,2-diaminocyclohexane (0.48 mL, 4 mmol) in ethanol (60 mL) was introduced into a 250 mL three-neck flask and subjected to vacuum. The mixture was stirred for 30 minutes under an argon atmosphere at room temperature. The temperature was then raised to 80 °C, and a separate solution of 5-bromo-3-tert-butylsalicylidene (2.056 g, 8 mmol) in tetrahydrofuran (10 mL) was added dropwise over 30 minutes. The reaction mixture was maintained at 80 °C with continuous stirring for 4–5 hours, then allowed to cool to room temperature. Subsequently, water (60 mL) was added, and the mixture was stirred further at ambient temperature. The resulting precipitate was collected by filtration and dissolved in diethyl ether. The ether layer was washed several times with saturated sodium chloride solution and water to remove residual impurities. After solvent removal, a yellow powder was obtained, which was dried under vacuum at 50 °C for 24 hours, yielding 1.91 g of product (80.2%). The resulting Salen ligand (yellow powder) was characterized by ^{1}H NMR spectroscopy (500 MHz, $CDCl_3$) as follows: δ 13.75 (s, 2H), 8.20 (s, 2H), 7.32 (d, 4 J = 2.0 Hz, 2H), 7.10 (d, 4 J = 2.0 Hz, 2H), 3.32 (br, 2H), 2.03 (br, 2H), 1.88 (br, 2H), 1.76 (m, 2H), 1.48 (m, 2H), 1.38 (s, 18H).

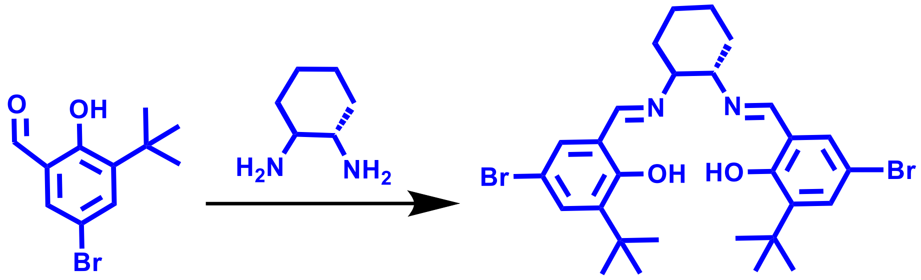

5.2.4 Synthesis of Salen-Co (II)[26]

A solution of cobalt (II) acetate $Co(OAc)_2{\cdot}4H_2O$ (239 mg, 0.96 mmol) in methanol (10 mL) was added dropwise via syringe to a stirred solution of Salen ligand (400 mg, 0.675 mmol) in toluene (10 mL) under an argon atmosphere, leading to the immediate formation of a dark red precipitate. The mixture was then heated to 80–85 °C and stirred for 5–6 hours. After cooling to room temperature, the reaction mixture was concentrated under reduced pressure. The resulting residue was dissolved in dichloromethane (80 mL) and filtered through a Celite pad to remove unreacted cobalt salt. Evaporation of the solvent afforded a dark red solid (79.9 % yield).

Synthesis of Salen-Zn (II)

The compound Salen-Zn (II) was prepared following a procedure analogous to that used for Salen-Co (II), with the substitution of $Co(OAc)_2{\cdot}4H_2O$ by $Zn(OAc)_2{\cdot}2H_2O$ (0.027 g, 0.125 mmol). The reaction yielded a yellow solid with a yield of 62%.

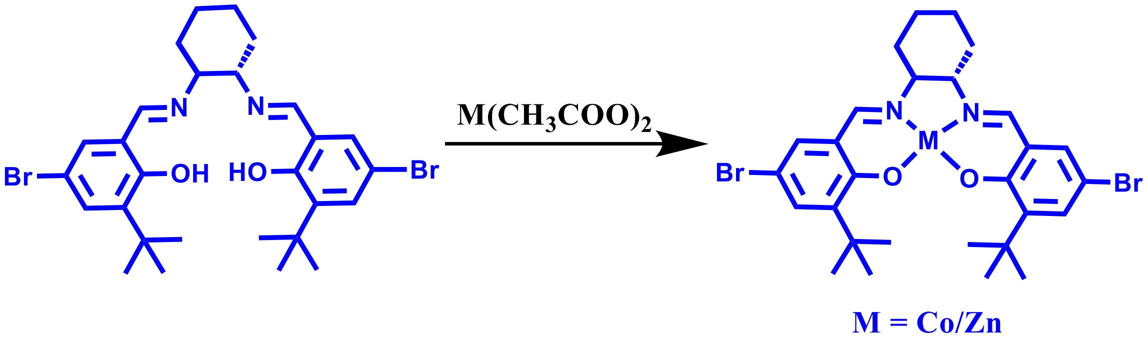

5.2.5 Synthesis of salen-CMP@Co[26]

To synthesize the salen-CMP@Co polymer, 1,3,5-triethynylbenzene (180 mg, 1.2 mmol) and Salen-Co(II) (400 mg, 0.6 mmol) were combined with CuI (50 mg) and tetrakis(triphenylphosphine)palladium(0) (100 mg) in a solvent mixture of toluene (15 mL) and triethylamine (6 mL). The resulting solution was first stirred at 40 °C for 1 hour under an argon atmosphere to minimize oxygen interference and suppress homocoupling of the alkyne units. Subsequently, the reaction mixture was heated to 80 °C and maintained under continuous stirring for 72 hours. Upon completion, the mixture was cooled to room temperature, and the resulting insoluble polymer was collected by filtration. The crude product was thoroughly washed with dichloromethane, methanol, water, and acetone to remove residual monomers and catalyst byproducts. Further purification was achieved via Soxhlet extraction using a 1:1 (v/v) mixture of methanol and dichloromethane over 48 hours. The final polymer was dried under vacuum at 70 °C for 24 hours, affording a brown powder with an isolated yield of 79.3%.

5.2.6 Synthesis of salen-CMP@Zn[26]

Salen-CMP@Zn was prepared using the same synthetic protocol as employed for salen CMP@Co, with the only modification being the substitution of the Salen-Co (II) complex with its zinc analogue, Salen-Zn(II). The reaction yielding a brown solid product with an isolated yield of 75.2%.

5.2.7 Characterization methods

The Fourier transform–infrared (FT–IR) spectra of salen-CMP@Co and salen-CMP@Zn were collected on a Bruker FTIR 4000 instrument equipped with a zinc selenide (ZnSe) ATR. The powder X-ray diffraction (PXRD) data of salen-CMP@Co and salen-CMP@Zn were collected with Bruker D8 Advance X-ray diffractometer (XRD) at room temperature using Cu Kα radiation (λ = 1.548 Å) in a 2θ range of 3–55°. Thermogravimetric analyses (TGA) were done at a ramp rate of 10 °C min−1 under N_2 atmosphere with Perkin Elmer Pyris Diamond TG–DTA instruments. The solid-state UV/Vis spectra of Zr-NDI MOF and Zr-NDI@Ru-tpy were measured using Lamda 750, Make perkin elmer. Fluorescence emission spectra were collected on a HORIBA Fluoromax-4 fluorometer. Nitrogen gas adsorption–desorption of the samples was performed to obtain BET-specific surface area (S_{BET}) using Quanta chrome Autosorb iQ2 Instruments at liquid N_2 temperature (77 K). The samples were degassed under a high vacuum (10^{-6} torr) at 185 °C for 10 h. After degassing, the sample tube was then transferred to the analysis port of the sorption analyzer. Pore size distribution was calculated by non-local density functional theory (NLDFT) using the 'carbon slit pore' model. Field emission scanning electron microscope (FE-SEM) images were obtained using a Carl Zeiss SUPRA 55VP FESEM instrument. Energy dispersive X-ray spectroscopy (EDS) was performed by Oxford Instruments X-Max with INCA software coupled to the FE-SEM. The Hitachi, S-4800, EDS detector was introduced to analyze the morphology and EDS of the samples. X-ray photoelectron spectroscopy (XPS) measurement was conducted by the Thermo Fisher ESCALAB Xi+ microProbe instrument with a monochromatic Al-Kα target, 1486.6 eV energy, and a maximum power of 15.0 KW. After the photocatalysis, gaseous and liquid products were analyzed. The gaseous products were analyzed and quantified using TCD and FID detector in High-performance gas chromatography (Agilent 8860). GC was calibrated with known standard for H^2, CO. Liquid products were analysed through ^{1}H NMR.

Electrochemical characterization

The Mott-Schottky analysis and impedance measurement were conducted using CHI760E workstation (CHI Instruments, USA) through a conventional three-electrode system immersed in a 0.2 M Na_2SO_4 aqueous solution.

Preparation of working electrode for Mott-Schottky measurement

2.5 mg of respective materials were dispersed in a solution of 250 µL water, 250 µL isopropyl alcohol (IPA), and 10 µL of Nafion to prepare a homogenous slurry. Subsequently, 12 µL of slurry was coated on a glassy carbon electrode and then dried at room temperature. The Ag/AgCl electrode was employed as the reference electrode, and the platinum plate was used as the counter electrode, respectively. The measurements were carried out under frequencies of 0.5, 1, and 1.5 kHz.

Preparation of working electrode for impedance measurement

2.5 mg of respective materials were dispersed in a solution of 250 µL water, 250 µL isopropyl alcohol (IPA), and 10 µL of Nafion to prepare a homogenous slurry. Subsequently, 12 µL of slurry was coated on a glassy carbon electrode and then dried at room temperature. The Ag/AgCl electrode was employed as the reference electrode, and the platinum plate was used as the counter electrode, respectively. A 0.2 M Na_2SO_4 solution was used as an electrolyte. The measurements were carried out with a bias potential of 0.6 V with a frequency range from 10 2to 105 Hz under a nitrogen atmosphere.

Photocatalytic testing

Photocatalytic CO_2 reduction experiments were carried out using a 300 W xenon lamp equipped with a 420 nm cut-off filter. In a typical reaction, 1 mg of the activated catalyst, 12 mg of $[Ru(bpy)_3]Cl_2{\cdot}6H_2O$ and 10 mg of 2,2'-bipyridine were dispersed in a solvent mixture consisting of 1.0 mL triethanolamine (TEOA), and 3.8 mL acetonitrile 0.2 mL deionized water in a quartz reaction tube. Further we also varied the acetonitrile (3.5 ml) and H_2O (0.5 ml) ratio. Prior to irradiation, the solution was purged with nitrogen gas for 20 minutes to eliminate dissolved oxygen, followed by CO_2 bubbling (99.999%, Airgas) in the dark for an additional 30 minutes to saturate the system.

The reaction mixture was then exposed to visible light under continuous stirring at room temperature. Gaseous products generated in the headspace were periodically sampled using a gas-tight syringe and analyzed using an Agilent 8860 gas chromatograph equipped with both thermal conductivity (TCD) and flame ionization detectors (FID), along with a 60/80 Carboxen-1000 packed column (Supelco). Liquid-phase products were identified and quantified using ion chromatography and proton nuclear magnetic resonance (^1H NMR) spectroscopy. Control experiments were systematically conducted under identical conditions by omitting one component at a time—light, catalyst, photosensitizer, sacrificial donor, or CO_2—to confirm the necessity of each component in the photocatalytic process.

5.3 Results and Discussions

5.3.1 Characterization of the synthesized polymers

The metal–salen complex monomers were first synthesized via a conventional Schiff-base condensation reaction, followed by metalation with the corresponding metal salts (see section

4.2.3 and 4.2.4 for more details). These preformed metal–salen complexes were then used as building blocks, along with 1,3,5-triethynylbenzene, to construct two conjugated microporous polymers (CMPs), referred to as Salen-CMP@Co and Salen-CMP@Zn (Figure 5.1) The polymerization was carried out using a Pd-catalyzed Sonogashira–Hagihara C–C coupling reaction. Both CMPs were obtained as insoluble brown solids, a result of their rigid and highly cross-linked polymeric frameworks.

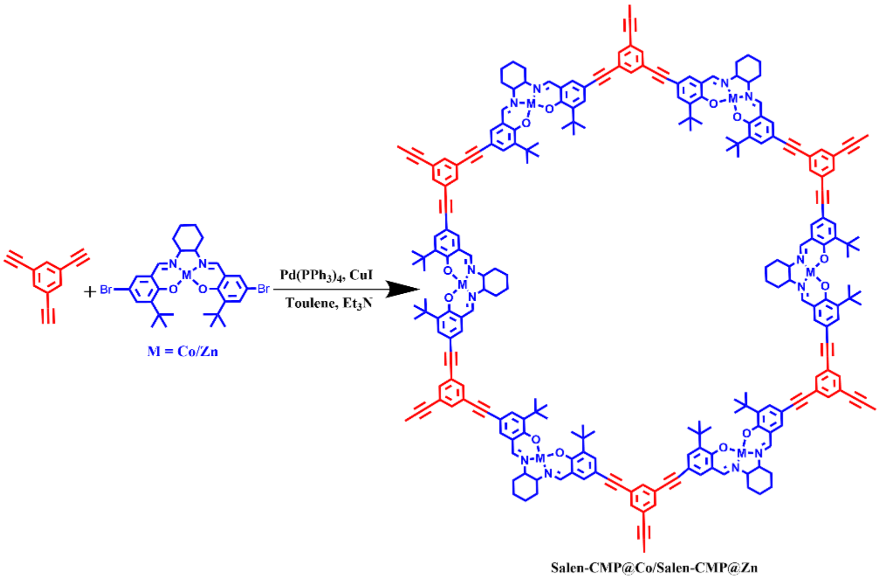

Figure 5.1: Schematic illustration for the synthesis of salen-CMP@Co and salen-CMP@Zn.

Comprehensive characterization using various spectroscopic and microscopic techniques confirmed the successful synthesis and structural integrity of the target polymers. The Fourier-transform infrared (FT-IR) spectra of both synthesized conjugated microporous polymers (CMPs) exhibited a distinct absorption band at approximately 2202 cm^{-1}, corresponding to the C≡C stretching vibration of the acetylene moiety (Figure 5.2).[27] This observation confirms the successful

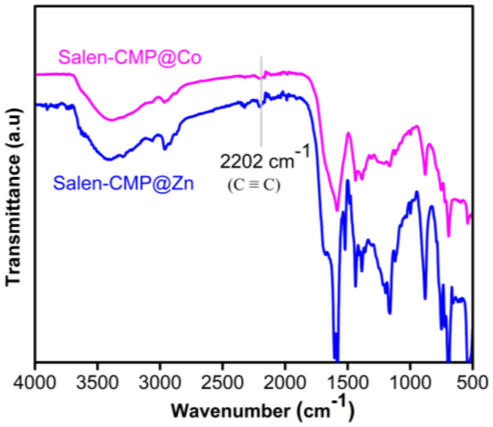

Figure 5.2: FT-IR spectra of salen-CMP@Co and salen-CMP@Zn.

incorporation of acetylene linkages, indicating effective coupling copolymerization between the metal–salen monomers and the acetylene cores.

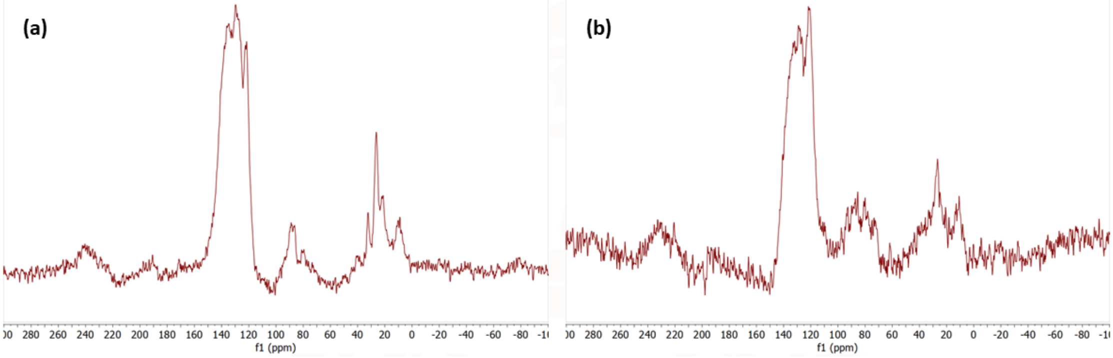

Figure 5.3: Solid state ^{13}C NMR spectra of (a) salen-CMP@Zn and (b) salen-CMP@Co.

Furthermore, the chemical structure of both the CMPs were analyzed using solid-state ^{13}C cross-polarization magic angle spinning (CP-MAS) NMR spectroscopy (Figure 5.3). The ^{1}H NMR spectra revealed a broad signal in the range of 114.5–148.2 ppm, attributed to the carbon atoms of the benzene rings in the synthesized salen-based CMPs.[28,29] A peak at approximately 26 ppm was assigned to the CH_3 carbon atoms, while the signal at 32.8 ppm corresponded to sp3-hybridized carbon atoms of the -C(CH_3) moiety. Additionally, chemical shifts around 80 ppm and 90 ppm were observed, which were ascribed to the sp-hybridized carbon atoms (C≡C) present in the polymer structure.[30] The FT-IR and (CP-MAS) NMR spectroscopy spectra confirm the successful incorporation of salen units into the CMP frameworks. The PXRD patterns of both the polymers exhibit only broad and weak diffraction peaks at around 2ϴ = 19.2°, confirming their lack of crystallinity and indicating that the materials are amorphous in nature (Figure 5.4a).[31,32] The thermal stability of the two polymers was evaluated using

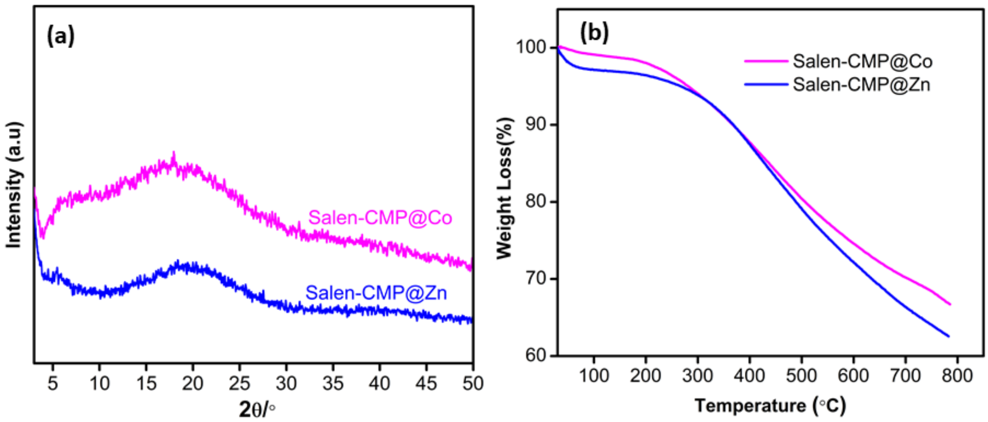

Figure 5.4: (a) PXRD pattern of salen-CMP@Co and salen-CMP@Zn; (b) TGA profile of salen-CMP@Co and salen-CMP@Zn.

thermogravimetric analysis (TGA). Both materials exhibited stability up to approximately 300 °C, followed by a gradual weight loss extending to 800 °C (Figure 5.4b). An initial weight loss of around 7% observed in both cases is likely due to the release of adsorbed water and residual solvent molecules from the porous structure. Further, to gain insight into the surface morphology of salen-CMP@Co and salen-CMP@Zn, their microstructures were examined using scanning electron microscopy (SEM), as shown in Figure 5.5a,b,d,f. The SEM images show the absence of any well-defined or ordered morphology, indicating amorphous morphology of the salen-CMPs characterized by large agglomerated spherical particles. Furthermore, energy-dispersive X-ray (EDX) mapping analysis of the salen-CMPs confirmed the uniform distribution of cobalt, zinc, oxygen, nitrogen, and carbon elements throughout the catalyst matrix (Figure 5.5c, f).

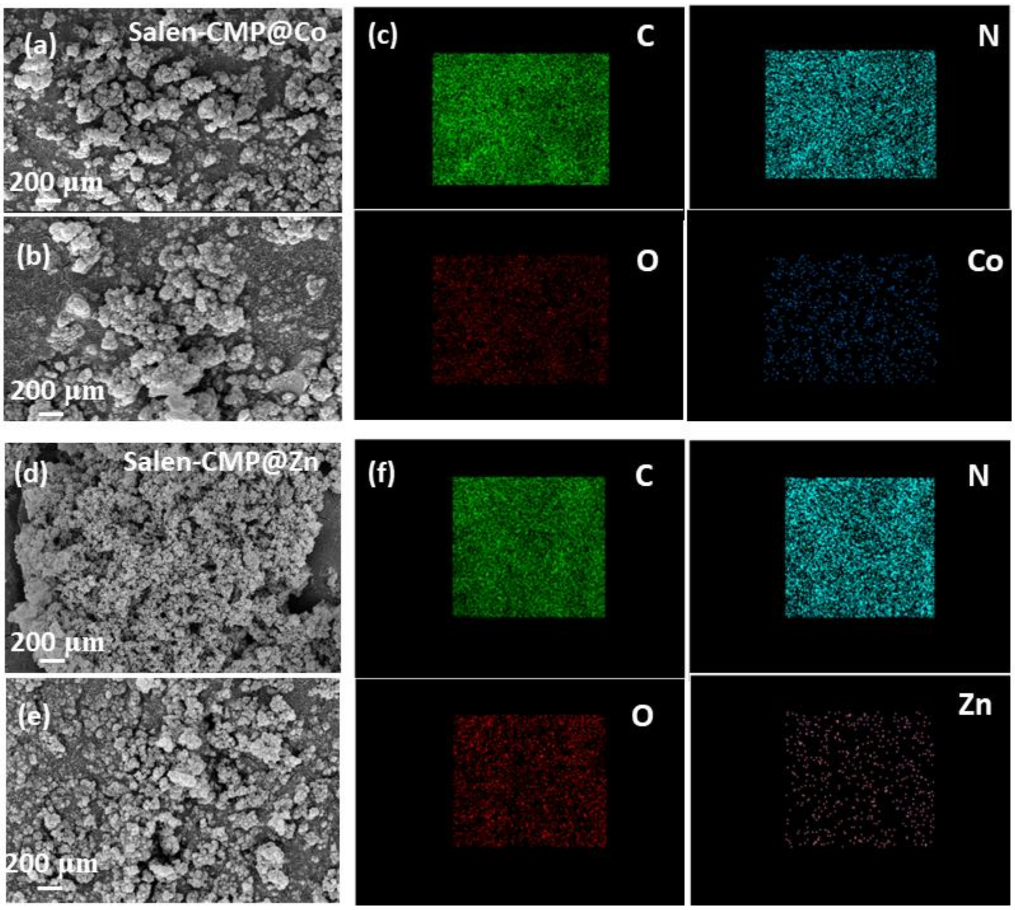

Figure 5.5: SEM images of salen-CMP@Co (a,b) and salen-CMP@Zn (d,e); elemental mapping study of salen-CMP@Co (c) and salen-CMP@Zn (f).

The porosity of both polymers was evaluated through nitrogen adsorption measurements at 77 K, following sample activation under vacuum at 120 °C for 8 hours. Both polymers exhibited type I nitrogen adsorption isotherms, as classified by IUPAC[33], indicating the presence of predominantly microporous structures (Figure 5.6a). The pore size distribution profiles of salen-CMP@Co and salen-CMP@Zn showed no significant differences. Based on NLDFT calculations, the dominant half pore width in both polymers was approximately 10 Å (Figure 5.6b), demonstrating the polymer's intrinsic microporous characteristics. The pore volume of salen-CMP@Co and salen-CMP@Zn was determined to be 0.54 cc/gm and 0.61 cc/gm respectively. The Brunauer Emmett–Teller (BET) surface areas of salen-CMP@Co and salen-CMP@Zn were determined to be 645 m^2/g and 717 m^2/g, respectively.

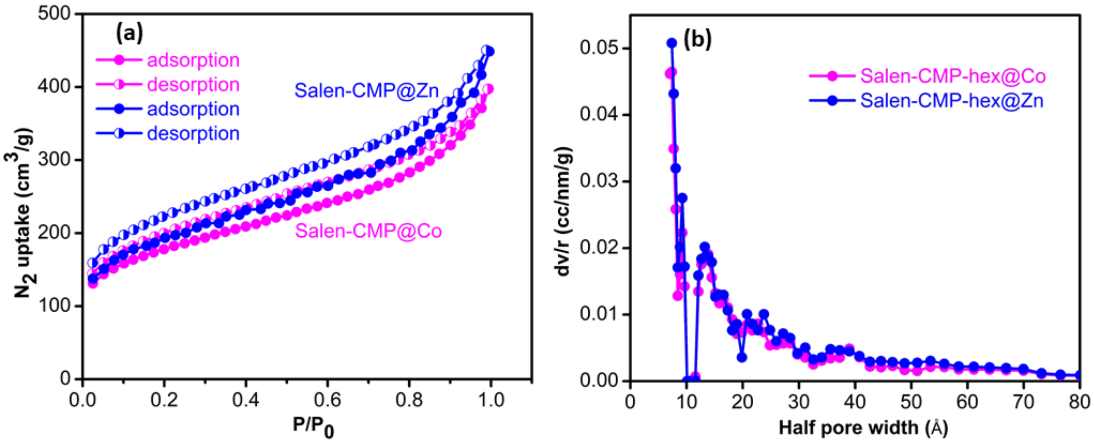

Figure 5.6: (a) N_2 adsorption and desorption isotherm of salen-CMP@Co and salen-CMP@Zn. (b) Pore size distribution curves of salen-CMP@Co and salen-CMP@Zn.

Among the two salen-CMPs, salen-CMP@Co was particularly noteworthy due to its superior catalytic performance under optimized conditions. Therefore, salen-CMP@Co was selected for further investigation through X-ray photoelectron spectroscopy (XPS) to investigate the chemical composition and to determine the oxidation state of cobalt within the framework. X ray photoelectron spectroscopy (XPS) analysis indicated the presence of all the expected elements, including C 1s, N 1s, O 1s, and Co 2p, in the salen-CMP@Co material (Figure 5.7). The deconvoluted C 1s XPS spectrum exhibited distinct binding energy peaks at 284.71 eV, 286.18 eV, and 288.69 eV, and 292.54 eV which can be attributed to C–C/C=C bonds, C=N imine functionalities, C–O and C≡C bonds respectively (Figure 5.7a).[34,35] The deconvoluted O 1s XPS spectrum revealed two distinct binding energy peaks at 531.76 eV and 533.37 eV, corresponding to C-O bonds and Co^{2+}–O interactions, respectively, indicating their presence within the polymeric framework (Figure 5.7b).[36] Similarly, the deconvoluted N 1s XPS spectrum of salen-CMP@Co displayed two binding energy peaks at approximately 400.2 eV and 399.32 eV, which can be attributed to metal-coordinated nitrogen (M^{2+}–N) and C–N bonds within the salen framework, respectively (Figure 5.7c).[37] Furthermore, the successful incorporation of Co^{2+} into the salen-CMP@Co framework was confirmed by the Co 2p XPS spectrum, which exhibited two characteristic peaks at 781.24 eV and 797.25 eV, corresponding to Co $2p_{3/2}$ and Co $2p_{1/2}$ of Co(II), respectively (Figure 5.7d).[38] Furthermore, the satellite peaks observed at 803.6 eV (Co $2p_{1/2}$) and 786.65 eV (Co $2p_{3/2}$) are indicative of +2 oxidation state of Co.[39]

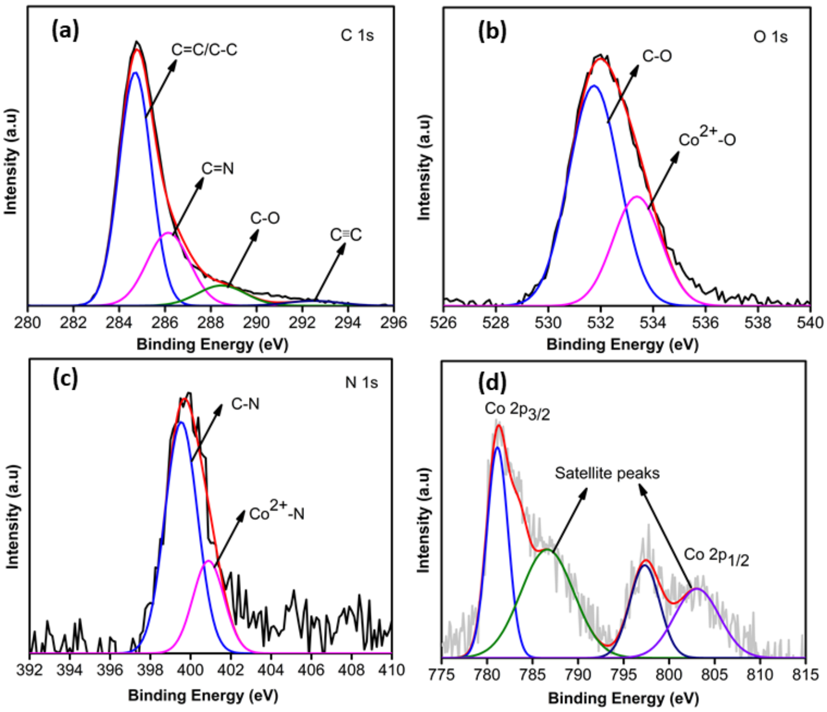

Figure 5.7: High-resolution XPS spectra corresponding to (a) C 1s, (b) O 1s, (c) N 1s, and (d) Co 2p core levels.

5.3.2 Photocatalytic CO_2 reduction

Upon successful synthesis of the photocatalysts salen-CMP@Co and salen-CMP@Zn, their efficiency towards photocatalytic CO_2 reduction was systematically investigated under visible light irradiation (λ > 400 nm). Photocatalytic CO_2 reduction was conducted in 5 mL of a mixed solvent system comprising H_2O, CH_3CN, and triethanolamine (TEOA), using 1 mg of the respective catalyst. The reaction system included $[Ru(bpy)_3]Cl_2\cdot 6H_2O$ as the photosensitizer, TEOA as the sacrificial electron donor, and 2,2′-bipyridine as the cocatalyst. The efficient photocatalytic reduction of CO_2 depends on the presence of all the essential components, including the sacrificial electron donor, photosensitizer, water, and catalyst. Each of these elements plays a crucial role and together they determine the overall performance of the photocatalytic system. The photocatalytic reduction of CO_2 using salen-CMP@Co and salen CMP@Zn led to the production of syngas (a mixture of CO and H_2 that serves as a key intermediate for the synthesis of various fuels). This CO_2 conversion to syngas approach has gained considerable interest in recent years due to its eco-friendly nature, high safety, and the ability to operate under mild reaction conditions.[40]

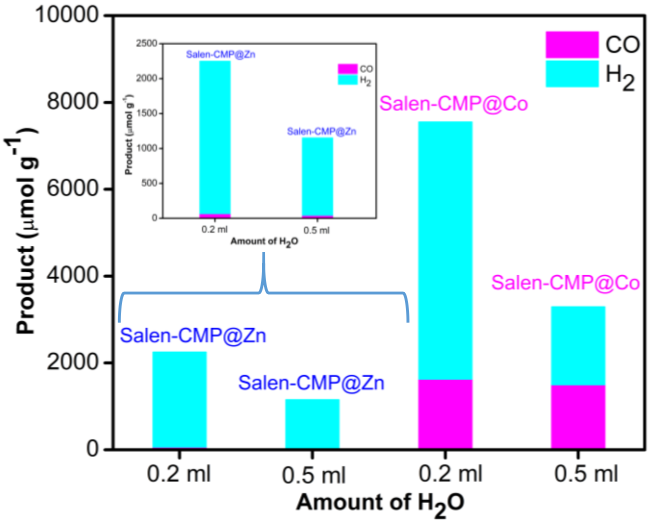

Figure 5.8: Photocatalytic activity of salen-CMP@Co and salen-CMP@Zn towards CO_2 reduction in varying amount of H_2O within 1 h photocatalytic run.

Based on the photocatalytic experiments, the Zn-containing catalyst, salen-CMP@Zn, demonstrated lower overall photocatalytic activity. It exhibited a H_2 evolution of 2188 μmol g^{-1} and CO evolution of 64 μmol g^{-1} under conditions using 0.2 mL of water within 1 h (Figure 5.8). Furthermore, increasing the water content to 0.5 mL in the CO_2 reduction reaction led to a decrease in overall photocatalytic activity, yielding 1115 μmol g^{-1} of H_2 and 40 μmol g^{-1} of CO (Figure 5.8). Notably, substituting Zn with Co as the catalytic center significantly enhanced the photocatalytic activity toward CO_2 reduction, showing a substantial increase in performance (Figure 5.8). Specifically, salen-CMP@Co with Co as the metal center produced 1628 μmol g^{-1} of CO and 5922 μmol g^{-1} of H_2 using 0.2 mL of water within 1 hour. However, when the water content was increased to 0.5 mL, the CO and H_2 yields decreased to 1499 μmol g^{-1} and 1796 μmol g^{-1}, respectively. These results clearly indicate that among the two photocatalysts, salen-CMP@Co exhibits superior photocatalytic activity for syngas generation. Therefore, extended photocatalytic CO_2 reduction experiments were performed using salen-CMP@Co, with varying H_2O content, to further explore the tunability of syngas composition. After 6 hours of continuous photo-irradiation, salen-CMP@Co generated 3041 μmol g^{-1} of CO and 20,212 μmol g^{-1} of H_2, corresponding to an H_2:CO ratio of approximately 6.6:1.0, using 0.2 mL of water in the solvent mixture (Figure 5.9a). While increasing the volume of H_2O (O.5 ml) in the solvent mixture, yields CO and H_2 evolution of 4073 μmol g^{-1} and 7029 μmol g^{-1} respectively with H_2:CO ratio of approximately 1.7:1.0 (Figure 5.9b). Hence, by varying the ratio of MeCN to H_2O in the solvent mixture we can significantly tune the amount of syngas production (Table 5.1). The syngas production values achieved using the salen-CMP@Co photocatalyst are comparable to those reported in previous studies (Table 5.2).

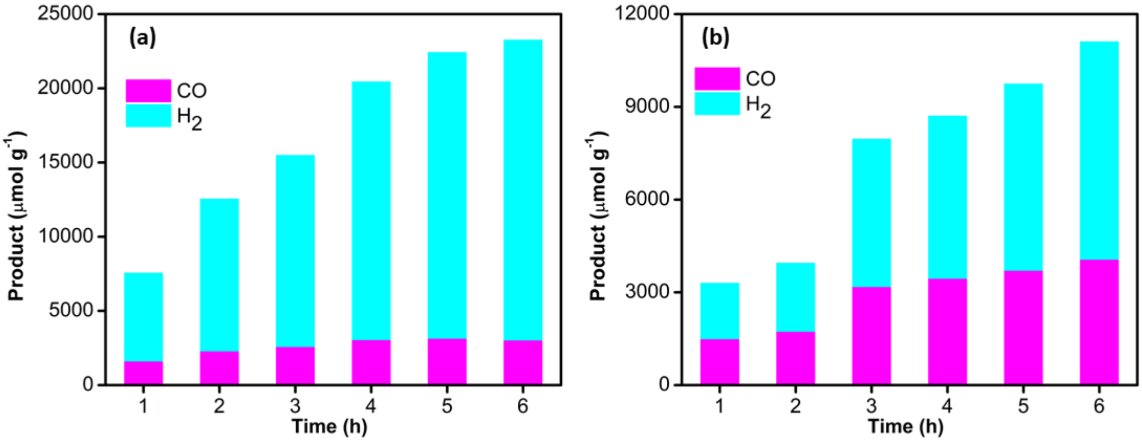

Figure 5.9: Time dependent photocatalytic CO_2 reduction over salen-CMP@Co using (a) MeCN (3.8 ml) + H_2O (0.2 ml) and (b) MeCN (3.5 ml) + H_2O (0.5 ml).

Table 5.1: Tunable syngas (CO + H_2) generation using salen-CMP@Co in varying acetonitrile–water (MeCN–H_2O) mixtures.

Solvent mixture (MeCN+H_2O)	Photocatalytic run time (h)	H_2 (µmol g^{-1})	CO (µmol g^{-1})	H_2:CO
MeCN (3.8 ml) + H_2O (0.2 ml)	1	5922	1628	3.6:1
MeCN (3.5 ml) + H_2O (0.5 ml)	1	1796	1499	1.2:1
MeCN (3.8 ml) + H_2O (0.2 ml)	6	20212	3041	6.6:1
MeCN (3.5 ml) + H_2O (0.5 ml)	6	7029	4073	1.7:1

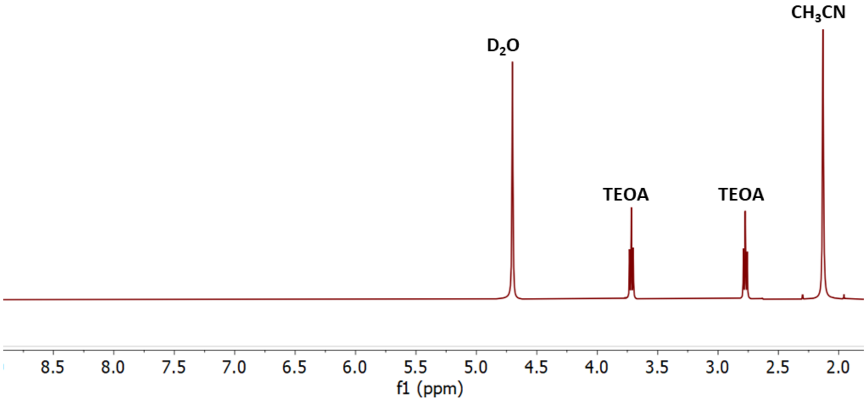

Figure 5.10: ^1H NMR spectrum of the reaction mixture obtained after photocatalytic CO_2 reduction.

Apart from CO and H_2, no additional liquid products such as CH_3OH, HCHO, C_2H_5OH, HCOOH were detected under the applied reaction conditions as revealed by the ^1H NMR spectroscopy of the reaction mixture (Figure 5.10). To elucidate the role of individual components in the enhanced syngas production over salen-CMP@Co, a series of controlled experiments were performed (Figure 5.11a). A marked decrease in H_2 and CO evolution to 2129 µmol g^{-1} and 779 µmol g^{-1} in the absence of H_2O indicates that H_2 generation likely originates from either H_2O or TEOA. Notably, the exclusion of TEOA from the reaction system resulted in an almost complete loss of photocatalytic activity, highlighting its essential role as a sacrificial electron donor. These observations imply that TEOA and H_2O function as the electron donor and proton source, respectively, in this photocatalytic CO_2 reduction system. Interestingly, the addition of 2,2′-bipyridine significantly enhanced CO and H_2 evolution, yielding 1628 µmol g^{-1} of CO and 5922 µmol g^{-1} of H_2, compared to just 395 µmol g^{-1} of CO and 1276 µmol g^{-1} of H_2 in its absence (Figure 5.11a), underscoring its role as a key co-catalyst. These findings confirm that TEOA, H_2O, and 2,2′-bipyridine are all critical for achieving high photocatalytic efficiency. The system exhibited no detectable photocatalytic performance in the absence of either the photosensitizer, indicating that electron transfer necessary for CO_2 conversion is driven by the photosensitizer under visible light irradiation (Figure 5.11a). In contrast, when the catalyst salen-CMP@Co was omitted, only trace amounts of CO (0.048 µmol) and H_2 (0.055 µmol) were detected. These observations highlight the essential role of each component in the photocatalytic system. Furthermore, when N_2 was used in place of CO_2, no CO formation was observed, confirming that the source of CO is indeed the reduction of CO_2 and not the degradation of the catalyst or the organic solvents such as TEOA and CH_3CN.

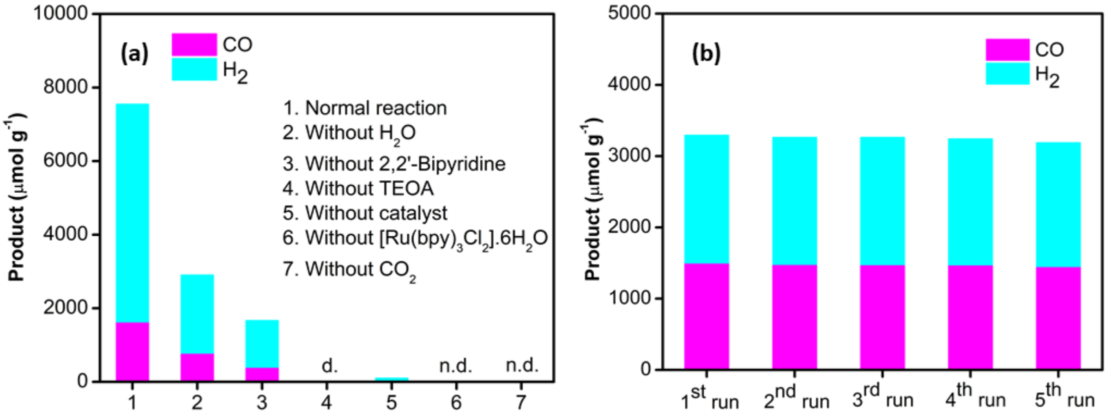

Figure 5.11: (a) Photocatalytic activity over salen-CMP@Co uder different conditions. (b) Recyclability test of salen-CMP@Co in MeCN (3.5 ml) and H_2O (0.5 ml) solvent mixture.

The catalyst's heterogeneous behavior was further validated through recyclability and reusability experiments (Figure 5.11b). The photocatalytic activity of salen-CMP@Co remained consistent over five consecutive 1-hour illumination cycles, indicating excellent long-term stability. Additionally, post-reaction analysis via PXRD and FT-IR revealed no significant changes, further supporting the structural stability of under photocatalytic conditions (Figure 5.12a, b).

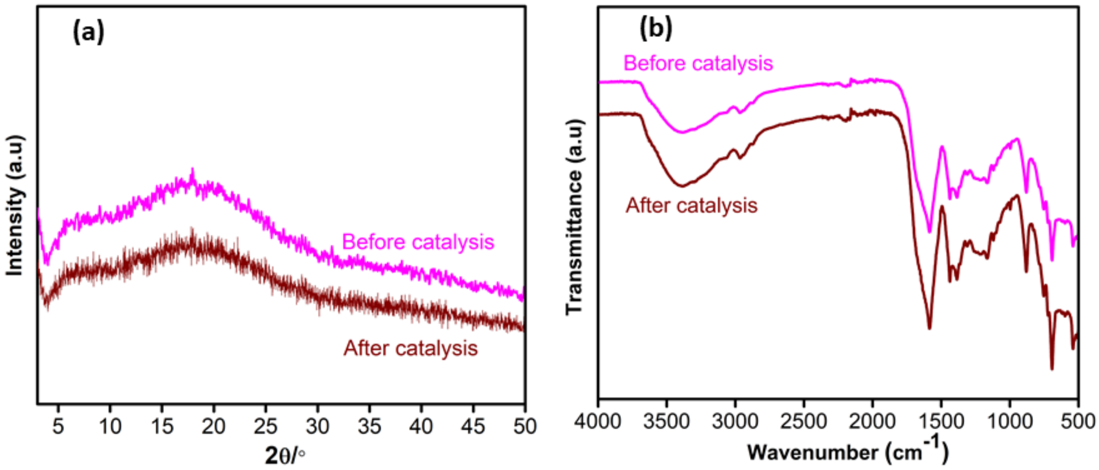

Figure 5.12: (a) PXRD pattern and (b) FT-IR spectra of salen-CMP@Co after and before photocatalysis

5.3.3 Plausible mechanisms

To provide the detailed understanding of the underlying mechanism of photocatalytic CO_2 reduction by the salen CMP@Co system, comprehensive photophysical and electrochemical characterizations were conducted. The photocatalytic performance is largely governed by two key parameters: the material's efficiency in absorbing visible light and its efficiency in generating and transporting photoinduced charge carriers. To assess the light-harvesting capabilities, solid state UV-Vis absorption spectra were recorded for both salen-CMP@Co and salen-CMP@Zn (Figure 5.13a). Both materials displayed a maximum absorption (λmax) at 325 nm. Using Tauc plots derived from the UV-Vis spectra, the optical band gaps were estimated to be 2.54 eV for salen-CMP@Co and 2.61 eV for salen-CMP@Zn (Figure 5.13c,d). To further investigate charge recombination behavior, photoluminescence (PL) spectroscopy was performed with excitation at 330 nm. Both catalysts showed emission peaks centered around 451 nm (Figure 5.13b). However, the PL intensity of salen-CMP@Co was significantly quenched in comparison to salen-CMP@Zn, indicating more efficient charge separation and a reduced recombination rate of photoinduced electron–hole pairs in the Co-based system.

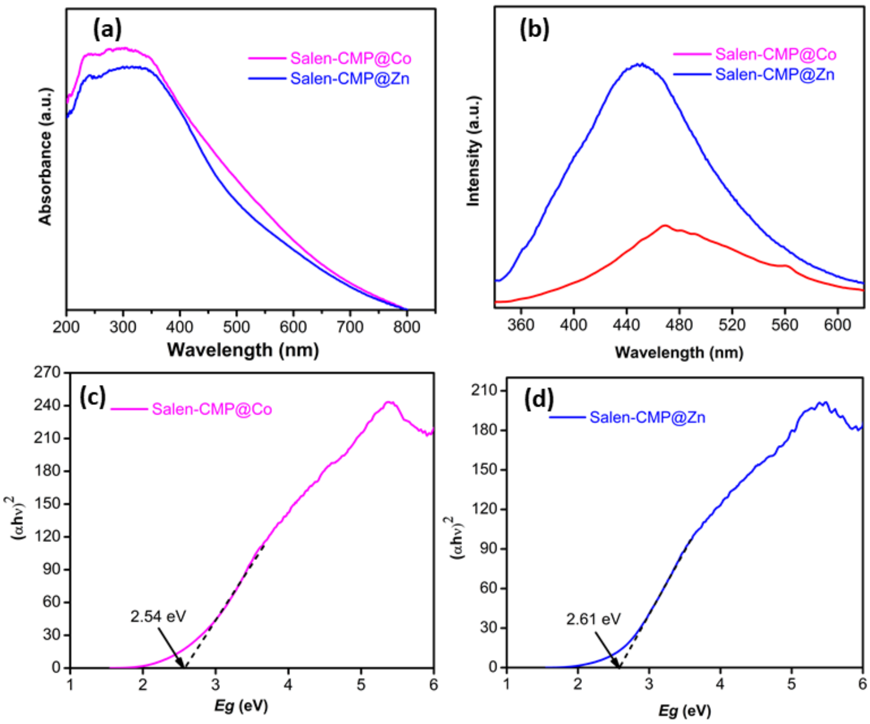

Figure 5.13: (a) Solid state UV-VIS spectra of salen-CMP@Co and salen-CMP@Zn. (b) Photoluminescence spectra of salen-CMP@Co and salen-CMP@Zn. (c) Tauc plot for salen-CMP@Co and (d) salen-CMP@Zn.

Electrochemical impedance spectroscopy was performed to study charge transfer characteristics of the materials. As shown in Figure 5.14, the Nyquist plot of salen CMP@Co exhibited a smaller semicircular diameter compared to that of salen-CMP@Zn, indicating a lower charge transfer resistance and enhanced electron mobility in the cobalt-based system. This improved charge transport efficiency is consistent with the higher photocatalytic performance observed for salen-CMP@Co. This observation is consistent with the photoluminescence study.

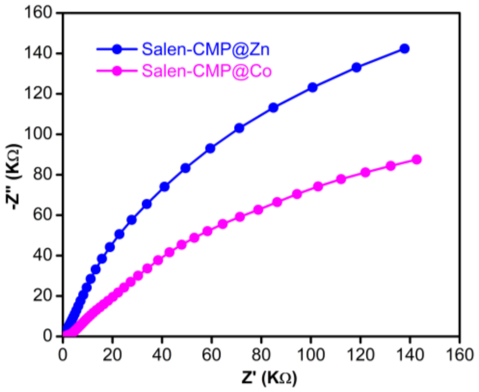

Figure 5.14: Electrochemical impedance spectroscopy of salen-CMP@Co and salen-CMP@Zn.

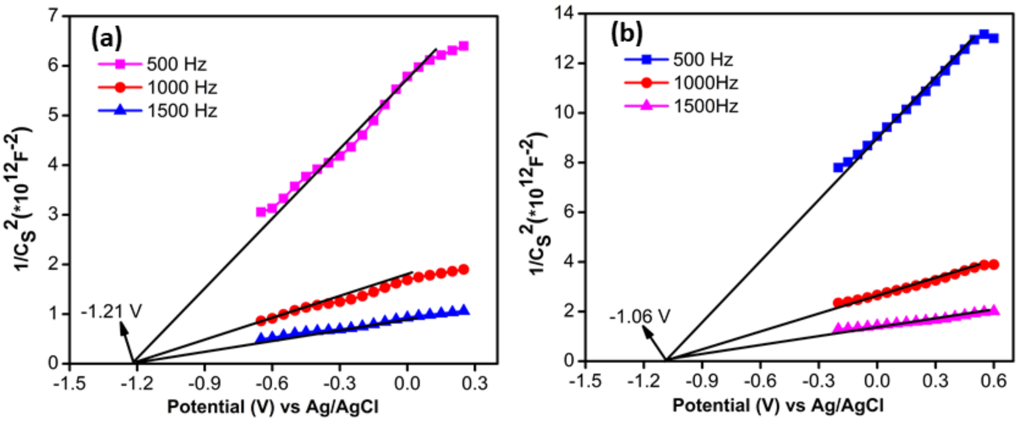

Figure 5.15: Mott-Schottky plot of (a) salen-CMP@Co and (b) salen-CMP@Zn showing flat band.

To assess the suitability of the material for photocatalytic CO_2 reduction, Mott–Schottky (M–S) measurements were conducted at three distinct frequencies (500, 1000, and 1500 Hz) in a 0.2 M Na_2SO_4 electrolyte solution at pH 7 (Figure 5.15). The positive slope in the Mott-Schottky plot confirmed the n-type semiconductor behavior of salen-CMP@Co and salen-CMP@Zn. The flat-band potential (V_{fb}) was determined to be –1.21 V and –1.06 V vs. Ag/AgCl (i.e., –1.01 V and –0.86 V vs. NHE) at pH 7 for salen-CMP@Co and salen-CMP@Zn respectively. In n-type semiconductors, the conduction band minimum is typically considered to be closely aligned with the flat-band potential.[19] Based on this approximation, the conduction band (CB) edge was estimated to lie at approximately –1.01 V and –0.86 V versus the normal hydrogen electrode (NHE) for salen-CMP@Co and Salen-CMP@Zn respectively, which is more negative than the standard reduction potentials for both CO_2 to CO (−0.53 V) and H_2O to H_2 (−0.41 V), as shown in Figure 5.16(a). Using the V_{CB} value and the optical band gap derived from the Tauc plot, the valence band (VB) edge for salen-CMP@Co and salen-CMP@Zn was estimated to be 1.53 V and 1.75 V vs. NHE respectively. These band structure parameters suggest that the reduction potential of CMPs lies between that of the excited-state $[Ru(bpy)_3]^{2+}$ complex (−1.25 V vs. NHE) and the thermodynamic potential for CO_2-to-CO conversion (−0.53 V vs. NHE) (Figure 5.16a).[19,38] This positioning implies that photoinduced electrons from $[Ru(bpy)_3]^{2+}$ can be effectively transferred to salen-CMPs, which in turn facilitates the reduction of CO_2 to CO through subsequent electron transfer steps.

Based on the preceding experimental findings and analysis, a plausible photocatalytic mechanism for CO_2 reduction is proposed, as illustrated in Figure 5.16. Upon visible light irradiation, $[Ru(bpy)_3]^{2+}$ become photoexcited, generating electron–hole pairs. The excited

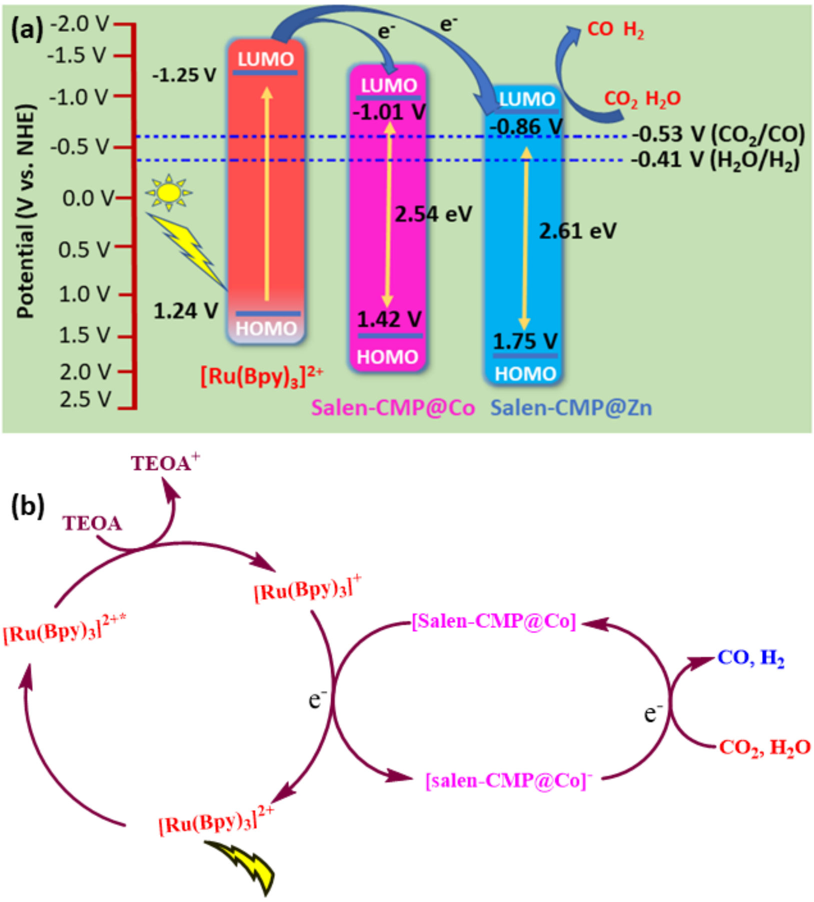

Figure 5.16: (a) Energy level diagram of $[Ru(bpy)_3]^{2+}$, salen-CMP@Co, and salen-CMP@Zn, illustrating the favourable electron transfer pathways for photocatalytic CO_2 reduction. (b) Possible CO_2 Photoreduction cycle.

state $[Ru(bpy)_3]^{2+}*$ is subsequently quenched by triethanolamine (TEOA) through a reductive pathway, yielding the reduced species $[Ru(bpy)_3]^{+}$. This reduced photosensitizer then acts as an electron donor, transferring the photogenerated electrons to the cobalt catalytic sites embedded within the framework, thereby facilitating the reduction of CO_2, H_2O to CO and H_2 leading to the formation of syngas. Notably, in the control experiments we have observed a significant hydrogen production in the absence of H_2O which indicate that the protons also coming from the TEOA as it can also act as proton donor. The surplus protons provided by TEOA in the reaction environment can be readily reduced to produce H_2 by photoexcited electrons.

5.4 Conclusion

In summary, we have successfully developed two novel metal–salen-based CMPs named as salen-CMP@Co and salen-CMP@Zn, exhibited excellent stability and efficiency for visible light-driven CO_2 photoreduction. These materials demonstrate remarkable capability in converting CO_2 into syngas (a mixture of CO and H_2), offering tunable product ratios and strong potential for sustainable solar-to-fuel applications. Among the synthesized catalysts, salen CMP@Co exhibited the highest photocatalytic performance, significantly outperforming its zinc-based counterpart, salen-CMP@Zn. Salen-CMP@Co exhibited enhanced CO and H2 evolution of 779 μmol g^{-1} and 2129 μmol g^{-1} respectively within 1 hr. We have controlled the syngas production by varying the acetonitrile:water ratio. The ratio of H_2:CO can be tuned from 6.6:1 to 1.7:1 by using different acetonitrile and water ratio. Overall, this study presents an innovative approach for the photocatalytic production of syngas with a tunable H_2/CO ratio, offering valuable flexibility for meeting diverse industrial and energy-related demands.

5.5 References

1. T.-Z. Ang, M. Salem, M. Kamarol, H. S. Das, M. A. Nazari, and N. Prabaharan, *Energy Strategy Reviews*, 2022, **43**, 100939.
2. N. Yusuf, F. Almomani and H. Qiblawey, *Fuel*, 2023, **345**, 128178.
3. S. Fang, M. Rahaman, J. Bharti, E. Reisner, M. Robert, G. A. Ozin and Y. H. Hu, *Nat. Rev. Methods Primers*, 2023, **3**.
4. Y. Wang, N.Y. Huang, J.Q. Shen, P.Q. Liao, X.M. Chen and J.P. Zhang, *J. Am. Chem. Soc.*, 2018, ***140***, 38-41.
5. W. Zhu, C.F. Zhang, Q. Lia, L.K. Xiong, R.X. Chen, X.B. Wan, Z. Wang, W. Chen, Z. Den G and Y. Peng, *Appl. Catal. B: Environ.*, 2018, **238**, 339-345.
6. S. Chu, S. Z. Fan, Y. Wang, D. Rossouw, Y. Wang, G.A. Botton and Z.T. Mi, *Angew. Chem. Int. Ed.*, 2016, **55**, 4262-14266.
7. Y. Cao, Z.Y. Gao, J. Jin, H.C. Zhou, M. Cohron, H.Y. Zhao, H.Y. Liu and W.P. Pan, *Energy Fuels*, 2008, **22**, 1720-1730.
8. P. Furler, J.R. Scheffe and A. Steinfeld, *Energy Environ. Sci.*, 2012, **5**, 6098-6103.
9. J.S. Lee, D.I. Won, W.J. Jung, H.J. Son, C. Pac and S.O. Kang, *Angew. Chem. Int. Ed.*, 2017, **56**, 976-980.
10. M.E. Dry, *Catal. Today*, 2002, **71**, 227-241.
11. P. Huang, J. Huang, S. A. Pantovich, A. D. Carl, T. G. Fenton, C. A. Caputo, R. L. Grimm, A. I. Frenkel and G. Li, *J. Am. Chem. Soc.* 2018, **140**, 16042–16047.
12. R. Kuriki, M. Yamamoto, K. Higuchi, Y. Yamamoto, M. Akatsuka, D. L. Lu, S.Yagi, T. Yoshida, O. Ishitani, K. Maeda, *Angew. Chem., Int. Ed.*, 2017, **56**, 4867–4871

13. J. S. Lee, D. I. Won, W. J. Jung, H. J. Son, C. Pac and S. O. Kang, *Angew. Chem., Int. Ed.*, 2017, **56**, 976–980.

14. T. W. Woolerton, S. Sheard, E. Reisner, E. Pierce, S. W. Ragsdale and F. A. Armstrong, *J. Am. Chem. Soc.*, 2010, **132**, 2132–2133.

15. P. Li, Y. Zhou, Z. Zhao, Q. Xu, X. Wang, M. Xiao and Z. Zou, *J. Am. Chem. Soc.*, 2015, **137**, 9547–9550.

16. X. Li, Y. Sun, J. Xu, Y. Shao, J. Wu, X. Xu, Y. Pan, H. Ju, J. Zhu and Y. Xie, *Nature Energy*, 2019, **4**, 690–699.

17. J. Wang, T. Xia, L. Wang, Z. Xheng, Z. Qi, C. Gao, J. Zhu, Z. Li, H. Xu and Y. Xiong, *Angew. Chem., Int. Ed.*, 2018, **50**, 16447–16451.

18. U. Ulmer, T. Dingle, P. N. Duchesne, R. H. Morris, A. Tavasoli, T. Wood and G. A. Ozin, *Nat. Commun.*, 2019, **10**, 3169.

19. A. Jana, A. Maity, A. Adalder, S. Saha and Asamanjoy Bhunia, *Nanoscale*, 2025,**17**, 12235-12244.

20. A. Jana, S. Saha, S. S. Mondal, N. Kaur, A. Bhunia, *Chem Asian J*., 2025, **20**, e20240140.

21. D. A.Popov, J.M. Luna, N.M. Orchanian, R. Haiges, C.A. Downes, and S.C. Marinescu, *DaltonTrans.*, 2018, **47**, 17450−17460.

22. E.M. Johnson, R. Haiges and S.C. Marinescu, *ACS Appl. Mater. Interfaces*, 2018, **10**, 37919−37927.

23. C. Yang, W. Huang, L.C. daSilva, K. A. I. Zhang and X. Wang, *Chem.-Eur. J.*, 2018, **24**, 17454−17458.

24. C.L. Smith, R. Clowes, R.S. Sprick, A.I. Cooper, and A. J. Cowan, *Sustainable Energy Fuels*, 2019, **3**, 2990−2994.

25. C. Gu, N. Huang, Y. Chen, L. Qin, H. Xu, S. Zhang, F. Li, Y. Ma and D. Jiang, *Angew.Chem., Int.Ed.*, 2015, **54**,13594−13598.

26. Y. Xie, T.-T Wang, X.-H. Liu, K. Zou and W.-Q. Deng, *Nat. Commun.*, 2013, **4**, 1960.

27. F. A. Rahimi, A. Singh, R. Jena, A. Dey, and T. K. Maji, *ACS Appl. Mater. Interfaces,* 2024, **16**, 43171−43179.

28. W. Wu, C. Dai, M. Wu, Y. Chen, C. Zeng and F. Li, *Solar RRL*, 2023, **2**, 2200907.

29. W. Wu, M. Chen and Y. Deng, *Polym. Chem*., 2023, **40**, 4679-4684.

30. F. Zhou, Q. Deng, N. Huang, W. Zhou, and W. Deng, *Chemistry Select,* 2020, **5**, 10516 10520.

31. C. Dai, L. Zhong, X. Gong, L. Zeng, C. Xue, S. Li and B. Liu, *Green Chem.*, 2019, **21**, 6606−6610.

32. X. Yu, Z. Yang, B. Qiu, S. Guo, P. Yang, B. Yu, H. Zhang, Y. Zhao, X. Yang, B. Han and Z. Liu, *Angew. Chem., Int. Ed.*, 2019, **58**, 632−636.

33. K. S. Sing, *Pure Appl. Chem.*, 1985, **57**, 603.

34. S. R. V. Parambil, F. A. Rahimi, R. Ghosh, S. Nath and T. K. Maji, *Inorg. Chem.*, 2023, **62**, 19312–19322.

35. F. A. Rahimi, S. Dey, P. Verma, and T. K. Maji, *ACS Catal.*, 2023, **13**, 5969−5978.

36. a) R. Paul, S. C. Shit, T. Fovanna, D. Ferri, B. Srinivasa Rao, G. T. K. K. Gunasooriya, D. Q. Dao, Q. V. Le, I. Shown, M. P. Sherburne, Q. T. Trinh and J. Mondal, *ACS Appl. Mater. Inter faces*, 2020, **12**, 50550–50565; b) T. Senthamarai, V. G. Chandra shekhar, M. B. Gawande, N. V. Kalevaru, R. Zbořil, P. C. J. Kamer, R. V. Jagadeesh and M. Beller, *Chem. Sci.*, 2020, **11**, 2973-2981.

37. R. Paul, R. Das, N. Das, S. Chakraborty, C.-W. Pao, Q. T. Trinh, G. T. K. K. Gunasooriya, J. Mondal, and S. C. Peter, *Angew.Chem. Int.Ed.*, 2023, **62**, e202311304.

38. A. Jana, A. Maity, A. Sarkar, B. Show, P. A. Bhobe and A. Bhunia, J. Mater. Chem. A, 2024, **12**, 5244-5253.

39. P. F. Ji, Y. Song, T. Drake, S. S. Veroneau, Z. K. Lin, X. D. Pan and W. B. Lin, J. *Am. Chem.*
Soc., 2018, **140**, 433–440.

40. A. Virgil, R. Bertrand and R. Erwin, *Nat. Mater.*, 2020, **19**, 189–194.

Chapter 6

Summary

Harnessing solar energy for CO_2 reduction presents a sustainable and environmentally friendly approach to address both energy and climate challenges. Converting carbon dioxide into solar fuels through artificial photosynthesis is a vital strategy in achieving a closed carbon cycle and advancing renewable energy technologies. In this context, the development of efficient materials for CO_2 transformation into value-added chemical fuels represents a key research focus in contemporary materials chemistry. While inorganic semiconductors like metal oxides have been extensively explored for this purpose, their limited tunability in electronic band structures often restricts their effectiveness. Similarly, homogeneous molecular catalysts, although synthetically flexible, generally suffer from poor stability during extended use.

In contrast, porous materials such as metal–organic frameworks (MOFs), covalent organic frameworks (COFs), conjugated microporous polymers (CMPs), and covalent triazine frameworks (CTFs) have emerged as promising candidates for photocatalytic CO_2 conversion. These materials offer exceptional surface areas, chemical and thermal robustness, adjustable pore structures, and functional tunability, making them well-suited for photocatalytic applications.

In this thesis, we focused on the rational design and synthesis of MOFs, CTFs and CMPs as porous scaffolds to introduce redox-active metal centers and metal coordination complexes, through various post-synthetic modification strategies with the aim of developing efficient photocatalysts for CO_2 reduction. These engineered materials were systematically studied for their photocatalytic performance in CO_2 reduction. The main outcomes and insights derived from this work are summarized below:

In chapter 2, we report the successful synthesis of a chemically and thermally robust covalent triazine framework (CTF-TPE) constructed from tetra(4-cyanophenyl) ethylene (TPE) under solvothermal conditions using trifluoromethanesulfonic acid (CF_3SO_3H) as a catalyst. The structural and physicochemical properties of the CTF-TPE were comprehensively characterized by X-ray photoelectron spectroscopy (XPS), powder X-ray diffraction (PXRD), thermogravimetric analysis (TGA), scanning electron microscopy (SEM), infrared (IR) spectroscopy, and solid-state ^{13}C CP-MAS NMR spectroscopy. The resulting material exhibited a high surface area of 434 m^2/g.

We have used this framework as solid supports for anchoring Co^{2+} single metal sites within the framework through N atom of the triazine ring to develop robust single atom photocatalyst. The presence of atomically dispersed cobalt was confirmed using extended X-ray absorption fine structure (EXAFS) spectroscopy,extended X-ray absorption near-edge structure (XANES) spectra, XPS, and high-angle annular dark-field scanning transmission electron microscopy (HAADF-STEM). The resulting single-atom catalyst, Co@CTF-TPE system demonstrated outstanding performance in photocatalytic CO_2 reduction, achieving a CO evolution rate of 6616 μmol/g over 7 hours under visible light irradiation, surpassing many previously reported CTF-based catalysts.

Moreover, the catalyst exhibited excellent stability and reusability, maintaining consistent CO production over five consecutive cycles. Photophysical and electrochemical analyses indicated that the incorporation of isolated Co^{2+} sites significantly enhanced charge separation and transfer while suppressing electron-hole recombination. We have also give forward a plausible plausible mechanism for the photocatalytic CO_2 reduction. These results highlight the potential of single-atom cobalt-modified CTFs as a promising platform for efficient and durable photocatalytic CO_2 reduction.

In Chapter 3, the imidazolate framework Potsdam (IFP) was selected as a platform due to its exceptional chemical stability and accessible sites for post-synthetic functionalization. This study focuses on the development of transition metal-based photocatalysts using the IFP structure, a subclass of zeolitic imidazolate frameworks (ZIFs), which features pentacoordinated secondary building units of Zn(II) in IFP-1(Zn) and Co(II) in IFP-5(Co), bridged by 2-methylimidazolate-4-amide-5-imidate (MIAI) linkers. Furthermore, a bimetallic photocatalyst, IFP-1(Zn/Co), was synthesized by partially replacing the redox-inactive Zn(II) with redox-active Co(II) in IFP-1(Zn), enabling the study of cooperative effects in photocatalysis. A comparative evaluation of the photocatalytic activity of IFP-1(Zn), IFP-5(Co), and the bimetallic IFP-1(Zn/Co) was conducted to assess their performance in CO_2 reduction. The efficiency of photocatalytic CO_2 conversion of the synthesized catalysts demonstrated a clear trend in activity: IFP-1(Zn) < IFP-1(Zn/Co) < IFP-5(Co). IFP-1(Zn) showed limited photocatalytic efficiency, yielding only 29 $\mu mol\ g^{-1}$ of CO and 24 $\mu mol\ g^{-1}$ of H_2 within 1 hour, indicating its inadequacy for effective CO_2 photoreduction. Incorporation of Co^{2+} ions into IFP-1(Zn) via metal ion exchange significantly enhanced its catalytic behavior, with the resulting IFP-1(Zn/Co) achieving 636 $\mu mol\ g^{-1}$ of CO and 1036 $\mu mol\ g^{-1}$ of H_2 in the same duration. Extended photocatalytic evaluation of IFP-5(Co) over 5 hours further confirmed its robustness, with cumulative CO and H_2 production reaching 10,301 $\mu mol\ g^{-1}$ and 6868 $\mu mol\ g^{-1}$, respectively corresponding to the production rates of 2060 $\mu mol\ g^{-1}\ h^{-1}$ and 1373 μmol g^{-1} h^{-1}. These results underscore the critical role of Co centers in enhancing photocatalytic activity and establish IFP-5(Co) as a highly promising candidate among MOF-based photocatalysts for efficient CO_2 reduction. To understand the mechanisms behind the CO_2 reduction process, a thorough study combining photophysical characterization, electrochemical analysis, and Density Functional Theory (DFT) calculations was conducted. This study highlights the promise of IFP-based MOFs and strategic metal ion substitution as effective approaches for designing advanced photocatalysts aimed at sustainable CO_2 conversion.

In Chapter 4, we synthesized a redox-active ruthenium (II) complex, $[Ru(cptpy)_2]$ (where cptpy = 4′-(4-carboxyphenyl)-2,2′:6′,2″-terpyridine), designed for photocatalytic CO_2 reduction. This metallo-ligand was successfully integrated into a robust Zr-NDI metal-organic framework (MOF) using two synthetic approaches: solvent-assisted ligand exchange (SALE) and mixed-ligand solvothermal synthesis. The resulting hybrid materials, denoted as Zr-NDI@Ru-tpy and Zr-NDI@Ru-tpy-m. Comprehensive characterization including ^{1}H NMR, FT-IR, PXRD, UV-Vis spectroscopy, X-ray photoelectron spectroscopy (XPS), and cyclic voltammetry verified the successful incorporation of the $[Ru(cptpy)_2]$ complex into the MOF scaffold. Under visible-light irradiation in the presence of BIH and TEOA as sacrificial electron donors, and $[Ru(bpy)_3]^{2+}$ as a photosensitizer in DMF, Zr-NDI@Ru-tpy exhibited exceptional photocatalytic activity, achieving CO and H_2 evolution of 14,698 μmol g^{-1} and 606 μmol g^{-1}, respectively, over 6 hours. Notably, the CO selectivity reached ~97%, and the turnover number (TON) was calculated to be 123, significantly higher than the homogeneous $[Ru(cptpy)_2]$ complex, which showed a TON of only 48 under identical conditions. This enhancement in photocatalytic activity can be ascribed to the presence of NDI units in the MOF, which likely serve as electron mediators or reservoirs, promoting more efficient charge separation and transfer. In situ diffuse reflectance infrared Fourier transform (DRIFT) spectroscopy provided evidence for CO_2 adsorption and activation on the catalyst surface, revealing the formation of the COOH* intermediate as a key step in the reaction pathway. Based on photophysical, electrochemical, and in situ spectroscopic analyses, a plausible reaction mechanism has been proposed.

Overall, this study demonstrates that anchoring redox-active molecular catalysts within MOF matrices can significantly improve their photocatalytic efficiency, stability, and recyclability, offering a promising strategy for the development of advanced materials for CO_2 reduction.

In Chapter 5, we successfully designed and synthesized two novel metal–salen-based conjugated microporous polymers, denoted as salen-CMP@Co and salen-CMP@Zn. These frameworks were constructed via a Sonogashira–Hagihara C–C coupling reaction, employing Salen-Co/Zn complexes and 1,3,5-triethynylbenzene as the core building blocks. The polymers obtained were systematically analyzed through a range of characterization methods, including FT-IR spectroscopy, solid-state ^{13}C NMR, nitrogen adsorption–desorption isotherms, powder X-ray diffraction (PXRD), thermogravimetric analysis (TGA), field-emission scanning electron microscopy (FE-SEM), and X-ray photoelectron spectroscopy (XPS), to comprehensively assess their structural, thermal, morphological, and surface chemical properties. These materials were applied as photocatalysts for visible-light-driven CO_2 reduction and proved to be potential candidate to generate syngas (a valuable mixture of CO and H_2) in significant quantities. Among the two catalysts, salen-CMP@Co exhibited superior photocatalytic performance compared to its zinc-based counterpart, salen-CMP@Zn, achieving CO and H_2 evolution rates of 3041 $\mu mol\,g^{-1}$ and 20,212 $\mu mol\,g^{-1}$, respectively. Notably, the syngas composition could be effectively tuned by varying the acetonitrile-to-water ratio in the reaction medium. Given the limited number of studies exploring conjugated microporous polymers (CMPs) as photocatalysts for CO_2 reduction, this work offers a promising foundation for creating enhanced CMP-based materials with improved stability and efficiency for solar fuel applications.

Taken together, the findings presented in this thesis clearly demonstrate that covalent triazine frameworks (CTFs), metal-organic frameworks (MOFs) and conjugated microporous materials (CMPs) serve as highly effective porous scaffolds for anchoring molecular catalysts or redox-active metal centers. These hybrid materials enable the construction of robust heterogeneous photocatalysts capable of facilitating CO_2 reduction under various experimental conditions. The synthesized catalysts exhibit notable activity under visible-light irradiation, efficiently driving the photocatalytic CO_2 reduction to CO and H_2, thereby highlighting their potential for solar-to-chemical energy conversion applications.

Photocatalytic CO_2 reduction remains a significant challenge, particularly when aiming to generate valuable products such as methane or methanol. These products, while more difficult to obtain, are also more desirable due to their practical applications. Achieving this without relying on sacrificial electron donors remains a key hurdle. Ideally, future systems will use only water as the electron source, paired with earth-abundant cocatalysts and low-cost porous semiconductors. This thesis highlights the potential of MOFs, CTFs and CMPs as promising platforms for photocatalytic CO_2 reduction, primarily due to their high surface area, tunable porosity, and the capacity to precisely engineer functional sites at the molecular level. However, their practical viability depends on ensuring sufficient structural and chemical stability under reaction conditions. Strategies such as incorporation of single metal sites, metal ion exchange, and solvent-assisted ligand exchange have been employed here to enhance photocatalytic efficiency. It is anticipated that the findings presented will inspire continued development of porous organic and organic-inorganic hybrid materials for photocatalytic CO_2 reduction, moving closer to the ultimate goal of producing useful carbon-based fuels without the need for sacrificial agents.

List of Publications

1. **A. Jana**, A. Maity, A. Sarkar, B. Show, P. A. Bhobe and A. Bhunia, *J. Mater. Chem. A*, 2024, **12**, 5244-5253.

2. **A. Jana**, S. Saha, S. S. Mondal, N. Kaur, A. Bhunia, *Chem Asian J.*, 2025, **20**, e202401401.

3. **A. Jana**, A. Maity, S. Saha, A. Adaldar, Asamanjoy Bhunia, *Nanoscale, 2025, Just Published.*

4. **A. Jana**, J. Mandal, S. S. Mondal, R. Patra, A. Bhunia, *Inorganica Chimica Acta*, 2023, **549**, 121409.

5. O. Ali, **A. Jana**, A. Das, S. K. Dey, A. Bhunia, *Materials Advances*, 2024, **5**, 4720-4727.

6. A. Das, O. Ali, S. Paul, **A. Jana**, A Bhunia, *Inorganica Chimica Acta*, 2024, **570**, 122163.

7. A. Maity, M. Siebels, **A. Jana**, M. Eswaran, R. Dhanusuraman, C. Janiak, *ChemSusChem*, 2025, 18, e202401716.

8. A. Maity, **A. Jana**, S. Dey, C. Janaick, A. Bhunia, *Mater. Adv., 2025, Advance Article*.

9. A. Jana, S. Saha, A. Bhunia, Metallosalen-Integrated Conjugated Microporous Polymers for scalable Syngas Production from Visible-Light-Driven CO_2 Reduction (***In Preparation***).